# Assessing the performance of forthcoming Infrared telescopes

Bisigello, Laura

rijksuniversiteit
groningen

# Assessing the performance of forthcoming Infrared Telescopes

**PhD thesis**

to obtain the degree of PhD at the
University of Groningen
on the authority of the
Rector Magnificus, prof.dr. E. Sterken,
and in accordance with
the decision by the College of Deans.

This thesis will be defended in public on

Monday 13 November 2017 at 14.30 hours

by

**Laura Bisigello**

born on 7 august 1988
in Vicenza, Italia

**Supervisors**
Prof. A.M. Baryshev
Prof. K.I. Caputi
Prof. P. van der Werf

**Co-supervisor**
Dr. S.J.C. Yates

**Assessment Committee**
Prof. P. de Bernardis
Prof. H. Dole
Prof. S. Trager

ISBN: 978-94-034-0014-3 (printed version)
ISBN: 978-94-034-0013-6 (electronic version)
Cover: Artist's concept of the James Webb Space Telescope and the Atacama Pathfinder Experiment observing galaxies in the sky. Drew and painted by Tommaso Bertola, Laura Bisigello and Ornella Dalla Pozza

# Contents

# 1. Introduction

Less than a century ago our view of the Universe expanded from our own Milky Way to a vast Universe populated with numerous galaxies. It was thanks to the pioneer study of E. Hubble (1925), who measured the distance of NGC 6822, that astronomers understood that the nebulae that they were observing were other galaxies outside the galactic system. From that moment galaxies have been studied as building blocks of the Universe and the frontier of their observations has been pushing farther and farther away every decade.

Hubble's work was not limited to the derivation of galaxy distances, but he also laid the foundations for the study of galaxy formation and evolution with his morphological classification of galaxies. Indeed, in the famous Hubble Sequence, galaxies are classified as early type, i.e. elliptical galaxies, and late types, i.e. spirals, depending on their morphological appearance. Indeed, Hubble's idea was that elliptical galaxies would evolve into disk galaxies, because of the old ages of their stellar populations (Hubble, 1936). It is now clear that gravitational instabilities can result on the disruption of the disk, but the morphology of a galaxy is anyway the results of its evolutionary track. The large variety of galaxy morphologies are indeed a clear indicator of the variety of processes involved in the evolution of a galaxy.

Another way to study galaxy evolution is to investigate their stellar masses and instantaneous star formation, to compare the mass build-up on different time scales. The analyses of these quantities have shown that the majority of galaxies show a tight relation between the star-formation-rate (SFR) and the stellar masses indicating a quasi-steady, long-lasting mode of star formation (Noeske et al., 2007; Rodighiero et al., 2011). Other galaxies, instead, show extremely high star formation activity or almost no star formation. These different modes are due to the interplay between gas outflows and inflows, due to supernovae, star winds, active galactic nuclei, cold inflows, mergers and gravitational instabilities. Moreover, when looking at the integrated star-formation-rate density of the Universe, this is not constant over time, but evolves with redshifts with a maximum around z$\sim$2 ($\sim$10 Gyr ago; Behroozi et al., 2013; Madau & Dickinson, 2014). Therefore, the study of the formation and evolution of galaxies needs to be performed on a wide range of wavelengths, to have a clear picture of different phenomena, and at different redshifts, to understand its evolution with time.

Technology development has always been an important aspect of astronomy. For example, Galileo Galilei's observations of Jupiter's moons with an early telescope was revolutionary for astronomy and our understanding of our place in the Universe. In the last decades, thanks to the boom of computer technology and the development of big facilities, observations of galaxies have been pushed to very high redshifts and widened to a large wavelength range. For example, the Cosmic Background Explorer (COBE) measured the cosmic infrared background. With this observation it led to the knowledge that half of the energy produced by star formation and accretion activity throughout the history of the Universe is emitted in the infrared (IR, 3-1000 $\mu$m) part of the spectrum (Puget et al., 1996; Dole et al., 2006). This range of the electromagnetic spectrum is important to observe both the obscure stellar light of low- and medium redshift galaxies, which is absorbed and re-emitted by dust, and the rest-frame optical light of high redshift galaxies, which is redshifted to infrared wavelengths.

The goal of this PhD thesis is to study different aspects of the performance of future key infrared instruments to study galaxy evolution. In particular, I focus on the expected instrumental performance of the Apex Microwave Kinetic Inductance Detector (A-MKID), which will be operational on the APEX telescope and the imaging cameras (MIRI and NIRCam) for the *James Webb Space Telescope* (JWST). In addition, I conduct a study of the SFR-stellar mass plane with available optical-to-far-IR data up to z=3.

## 1.1 THE GALAXY SPECTRAL ENERGY DISTRIBUTION

The spectral energy distribution (SED) of a galaxy is the distribution of emitted light as a function of wavelength, and it is our main source of information about unresolved galaxy properties. Each part of the SED is dominated by different physical processes whose contribution varies among different type of galaxies. In particular, focusing on the rest-frame ultraviolet (UV) to sub-millimetre (sub-mm) considered in this thesis, the SED of a galaxy can be separated into two parts: a first one dominated by the direct stellar light ($\lambda < 3\mu$m) and a second part dominated by stellar light re-radiated by dust. Figure 1.1 shows some examples of the rest-frame UV-to-mm of the SED of different types of galaxies, with different star formation activities and dust extinctions.

In particular, focusing on the part dominated by dust emission in star-forming galaxies, between 3 and 17 $\mu$m, there are multiple broad emission line features originated from small carbonaceous grains, i.e. polycyclic aromatic hydrocarbons (PAH), which predominately originate from photodissociation regions illuminated by UV-bright stars (see Desert et al., 1986; Dale & Helou, 2002; Tielens, 2008, among others). The SED at $\lambda = 17 - 80\,\mu$m is dominated by warm dust grains heated by energetic photons produced by young stars or active galactic nuclei (AGN; Sturm et al., 1999). Finally, the SED at longer wavelength is dominated by the UV-light re-emitted by large, cold dust grains at their equilibrium temperature (Buat & Xu, 1996; Lagache et al., 2005). The dust component is particularly prominent in galaxies with high level of star formation, making this wavelength range ideal to observe and detect them (e.g. sub-mm galaxies). Overall, the SED of a galaxy depends on multiple factors, e.g. stellar mass, age of the galaxy, star formation history, metallicity, dust content, initial mass function and redshift, among others; therefore, ideally, all this information can be derived from the analysis of the SED of a galaxy.

Galaxies are generally observed through spectroscopy or photometry. The first method allows for observing the SED of a galaxy in a specific wavelength range, allowing for a detailed study of particular features of the SED, such as emission or absorption lines. On the other hand, using photometry, with broad or narrow bands, the SED is convolved with the transmission curve of the used filters and only the strongest features of an SED can be identified. In general, with spectroscopy it is possible to derive some galaxy properties, such as redshift or metallicity, with much higher precision than photometry, given the highest spectral resolution. On the other hand, with a single photometric pointing it is possible to simultaneously observe a large number of distant galaxies, which is only

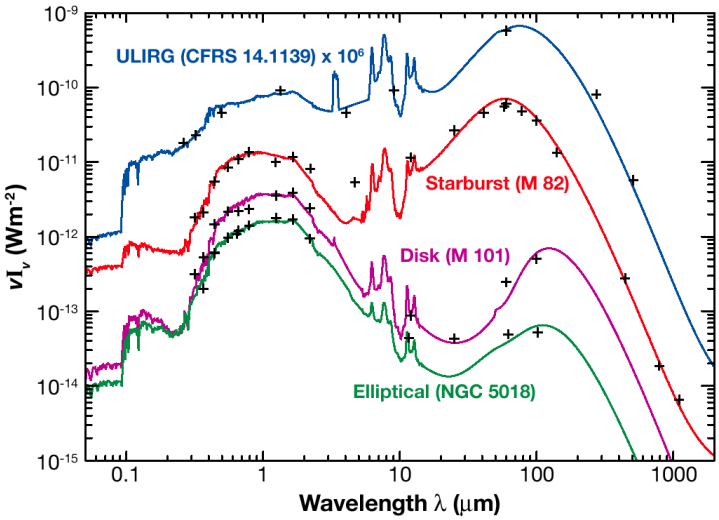


**Figure 1.1:** Some example of SED templates at rest-frame UV-to-mm (Galliano, 2004).

possible with the largest multi-object spectrographs. Moreover, the faintest objects detected in photometric maps are beyond the technical possibility of modern spectrographs (Caputi et al., 2012, 2015) and even faint but detectable objects usually require very long exposure times (Le Fèvre et al., 2015). Therefore, photometry is ideal to carry out large galaxy surveys up to high redshift or low stellar mass. However, a careful fitting of the SED is necessary to derive the physical properties of the galaxies, whose derivation will depend highly on the number and the wavelength coverage of the filters used.

## 1.2 GALAXY EVOLUTION AND STELLAR MASS BUILD-UP

When discussing the stellar mass build-up of galaxies, an obvious starting point is the cosmic star-formation history. In this age of large, multi-wavelength surveys, it has been possible to map the amount of star-formation per unit volume, i.e. the star-formation rate density, up to $z\sim10$ (Bouwens et al., 2014). The emerging picture is that the Universe had a peak in the star-formation rate around $z\sim2$ ($\sim$3.2 Gyr after the Big Bang) and the amount of star formation steadily declined before and after this peak, up to $z\sim8$ (Fig. 1.2; Madau & Dickinson, 2014). The number

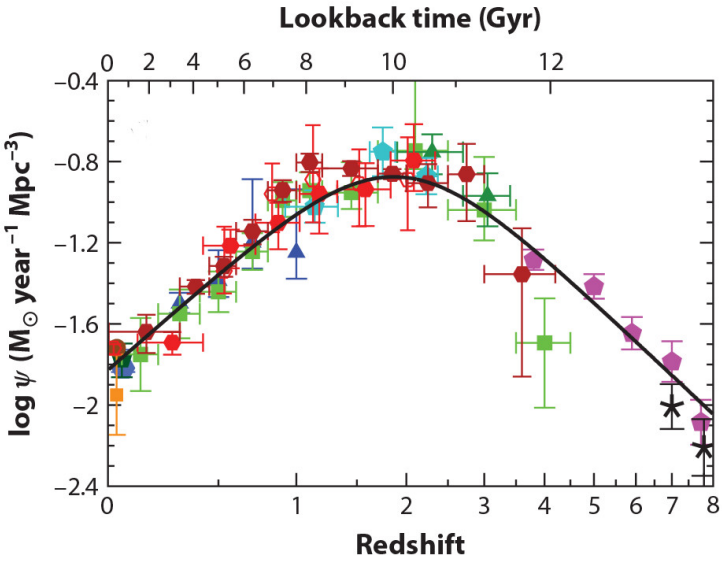


**Figure 1.2:** The history of cosmic star formation using a combination of UV and IR measurements (Madau & Dickinson, 2014). Each data point is a separate determination of the cosmic star-formation density from other works. The solid line is the best-fit SFR density taken from equation 15 of Madau & Dickinson (2014).

of galaxies detected at higher redshifts is limited, making an accurate SFR density derivation still challenging.

The complementary nature of the UV and IR wavelengths is evident when separating the measurements of the SFR densities between these two wavelength ranges (Fig. 1.3). Indeed, the rest-frame UV light is highly obscured by dust and only a minority of this light can escape the galaxy and be observed, causing the derived SFR density to be underestimated. On the other hand, it is possible to observe the rest-frame UV light over a wider range in redshift with respect to the rest-frame IR light, which is redshifted to sub-mm wavelengths at high-z and at which wavelengths large surveys are generally less sensitive. Indeed, the SFR density above z>3-4 is mainly derived from the rest-frame UV (Bouwens et al., 2012), corrected for dust extinction, and a direct comparison with an IR-derived SFR density is only possible at high stellar masses and for small galaxy sample (Bourne et al., 2017; Dunlop et al., 2017). Overall, observations at IR wavelengths are essential to detect both the dust reprocessed stellar light and the rest-frame

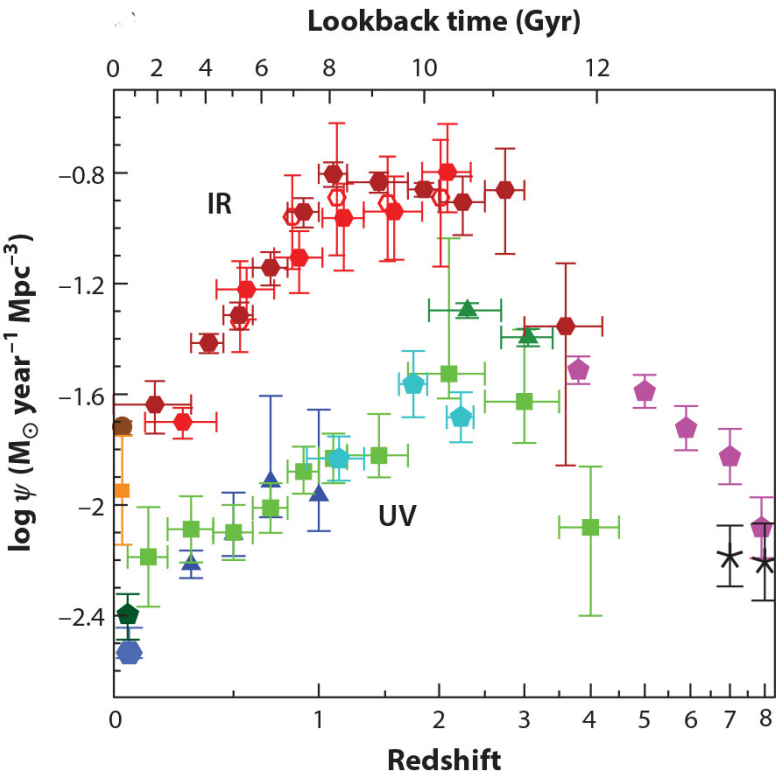


**Figure 1.3:** Star-formation-rate densities from UV, uncorrected for dust attenuation (*green and blue points*), and IR (*red points*; Madau & Dickinson 2014). Each data point is a separate determination of the cosmic star formation density from other works.

UV stellar light at high-z redshifted to IR wavelengths in order to have a comprehensive study of the star-formation history of the Universe.

To investigate which processes influence the global SFR density, it is possible to analyse the star-formation-rate - stellar mass plane (SFR-M*) for single galaxies, at different cosmic times. In particular, the majority of the galaxies contributing to the SFR density follow a tight relation, called main-sequence of star-forming galaxies, whose normalisation increases with time (Noeske et al., 2007; Rodighiero et al., 2014; Speagle et al., 2014). This suggests that the majority of galaxies have a long-lasting star-formation mode, where gas accretion and feedback processes are well balanced, and which dominates over stochastic and violent events, such

as mergers. Indeed, main-sequence galaxies are the majority of galaxies, but there is a fraction of galaxies which form very few stars respect to their stellar mass and almost do not contribute to the star formation rate density, i.e. quenched galaxies, and galaxies which show bursts of star-formation, i.e. starburst galaxies, which are rare and seem to have a minor contribution to the SFR density (Rodighiero et al., 2011; Sargent et al., 2012; Schreiber et al., 2015). An accurate census of these galaxies in different star-formation modes in a wide range of stellar mass and redshift is necessary to investigate the galaxy evolution, by analysing the physical phenomena behind the quenching of star formation or its rapid increase.

## 1.3 INFRARED TELESCOPES

The first use of IR detectors in astronomy occurred about 70 years ago (Kuiper et al., 1947), first to study planets and later in extragalactic astronomy (Low & Tucker, 1968; Low, 1969), but IR observations still remain challenging despite enormous improvements in their technology.

First, IR observations are very sensitive to the presence of water vapour which absorb this radiation (Pardo et al., 2001). For this reason, there are really few places on Earth that are dry and high enough to allow for these kinds of observations, like Llano de Chajnantor in Chile. Another possibility is, of course, to observe from space, increasing the cost of the instrument.

Second, the instrument itself and all its environment are a source of noise, because their thermal radiation peaks at IR wavelength. Therefore, sophisticated cooling and screening mechanisms are necessary to thermally isolate the full detector system. This is particularly a limitation for a space mission, which needs the cooling liquid to be present from the beginning, increasing the initial weight of the telescope and limiting the duration of the mission to the available storage space.

Third, the material and composition of IR detectors largely depend on the wavelength range to be observed. Due to different detector technology and to fundamental physical reasons, all IR detectors are generally less sensitive and have lower angular resolution with respect to optical detectors, making observations more time-expensive and more difficult to interpret.

In the next sections I give a brief overview of the main instruments that I deal with in this PhD thesis, i.e., A-MKID and the imaging cameras for the JWST.

### 1.3.1 The APEX Microwave Kinetic Inductance Detector

A-MKID[1] is an instrument for the Atacama Pathfinder Experiment (APEX; Güsten et al., 2006), a radio telescope located at an altitude of 5105 meters at the Llano de Chajnantor Observatory in the Chilean High Andes, operational since 2005. Chajnantor was chosen as the location for APEX because of its low level of water vapour, which absorbs sub-millimetre radiation. APEX is a collaboration between the Max Planck Institute for Radio Astronomy (MPIfR), Onsala Space Observatory (OSO) and the European Organisation for Astronomical Research in the Southern Hemisphere (ESO). It is the largest single dish sub millimetre-wavelength telescope operating in the southern hemisphere, with a diameter of 12 meters. APEX is an ALMA (Atacama Large Millimetre Array) prototype antenna, which is also located at the same site. This telescope is designed to work at sub-millimetre regime and to find targets which ALMA will be able to study in greater detail.

A-MKID is the German-Dutch microwave kinetic inductance detector (MKID) instrument for APEX that will observe through the 350 $\mu$m and 850 $\mu$m atmospheric transmission windows with a resolution of 7 arcsec at 350 $\mu$m, comparable to SCUBA-2 (Submillimetre Common-User Bolometer Array 2; Holland et al., 2013), and 17 arcsec at 850 $\mu$m. The main strength of A-MKID is in its wide field of view ($>$ 15x15 $\mathrm{arcmin}^2$) due to the high number of pixels of the camera, which is possible because of the high multiplexing capabilities of MKIDs. This large field of view is important to carry out large galaxy surveys at sub-millimetre wavelengths, allowing us to obtain a statistically large sample of sub-mm galaxies.

#### 1.3.1.1 Microwave kinetic inductance detectors

Until now, most of the available total power instruments at sub-millimetre wavelengths use bolometers as detectors, by measuring the heating produced by incident radiation. To improve the resolution and increase the field-of-view of any detector, it is necessary to increase the number of pixel in the array. However, bolometers are difficult to multiplex and, therefore, they have been growing in size and complexity (Chervenak et al., 1999; Irwin, 2002; Irwin et al., 2004; Bender et al., 2016). Arrays using Microwave Kinetic Inductance Detectors (MKIDs; Day et al., 2003; Baselmans, 2012; Zmuidzinas, 2012) offer a potential solution, thanks of their frequency multiplexing capability. Indeed, with these detectors, it

[1] http://www3.mpifr-bonn.mpg.de/div/submmtech/bolometer/A-MKID/a-mkidmain.html

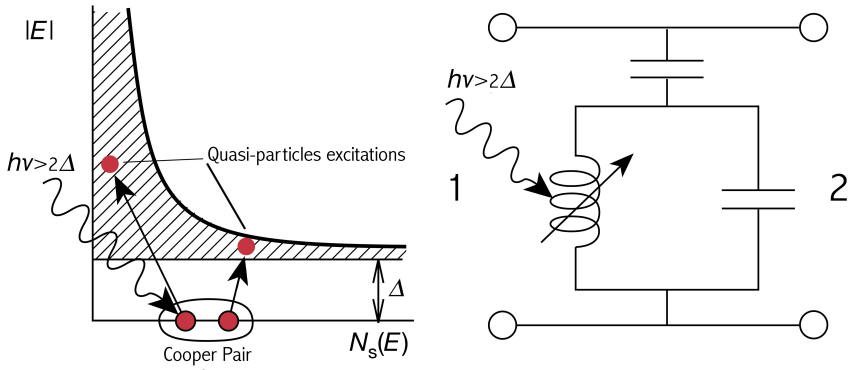


**Figure 1.4:** KID operation principle. *Left:* a photon with h$\nu > 2\Delta$ breaks a Cooper pair at the Fermi level creating quasi-particles. The shaded area is the density of states of quasi-particles ($N_S$) as a function of the quasi-particle energy. *Right:* the superconductor is part of a resonant circuit in order to read the difference in the surface impedance as a change in the transmission. Figure adapted from Day et al. (2003).

is possible to read out thousands pixels at the same time using a single coaxial transmission line, reducing space, time costs and complexity of big arrays (van Rantwijk et al., 2016).

Kinetic inductance detectors (KIDs) are a pair-breaking detector made with a superconductive thin film. In a superconductive material, depending on its temperature, electrons can be paired (i.e. Cooper pairs) and carry a current without resistance or be independent (i.e. quasi-particles) and their charge transport is resistive. At very low temperatures, much smaller than the superconductive transition temperature ($T_c$), Cooper pairs dominate in number and they are bound with a binding energy of $2\Delta \approx 3.5 k_B T_c$ (Bardeen et al., 1957). Superconductors have zero resistance to a direct current but non-zero surface impedance for alternate current. In particular, this surface impedance includes a surface inductance, due to the fact that a magnetic field can penetrate inside the superconductor for a short distance, and a surface resistance due to the quasi-particles. Therefore, when a photon with enough energy to break a Cooper pair is absorbed by the superconductor, the number of quasi-particle varies creating a change on the surface impedance (Fig.1.4 *left*). This change on the surface impedance can be measured by making the superconductor part of a resonant circuit and measuring the change on the resonance frequency and the transmission (Day et al., 2003) (Fig.1.4 *right*).

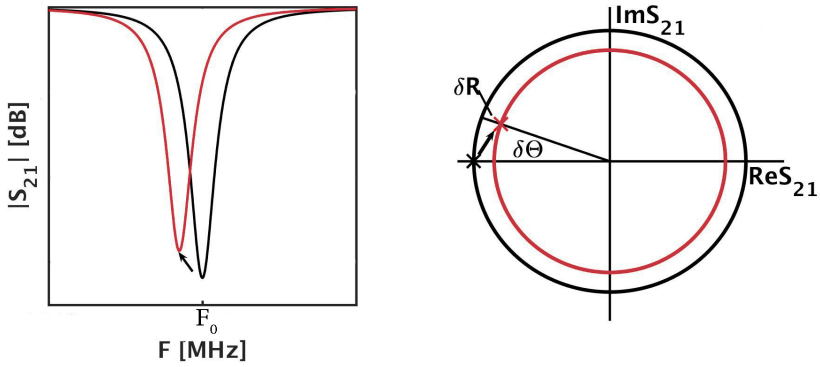


**Figure 1.5:** Transmission vs. readout frequency (*left*) and transmission in the complex plane (*right*). The black line is the transmission without any signal, while the red line is the transmission after radiation is absorbed.

Changes of the transmission ($S_{21}$) of the circuit are visible in the transmitted magnitude of a resonator and as a shift of the resonance frequency (Fig. 1.5 *left*), as well as a change in the phase and radius of transmission in the complex plane (Fig. 1.5 *right*). Multiple KIDs can be linked to the same transmission line and read-out simultaneously by tuning each one to a different resonance frequency, making it possible to create an array with thousands of pixels.

#### 1.3.1.2 Sub-millimetre galaxies

The first sub-mm surveys (Hughes et al., 1997; Smail et al., 1997) were preformed with the Sub-millimetre Common-User Bolometer Array (SCUBA; Holland et al., 1999) at 450 $\mu$m and 850 $\mu$m. The starting idea was to look at galaxies at high redshift, by observing at the UV stellar light re-emitted by the dust at the rest-frame far-infrared, which corresponds to sub-mm wavelengths at z$\sim$3. This survey revealed a population of extremely luminous and obscured galaxies with median redshift around 2.5-3 (Smail et al., 2000) and very high SFR (several 100 $M_{\odot}yr^{-1}$), similar to local starbursts. Recent studies of these galaxies have pointed out that they could be a crucial evolutionary phase in the formation of the most-massive, compact and quiescent galaxies observed at low redshifts (Ikarashi et al., 2017). Because of the high dust attenuation, the rest-frame UV light of these galaxies is very faint and sub-mm observations are necessary to quantify the contribution of these objects to the SFR density of the Universe.

However, sub-mm galaxies are quite rare, with a surface density of 0.1-0.2 arcmin$^{-2}$, therefore it is necessary to observe a large area of the sky to have a statistically significant sample of them. This is the reason why the key strength of A-MKID is in its wide field of view, thanks to which it should be possible to observe large areas of the sky and obtain a statistically large sample of sub-mm galaxies.

### 1.3.2 The James Webb Space Telescope

The *James Webb Space Telescope* (JWST; Gardner et al., 2009) is a space telescope with a 6.5 m primary mirror that will be launched in 2018 and will operate for 5-10 years. It is a collaboration between the National Aeronautics and Space Administration (NASA), European Space Agency (ESA) and the Canadian Space Agency (CSA). By the time of its launch, it will be the largest civilian infrared telescope ever sent to space, and it is the awaited successor of the *Spitzer Space Telescope* and the *Hubble Space Telescope*.

JWST will observe at IR wavelengths between 0.6 $\mu$m and 28.5 $\mu$m with sub-arsec angular resolution. There will be four instruments on board, covering different wavelength ranges, with multiple imaging, spectroscopic, and coronographic modes. These instruments are the Near Infrared Camera (NIRCam; Rieke et al., 2005), the Mid-Infrared Instrument (MIRI; Rieke et al., 2015; Wright et al., 2015), the Near-InfraRed Imager and Slitless Spectrograph (NIRISS; Doyon et al., 2012) and the Near Infrared Spectrograph (NIRSpec; Bagnasco et al., 2007). The construction and design of JWST incorporate several innovative technologies, ranging from the microshutters used in NIRSpec to the sunshield, and will hopefully bring exciting astronomical discoveries by observing the Universe at its cosmic dawn.

The focus of this thesis is on the two imaging cameras of JWST, i.e. NIRCam and MIRI. In particular, NIRCam has 29 filters, with extra-wide, wide, medium and narrow passbands, covering between 0.6-5 $\mu$m with a $2 \times 2.2' \times 2.2'$ field of view. On the other hand, MIRI provides imaging with nine broad-band filters from 5 to 28 $\mu$m and a filed of view of $74'' \times 113''$. These two instruments are complementary in wavelength and together will allow us to study the rest-frame optical light of galaxies up to z=10.

#### 1.3.2.1 The study of high-redshift galaxies with JWST

The JWST will be the largest space telescope ever launched with unprecedented infrared sensitivity, making it an extraordinary instrument

for exploring the Universe. Indeed, its predecessor was the *Spitzer Space Telescopes*, which has allowed for numerous interesting studies of IR galaxies (Soifer et al., 2008) with only an 85 cm primary mirror. Among JWST's scientific aims is the study of the formation and evolution of galaxies at early cosmic times, observing the rest-frame optical light of galaxies redshifted to IR wavelength. In this way it will allow for studying the first galaxies and compare them to today's galaxies, to understand how they form and how their mass built-up proceed through time. The general idea is that with JWST it will be possible to perform the same analyses which have been done until now on galaxies at z=3, but for high-redshift galaxies at z∼8. Moreover, it will enable much more detailed studies of galaxy morphologies and structure, thanks to its angular resolution.

## 1.4 THIS THESIS

The aim of this thesis is to assess different aspects of the performance of two upcoming IR telescopes, i.e. A-MKID and JWST. These two telescopes cover two complementary wavelength ranges, sub-mm and IR wavelengths respectively, and they are in two different phases of development. A-MKID is still in construction and several tests were necessary in the past years to develop the necessary technology to match the instrument technical requirement, taking also into account that KIDs are a quite new technology. On the other hand, JWST is almost finished and it is already necessary to concentrate on the observational strategies and future targets, even more because the mission will have a limited duration of 5-10 years.

A-MKID is a very large sub-mm array and the use of a traditional calibration method, i.e. by observing an astronomical point source with every pixel, is not feasible, due to the large number of pixels in the array. For this reason, I test an alternative calibration method, based on MKID readout frequency response, which is fast enough to be used on large arrays and it is based on data already used to measure the KID position (Chapter 2).

Each KID in the array is tuned to a specific resonance frequency. However, in order to have as many KIDs as possible on the array, these resonance frequencies may be too close one to the other, resulting in coupling between KIDs, called crosstalk. Unfortunately, crosstalk can be only minimised with a careful design of the array and it is usually necessary to correct for this effect a posteriori. In Chapter 3, I analyse and model the crosstalk present on a MKID array and demonstrate that it is possible to post-process astronomical images.

With respect of JWST, I focus on the planning of future galaxy surveys, using the two imaging camera on board (i.e. NIRCam and MIRI) and their available broad-band filters. In particular, I simulate observations with the JWST broad-band filter of galaxies between z=0.5-10, using both observed and simulated galaxies. I first test the photometric redshift estimation trough SED fitting, by using different JWST broad-band filters and possible ancillary ground-based and *Hubble Space Telescope* (*HST*) data (Chapter 4). I then continue these tests by analysing the recovery of galaxy properties, such as stellar mass, colour excess, age and star-formation-rate, for the high-z sample of simulated galaxies between z=7-10 (Chapter 5).

In Chapter 6 I conduct a study that illustrates the scientific importance of obtaining reliable SFR and stellar mass. In particular, I analyse the star-formation-rate - stellar mass plane using a multi-Gaussian decomposition at redshift z=0.5-3, which allows for deriving the main-sequence of star-forming galaxies without pre-selecting star-forming galaxies and for analysing at the same time starburst and quenched galaxies. With JWST will be possible to observe large samples of galaxies at z>3 and extend this type of analyses to higher redshifts.

Finally, in Chapter 7 I present my conclusions and discuss briefly some future prospects.

# 2. Calibration scheme for large Kinetic Inductance Detector Arrays based on Readout Frequency Response

*L. Bisigello, S. J. C. Yates, V. Murugesan, J. J. A. Baselmans and A. M. Baryshev*
*2016, Journal of Low Temperature Physics, 184, 161*

*A microwave kinetic inductance detector (MKID) provides a way to build large ground-based sub-mm instruments, such as NIKA and A-MKID. Therefore, it is important to understand and characterize their response to ensure a good linearity and calibration over a wide dynamic range. We propose to use the MKID readout frequency response to determine the MKID responsivity to an input optical source power.*

*A signal can be measured in a KID as a change in the transmission both in phase and magnitude. Fundamentally, an absorbed radiation induces a change in the quasiparticle number inside the superconducting resonator, which produces a change in the KID resonance frequency and in the transmission phase. We show that the shift in the resonance frequency can be predicted from the transmission phase, by using the relation between the KID phase and readout frequency previously measured on a KID. By working in this calculated resonant frequency, we gain near linearity and a constant noise equivalent temperature to a constant optical signal, over a wide range of readout power and readout frequency offset.*

*This calibration method has three particular advantages: first, it is fast enough to be used to calibrate large arrays, with even thousand of pixels; second, it is based on data that are already necessary to determine the KID positions; third, it can be done without applying any optical source in front of the array.*

## 2.1 INTRODUCTION

Microwave kinetic inductance detectors (MKID) (Zmuidzinas, 2012; Baselmans, 2012; Day et al., 2003) are ideal to build large ground-based sub-millimetre instruments, such as A-MKID[1] and NIKA (Monfardini et al., 2010, 2011), because it is possible to read out simultaneously up to a thousand pixels with a single readout line (van Rantwijk et al., 2016).

When a photon is absorbed by a KID, it produces a change in the kinetic inductance of the superconductor, which is observable both as a shift in the resonance frequency (Fig. 2.1a) and as a change in the transmission phase in the complex plane (Fig. 2.1b). In particular, the change in the resonance frequency is proportional to the change in the kinetic inductance and is therefore ideal to calibrate the instrument. However, this shift in the resonance frequency is not directly measured with a single fixed bias frequency, unless a modulation readout scheme is used (Swenson et al., 2010; Calvo et al., 2013).

There are different primary and secondary calibration methods, which allow for converting measured quantity, such as phase difference, to the corresponding black body temperature difference and input signal. On sky, it is possible to use a primary calibration source, i.e. an astronomical point source, but this method requires time in order to observe this calibration source with every pixel in the array. Another way is to use a sky dip, where an elevation change of the telescope is used to calibrate the temperature scale. However, this procedure is not always possible, because it requires a good magnetic shielding and a good knowledge of the sky transmission. In the lab, it is possible to calibrate an MKID by using a polariser grid sweep, enabling going from 300K load to typically 77K by varying the angle of the polariser. Unfortunately, this method can not be used to calibrate the entire telescope, because it is physically difficult to place this grid in front of the telescope and the calibration done in the lab may not be at the loading condition used on the sky. A secondary calibration source in the lab is the gortex sheet, which is slightly grey in band and is pre-calibrated by using a polariser grid. The calibration time depends on the used calibration scheme, however, it requires more time to measure a source for every detector than to do a gortex sweep, which is, therefore, preferable. However, these methods can only be apply in the lab, because it is physically difficult to place the necessary equipment in front of the telescope.

[1] http://www3.mpifr-bonn.mpg.de/div/submmtech/bolometer/A-MKID/a-mkidmain.html

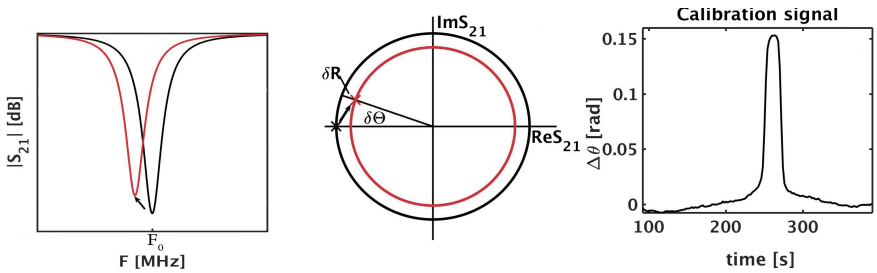


(a) (b) (c)

**Figure 2.1:** (a) Transmission vs. readout frequency and (b) transmission in the complex plane. The black line is the transmission without any signal, while the red line is the transmission when a signal is detected. (c) Readout phase versus time, as measured to calibrate using the calibrated optical signal. The feature is created at the moment when a gortex strip is between the optical source and the detector.

The linearisation of the signal can be done by using the polariser grid sweep, when available, or the sky dip, but different working states, e.g. the sky condition or the elevation which varies the load temperature, shift the resonance, making the calibration less precise. The grid calibration can, therefore, become invalid or not the optimum operation point to obtain the best signal to noise. Consequently, having a calibration scheme base on the underlying operating principle, i.e. the KID resonant frequency change, enables more flexibility in particular to extrapolate between different operating points and the primary calibration. Also, such a scheme allows for linearisation in lab experiments where other schemes are not available.

This Chapter is organised as follows. In Section 2, we describe the calibration model based on the KID resonance frequency change and the experiment done to test this calibration method. In Section 3, we explain and discuss our experimental results and, in Section 4, we report our conclusions.

## 2.2 EXPERIMENTAL DETAILS

We start from the assumption that the responsivity of a KID is:

$$\frac{\partial f}{\partial T} = \frac{\partial f}{\partial \theta} \cdot \frac{\partial \theta}{\partial T} \tag{2.1}$$

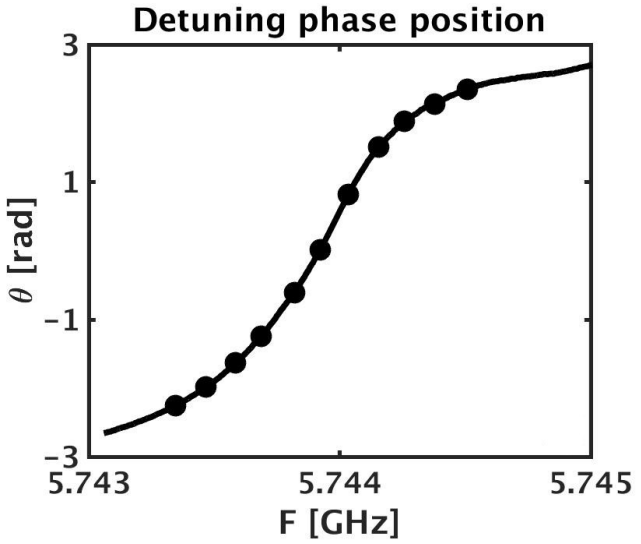


(a)

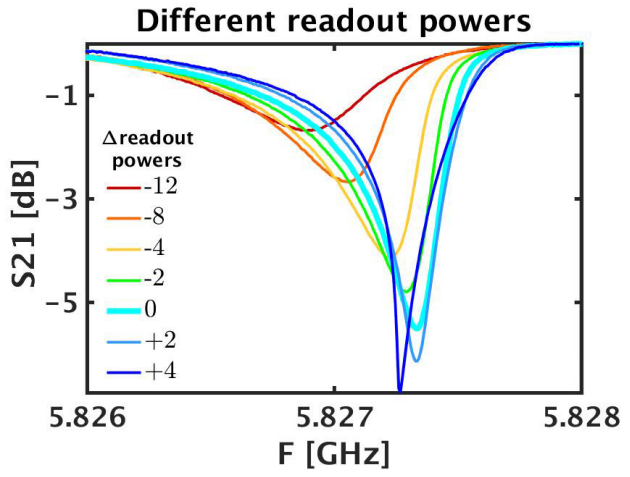


(b)

**Figure 2.2:** Readout frequencies (a) and readout powers in dBm (b) used during the measurements. In the top panel, the black line is the relation between phase and frequency, which can be approximated to a linear relation only within $\pm 1$ rad.

where f is the readout frequency, T is the optical load temperature and $\theta$ is the phase transmission. $\partial f/\partial T$ is the responsivity, $\partial f/\partial \theta$ can be obtained directly from the transmission by using the phase readout frequency relation (Fig. 2.2(a)), while $\partial \theta/\partial T$ can be calculated by using the calibration method based on a calibrated optical signal. For very large changes in the optical power, $\partial f/\partial T$ will have a power dependence, but it can be assumed to be linear for these devices over a narrow range of optical power (Calvo et al., 2013). Under this condition, the terms in the right part of the equation are inversely proportional to each other and $\partial f/\partial \theta$ can be used to estimate $\partial \theta/\partial T$ and calibrate the instrument. Therefore, we test under which condition this assumption holds experimentally.

We use a test system created for A-MKID that allow us to measure the readout phase and frequency of an input signal on a 880 pixel 350GHz A-MKID subarray. We perform two sets of measurements, one to calibrate and the other to study the noise. We repeat all these measurements for different readout frequencies and different readout powers (Fig. 2.2). The detuning positions are within $\pm 1$ resonant bandwidths, which is the width of the resonance at half minimum dip depth. This range is wider than $\pm 1$ rad which corresponds to quasi-linear regime in the phase-frequency relation, as it is visible in Fig. 2.2(a). This allows us to analyse linearisation far off resonance, i.e. large signal response. Here, we present the results for a representative KID.

Firstly, we measure the signal of a liquid-nitrogen background while moving a gortex strip in front of the array (Fig. 2.1c) in order to partially obscure the signal. This obscuration have been previously calibrated to give a 21K signal difference on top of a liquid nitrogen background load by comparing it to a polariser grid sweep between the liquid-nitrogen temperature and 300K. In particular, we measure the output phase in two moments, when the optical source is directly observed and when the gortex strip is between the detector and the optical source. In this way, because we previously calibrated the strip, we can calculate the derivative of the phase respect to the temperature (Fig. 2.3(left)). In addition, we calculate the derivative of the phase respect to the frequency (Fig. 2.3(rigth)), in order to test the calibration method based on the readout frequency response by checking if $\partial f/\partial \theta$ is inversely proportional to $\partial \theta/\partial T$.

Secondly, in order to study the noise, we measure the signal over an interval of 40 seconds and we calculate the Power Spectral Density (PSD). From the PSD we evaluate the detector photon noise, by subtracting from the measured noise the noise level above the KID roll-off, which corresponds to the amplifier contribution. Then, we divide the detector

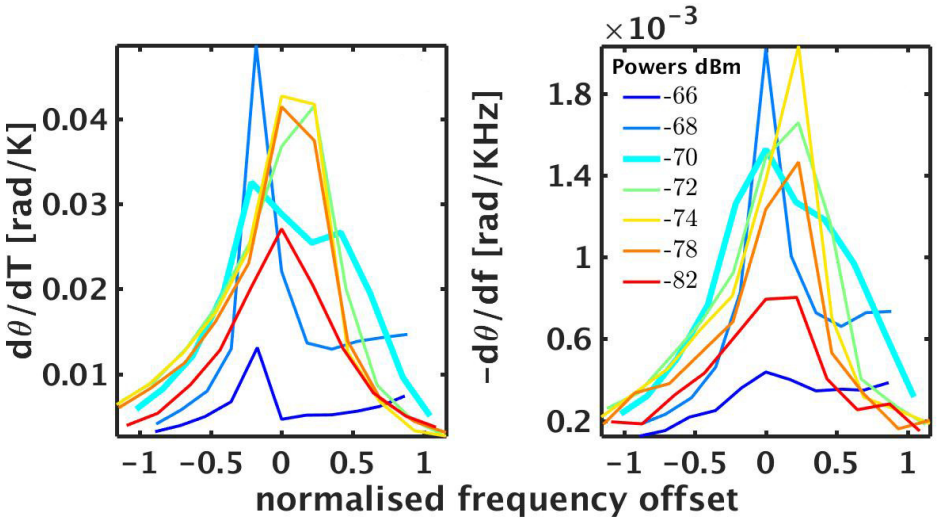


**Figure 2.3:** Comparison between the responsivity measured using the optical source $\frac{\partial\theta}{\partial T}$ (*left*) and the responsivity predicted using the readout frequency $\frac{\partial\theta}{\partial f}$ (*right*). Colours correspond to different readout powers in dBm. Frequency offsets are normalised with respect to the KID bandwidths.

photon noise for the responsivity calculated using both methods in order to obtain the Noise Equivalent Temperature (NET) (Fig. 2.5).

## 2.3 EXPERIMENTAL RESULTS AND ANALYSIS

Figure 2.3 shows the comparison between the responsivity based on the calibrated optical source $\frac{\partial\theta}{\partial T}$ and the responsivity predicted using the readout frequency response $\frac{\partial\theta}{\partial f}$. The phase responsivity is clearly non-linear and it changes while varying the readout frequency and readout power. Therefore, before observing, it is important to know the combination of readout frequency and power that maximises the responsivity and, as a consequence, the performance of the instrument. The general shape of the optical responsivity $\frac{\partial\theta}{\partial T}$ is similar to that derived using the frequency dependence $\frac{\partial\theta}{\partial f}$. The derived frequency responsivity, $\frac{\partial f}{\partial T}$ (Fig. 2.4), increases slightly with the readout power and it is roughly constant with the readout frequency, but with some deviations for the highest and hence overdriven readout powers. Therefore, $\frac{\partial\theta}{\partial T}$ and $\frac{\partial\theta}{\partial f}$ are generally inversely

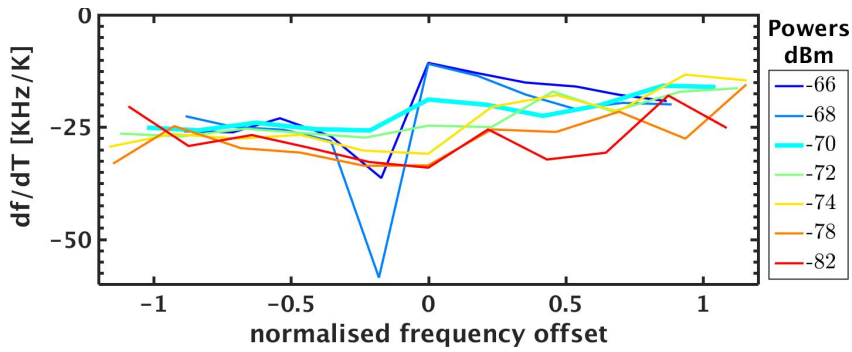


**Figure 2.4:** Responsivity $\frac{\partial f}{\partial T}$ vs normalised frequency offset. The responsivity slightly increases with the readout power and it is roughly constant with the readout frequency, but with some deviations for the highest readout powers. Colours correspond to different readout powers in dBm. Frequency offsets are normalised with respect to the KID bandwidths.

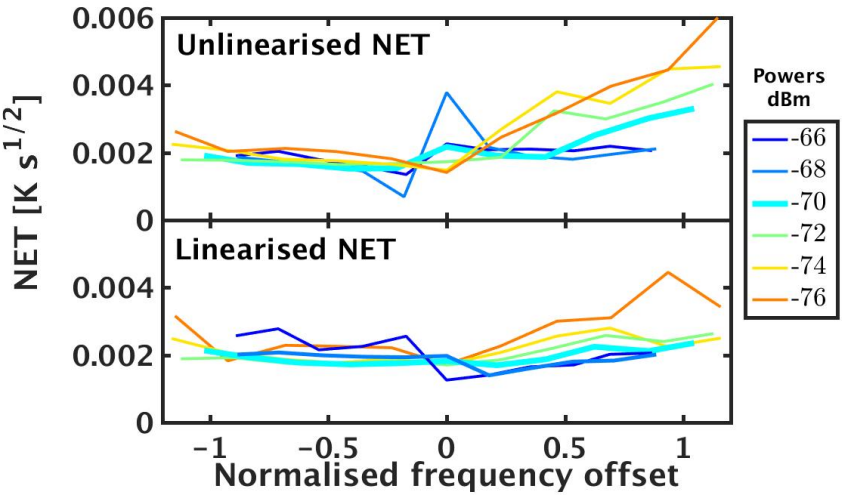


**Figure 2.5:** Comparison between the NET calculated using a calibrated optical source, and the NET predicted using the calibration method based on the readout frequency response. Colours correspond to different readout powers in dBm. The readout power gives some asymmetry also in the linearised NET, but the most symmetric NET ($\sim -70$ dBm) is linear to $\pm 10\%$ over a very large range. Frequency offsets are normalised with respect to the KID bandwidths.

proportional over a wide range of readout powers and readout frequency offset.

Figure 2.5 shows the comparison between the NET obtained by using the two calibration methods. Some readout powers give some asymmetry also in the linearised NET, but the most symmetric NET ($\sim -70$ dBm) is linear to $\pm 10\%$ over a very large range of readout frequencies and much superior to the NET calculated directly from $\frac{\partial \theta}{\partial T}$.

## 2.4 CONCLUSIONS

We have proposed and tested a calibration method based on MKID readout frequency response that could be used in large ground-based sub-millimetre instruments. This method has the advantage that it is fast enough to be used in large arrays and it is based on data that are already used to measure the KID positions.

We measured the responsivity based on the readout frequency response, $\frac{\partial \theta}{\partial f}$, and we confirmed that it is inversely proportional to the responsivity based on a calibrated optical source, namely $\frac{\partial \theta}{\partial T}$. Therefore, by measuring the change in the phase response it is possible to predict the change in the resonance frequency, by using the relation between transmission phase and readout frequency, and, then, to derive the change in the kinetic inductance. In other words, this method can be used to calibrate MKIDs. Moreover, we calculated the NET and confirmed that this method allows for linearisation to $\pm 10\%$ over a wider range of readout frequencies and readout powers than the optical source calibration method.

*Acknowledgements:* This project was supported by the ERC starting grant ERC-2009-StG Grant 240602 TFPA and the Netherlands Research School for Astronomy (NOVA).

# 3. Measurements and analysis of optical crosstalk in a microwave kinetic inductance detector array

*L. Bisigello, S. J. C. Yates, L. Ferrari,*
*J. J. A. Baselmans and A. M. Baryshev*
*2016, Proc. SPIE vol. 9914 (2016)*

*The main advantage of Microwave Kinetic Inductance Detector arrays (MKID) is their multiplexing capability, which allows for building cameras with a large number of pixels and good sensitivity, particularly suitable to perform large blank galaxy surveys. However, in order to have as many pixels as possible it is necessary to arrange detectors close in readout frequency. Consequently, KIDs overlap in frequency and are coupled to each other producing crosstalk. Because crosstalk can be only minimised by improving the array design, in this Chapter we aim to correct for this effect a posteriori. We analyse a MKID array consisting of 880 KIDs with readout frequencies at 4-8 GHz. We measure the beam patterns for every detector in the array and describe the response of each detector by using a two-dimensional Gaussian fit. Then, we identify detectors affected by crosstalk above -30 dB level from the maximum and removed the signal of the crosstalking detectors. Moreover, we modelled the crosstalk level for each KID as a function of the readout frequency separation starting from the assumption that the transmission of a KID is a Lorenztian function in power. We describe the general crosstalk level of the array and the crosstalk of each KID within 5 dB, so enabling the design of future arrays with the crosstalk as a design criterion. In this Chapter, we demonstrate that it is possible to process MKID images a posteriori to decrease the crosstalk effect, subtracting the response of each coupled KID from the original map.*

## 3.1 INTRODUCTION

In astronomy, several blank imaging surveys at different wavelengths have been carried out to study the formation and evolution of galaxies at different cosmic epochs (Lagache et al., 2005; Weiß et al., 2009; Geach et al., 2013; Lutz, 2014; Madau & Dickinson, 2014). A multi-wavelength approach is essential to have a more complete view of galaxy properties and, in particular, sub-millimetre observations are necessary to explore the dust component of galaxies. Microwave kinetic inductance detectors (MKID; Day et al., 2003; Baselmans, 2012; Mazin, 2009) are the ideal technology to build fast and large cameras, such as A-MKID[1] or NIKA (Monfardini et al., 2010, 2011), to carry out deep and large blank galaxy surveys in the sub-millimetre regime. The main advantage of this technology is the possibility to read out all detectors simultaneously throughout a single readout line. This is possible because each detector is tuned to a specific resonance frequency and they are read out by sending wave tones though the readout line.

We use an array of 880 twin-slot antenna coupled hybrid MKIDs made for development and test in view of the SPACEKIDS[2] project. This technology has been already applied to similar array showing good efficiency and sensitivity (Janssen et al., 2013). KIDs are tuned to absorb 350 GHz and have resonance frequencies between 4 GHz and 8 GHz with a design separation in readout frequency of 2.64-5.28 MHz and designed quality factors (Q-factors) around 40000. Detectors are organised in the array such that the nearest spatial neighbours are always separated by at least one other KID in the readout frequency domain (Yates et al., 2014), in order to minimise the number of crosstalking KIDs. The remaining crosstalk in this array is therefore due to the overlapping resonant dips of the KIDs themselves. This is both due by design, to maximise the number of KIDs per readout line, and due to scatter in the KID placement due to lithographical and film thickness variations.

The aim of this Chapter is to correct for the crosstalk a posteriori, both by describing the point spread function (PSF), as well as by deriving a theoretical model to predict the crosstalk as a function of the separation in readout frequencies of the KIDs from the resonance frequency and the quality factor of each KID.

[1] http://www3.mpifr-bonn.mpg.de/div/submmtech/bolometer/A-MKID/a-mkidmain.html

[2] http://www.spacekids.eu

## 3.2 BEAM MAP MEASUREMENT AND PSF CHARACTERISATION

### 3.2.1 Measurements

In order to analyse the level of crosstalk, we use two types of measurements: beam maps and frequency sweeps.

First, we measure the frequency sweep for each detector in order to recover the resonance frequency of each KID and analyse the level of crosstalk as a function of the separation in readout frequency. In this way we obtained the complex transmission over a range in readout frequency of 2 MHz for all KIDs. It is possible to assess the presence of crosstalking detectors also by analysing the transmission. In particular, when a detector is isolated, its transmission is a circle in the complex plane (Fig. 3.1(a)) and a Lorentzian function in power (Fig. 3.1(b)). When crosstalk is present and the coupled detector is in the wavelength range scanned in the frequency sweep, two or more circles are visible in the complex plane (Fig. 3.1(c)), depending on the number of coupled KIDs, while the power of the transmission is formed by two or more Lorentzian functions (Fig. 3.1(d)).

Second, we measure the beam maps for all detectors in the array. We use the Groningen Beam-mapping facility that allows us to scan a hot source across the array by illuminating every detector once each time. The hot source is chopped at 80 Hz. Further drifts in the total optical loading are removed by using linearisation via frequency sweep (Bisigello et al., 2016b). This improves the linearity, but breaks down for very close KIDs where the frequency sweep is no longer described locally by a single Lorentzian. A 2 GHz subset of the array is read out at one time using the multiplexed readout presented in van Rantwijk et al. (2016). This array is not designed to be read out with this readout, so 4 measurements at different local oscillator settings are required to get complete coverage of the entire array, with 200 to 400 pixels measured at a time. In the ideal case of no crosstalk, each beam map should contain a single image of the chopped source (Fig. 3.2 left), i.e. the PSF. In the case of crosstalk, there will be more than one peak in the beam map, corresponding to the expected response of the KID of the map plus the response of crosstalking detectors (Fig. 3.2 right). Therefore, for each map we first identify every peak above -30 dB to recognise all detectors that are cross talking and, then, we measure the response of each KID in each map to obtain the level of crosstalk.

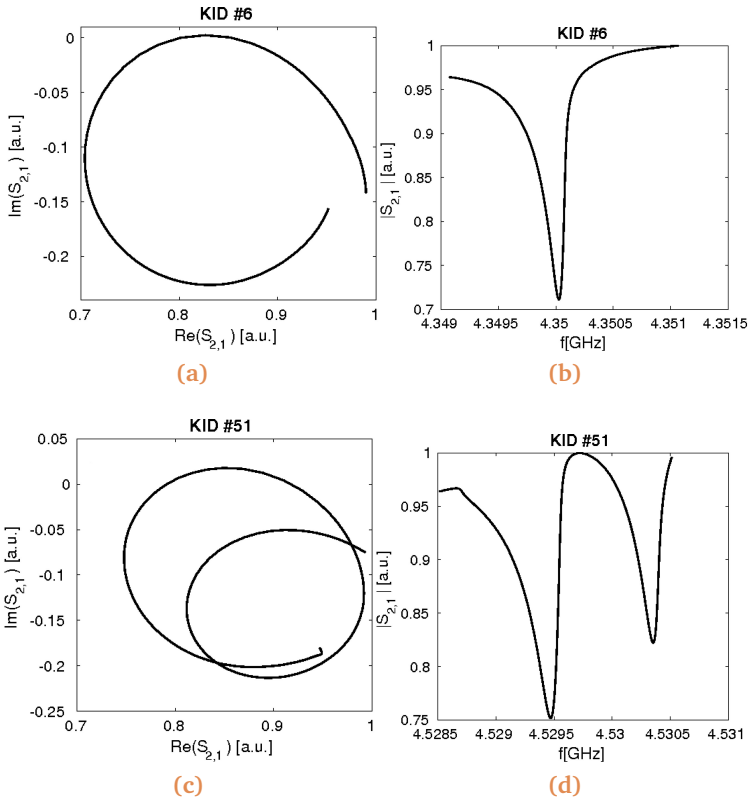


**Figure 3.1:** Transmission in the complex plane (a) and power of transmission versus the readout frequency (b) for an isolated KID. Transmission in the complex plane (c) and power of the transmission versus readout frequency (d) for two coupled KIDs.

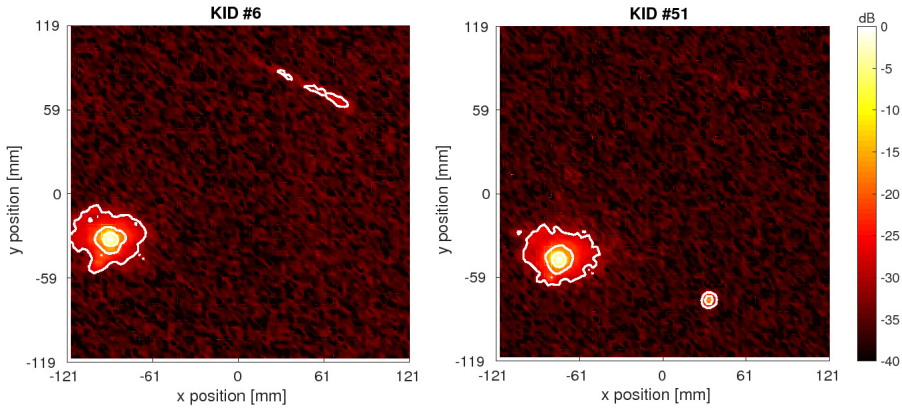


**Figure 3.2:** Two examples of beam maps. *Left:* Beam map of a detector that is not cross talking. Only one PSF is present in this map. Some low level (-30 dB) ghosting from inside the cryostat is visible in the top right. This ghosting is not dealt within the work, however in principle it can be corrected for. *Right:* Beam map of a detector that is coupled with another detector. Here a second response from the crosstalking KID is present. Contour lines are for -10, -20 and -30 dB from the maximum of the peak.

### 3.2.2 PSF characterisation and cross-talk correction

The response of a detector is the flux integral of the chopped signal in the image, therefore it is necessary to have a complete characterization of the PSF to properly measure the response of each KID. With this intention, we consider a two-dimensional Gaussian beam to describe each PSF separately, in order to take into account for differences of the PSF through the array. After we derive the best fit for each PSF, we integrate the two-dimensional Gaussian to derive each response. Then, we subtract the best fit two-dimensional Gaussian to each coupled detector to clean each map from the crosstalk (Fig. 3.3).

After we correct every beam map for the crosstalk above -30 dB from the maximum of the peak, we align all beam maps to the same beam centre and we stack them together. In this way we obtain the image of the input chopped source. In Figure 3.4 is shown the co-added map before and after the crosstalk correction, together with the residuals. Because the crosstalking KIDs are averaged out when creating the co-add map, their response is under -30 dB in the majority of the cases. For this reason, to evaluate the crosstalk correction applied in this work we also include the residuals, where all subtracted two-dimensional Gaussian are evident.

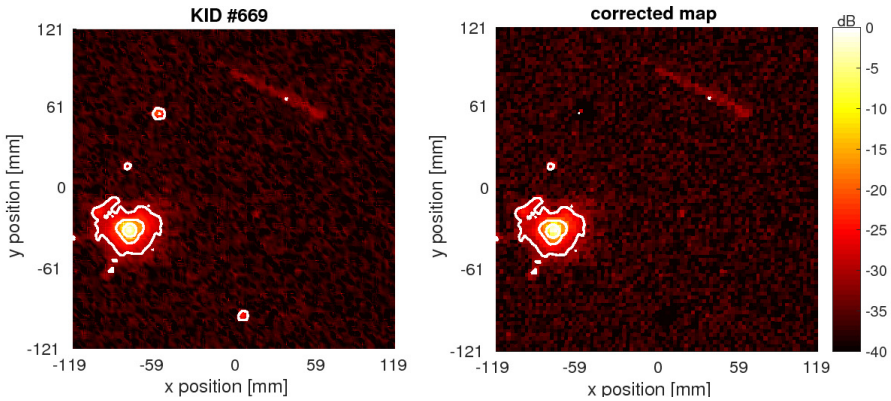


**Figure 3.3:** *Left:* This is an example of one original beam map where coupled KIDs are present, contour lines are for -10, -20 and -30 dB from the maximum of the peak. *Right:* This is the same beam map, but after the crosstalk correction. The PSFs of each coupled KID have been subtracted from the original map, contour lines are for -10, -20 and -30 dB from the maximum of the peak.

## 3.3 CROSSTALK LEVEL

Because the detectors are sorted by their resonance frequencies, KIDs with close identification numbers are also close in readout frequency. Around 15% (136 out of 880) of all the detectors are not identified during the measurements, therefore we do not measure neither the beam patterns nor the frequency sweeps of these KIDs. Because we can not derive their resonance frequencies, we do not include them in the crosstalk analysis. However, they have been removed from the beam map, where they can still be observed even if they are not identified. By comparing the identification numbers of the KIDs that are cross talking, it is possible to derive the nature of the crosstalk. It is evident from figure 3.5 that most of the coupled detectors are close in readout frequencies. Those few cases that are distant in readout frequency are likely caused by reflections or noise in determining the crosstalk, e.g. missidentification and missfited KIDs. Therefore, this result supports our assertion earlier that the main cause of crosstalk in this array is the overlap of readout frequencies and that the level of crosstalk is inversely proportional to the KID separation in readout frequencies. About 28% of the detectors in this array are isolated and are not coupled with any other detector above -30 dB from the maximum. On

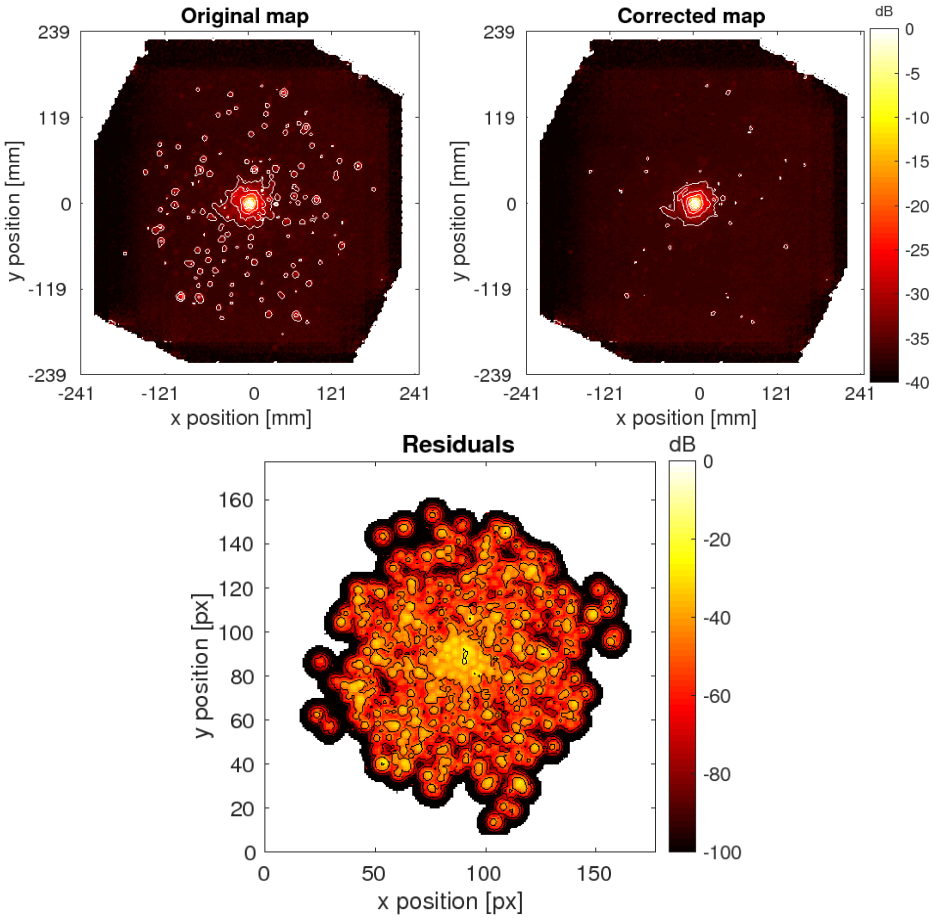


**Figure 3.4:** Final map derived stacking all the original beam maps (*top left*) and all the corrected beam maps (*top right*). The contour lines represent differences of 5 dB. The *bottom* panel shows the residuals and the contour lines indicate differences of 20 dB.

the other hand, ∼48% of all KIDs are coupled with another detector, ∼16% with other two KIDs and ∼7% with other three KIDs.

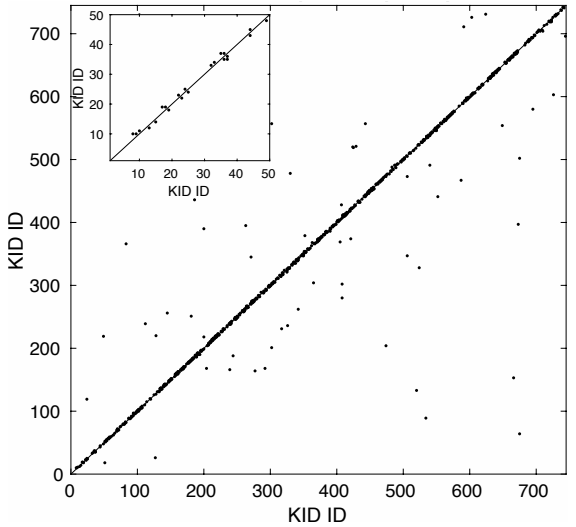


**Figure 3.5:** Cross talking KIDs in our array. Both axis show the identifier numbers of the detectors and the insert panel shows a zoom in of the first 50 KIDs. Since KIDs are sorted by their resonance frequencies, detectors with similar ID are close in readout frequency. Each point identifies two KIDs that are cross talking and there are no points on the identity line, because a KID does not cross talk with itself. The majority of the points lies close to the one-to-one line, thus crosstalk is almost only due to KIDs close in readout frequency.

It is possible to calculate the level of crosstalk for each coupled KID by using the response derived from the two-dimensional Gaussian fitting. The level of crosstalk between two KIDs is given by

$$K_{1,2} = \frac{R_2}{R_1}\,, \tag{3.1}$$

where $R_1$ is the response of KID 1 that was illuminated, $R_2$ is the response of the coupled KID, called KID 2, as a result of the signal measured by KID 1. Thus $K_{1,2}$ is the level of crosstalk of KID 2 due to KID 1. It is worth mentioning here that, in general, $K_{1,2} \neq K_{2,1}$. In this way we measure the level of crosstalk for the array, as it is shown in figure 3.6, where we consider the maximum level of crosstalk for each KID and we assign a crosstalk level of -40 dB to isolated detectors. Around 48% of all detectors are at least coupled with another detector with $K_{1,2} > -20$ dB.

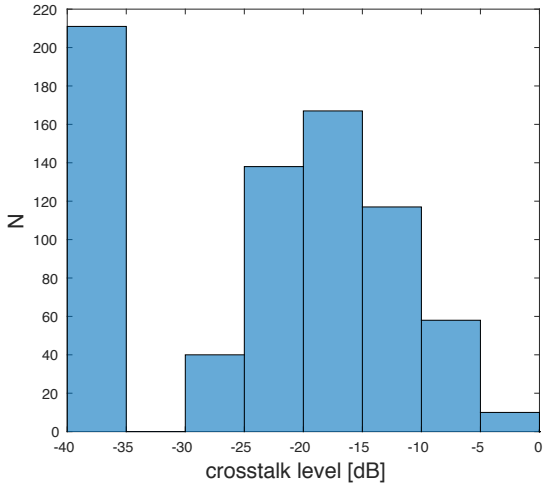


**Figure 3.6:** Level of crosstalk present in the array. We assign a level of crosstalk of -40 dB to isolated KIDs.

In addition, we derive the resonance frequency and Q-factor of each KID from the frequency sweep, in order to analyse the dependence of the crosstalk level on the readout frequency separation of the detectors. In particular, we fit a Lorenztian function to the power of the transmission measured in the frequency sweep (Mazin, 2005):

$$S_{2,1}^2 = 1 - \frac{(1 - S^2)}{1 + (\frac{2Q(f-f_0)}{f})^2}, \tag{3.2}$$

where $S_{2,1}$ is the transmission, S is the minimum of the dip transmission, $f_0$ is the resonance frequency, Q is the quality factor of the considered KID and f the analysed readout frequency. From this fit we derive both the resonance frequency and the Q-factor of all KIDs, as well as the bandwidth. Then we compare the level of crosstalk with the readout frequency separation in bandwidths of the crosstalking KIDs (Fig. 3.7). In general, the level of crosstalk decreases with the increasing readout frequency distance of the crosstalking KIDs, with a final plateau probably due to the noise level of the beam maps.

Additionally, we describe the relation between the crosstalk level and readout frequency separation, first with a simple model and then with a more complex one. We start from the fact that the response of a KID is a Lorentzian in power. From equation 3.2 and defining X$\equiv Q\frac{f-f_0}{f_0}$, we obtain

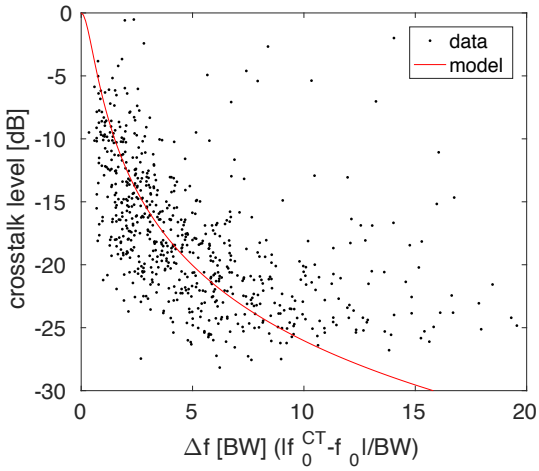


**Figure 3.7:** Crosstalk level versus readout frequency separations in units of bandwidths for all coupled KIDs of the array (black points). The red dashed line is the theoretical description given by the equation 3.6.

that the power and the phase of the transmission can be written as:

$$|S_{2,1}|^2 = 1 - \frac{1 - S^2}{1 + 4X^2} \quad , \tag{3.3}$$

$$\tan(\theta) = \frac{4X}{X^2 - 1}, \tag{3.4}$$

where $S_{2,1}$ is the transmission and $\theta$ is the transmission phase, S is the minimum of the dip transmission, $f_0$ is the resonance frequency and Q is the quality factor of the KID. Then, from eq. 3.4 we can derive that:

$$\frac{\delta\theta}{\delta X} = \frac{4(4X^2 + 1)}{16X^2 + (4X^2 - 1)^2}, \tag{3.5}$$

If we assume that the two coupled KIDs have the same dip depth and Q-factor, their complex transmission will be the same. Therefore, a signal will produce the same phase shift in both detectors. Moreover, we can consider that $\Delta\theta = \Delta X \cdot \delta\theta/\delta X$ and, from equation 3.5, we can derive that $\theta$ =4X in the limit for f$\rightarrow$ $f_0$, assuming that system effects are calibrated out. Therefore, the crosstalk level between two KIDs can be expressed as:

$$K_{1,2} = \frac{\Delta X_2}{\Delta X_1} = \frac{1}{4}\frac{\delta\theta}{\delta X} = \frac{(4X^2 + 1)}{16X^2 + (4X^2 - 1)^2} \tag{3.6}$$

By considering that the dip depths and the Q-factors are the same for all the KIDs, it is possible to describe the general relation between crosstalk level and separation in readout frequencies (Fig. 3.7).

In order to predict the crosstalk level for each KID more precisely, we include in equation 3.6 both the Q-factor and the dip depth of each KID. The resulting formula is:

$$K_{1,2} = \frac{\Delta X_2}{\Delta X_1} = \frac{1}{4}\frac{Q_1}{Q_2}\frac{(1-S_2)}{(1-S_1)}\frac{\delta\theta}{\delta X} \tag{3.7}$$

where $Q_i$ and $S_i$ are the Q-factor and the minimum of the dip transmission for the KID i, respectively. The comparison between the measured crosstalk level and the theoretical one is shown in figure 3.8. The root mean square of the difference between the modelled crosstalk and the measured one is $\sim$5 dB. The scatter could be due to missidentified (e.g. missing) and missfitted KIDs. In addition, the KID shape has strong readout power dependence (de Visser et al., 2014) so is not described by only a single Lorentzian fit to the frequency sweep, particularly off-resonance. To conclude, a model that takes into account more parameters is necessary to describe the crosstalk level of the full array, but this model is still valid as a first order approximation.

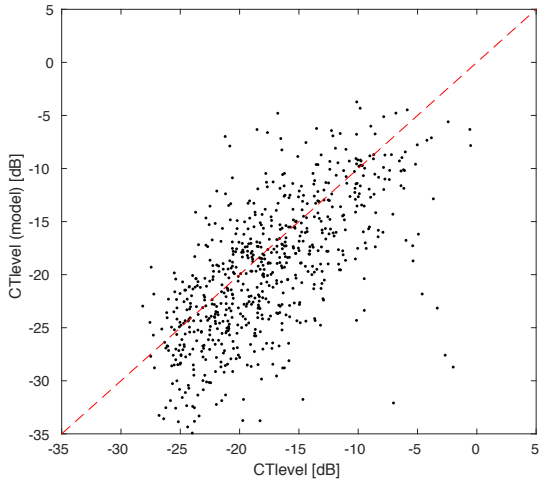


**Figure 3.8:** Comparison between the measured crosstalk level (x axis) and the theoretical one (y axis) given by equation 3.7. The dashed line represent the one-to-one relation.

## 3.4 SUMMARY

In this work we have characterised the level of crosstalk of an MKID array in order to correct images for crosstalk a posteriori. We measured beam maps for all KIDs in the array and we described the PSF as a two-dimensional Gaussian function, for each KID with the response above -30dB respect to the maximum. We subtracted the best-fit PSF of all coupled KID from the original beam map in order to remove the crosstalk present. Following this procedure, it is possible to correct astronomical images for crosstalk a posteriori. By analysing the level of crosstalk present in the array, we derived that about 72% of KIDs in the array crosstalk above -30 dB level while ∼48% crosstalk above -20 dB level. In the full array above the -30dB level, 48% of all KIDs are coupled to another detector, 16% are coupled to other two detectors and 7% are coupled to other three KIDs.

In addition, we estimated the resonance frequency and the quality factor of each KID by measuring the frequency sweep and describing the power of the transmission as a Lorenztian function. By using these parameters we derived a model of the crosstalk level by assuming that all KIDs have the same dip depth of the transmission and Q-factor. This model describes the expected general level of crosstalk as a function of the readout frequency separation of the detectors. This shows, both experimentally and using a simple model, that the rule of thumb is that KID-KID separation higher than 10 KID bandwidth corresponds to ∼-25 dB crosstalk. This can be taken as a design criterion, as required, and as a way to estimate crosstalk in future arrays.

*Acknowledgements:* The authors thank the team of the SPACEKIDS project for the collaboration.This project was supported by ERC starting grant ERC-2009-StG Grant 240602 TFPA and Netherlands Research School for Astronomy (NOVA).

# 4. The impact of *JWST* broad-band filter choice on photometric redshift estimation

*L. Bisigello, K. I. Caputi, L. Colina, O. Le Fèvre,*
*H. U. Nørgaard-Nielsen, P. G. Pérez-González, J. Pye,*
*P. van der Werf, O. Ilbert, N. Grogin, A. Koekemoer*
*2016, ApJS, 227, 19*

*The determination of galaxy redshifts in the* James Webb Space Telescope (JWST)*'s blank-field surveys will mostly rely on photometric estimates, based on the data provided by* JWST*'s Near-Infrared Camera (NIRCam) at* $0.6 - 5.0\,\mu$m *and Mid Infrared Instrument (MIRI) at* $\lambda > 5.0\,\mu$m*. In this work we analyse the impact of choosing different combinations of NIRCam and MIRI broad-band filters (F070W to F770W), as well as having ancillary data at* $\lambda < 0.6\,\mu$m*, on the derived photometric redshifts (*$z_{\rm phot}$*) of a total of 5921 real and simulated galaxies, with known input redshifts* $z = 0 - 10$*. We found that observations at* $\lambda < 0.6\,\mu$m *are necessary to control the contamination of high-*$z$ *samples by low-*$z$ *interlopers. Adding MIRI (F560W and F770W) photometry to the NIRCam data mitigates the absence of ancillary observations at* $\lambda < 0.6\,\mu$m *and improves the redshift estimation. At* $z = 7 - 10$*, accurate* $z_{\rm phot}$ *can be obtained with the NIRCam broad bands alone when* $S/N \geq 10$*, but the* $z_{\rm phot}$ *quality significantly degrades at* $S/N \leq 5$*. Adding MIRI photometry with one magnitude brighter depth than the NIRCam depth allows for a redshift recovery of* $83 - 99\%$*, depending on the spectral energy distribution type, and its effect is particularly noteworthy for galaxies with nebular emission. The vast majority of NIRCam galaxies with [F150W]=29 AB mag at* $z = 7 - 10$ *will be detected with MIRI at [F560W, F770W]< 28 mag if these sources are at least mildly evolved or have spectra with emission lines boosting the mid-infrared fluxes.*

## 4.1 INTRODUCTION

The power of multi-wavelength photometric observations to recover galaxy redshifts has been known since the late fifties (Baum, 1957) and it has been confirmed in the last decade with deep blank-field imaging surveys (e.g. Ilbert et al., 2009; Cardamone et al., 2010; Dahlen et al., 2013; Rafelski et al., 2015). Although spectroscopic redshifts are much better in precision than photometric estimates, photometry has two important advantages with respect to spectra: the number of sources that can be observed at the same time and sensitivity. Indeed, with a single photometric pointing it is possible to observe a large number of sources, while in general only a limited number of objects can simultaneously be targeted with spectroscopy. In addition, the spectroscopic observation of faint targets usually requires very long exposure times (e.g. Le Fèvre et al., 2015), and the faintest objects detected in photometric maps are beyond the technical possibilities of contemporary spectrographs (Caputi et al., 2012, 2015).

Photometric redshift determinations usually rely on the identification of strong features, such as the Lyman or $4000\,\text{Å}$ break, in a galaxy spectral energy distribution (SED), after they are convolved with the transmission functions of the filters utilised in the observations. This is the reason why it is necessary to do a careful filter selection when planning observations, balancing depth and wavelength coverage, in order to minimise degeneracies and misidentifications when obtaining photometric redshifts.

The *James Webb Space Telescope* (*JWST*[1], Gardner et al. 2009) is a foremost space mission for the coming years and the awaited successor of the *Hubble Space Telescope (HST)* and *Spitzer Space Telescope* at infrared wavelengths. It will have four instruments on board for imaging, spectroscopy and coronography, covering a wide range of wavelengths from 0.6 $\mu$m through 28.3 $\mu$m with sub-arcsec angular resolution.

One of *JWST*'s main scientific aims is to study the formation and evolution of galaxies at early cosmic times. For this purpose, deep blank-field imaging surveys will be carried out with two imaging cameras, namely the Near Infrared Camera (NIRCam; Rieke et al., 2005) and the Mid Infrared Instrument (MIRI; Rieke et al., 2015; Wright et al., 2015). In the vast majority of cases, galaxy redshift determinations will be done through SED-fitting analysis and, therefore, it is crucial to understand the impact of choosing different filter combinations on the ability to recover the right redshifts for all the observed sources.

[1] http://www.jwst.nasa.gov

NIRCam's filter wheels include eight broad-band filters, namely F070W, F090W, F115W, F150W, F200W, F277W, F356W and F444W, as well as a number of medium and narrow-band filters, covering the wavelength range $0.6 - 5.0\,\mu\mathrm{m}$[2]. The MIRI imager[3] contains nine different broad-band filters between 5 and 28 $\mu$m. This latter wavelength range encompasses the redshifted stellar light of high-$z$ galaxies, as well as the hot dust radiation emitted by low-$z$ sources. The two shortest-wavelength bands that we consider here (i.e., F560W and F770W) are the most sensitive in MIRI, so will be those primarily used for high-$z$ galaxy studies.

The complementarity of NIRCam's and MIRI's wavelength coverages makes that both cameras should ideally be considered for deep galaxy surveys. While surveys with NIRCam alone will be sufficient to encompass the $4000\,$Å break of galaxies at $0.6 < z < 10$, a secure measurement of the evolved stellar light (around rest $1\,\mu\mathrm{m}$) in $z > 4$ galaxies will also require observations with the MIRI filters. However, due to different detector technology in the near- and mid-IR range, MIRI's sensitivity is significantly lower than that of NIRCam, making observers doubt whether it is convenient to invest time on long MIRI observations when planning deep galaxy surveys. At the same time, the lack of *JWST* coverage below $0.6\,\mu\mathrm{m}$ requires considering whether observing fields with no ancillary shorter wavelength imaging can be effective to study galaxy evolution. Here we address these issues through the analysis of galaxy redshift recovery in different data availability situations, all treated on an equal basis, in order to allow the reader decide which camera and filter configuration would be optimal for their scientific interests.

The aim of this work is to assess the impact of different *JWST* broad-band filter combinations on recovering reliable photometric redshifts for galaxies at $z = 0 - 10$. In addition to considering the NIRCam broad bands and MIRI F560W and F770W filters, we tested the need of ancillary data at $\lambda < 0.6\,\mu\mathrm{m}$, such as those provided by *HST* observations. We applied our tests to three different galaxy samples with known redshifts: 1) a spectroscopic galaxy sample at $z = 0 - 6$; 2) a galaxy sample with consensus photometric redshifts at $z = 4 - 7$ from the CANDELS survey; and 3) a mock galaxy sample generated with different spectral templates at $z = 7$, 8, 9 and 10.

The structure of the Chapter is as follows. In Section 4.2 we describe our three sample selections, the acquisition of photometry in the relevant NIRCam and MIRI bands, and photometric redshift test methodology. In

[2]http://www.stsci.edu/jwst/instruments/nircam
[3]http://www.stsci.edu/jwst/instruments/miri

Section 4.3 we analyse our results at different redshifts, while in Section 4.4 we summarise our main findings and conclusions. Throughout this chapter, we adopt a cosmology with $H_0$ =70 $\mathrm{km\,s^{-1}\,Mpc^{-1}}$, $\Omega_M = 0.27$, $\Omega_\Lambda = 0.73$. All magnitudes refer to the AB system (Oke & Gunn, 1983).

## 4.2 SAMPLE SELECTION AND TEST METHODOLOGY

### 4.2.1 Galaxy sample selection

We select three different galaxy samples spanning rather complementary redshift ranges:

1. a sample of 2422 galaxies with secure spectroscopic redshifts at $z = 0 - 6$;
2. a sample of 1375 galaxies with consensus photometric redshifts at $z = 4 - 7$;
3. a sample of 2124 simulated galaxies at $z = 7 - 10$.

These three samples allow us to investigate the different problems arising when trying to recover redshifts photometrically using different combinations of *JWST* filters. By no means are these samples trying to emulate a complete, flux-limited galaxy population at $z = 0 - 10$ as it will be seen in a blank *JWST* field, and this is not necessary given the scope of this chapter.

#### 4.2.1.1 Sample 1

Our first galaxy sample contains 2422 galaxies with secure spectroscopic redshifts ($z_{\mathrm{spec}}$) from the ESO public compilation in the Chandra Deep Field South (CDFS; Cristiani et al., 2000; Croom et al., 2001; Bunker et al., 2003; Dickinson et al., 2004; Stanway et al., 2004b,a; Strolger et al., 2004; Szokoly et al., 2004; van der Wel et al., 2004; Doherty et al., 2005; Le Fèvre et al., 2005; Mignoli et al., 2005; Ravikumar et al., 2007; Popesso et al., 2009; Balestra et al., 2010; Silverman et al., 2010; Kurk, J. et al., 2013; Vanzella et al., 2014), and from Morris et al. (2015). In order to obtain multiwavelength photometry for these galaxies, we cross-match this sample with the public Cosmic Assembly Near-infrared Deep Extragalactic Legacy Survey (CANDELS; Grogin et al., 2011; Koekemoer et al., 2011) catalogue for the Great Observatory Origins Deep Survey South field (GOODS-S) obtained by Guo et al. (2013). This catalogue contains photometry in 17 broad bands, from 0.37 $\mu$m through 8.0 $\mu$m, obtained with ground-based and space telescopes, including *HST* and *Spitzer* (Ashby et al., 2015). This wavelength sampling allows for a good-quality SED fitting of the galaxy

stellar emission and a proper redshift recovery in the vast majority of cases, using standard galaxy spectral templates and photometric redshift codes.

Our aim here is to assess the impact of choosing different *JWST* filter sets on the derived photometric redshifts, rather than the performance of different photometric redshift codes and/or SED template libraries. Therefore, we explicitly exclude from our analysis any galaxy from the parent spectroscopic sample for which we can not correctly recover the redshift photometrically using all the CANDELS photometry up to $4.5\,\mu\mathrm{m}$. We do not use the two IRAC band data at longer wavelengths because their $S/N$ is considerably lower than for the other bands and they can be contaminated by polycyclic aromatic hydrocarbon emission at low $z$. The excluded galaxies are only $\sim 8\%$ of all the galaxies with publicly available $z_{\mathrm{spec}}$ in the CDFS.

To obtain photometric redshift estimates for all the galaxies in the parent spectroscopic sample, we run the public code *LePhare* (Arnouts et al., 1999; Ilbert et al., 2006) using templates from Bruzual & Charlot (2003, BC03 hereafter) with solar metallicity, a range of exponentially declining star formation histories with different characteristic times $\tau$ from 0.01 to 10 Gyr and ages from 0.01 to 10 Gyr. We allow for emission lines in *LePhare*, and apply the Calzetti et al. reddening law (Calzetti et al., 2000) with $A_V$ extinction values from 0 to 4.

We consider the subsample of 2422 objects with resulting photometric redshifts within $2\sigma$ ($\sigma$ =0.13) of the spectroscopic redshifts (Fig. 4.1), which constitute 92% of the parent spectroscopic sample, and adopt it as our Sample 1 for all further analysis. The Sample 1 redshift distribution is shown in Figure 4.2. This distribution peaks around $z \sim 1$ and has a high-$z$ tail up to $z = 6$, although the statistics are rather poor at $z > 4$. So, our main purpose with Sample 1 is to study the percentage of low-redshift galaxies that can leak to high $z$ when different filter sets, and thus different wavelength coverages, are available.

#### 4.2.1.2 Sample 2

Our second sample consists of 1375 galaxies at $z = 4 - 7$ taken from the CANDELS GOODS-S public catalogue. For this sample, we consider as fiducial redshifts the consensus photometric redshifts that have been compiled by Dahlen et al. (2013). The CANDELS consensus photometric redshifts result from the comparison of 11 independent SED fitting runs. We consider only CANDELS galaxies with $z > 4$ here, as lower redshifts are well represented in our Sample 1.

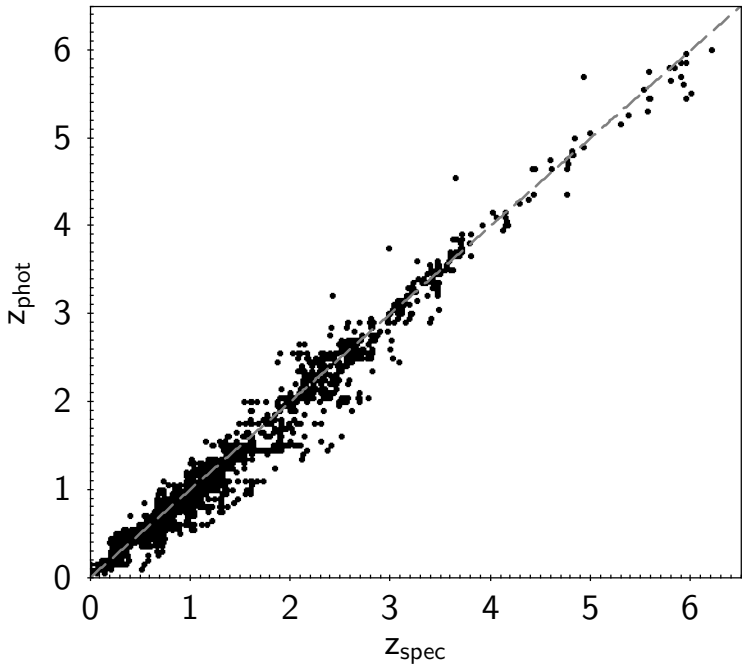


**Figure 4.1:** Photometric redshifts obtained with CANDELS 15-band photometry versus spectroscopic redshifts for Sample 1.

As we did for the sample with spectroscopic redshifts (Sample 1), we obtain our own photometric redshifts by running *LePhare* on the CANDELS 15-band photometry and using the same SED templates and parameter values stated before. In this case, our own photometric redshifts agree within $2\sigma$ ($\sigma$ =0.10) with the CANDELS consensus redshifts for 1375 (95%) of the GOODS-S galaxies with CANDELS redshifts $z_{\rm CANDELS} = 4-7$ (Fig. 4.3), consistently with the typical level of dispersion present in the individual SED fitting CANDELS runs. We adopt these 1375 galaxies as our Sample 2. The resulting redshift distribution is shown in Figure 4.2.

#### 4.2.1.3 Sample 3

We build our third sample with mock galaxies at fixed redshifts z= $7, 8, 9$ and $10$ (for an analysis of more redshifts see Appendix 5.A), simulating their SEDs with two different methods. Firstly, we consider the BC03 synthetic galaxy templates with four metallicities ($Z_\odot$, 0.4 $Z_\odot$, 0.2 $Z_\odot$, and 0.02 $Z_\odot$), exponentially declining star formation histories and five different ages, depending on redshift. We apply dust extinction by using the Calzetti

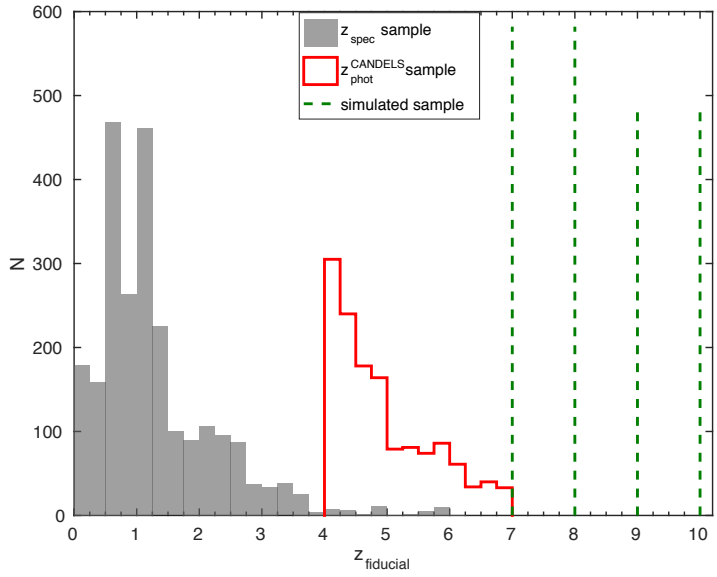


**Figure 4.2:** Redshift distribution of the three galaxy samples considered in this work: a galaxy sample with spectroscopic redshifts in the GOODS-S field (full grey; Sample 1), a galaxy sample with well established CANDELS photometric redshifts, also in GOODS-S (red line; Sample 2) and a sample of simulated galaxies with known input redshifts (dashed line; Sample 3).

et al. reddening law with $A_V = 0 - 1$, and the effect of absorption by the intergalactic medium (IGM; Madau, 1995).

The BC03 models do not include emission lines, so we manually add the H$\alpha$, H$\beta$, [O III]5007 Å and [O II]3727 Å emission lines to those templates for which the age is equal or lower than the characteristic $\tau$ of the exponentially declining star formation history, as follows. We start from the observed mean value of the $H\alpha$+[N II]+[S II] equivalent width (EW), which is 422-423 Å at $z = 3.8 - 5$ (Smit et al., 2016). Then, we assume line ratios from Anders & Fritze-v. Alvensleben (2003) in order to derive the equivalent widths of $H\alpha$ alone at different metallicities. Fumagalli et al. (2012) obtained a relation between H$\alpha$ equivalent width and redshift, namely EW(H$\alpha$) $\propto (1+z)^{1.8}$, which has been checked to be consistent with observations up to $z \sim 5$ (Stark et al., 2013) [4]. Following this relation, we derive EW(H$\alpha$) for all considered redshifts. We also

[4]This redshift dependence is slightly steeper than that obtained by e.g. Faisst et al. (2016), but adopting this other prescription would only change our assumed H$\alpha$ EW by a factor $< 1.3$.

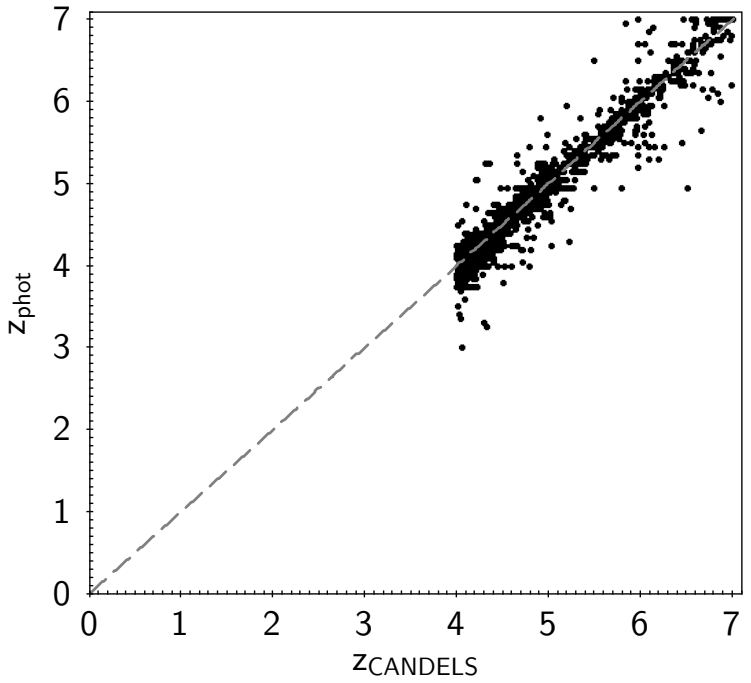


**Figure 4.3:** Photometric redshifts obtained with 15-band CANDELS photometry in this work versus the consensus CANDELS photometric redshifts for Sample 2.

derive equivalent widths for H$\beta$ assuming case B recombination and the corresponding equivalent widths for [O III] and [O II] by using the line ratios tabulated in Anders & Fritze-v. Alvensleben (2003). We explicitly decide not to include the Ly$\alpha$ line because the importance of its emission in galaxies at $z > 7$ is still unclear (e.g., Stark et al., 2013; Konno et al., 2014; Pentericci et al., 2014). Finally, we normalise every model at 29 AB mag at 1.5$\mu$m (corresponding to the NIRCam F150W filter pivot wavelength).

The complete list of adopted parameter values is summarised in Table 4.1, while some SED examples at z=7 are shown in Figure 4.4. Our sample contains a total of 864 galaxies, corresponding to 240 BC03-based SED models at each redshift 7 and 8, and 192 SED models at each redshift 9 and 10. For each model, we consider independently three possible $S/N$ values ($S/N = 3, 5$ and 10) for the flux corresponding to [F150W]=29 AB mag. The $S/N$ values of the photometry in all other bands have been scaled as we explain in §4.2.2.1.

Secondly, we simulate further $z = 7 - 10$ galaxy SEDs with the population synthesis code *Yggdrasil* (Zackrisson et al., 2011), which has

**Table 4.1:** Parameter values used to create BC03 SED models for simulated galaxies at z$= 7 - 10$.

| Parameter | Values |
|---|---|
| metallicity | $Z_\odot$, $0.4Z_\odot$, $0.2Z_\odot$,$0.02Z_\odot$[a] |
| SFH $\tau$ [Gyr] | 0.01,0.1,1,10 |
| $A_V$ | 0,0.5,1 |
| age [Gyr] | 0.01,0.05,0.2,0.4,0.6[b] |
| $z$ | 7,8,9,10 |
| $S/N$[c] | 3,5,10 |

[a] for metallicity $0.02Z_\odot$ we considered only ages $t$ <0.2 Gyr.
[b] we considered this age only up to redshift $z = 8$.
[c] for the flux corresponding to the normalization magnitude, i.e., [F150W]=29 mag.

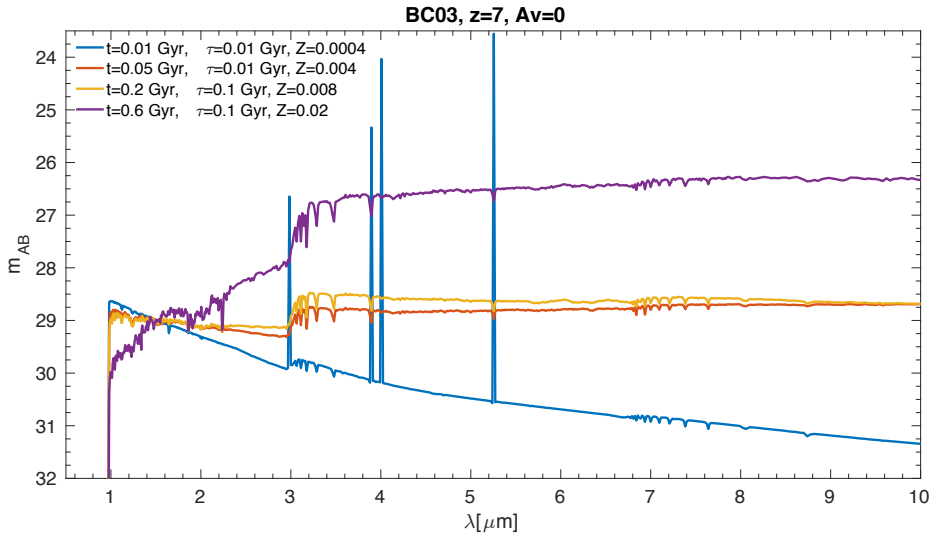


**Figure 4.4:** Four examples of BC03 SED templates at z=7 with $A_V = 0$ in the observed frame.

been designed specifically to model high-redshift galaxies. We use a set of parameter values similar to the ones used for the BC03 templates, except that the star formation histories are somewhat different, consisting of a

**Table 4.2:** Parameter values used to create *Yggdrasil* SED models for simulated galaxies at z$= 7 - 10$.

| Parameter | Values |
|---|---|
| metallicity | $Z_\odot$,0.4$Z_\odot$,0.2$Z_\odot$,0.02$Z_\odot$,0[a] |
| constant SFH for [Myr] | 10,30,100 |
| $A_V$ | 0,0.5,1 |
| age [Gyr] | 0.01,0.05,0.2,0.4,0.6[b] |
| $f_{\rm cov}$ | 0,1 |
| $z$ | 7,8,9,10 |
| $S/N$[c] | 3,5,10 |

[a] for this metallicity we considered only ages $t$ <0.2 Gyr.
[b] we considered this age only at redshift $z \leq 8$.
[c] for the flux corresponding to the normalisation magnitude, i.e., [F150W]=29 mag.

step function for which the duration of the constant star formation period is set as a free parameter. And, in addition to the normal stellar templates, we adopt also a template with a metal-free, population-III single stellar population (Schaerer, 2002). In all cases, we consider the two possible extreme gas covering factors, namely $f_{\rm cov} = 0$ and 1. The complete list of adopted parameter values is given in Table 4.2. We show four SED template examples for $z = 7$ galaxies in Figure 4.5.

The *Yggdrasil* models include the effects of nebular line and continuum emission, so we do not need to add any extra lines manually as we did for the BC03 templates. We include the effect of dust reddening and IGM absorption in the same way as for the BC03 models. We remove the Ly$\alpha$ emission line from the *Yggdrasil* models, because its presence and importance is debated at $z > 7$, as we explained before. Once again, we normalise every SED template to [F150W]=29 mag at 1.5 $\mu$m. Our *Yggdrasil* simulated sample comprises a total of 1260 galaxies, corresponding to 342 SED models at each redshift 7 and 8, and 288 SED models at each redshift 9 and 10. The complete redshift distribution of our galaxy Sample 3, simulated both with the BC03 and *Yggdrasil* templates, is shown in Fig. 4.2.

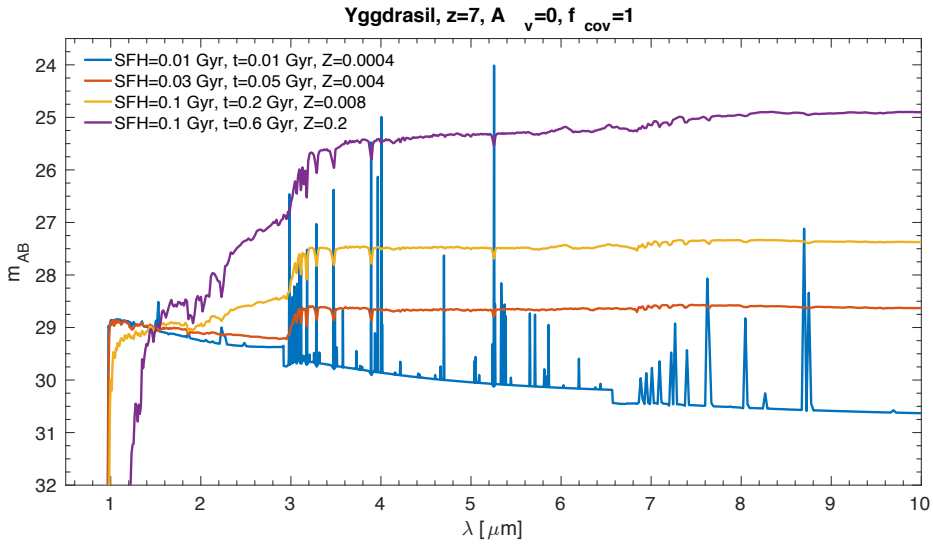


**Figure 4.5:** Four examples of *Yggdrasil* SED templates at $z = 7$ with $A_V = 0$. Note that templates with gas covering factor $f_{\rm cov} = 1$ have multiple emission lines, but only when a young stellar population, due to very recent star formation, is still present.

## 4.2.2 Test methodology

### 4.2.2.1 Interpolation/extrapolation of JWST photometry

Based on the best-fit SEDs obtained running *LePhare* on the CANDELS photometry for the galaxies in Samples 1 and 2, and the simulated SEDs for our mock galaxies in Sample 3, we measure the photometry expected at the 8 NIRCam broad bands and the two MIRI broad bands F560W and F770W for all our galaxies (see Table 4.3 for a summary of the different *JWST* filters considered in this work). Our procedure to interpolate/extrapolate the *JWST* photometry is similar for our three galaxy samples. The main difference is that in Samples 1 and 2, we simply adopt $S/N$ values for the photometry scaled from the CANDELS photometry, while for Sample 3 we test three different $S/N$ values in a controlled manner, in order to assess the effect of $S/N$ on our results.

As a first step, for every galaxy in our real galaxy samples (Samples 1 and 2), we derive NIRCam broad-band fluxes by convolving the best-fit SED template with the transmission curve of each *JWST* filter (Meyer et al., 2004). To each flux, we assign an error bar corresponding to a $S/N$ equal to that of the closest filter in the CANDELS catalogue. We adopt as NIRCam

flux a random value (selected from a uniform distribution) within the corresponding error bar.

Note that, in practice, NIRCam will reach the depth of the *HST* CANDELS photometry in very short integration times, so the $S/N$ achieved for CANDELS galaxies in typically deep NIRCam surveys will be higher than what we consider here. However, our assumed $S/N$ are already sufficiently high in most cases: virtually all galaxies in Sample 1 and more than 90% of galaxies in Sample 2 have $S/N \geq 5$ in their derived NIRCam F150W photometry. Thus, our results derived here for these real galaxy samples are mostly independent of $S/N$, as we explain below (the low $S/N$ effect will be more clearly manifested in our Sample 3, where we explicitly set three different $S/N$ values for each template, including a low value $S/N = 3$).

As a second step, we measure the photometry expected at the MIRI bands for our Sample 1 and 2 galaxies, which results from the extrapolation of the best-fit template redward of the CANDELS IRAC $4.5\,\mu\mathrm{m}$ coverage. We convolve the best SED model with the two MIRI bands' transmission curves (Bouchet et al., 2015; Glasse et al., 2015). To each MIRI band flux, we assign an error bar corresponding to a $S/N$ scaled using as reference the $S/N$ in the NIRCam F150W band: we assume that a MIRI F560W or F770W flux corresponding to a magnitude 28 (AB) would have the same $S/N$ as a NIRCam F150W flux corresponding to 29 mag (whose $S/N$ is, in turn, scaled assuming that the 'measured' NIRCam F150W flux $S/N$ for each galaxy is the same as the real CANDELS *HST* F160W flux $S/N$). Fixing the $S/N$ in the NIRCam and MIRI photometry implicitly assumes specific integration times with the *JWST* instruments. In practice, this assumption does not matter, as our results will be equally valid for any galaxies with similar $S/N$ values, independently of the MIRI fluxes at which these $S/N$ are reached.[5] Finally, we randomise every flux within its own error bar.

For Sample 3 with mock galaxies, we convolve every simulated SED template with the transmission curve of each NIRCam filter. In our sample every SED template is considered three times, in order to apply three fixed, reference $S/N$ values (10, 5 and 3) to the NIRCam F150W fluxes. We assume the same integration times for all the other NIRCam bands and took into account the differences in filter sensitivities to assign $S/N$ in each band. A different strategy that assumes the same observational depth for all NIRCam bands is presented in Appendix 4.B. We consider every flux below the $2\sigma$ level as a non-detection. The $2\sigma$ detection limits in each band

[5]This statement implicitly assumes that the fainter galaxy SEDs will be represented by those of the currently analysed galaxies. So far, this has been shown to be the case with progressively deeper galaxy surveys.

**Table 4.3:** List of *JWST* filters considered in this work, their pivot wavelengths and bandwidths.

| Filter name | $\lambda$ [$\mu$m] | Bandwidth [$\mu$m][a] |
|---|---|---|
| NIRCam/F070W | 0.70 | 0.18 |
| NIRCam/F090W | 0.90 | 0.23 |
| NIRCam/F115W | 1.15 | 0.30 |
| NIRCam/F150W | 1.50 | 0.38 |
| NIRCam/F200W | 1.99 | 0.53 |
| NIRCam/F277W | 2.77 | 0.82 |
| NIRCam/F356W | 3.56 | 0.99 |
| NIRCam/F444W | 4.41 | 1.29 |
| MIRI/F560W | 5.60 | 1.41 |
| MIRI/F770W | 7.70 | 2.30 |

[a] This bandwidth corresponds to the entire wavelength range in which the filter transmission is $> 1\%$.

**Table 4.4:** List of $2\sigma$ detection magnitude limits for different *JWST* filters corresponding to our fiducial source and each reference $S/N$ value considered for Sample 3.

| Band | S/N=10 [a] | S/N=5 [a] | S/N=3 [a] |
|---|---|---|---|
| F070W | 30.2 | 29.4 | 28.9 |
| F090W | 30.5 | 29.7 | 29.2 |
| F115W | 30.6 | 29.9 | 29.3 |
| F150W | 30.7 | 30.0 | 29.4 |
| F200W | 30.9 | 30.2 | 29.6 |
| F277W | 30.9 | 30.2 | 29.6 |
| F356W | 30.7 | 30.0 | 29.4 |
| F444W | 30.2 | 29.4 | 28.9 |
| F560W | 29.7 | 29.0 | 28.4 |
| F770W | 29.7 | 29.0 | 28.4 |

[a] $S/N$ value for [F150W]=29 mag.

for each fixed reference $S/N$ value at F150W are listed in Table 4.4. Note that, as a conservative approach, we adopt $3\sigma$ flux upper limits (rather than $2\sigma$) in all cases of non-detections for running the $z_{\rm phot}$ code, as explained below.

Finally, we obtain 10 random realisations of each NIRCam band flux within the corresponding error bar. Note that, in contrast, for Samples 1 and 2 we consider a single realisation of each flux, simply because in the case of real galaxies the NIRCam fluxes are well constrained by interpolation of the CANDELS fluxes, so their error bars are typically smaller than in Sample 3.

In a similar way, we derive fluxes in the MIRI bands by convolving all SED templates in the sample with the two MIRI filter transmission curves. Then, we scale each MIRI flux $S/N$, such that a mag$_{AB}$ =28 in MIRI has the same $S/N$ as a NIRCam magnitude [F150W]=29. This is a realistic assumption of how the NIRCam and MIRI data will typically be matched. As for the NIRCam bands, we randomise every MIRI flux 10 times within its own error bar.

### 4.2.3 Photometric redshift determinations

With the expected *JWST* photometry measured on the galaxy templates for the three samples, we can test how accurately it is possible to derive photometric redshifts by using different *JWST* band combinations. The band combinations that we analyse in this work are:

- 8 NIRCam broad bands
- *HST* F435W, F606W and 8 NIRCam broad bands
- VLT $U$ band, F435W, *HST* F606W and 8 NIRCam broad bands
- 8 NIRCam broad bands and 2 MIRI bands (F560W and F770W)
- 8 NIRCam broad bands and MIRI F560W only
- 8 NIRCam broad bands and MIRI F770W only
- *HST* F435W, F606W, 8 NIRCam broad bands and 2 MIRI bands
- *HST* F435W, F606W, 8 NIRCam broad bands and MIRI F560W
- *HST* F435W, F606W, 8 NIRCam broad bands and MIRI F770W

These different filter combinations have been chosen to test in which cases the NIRCam broad bands alone are sufficient to recover good photometric redshifts and in which cases the MIRI bands can improve these estimates. Because MIRI is considerably less sensitive than NIRCam, much longer integration times are necessary to reach comparable depths. Thus, many observing programs may opt for using a single MIRI filter (F560W or F770W) rather than both of them. This is why we test separately the cases in which a single and both MIRI bands are used.

In addition, we analyse the cases in which two short-wavelength *HST* bands and the $U$ band are included. All these bands are beyond *JWST*'s wavelength coverage, so they cannot be substituted with any *JWST* band. We use the CANDELS catalogue to recover observations in these bands for galaxies in Samples 1 and 2. We ignore these bands for Sample 3: they are irrelevant, as the Lyman break is completely contained within the NIRCam wavelength range at $z \geq 7$.

We note that *LePhare* has been run using the native BC03 models allowing the code to incorporate emission lines with its own prescription in the cases of Samples 1 and 2 (as it is described in Section 4.2.1.1). For our mock galaxies in Sample 3, we run *LePhare* using directly our own customised templates, i.e., the BC03 templates with emission lines incorporated as explained in Section 4.2.1.3 and the *Yggdrasil* templates. In addition, in the *LePhare* runs for Sample 3 we also include some older galaxy models (as in Samples 1 and 2), and allowe for extinction values from $A_V = 0$ to 4 in all cases, in order to test whether there could be degeneracies between redshift and dust/age produced in the photometric fitting. This consideration of a wide range of redshifts, ages and extinction values emulates the real situation in which one simply has a photometric input catalogue without knowing a priori which sources are at high or low redshifts. No extra consideration of emission lines has been allowed for Sample 3 in *LePhare*, as our young-galaxy models already account for them.

For all the filter combinations we run *LePhare* on the three galaxy samples, in order to recover the galaxy photometric redshifts and compare them with the fiducial redshift available for each galaxy. In the filter combinations with MIRI bands in Samples 1 and 2, and all cases for Sample 3, we choose the median photometric redshift of the 10 iterations done for each object (corresponding to different variations in the photometry, as explained above).

For each sample and filter set combination, in Section 4.3 we quote the resulting mean value of the normalised redshift difference distribution $\delta z = (z_{\rm phot} - z_{\rm fiduc.})/(1 + z_{\rm fiduc.})$ and the r.m.s. ($\sigma$) of the *normalised* absolute redshift difference distribution $|z_{\rm phot} - z_{\rm fiduc.}|/(1 + z_{\rm fiduc.})$. Note that, although we compute $\sigma$ independently for each sample and broad-band combination, we considere as reference to define outliers a single $\sigma$ value per sample (the minimum obtained with all the filter sets). This allows us to directly compare how the outlier fractions change among the different filter combinations.

We warn the reader that the specific values of the statistical quantities ($\sigma$, outlier percentages) quoted in this Chapter refer to the samples analysed

**Table 4.5:** Statistical properties of Sample 1 for all the different *JWST* and ancillary data broad-band combinations. The last two columns indicate the mean of $(z_{\rm phot} - z_{\rm spec})/(1 + z_{\rm spec})$ and the r.m.s. ($\sigma$) of $|z_{\rm phot} - z_{\rm spec}|/(1 + z_{\rm spec})$, respectively. The second column provides the number and percentages of $z = 1 - 4$ sources that become outliers, i.e., objects beyond $3\sigma$ in the $z_{\rm phot} - z_{\rm spec}$ relation, with $\sigma = 0.058$, which is the minimum $\sigma$ obtained with all the filter combinations considered for this galaxy sample. The total original number of $z = 1 - 4$ galaxies in Sample 1 is 1306.

| Bands | $z = 1 - 4$ | $< \delta z >$ | $\sigma_{\lvert\delta z\rvert}$ |
|---|---|---|---|
| 8 NIRCam broad bands | 134 (10.3%) | -0.024 | 0.115 |
| *HST* F435W + *HST* F606W + 8 NIRCam bands | 93 (7.1%) | -0.032 | 0.076 |
| VLT $U$ + *HST* F435W, F606W + 8 NIRCam | 89 (6.8%) | -0.043 | 0.058 |
| 8 NIRCam bands + MIRI F560W, F770W | 116 (8.9%) | -0.037 | 0.066 |
| 8 NIRCam bands + MIRI F560W | 120 (9.2%) | -0.029 | 0.077 |
| 8 NIRCam bands + MIRI F770W | 128 (9.8%) | -0.037 | 0.067 |
| *HST* F435W, F606W + 8 NIRCam bands + MIRI F560W, F770W | 109 (8.3%) | -0.042 | 0.062 |
| *HST* F435W, F606W + 8 NIRCam bands + MIRI F560W | 93 (7.1%) | -0.034 | 0.060 |
| *HST* F435W, F606W + 8 NIRCam bands + MIRI F770W | 106 (8.1%) | -0.042 | 0.064 |

here and may have variations for other galaxy samples with different redshifts and SED type distributions. Even so, as all our tests are internally consistent, our results constitute a useful reference to assess the ability to recover galaxy redshifts using different *JWST* filter combinations and ancillary data.

## 4.3 RESULTS

In this section we present our results for the three galaxy samples analysed in this work.

### 4.3.1 Results for Sample 1

In Figures 4.6 to 4.8 we show the comparison between the spectroscopic and our derived photometric redshifts obtained with different filter combinations for Sample 1. For each case, we quote the mean of the $(z_{\rm phot} - z_{\rm spec})/(1 + z_{\rm spec})$ distribution and the r.m.s. of $|z_{\rm phot} - z_{\rm spec}|/(1 + z_{\rm spec})$, computed considering all galaxies in the sample. We identify $3\sigma$ outliers using as reference $\sigma$ =0.058, which is the minimum of all the $\sigma$ values that we get for Sample 1. This galaxy sample is particularly useful to test the percentage of low-$z$ galaxies ($z < 4$) that leak to wrong redshifts

due to failures in the redshift recovery. The percentages of these low-$z$ sources that are leaking outliers for each filter combination is listed in Table 4.5. For this analysis, we consider only the redshift bin $z = 1 - 4$, avoiding lower $z$ galaxies, as the MIRI filters are not very suitable to trace the direct stellar emission at such low $z$. Note that, although these obtained outlier percentages apply particularly to this galaxy sample, the changes obtained with different passbands are of general validity and show the impact of incorporating different filters on the redshift recovery.

Firstly, we analyse the case of using the 8 NIRCam broad bands with and without ancillary *HST* and ground-based $U$-band data (Figure 4.6). When using only the 8 NIRCam broad bands, the percentage of $z = 1 - 4$ sources that are $3\sigma$ outliers is of 10.3%, including several extreme cases which appear as $z > 4$ contaminants. Besides, the r.m.s. of the $|z_{\rm phot} - z_{\rm spec}|/(1 + z_{\rm spec})$ distribution is high ($\sigma = 0.115$) compared with the typical precision that can currently be achieved for low-$z$ galaxies in deep surveys. When adding shorter-wavelength *HST* data, the normalised redshift difference distribution r.m.s. is significantly lower, the outlier percentage decreases to 7.1%, and the majority of the most extreme redshift outliers are corrected. When adding also the $U$ band, the r.m.s. reaches a minimum ($\sigma = 0.058$) and so does the outlier percentage (6.8%), leaving basically no catastrophic outlier cases. This is because it is necessary to cover wavelengths shorter than $0.7\,\mu$m in order to distinguish between the Lyman and $4000$ Å breaks at $z < 6$. The improvement on the photometric redshift estimation is also due to the mere increase in the wavelength coverage given by the larger number of bands. Besides, the incorporation of the *HST* and $U$-band data to the NIRCam photometry reduces the photometric redshift dispersion ($\sigma$) by about half (Fig. 4.6).

Secondly, we test the photometric redshift estimation when complementing the NIRCam photometry with MIRI photometry, instead of shorter wavelength data (Figure 4.7). When we incorporate both MIRI F560W and F770W bands, the resulting normalised redshift difference distribution r.m.s. is significantly lower ($\sigma = 0.066$) than in the case with NIRCam data alone, indicating that the presence of MIRI photometry can mitigate the absence of short-wavelength data. (Table 4.5).

Lastly, we consider the situation in which *HST* ancillary data along with NIRCam and MIRI data are available (Figure 4.8). We explicitly test a combination without $U$-band photometry, as ground-based $U$-band observations with matching depth to *JWST* observations will be time-consuming and difficult to achieve. The results are rather similar to the case with NIRCam and MIRI bands considered together: the obtained r.m.s. is $\sigma = 0.062$, with the fraction of redshift outliers being slightly reduced.

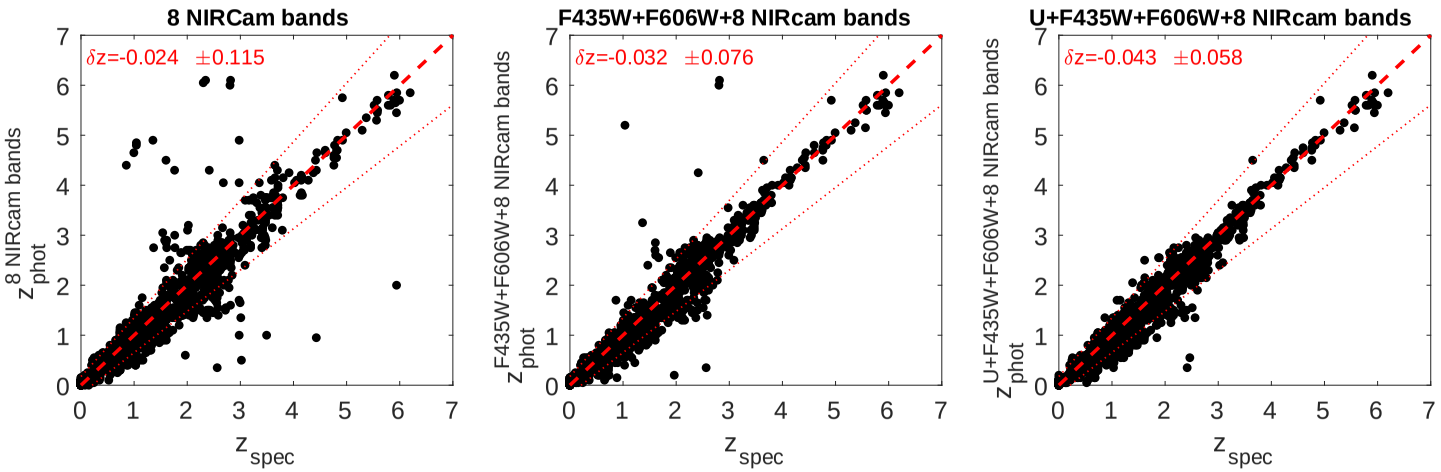


**Figure 4.6:** Photometric versus spectroscopic redshifts for galaxies in Sample 1. *Left*: photometric redshifts obtained with 8 NIRCam broad bands. *Centre*: photometric redshifts obtained with the *HST* F435W, *HST* F606W and 8 NIRCam broad bands. *Right*: the same as in the central panel, but considering also the VLT $U$ band for computing photometric redshifts. The dotted lines in each panel delimit the $3\sigma$ limit of the $|z_{\rm phot} - z_{\rm spec}|/(1 + z_{\rm spec})$ distribution, with $\sigma$ =0.058, which is the minimum value of $\sigma$ that we get for Sample 1 with all the considered filter combinations.

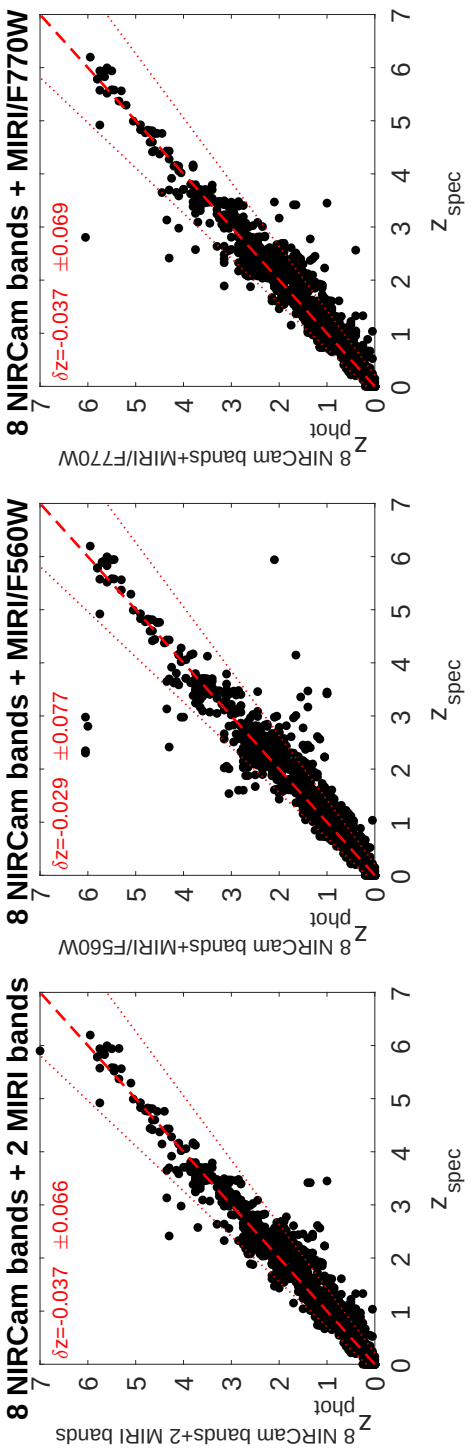


**Figure 4.7:** Photometric versus spectroscopic redshifts for galaxies in Sample 1. *Left*: photometric redshifts obtained with 8 NIRCam broad bands and MIRI F560W, F770W. *Centre*: Photometric redshifts obtained with 8 NIRCam broad bands and MIRI F560W only. *Right*: Photometric redshift obtained with 8 NIRCam broad bands and MIRI F770W only. The dotted lines in each panel delimit the $3\sigma$ limit of the $|z_{\rm phot} - z_{\rm spec}|/(1 + z_{\rm spec})$ distribution, with $\sigma$ =0.058, which is the minimum value of $\sigma$ that we get for Sample 1 with all the considered filter combinations.

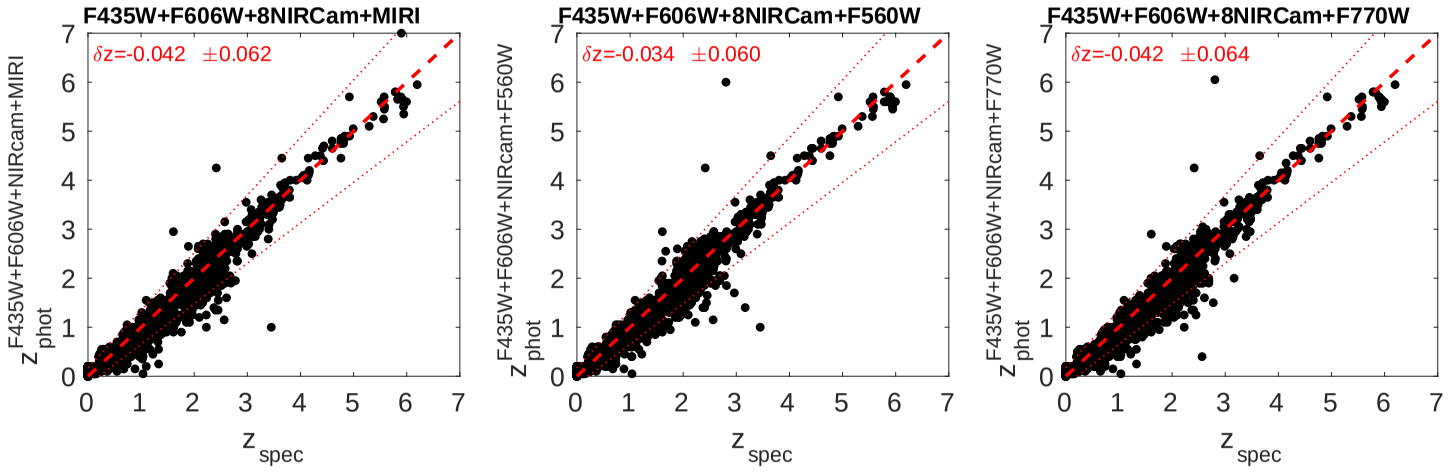


**Figure 4.8:** Photometric versus spectroscopic redshifts for galaxies in Sample 1. *Left*: photometric redshifts obtained with *HST* F345W, *HST* F606W, 8 NIRCam broad bands, and MIRI F560W, F770W. *Centre*: Photometric redshifts obtained with *HST* F345W, *HST* F606W, 8 NIRCam broad bands and MIRI F560W. *Right*: Photometric redshifts obtained with *HST* F345W, F606W, 8 NIRCam broad bands and MIRI F770W. The dotted lines in each panel delimit the $3\sigma$ limit of the $|z_{\rm phot} - z_{\rm spec}|/(1 + z_{\rm spec})$ distribution, with $\sigma$ =0.058, which is the minimum value of $\sigma$ that we get for Sample 1 with all the considered filter combinations.

**Table 4.6:** Statistical properties for Sample 2 for all the different *JWST* and ancillary data broad-band combinations. The last two columns indicate the mean of $(z_{\rm phot} - z_{\rm spec})/(1 + z_{\rm spec})$ and the r.m.s. ($\sigma$) of $|z_{\rm phot} - z_{\rm spec}|/(1 + z_{\rm spec})$, respectively. Columns 2 and 3 provide the numbers and percentages of galaxies leaking towards lower redshifts (see Fig. 4.6). These outliers are defined as galaxies beyond $3\sigma$, with $\sigma$ =0.065, which is the minimum $\sigma$ obtained with the different filter combinations considered for this galaxy sample. The total original number of $z = 4 - 5$ ($z = 5 - 7$) galaxies in Sample 2 is 887 (488).

| Bands | $z = 4 - 5$ | $z = 5 - 7$ | $< \delta z >$ | $\sigma_{<\|\delta z\|>}$ |
|---|---|---|---|---|
| 8 NIRCam broad bands | 190 (21.4%) | 46 (9.4%) | -0.111 | 0.218 |
| *HST* F435W, F606W + 8 NIRCam bands | 21 (2.4%) | 36 (8.0%) | -0.023 | 0.119 |
| VLT $U$ + *HST* F435W, F606W+ 8 NIRCam bands | 23 (2.6%) | 37 (8.2%) | -0.024 | 0.122 |
| 8 NIRCam bands + MIRI F560W, F770W | 68 (7.7%) | 14 (3.1%) | -0.034 | 0.099 |
| 8 NIRCam bands + MIRI F560W | 120 (13.5%) | 41 (9.1%) | -0.072 | 0.169 |
| 8 NIRCam bands + MIRI F770W | 90 (10.1%) | 31 (6.9%) | -0.049 | 0.127 |
| *HST* F435W, F606W + 8 NIRCam bands + MIRI F560W, F770W | 11 (1.2%) | 7 (1.4%) | -0.004 | 0.065 |
| *HST* F435W, F606W + 8 NIRCam bands + MIRI F560W | 20 (2.2%) | 32 (6.6%) | -0.019 | 0.113 |
| *HST* F435W, F606W + 8 NIRCam bands + MIRI F770W | 17 (1.9%) | 18 (4.0%) | -0.011 | 0.083 |

Interestingly, when only NIRCam and MIRI photometry are considered, the F770W data improves the overall redshift statistics. Instead, when *HST* data are also available, the incorporation of F560W alone provides slightly better results. (This is related to how the $\chi^2$-fitting procedure works, typically giving more weight to longer wavelength data where the sources are brighter).

To conclude, the 8 NIRCam broad bands alone are not adequate to obtain sufficiently good photometric redshifts at $z < 4$. Although for most galaxies the derived redshifts are correct, the overall obtained statistics is poor compared with the typical $z_{\rm phot}$ quality that can currently be achieved in deep surveys at these redshifts. Observations at wavelengths shorter than $0.7\,\mu$m are necessary to remove the most extreme redshift outliers. Incorporating MIRI longer-wavelength photometry instead can mitigate the absence of short-wavelength observations. Having a complete optical and infrared coverage up to $7.7\,\mu$m will allow us to keep the $z < 4$ redshift statistics well under control.

### 4.3.2 Results for Sample 2

In Figures 4.9 to 4.11 we show the comparison between our recovered photometric redshifts and fiducial CANDELS consensus redshifts for galaxies in Sample 2 (all of which have fiducial redshifts $z > 4$). As

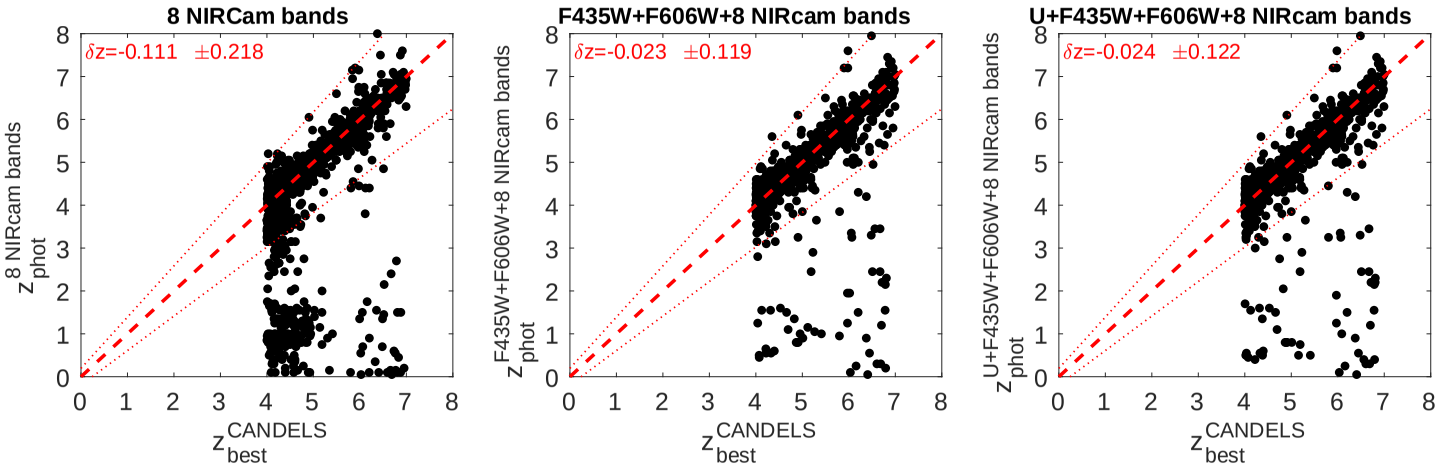


**Figure 4.9:** Our derived photometric redshifts versus CANDELS consensus photometric redshifts for galaxies in Sample 2. *Left*: Photometric redshifts obtained with 8 NIRCam broad bands. *Centre*: Photometric redshifts obtained with *HST* F435W, F606W and 8 NIRCam broad bands. *Right*: Photometric redshifts obtained with the same bands as in the central panel plus the VLT $U$ band. The dotted lines in each panel delimit the $3\sigma$ limit of the $|z_{\rm phot} - z_{\rm fiduc.}|/(1 + z_{\rm fiduc.})$ distribution, with $\sigma$ =0.065, which is the minimum value of $\sigma$ that we get for Sample 2 with all the considered filter combinations.

**Table 4.7:** Number of outliers among our 864 Sample 3 galaxies simulated with BC03 models and manual addition of emission lines for different *JWST* filter combinations and assumed $S/N$ values at F150W. Outliers are defined as galaxies with $|z_{\rm phot} - z_{\rm fiduc.}|/(1 + z_{\rm fiduc.}) > 0.15$.

| Bands | $S/N = 10$ | $S/N = 5$ | $S/N = 5$ (only EL)[a] | $S/N = 3$ |
|---|---|---|---|---|
| 8 NIRCam broad bands | 1 (0.1%) | 24 (2.8%) | 20[b](3.5%) | 87 (10.1%) |
| 8 NIRCam bands + MIRI F560W, F770W | 1 (0.1%) | 5 (0.6%) | 3[b](0.5%) | 26 (3.0%) |
| 8 NIRCam bands + MIRI F560W | 1 (0.1%) | 7 (0.8%) | 3[b](0.5%) | 29 (3.4%) |
| 8 NIRCam bands + MIRI F770W | 2 (0.2%) | 16 (1.9%) | 14[b](2.4%) | 45 (5.2%) |

[a] only templates with emission lines (EL).
[b] out of a total of 576 galaxies with emission lines. The percentages refer to this denominator.

**Table 4.8:** Number of outliers among our 1260 Sample 3 galaxies simulated with *Yggdrasil* models for different *JWST* filter combinations and assumed $S/N$ values at F150W. Outliers are defined as galaxies with $|z_{\rm phot} - z_{\rm fiduc.}|/(1 + z_{\rm fiduc.}) > 0.15$.

| Bands | $S/N = 10$ | $S/N = 5$ | $S/N = 5$ (only EL)[a] | $S/N = 3$ |
|---|---|---|---|---|
| 8 NIRCam bands | 11 (0.9%) | 257 (20.4%) | 118[b](49.2%) | 560 (44.4%) |
| 8 NIRCam bands + MIRI F560W, F770W | 1 (0.1%) | 152 (12.1%) | 41[b](17.1%) | 462 (36.7%) |
| 8 NIRCam bands + MIRI F560W | 13 (1.0%) | 188 (14.9%) | 68[b](28.3%) | 490 (38.9%) |
| 8 NIRCam bands + MIRI F770W | 8 (0.6%) | 196 (15.6%) | 79[b](32.9%) | 508 (40.3%) |

[a] only templates with emission lines (EL).
[b] out of a total of 240 galaxies with emission lines. The percentages refer to this denominator.

we did before, we derive $|z_{\rm phot} - z_{\rm fiduc.}|/(1 + z_{\rm fiduc.})$ for all our galaxies and we identify $3\sigma$ outliers, where we adopt $\sigma = 0.065$, which is the smallest r.m.s. value that we obtain with the different filter combinations. The percentages of outliers in each case are listed in Table 4.6.

As for Sample 1, our first step consist of analysing the resulting photometric redshifts obtained using the 8 NIRCam broad bands with and without the *HST* and $U$-band data (Figure 4.9). When using only the 8 NIRCam broad bands the percentage of outliers for Sample 2 is high. We do not show the percentage of low-$z$ contaminants because of the sample selection, which by construction only has $z > 4$ objects. The most evident effect in Sample 2 is the leakage of high-$z$ sources to low-$z$ values produced by the insufficient photometric coverage. This is particularly important for galaxies with input redshifts $z = 4 - 5$: a bit more than 20% of them are found $> 3\sigma$ away at lower redshifts (Table 4.6).

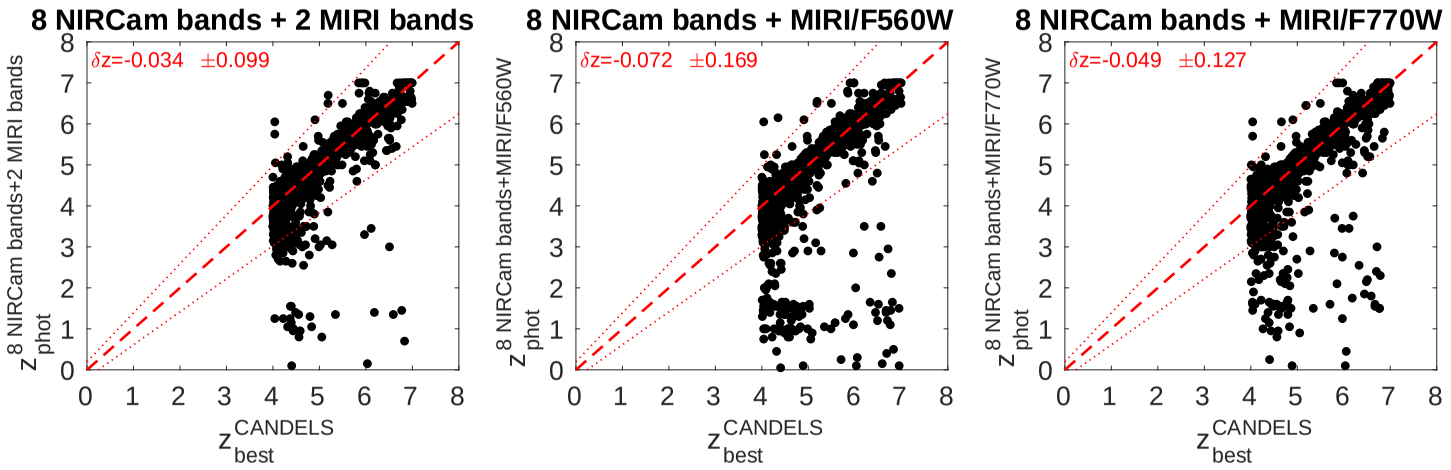


**Figure 4.10:** Our derived photometric redshifts versus CANDELS consensus photometric redshifts for galaxies in Sample 2. *Left*: photometric redshifts obtained with 8 NIRCam broad bands and MIRI F560W, F770W. *Centre*: Photometric redshifts obtained with 8 NIRCam broad bands and MIRI F560W only. *Right*: Photometric redshifts obtained with 8 NIRCam broad bands and MIRI F770W only. The dotted lines in each panel delimit the $3\sigma$ limit of the $|z_{\rm phot} - z_{\rm fiduc.}|/(1 + z_{\rm fiduc.})$ distribution, with $\sigma$ =0.065, which is the minimum value of $\sigma$ that we get for Sample 2 with all the considered filter combinations.

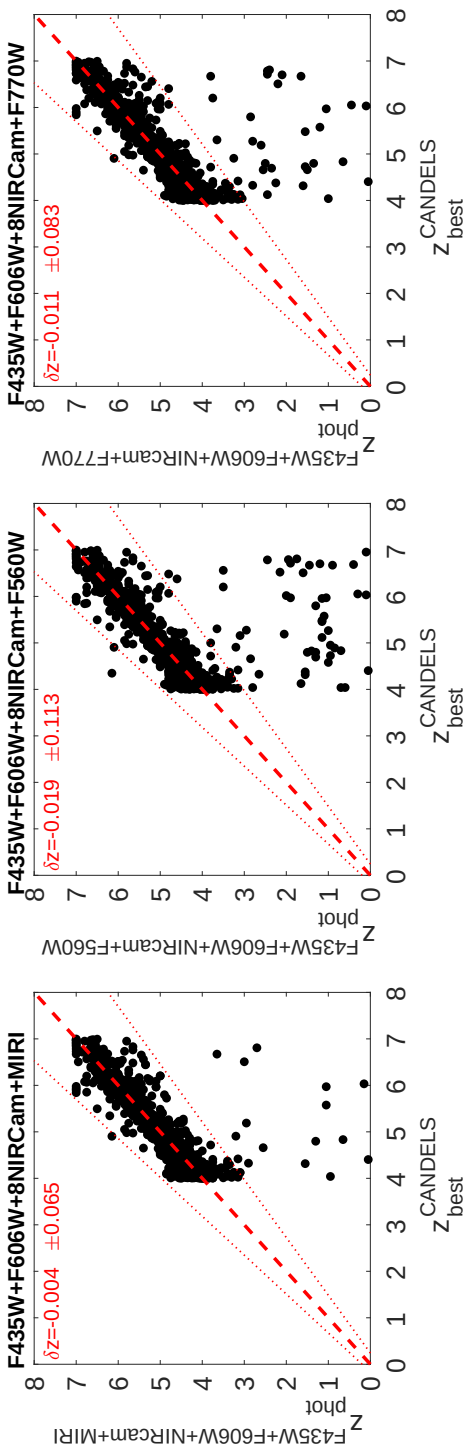


**Figure 4.11:** Our derived photometric redshifts versus CANDELS consensus photometric redshifts for galaxies in Sample 2. *Left*: photometric redshifts obtained with *HST* F345W, F606W, 8 NIRCam broad bands, and MIRI F560W, F770W. *Centre*: Photometric redshifts obtained with *HST* F345W,F606W, 8 NIRCam broad bands, and MIRI F560W. *Right*: Photometric redshift is obtained with *HST* F345W, F606W, 8 NIRCam broad bands and MIRI F770W. The dotted lines in each panel delimit the $3\sigma$ limit of the $|z_{\rm phot} - z_{\rm fiduc.}|/(1 + z_{\rm fiduc.})$ distribution, with $\sigma$ =0.065, which is the minimum value of $\sigma$ that we get for Sample 2 with all the considered filter combinations.

The redshift estimation is better at higher redshifts ($z = 5 - 7$). The percentage of sources leaking to lower $z$ is of only $\sim 9\%$. As we discussed before, the Lyman break enters the shortest-wavelength NIRCam band at $z \sim 5 - 6$, and therefore, the degeneracy between the $4000$ Å and Lyman breaks occurs mainly at lower redshifts. For this reason, adding the *HST* F435W and 606W photometry does not have an important effect on the redshift estimation at these higher redshifts, but it does at $z = 4 - 5$, where it reduces the percentage of leaking sources to only $\sim 2\%$. The overall redshift distribution dispersion reduces to a half when the *HST* data is considered along the NIRCam photometry (Fig. 4.9).

The addition of the $U$ band does not produce any obvious effect in the redshift estimation for Sample 2, once the *HST* photometry is also considered. The role of the $U$ band is more important for identifying low-redshift contaminants rather than preventing the leakage of high-$z$ sources to low $z$, because galaxies at z>4 are very faint or not detected in this band. As we will discuss later, the *HST* optical bands have a similar effect at z>5.

As a second step, we obtain photometric redshifts with the 8 NIRCam broad bands and two MIRI bands F560W and F770W, considered together and one at a time (Figure 4.10). Adding both MIRI bands significantly improves the photometric redshift estimates by decreasing the percentage of leaking sources to $< 8\%$ at $z = 4 - 5$ and $< 4\%$ at $z = 5 - 7$. Among the remaining $z = 4 - 5$ leaking sources, some are placed at $z \sim 1$ and a few at higher redshifts, i.e., $z \sim 6.5$. When considering one MIRI band at a time, F770W appears to be more effective at improving the photometric redshift estimation than F560W, but it is the combined effect of both MIRI bands which produces the substantial reduction in the fraction of leaking galaxies.

Adding MIRI photometry appears to be more important than adding *HST* photometry to minimise the dispersion in the obtained redshift distribution: the resulting r.m.s. in the case of NIRCam and MIRI data is $\sigma = 0.099$, which is slightly lower than for the *HST* and NIRCam filter combination ($\sigma = 0.119$).

Lastly, we consider *HST*, NIRCam and MIRI photometry altogether to obtain photometric redshifts (Figure 4.11). As expected, using all these bands jointly provides the best results in the identification of z$> 4$ galaxies. The presence of *HST* photometry at $\lambda < 0.6 - 0.7\,\mu$m helps to correctly identify the Lyman break at $z = 4 - 5$, while the MIRI mid-infrared bands provide a better wavelength coverage to correctly identify sources at z$= 5 - 7$. The resulting redshift dispersion gets a minimum value of

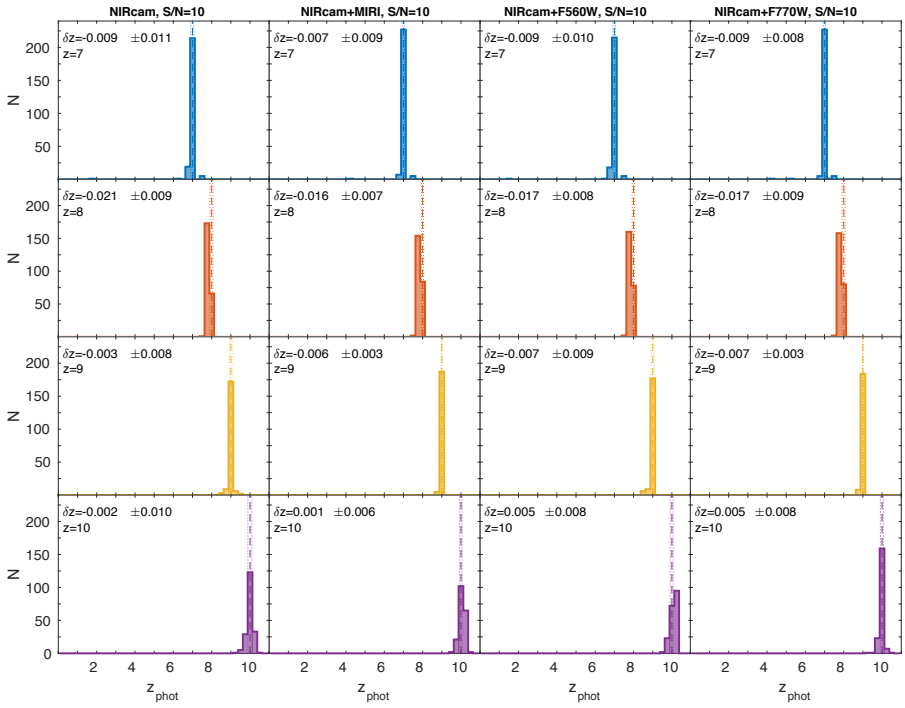


**Figure 4.12:** Photometric redshifts obtained for the BC03 simulated galaxies with (F150W) $S/N = 10$ at different fixed redshifts. *From top to bottom*: redshifts $z = 7, 8, 9$ and 10. Photometric redshifts in each column are obtained with different combinations of bands. *From left to right:* 8 NIRCam broad bands; 8 NIRCam broad bands, MIRI F560W and MIRI F770W; 8 NIRCam broad bands and MIRI F560W only; 8 NIRCam broad bands and MIRI F770W only. Each row corresponds to one of the four specific input redshifts. The vertical lines indicate the $3\sigma$ interval around the mean normalised redshift difference.

$\sigma = 0.065$ and the fraction of $z = 4 - 5$ sources leaking beyond $3\sigma$ in redshift decreases to $\sim 1\%$.

As before, the MIRI F770W filter appears to have a more important role in improving the redshift estimation than MIRI F560W, but both bands are necessary to properly identify all galaxies at $z = 4-7$. To sum up, the short-wavelength *HST* data and long-wavelength MIRI data have complementary roles in the correct identification of $z > 4$ galaxies.

We remind the reader that the photometry in our Samples 1 and 2 is of good quality ($S/N > 5$ in F150W for the vast majority of galaxies; see Section 4.2.2.1). The redshift outlier percentages that we quote here

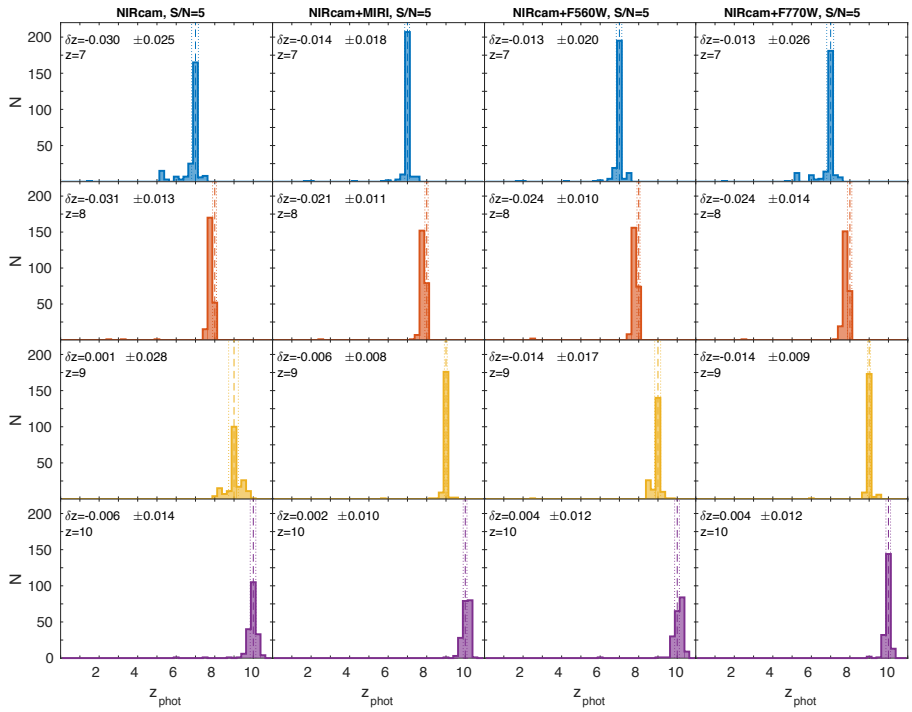


**Figure 4.13:** The same as Fig. 4.12, but for (F150W) $S/N = 5$.

correspond to this high-quality photometry, so they do not depend on the data quality, but are rather produced by the intrinsic limitations of the SED fitting with a limited number of photometric bands. We check the $S/N$ of the photometry for the $z_{\rm phot}$ outliers and found no significant difference with respect to the photometry of all other sources, confirming that Samples 1 and 2 results are not affected by the photometric $S/N$.

### 4.3.3 Results for Sample 3

With Sample 3 we aim to test the ability to recover photometric redshifts for simulated galaxies at $z = 7 - 10$, using the NIRCam broad bands alone and in conjunction with the MIRI F560W and F770W bands. For this sample, we do not consider the incorporation of the *HST* short-wavelength and $U$ filters, because these bands map rest wavelengths far blueward of the Lyman break at these redshifts, so they basically correspond to non-detections in all cases.

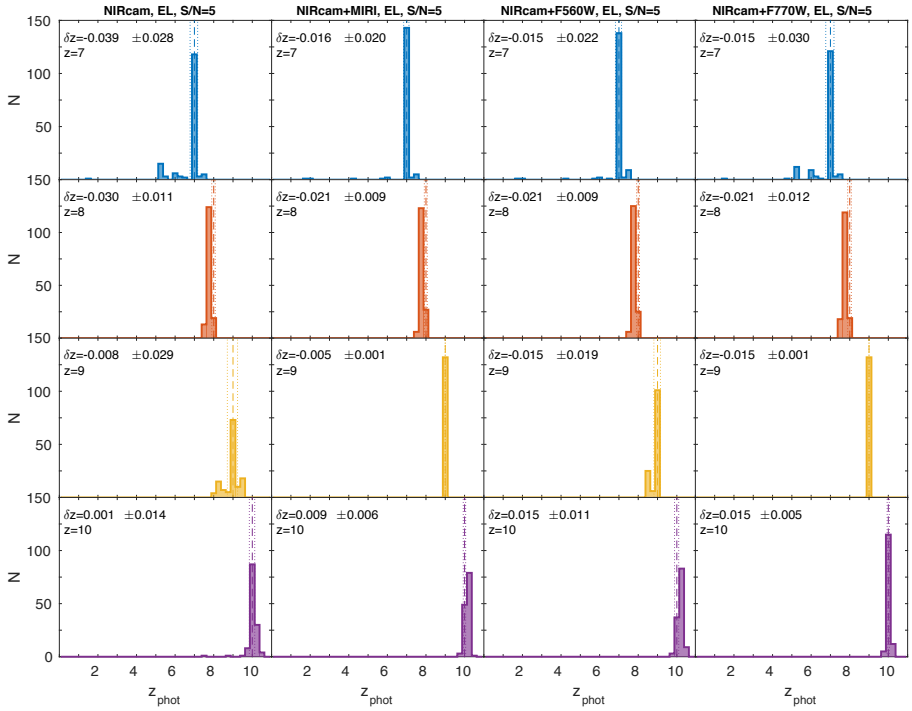


**Figure 4.14:** The same as Fig. 4.13, but only for galaxies with emission lines.

#### 4.3.3.1 Galaxies simulated with BC03 templates at $z = 7 - 10$

Figures 4.12 to 4.15 show the distributions of the recovered photometric redshifts for each input redshift ($z = 7, 8, 9$ and 10) for the Sample 3 galaxies simulated with the BC03 templates, obtained by running *LePhare* with different *JWST* filter combinations. As in this case the input redshifts are four fixed values, it is clearer to show the output $z_{\rm phot}$ distributions for each input redshift rather than $z_{\rm phot} - z_{\rm phot}$ plots, which would contain four vertical columns each.

As before, in each plot we quote the mean value of the normalised redshift difference distribution $\delta z = (z_{\rm phot} - z_{\rm fiduc.})/(1 + z_{\rm fiduc.})$, taking into account all galaxies. However, for Sample 3 galaxies, we adapt our method for the r.m.s. calculation. As it can be seen in Figures 4.12 to 4.15, the Sample 3 redshift histograms are characterised by quite a narrow distribution around the main peak and the presence of some catastrophic failures producing secondary peaks at much lower redshifts. These catastrophic redshift failures would significantly bias the computed

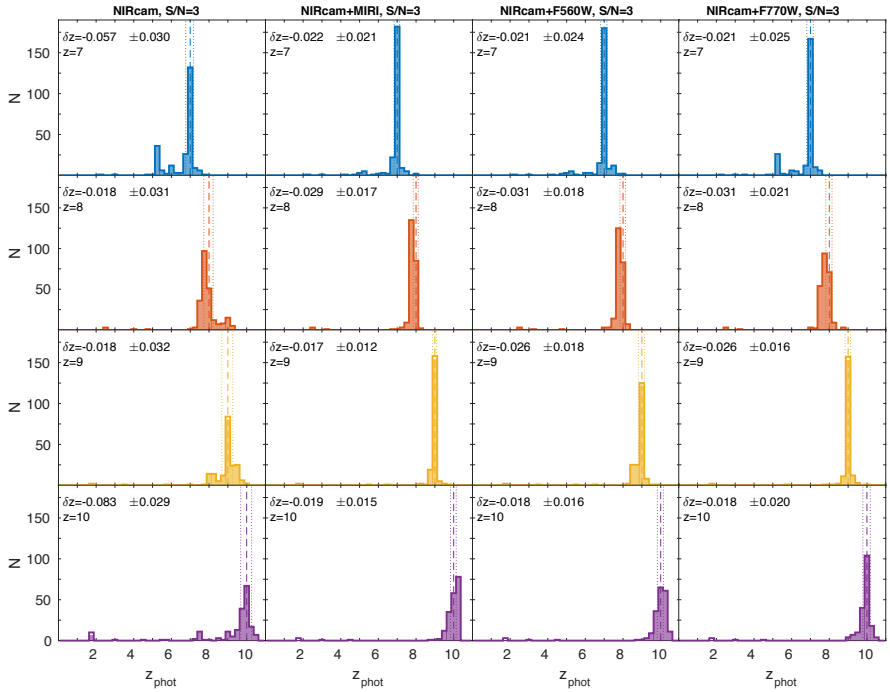


**Figure 4.15:** The same as Fig. 4.12, but for (F150W) $S/N = 3$.

$\sigma$ of $|z_{\rm phot} - z_{\rm fiduc.}|/(1 + z_{\rm fiduc.})$ if they were considered in the statistics. So, for Sample 3 galaxies (both based on the BC03 and *Yggdrasil* models) we explicitly exclud all galaxies with $|z_{\rm phot} - z_{\rm fiduc.}|/(1 + z_{\rm fiduc.}) > 0.15$ for the $\sigma$ computation, and we consider those excluded galaxies to be the outliers of our sample. We provide the statistics on the outlier fractions for the BC03-SED galaxies in Table 4.7.

For $S/N = 10$, the 8 NIRCam broad bands alone allow us to derive accurate redshift estimates, with mean values for the redshift distributions close to 0 and $\sigma \leq 0.011$ at all redshifts (Fig. 4.12). The percentage of outliers quoted in Table 4.7 is very small ($0.1\%$). Adding MIRI photometry to the NIRCam photometry only slightly enhances the already excellent quality of the output redshifts, resulting in $\sigma < 0.01$ at all redshifts. These results indicate that the incorporation of the MIRI photometry to the NIRCam photometry has in practice little effect to derive photometric redshifts for $z = 7 - 10$ galaxies with BC03-like SEDs when the NIRCam $S/N$ is very high.

The MIRI effect to the photometric redshift estimation is more evident at $S/N = 5$ (Fig. 4.13). The NIRCam data alone are sufficient for a

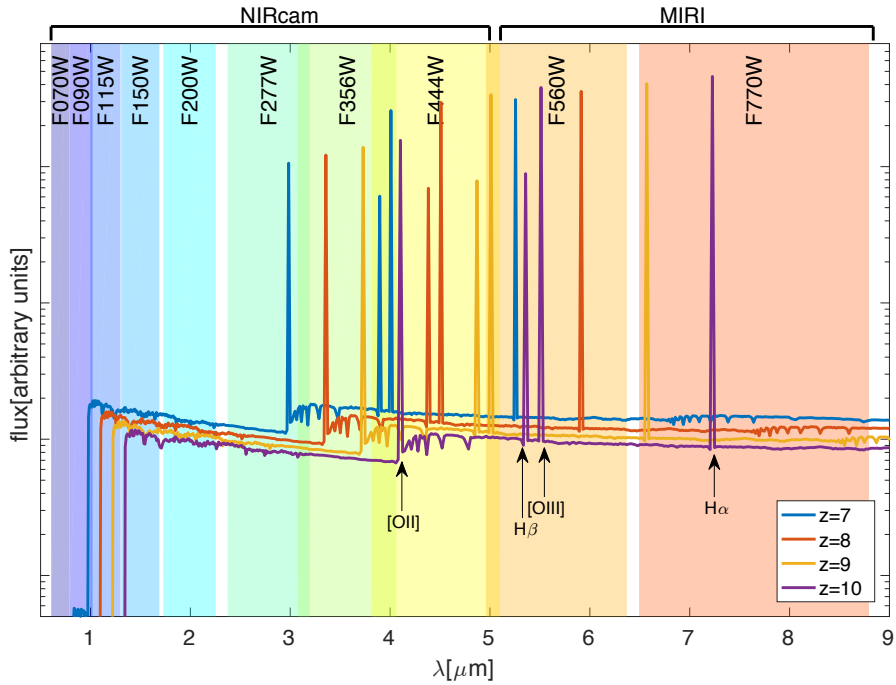


**Figure 4.16:** Four examples of SED templates from BC03 with manual emission line addition, considered for simulating galaxies for Sample 3. The coloured vertical strips indicate the wavelength coverage of the 8 NIRCam broad bands and MIRI F560W and F770W. This Figure shows in which *JWST* filters the main emission lines and most important SED features are observed at high redshifts.

reasonably good redshift recovery ($\sigma \approx 0.01 - 0.03$), but the addition of MIRI data improves the photometric redshift quality, taking the outlier percentage to $< 1\%$ (when F560W photometry is included). Inspection of Fig. 4.4 suggests that this is a k-correction effect: galaxies are brighter in the MIRI bands either because they are old or because of the presence of emission lines. Indeed, both effects are important. In Fig. 4.14 we show separately our results only for galaxies with emission lines: it can be seen that the effect of incorporating the MIRI photometry is similar as in the general case with $S/N = 5$. Note that, on the one hand, the presence of emission lines helps in the redshift identification, but on the other hand having prominent emission lines in contiguous broad bands makes the observed photometry mimic a less featured SED, resulting in a more difficult redshift recovery.

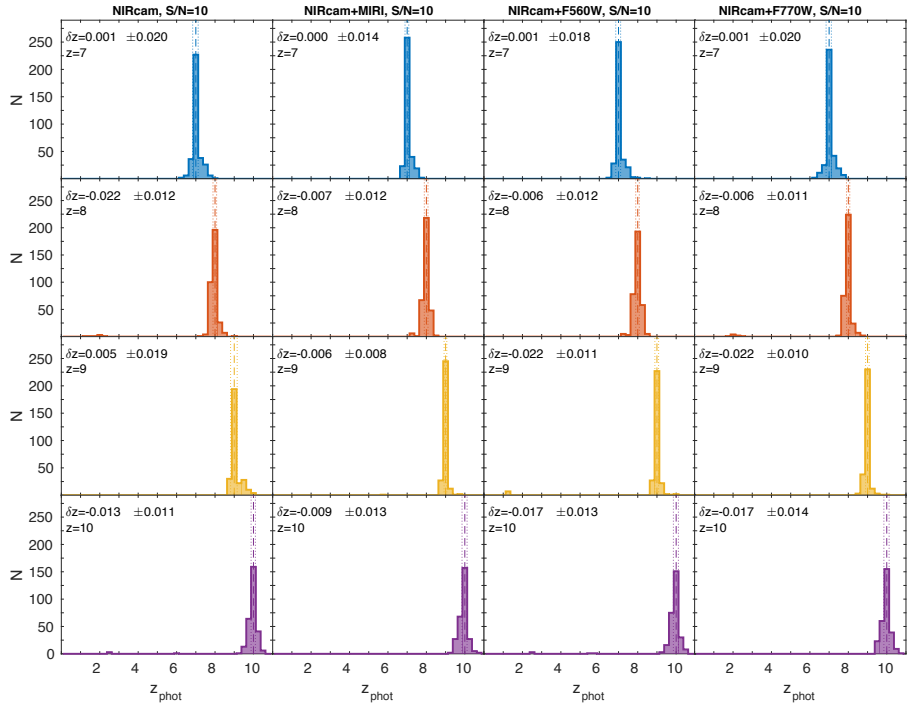


**Figure 4.17:** Photometric redshifts for the sample of *Yggdrasil* simulated galaxies with $S/N = 10$. *From top to bottom*: redshifts $z = 7, 8, 9$ and 10. Photometric redshifts in each column are obtained with different band combinations. *From left to right*: 8 NIRCam broad bands; 8 NIRCam broad bands and MIRI F560W, F770W; 8 NIRCam broad bands and MIRI F560W only; 8 NIRCam broad bands and MIRI F770W only. Each row corresponds to one of the four specific input redshifts. The vertical lines indicate the $3\sigma$ interval around the mean normalised redshift difference.

In the case of $S/N = 3$ at F150W (Fig. 4.15), assuming identical integration times in all NIRCam filters implies that some galaxies are undetected at the shortest wavelength NIRCam bands. In this case, having complementary MIRI photometry becomes very important, even with the assumption that we made here, i.e., that the MIRI depth will be one magnitude shallower than the NIRCam depth at $1.5\,\mu\mathrm{m}$. This assumption is reasonable, as achieving the same depth as in NIRCam will require too long exposure times[6].

[6]Even achieving a MIRI F560W depth only one magnitude shallower than the NIRCam depth at F150W will require an integration time $\sim 35$ times longer with MIRI than with NIRCam; see http://jwstetc.stsci.edu/etc/

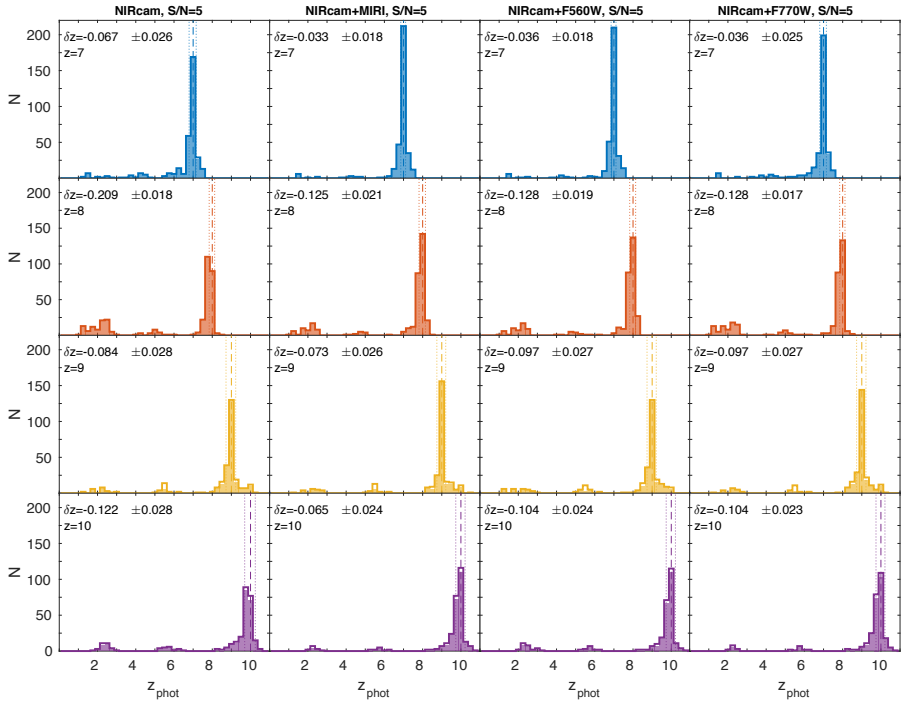


**Figure 4.18:** The same as Fig. 4.17, but for $S/N = 5$. The shaded area within each histogram corresponds to objects with more than 4 detections in total in the NIRCam and MIRI bands, while empty areas correspond to sources with less than 4-band detections.

The result of this poorer-quality photometry is that the output redshift distributions are broader and secondary peaks at lower redshifts become more significant (Fig 4.15). The incorporation of MIRI photometry has a significant effect in reducing the overall outlier fraction: it goes down from 10.1% with NIRCam data only to $3.0\%$ after adding the two MIRI bands (Table 4.7). Note that, among the two MIRI filters, F560W appears to have a more important effect in improving the $z_{\rm phot}$ determination of the BC03-SED sources at $z = 7 - 10$.

As a summary, we conclude that considering MIRI photometry of one magnitude shallower depth than the NIRCam photometry keeps the fraction of $z_{\rm phot}$ outliers low for the $z \geq 7$ galaxies which have a moderate or low $S/N$ in the NIRCam images. This effect is evident for different SED types (with or without emission lines).

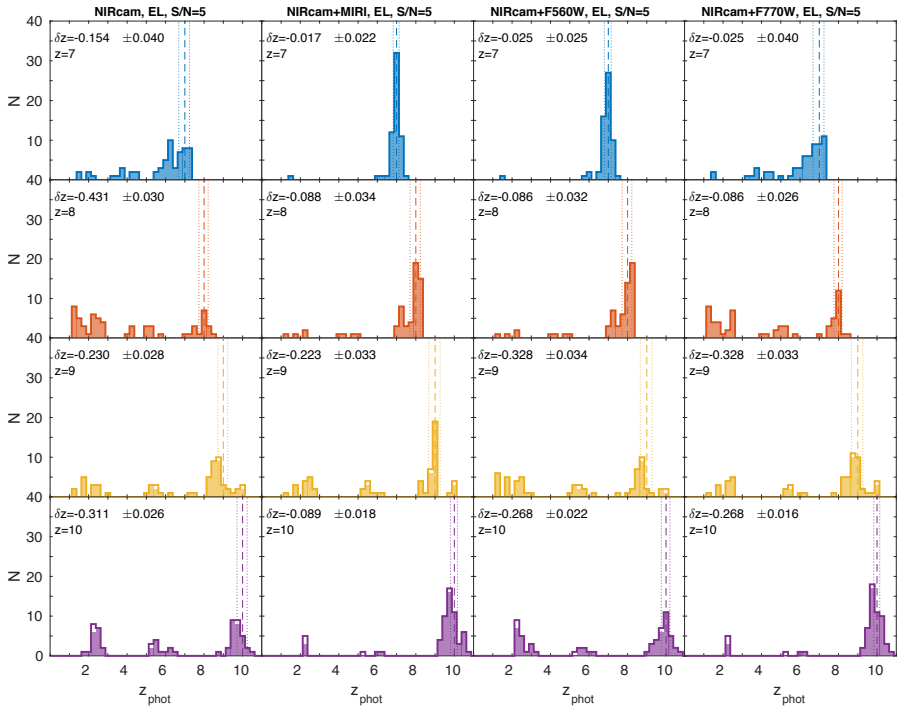


**Figure 4.19:** The same as Fig. 4.18, but only for galaxies with emission lines.

#### 4.3.3.2 Galaxies simulated with Yggdrasil templates at $z = 7 - 10$

Figures 4.17 to 4.20 show the distributions of the recovered photometric redshifts for the Sample 3 galaxies simulated with the *Yggdrasil* templates at each fixed redshift, obtained by running *LePhare* with different *JWST* filter combinations. The outlier percentages for each analysed $S/N$ value are listed in Table 4.8. *Yggdrasil* templates are more complex than the BC03 ones, given that *Yggdrasil* automatically incorporates nebular emission lines and continuum emission when galaxy ages are young and the gas covering factor is $f_{\rm cov} > 0$, which may be the case of many high-$z$ galaxies.

When considering objects with $S/N = 10$ at F150W (Figure 4.17), we see that the NIRCam data alone provides a good photometric redshift recovery ($\sigma = 0.01 - 0.02$). The incorporation of the MIRI bands has little effect on the resulting $\sigma$ values in most cases and the fraction of catastrophic outliers is only slightly reduced (see Table 4.8)

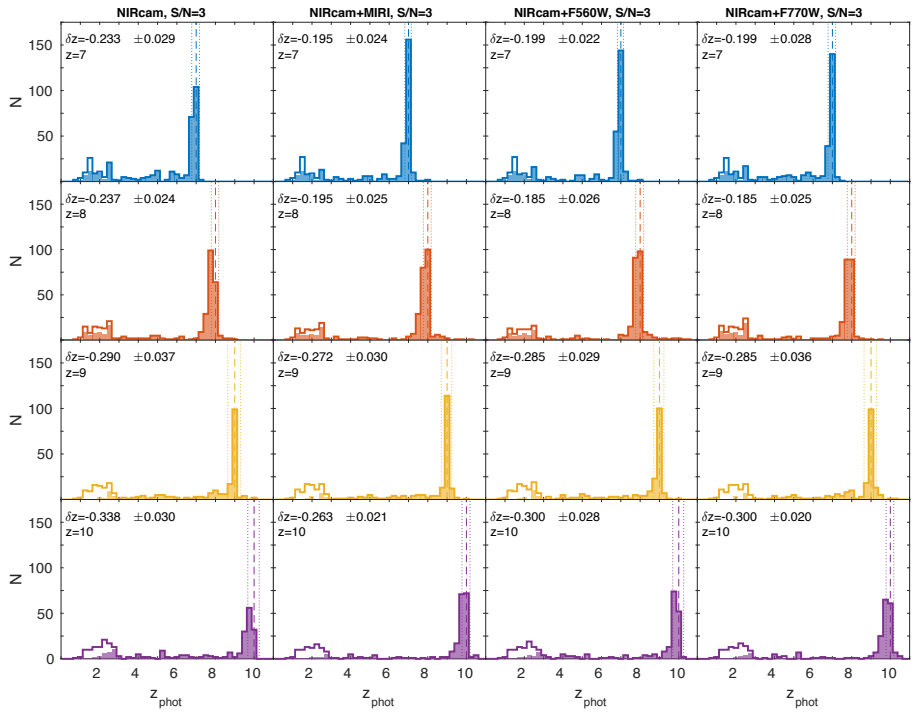


**Figure 4.20:** The same as Fig. 4.17, but for $S/N = 3$. The shaded area within each histogram corresponds to objects with more than 4 detections in total in the NIRCam and MIRI bands, while empty areas correspond to sources with less than 4-band detections.

As in the case of BC03-SED galaxies, the impact of incorporating MIRI photometry is more evident at $S/N = 5$ at F150W (Figure 4.18). The overall percentage of catastrophic outliers reduces from $20.4\%$ to $12.1\%$ by adding MIRI photometry in this case (Table 4.8).

If we consider only those galaxies with emission lines in their SEDs (i.e., young and with gas covering factor $f_{\rm cov} = 1$), also at $S/N = 5$, we see two interesting effects (Figure 4.19 and Table 4.8). Firstly, the degeneracies in redshift space are more important than for the general galaxy sample with $S/N = 5$. This is manifested in a much larger outlier percentage, namely $\sim 49\%$ when considering the NIRCam data alone. Secondly, the effect of incorporating MIRI photometry becomes more noteworthy: including both MIRI bands reduces the percentage of outliers to $\sim 17\%$. These effects are produced by two reasons: on the one hand, the nebular line emission boosts the MIRI fluxes and, thus, the $S/N$ of the MIRI data. On

the other hand, the multiple emission lines in the *Yggdrasil* templates with nebular emission result in similarly bright observed fluxes in contiguous filters, masking the continuum SED shape and making the SED fitting more difficult (as explained in Section 4.3.3.1), so having a longer baseline is necessary for a proper redshift recovery.

For the lowest quality photometry ($S/N = 3$; Figure 4.20), the percentage of catastrophic outliers in the entire sample is $44.4\%$ using only NIRCam photometry. The advantage of incorporating MIRI data, which also have lower $S/N$, is less obvious in this case, as the percentage of $z_{\rm phot}$ outliers still remains high even with the two MIRI bands ($36.7\%$). A significant fraction of galaxies are detected in only a few (NIRCam and MIRI) bands, so the photometry provides poor constraints for the SED fitting, making degeneracies in redshift space become evident.

Indeed, as it is the case for the BC03-SED galaxies, the catastrophic outliers correspond mainly to sources with detections in four or less *JWST* bands (empty regions in the histograms of Figure 4.20). However, in the case of the *Yggdrasil*-SED galaxies, the secondary peaks appearing in the output redshift distributions are quite more pronounced than for the BC03 galaxies. These secondary peaks are mainly produced by two kinds of templates that are not represented in our BC03-SED sample: 1) young galaxies with nebular emission. The combination of multiple emission lines and low $S/N$ produces an enhancement in the number of catastrophic outliers; 2) young galaxies with $f_{\rm cov} = 0$ (i.e., no emission lines) and the highest extinction adopted to build our mock sample (i.e., $A_V = 1$). These galaxies have no analogues either in the BC03-based sample, as we explicitly incorporated the main emission lines in all galaxies with ages lower than the characteristic $\tau$ in the star formation history.

As a summary, we conclude that the benefit of considering MIRI photometry along with the NIRCam data for *Yggdrasil*-SED galaxies is mainly obvious for NIRCam sources with moderate $S/N$ values, and particularly helpful in the case of SEDs with nebular emission. At low $S/N$ the advantage is less obvious. This is in contrast to our conclusion for the BC03-SED galaxies, indicating that at low $S/N$ the importance of having MIRI data depends significantly on the galaxy spectral type.

#### 4.3.3.3 MIRI magnitudes and NIRCam/MIRI colours

In this Section we show the MIRI magnitudes and NIRCam/MIRI colours of our simulated galaxies in Sample 3, as this can be a useful reference when planning *JWST* observations. In particular, we analyse how the MIRI detections vary with the galaxy SED type. Given our chosen

normalisation [F150W]=29 mag, all these galaxies will easily be observed in NIRCam deep surveys (as it takes only $\sim 30$ min integration per pointing to reach [F150W]=29 mag, $3\sigma$ with NIRCam, according to the public *JWST*/NIRCam exposure time calculator [7]). So our aim here is to discuss the fractions of such galaxies that will be detected in typically deep MIRI observations. Of course, these same results only need to be re-scaled to remain valid for other NIRCam magnitudes.

Figures 4.21 to 4.24 show the expected MIRI magnitude distributions for our Sample 3 galaxies generated with the BC03 and *Yggdrasil* models. As the NIRCam F150W magnitude for all these galaxies has been fixed to [F150W]=29 mag, there is a direct correspondence between the MIRI F560W magnitudes and the F150W-F560W colours, which are also shown in each plot. For the BC03 galaxies (Fig. 4.21 and 4.22), we analyse separately the cases with and without emission lines, which here correspond to galaxies with ages lower and higher than their characteristic SFH decay parameter $\tau$, respectively. For the *Yggdrasil* galaxies (Fig. 4.23 and 4.24), we analyse three cases: galaxies with ages larger that their constant star formation period, which are galaxies in passive evolution; and galaxies which are still forming stars with two different gas covering factors: $f_{\rm cov} = 0$ (implying no line or nebular continuum emission) and 1 (with nebular emission). The median values of all distributions are provided in Table 4.9 and 4.10.

The magnitude distributions in Fig. 4.21 show that the vast majority of BC03 galaxies with [F150W]=29 mag at $z = 7, 8$ and 10, and more than a half of those at $z = 9$, will be detected by a MIRI survey with a detection limit [F560W]$= 28$ mag. This result is valid for galaxies with or without emission lines. All the latter are cases in which a $4000$ Å break is at least partly developed, so the SEDs are brighter at the MIRI wavelengths than at $1.5\,\mu$m, particularly at $z = 7$ (see Fig. 4.4). This k-correction effect makes the median [F560W] value at this redshift brighter for galaxies without emission lines, as those with emission lines correspond to younger galaxies with fainter continua which partly cancel the emission line flux enhancement (Table 4.9). At $z = 8$ and 10, instead, the combination of the continuum k-correction and the nebular emission results in a net flux boosting in the case of emission-line galaxies.

For F770W (Fig. 4.22), the flux enhancement due to the emission line presence is only evident at $z = 9$ and 10, as the H$\alpha$ emission line enters the F770W wavelength window at these redshifts (Table 4.10). Most young galaxies at $z = 7$ and 8, instead, remain below our reference

[7] http://jwstetc.stsci.edu/etc/input/nircam/imaging/

[F770W]=28 mag detection limit, as their continua are blue and no emission line is present in this filter to help with the detection. So, the F770W filter will only allow us to detect evolved galaxies at $z \geq 7$ or young line emitters at $z = 9$ and 10 to a [F770W]=28 mag cut.

The vast majority of the *Yggdrasil*-SED galaxies with [F150W]=29 mag that finished forming stars at $z \geq 7$ will have mag$< 28$ in both MIRI bands (Fig. 4.23 and 4.24, and Tables 4.9 and 4.10). This is the result of the same k-correction effect discussed before.

For the *Yggdrasil* star-forming galaxies, there is a clear enhancement of the MIRI fluxes produced by the nebular lines (compare the cases with $f_{\rm cov} = 0$ and 1 in Fig. 4.23 and 4.24 and the corresponding Tables). In this case, the flux enhancement is more obvious than for the BC03 templates because here we are comparing only young galaxies with and without lines (segregated by their different gas covering factors), so all their continua are similarly blue. In both cases, however, the median MIRI magnitude values are $> 28$ mag. This implies that a MIRI galaxy survey to our reference depth will only detect a minority of star-forming galaxies with [F150W]=29 mag at $z \geq 7$ if their SEDs are similar to the *Yggdrasil* templates. Note that these galaxies are considerably brighter in F560W if they are at $z = 7$ or 8, while slightly brighter in F770W if at $z = 9$ or 10.

Note that, conversely, our colour analysis shows that detecting more than a half of red MIRI galaxies at $z \geq 7$ will require NIRCam data at least three magnitudes deeper. This is the case both for 'passive galaxies' (galaxies which finished forming stars) and for galaxies which are red simply because of the presence of prominent emission lines.

So, as a summary, 'old' galaxies at $z \geq 7$ will easily be detected with MIRI in reasonably deep surveys, independently of their galaxy type. For young galaxies, the situation is more complex, as it depends to which extent line emission can compensate for the very faint continua characteristic of these sources. F560W will provide more detections than F770W if maps to the same depth are obtained in both passbands.

## 4.4 SUMMARY AND CONCLUSIONS

In this work we have tested the impact of having data in different *JWST* filter combinations on deriving photometric redshifts for galaxies at different redshifts. We considered the 8 NIRCam broad bands and the two shortest wavelength MIRI bands (F560W and F770W), which are the most sensitive ones and, thus, those which will be preferred for the study of high-$z$ galaxies. In addition, we also investigated the

**Table 4.9:** Median MIRI [F560W] magnitudes for our Sample 3 galaxies at $z = 7 - 10$ (all normalised at [F150W]=29 mag).

| SED type | z=7 | z=8 | z=9 | z=10 |
|---|---|---|---|---|
| BC03 - No emiss. lines | 26.86 | 26.77 | 27.12 | 26.96 |
| BC03 - With emiss. lines | 27.08 | 26.49 | 28.08 | 26.17 |
| *Yggdrasil* - Passive evolution | 26.28 | 25.96 | 26.66 | 26.44 |
| *Yggdrasil* - Star formation, $f_{\rm cov} = 0$ | 29.50 | 29.43 | 29.35 | 29.27 |
| *Yggdrasil* - Star formation, $f_{\rm cov} = 1$ | 28.47 | 28.32 | 29.15 | 28.72 |

**Table 4.10:** Median MIRI [F770W] magnitudes for our Sample 3 galaxies at $z = 7 - 10$ (all normalised at [F150W]=29 mag).

| SED type | z=7 | z=8 | z=9 | z=10 |
|---|---|---|---|---|
| BC03 - No emiss. lines | 26.70 | 26.59 | 26.98 | 26.79 |
| BC03 - With emiss. lines | 28.64 | 28.68 | 27.52 | 26.51 |
| *Yggdrasil* - Passive evolution | 26.10 | 25.80 | 26.44 | 26.24 |
| *Yggdrasil* - Star formation, $f_{\rm cov} = 0$ | 29.64 | 29.62 | 29.58 | 29.47 |
| *Yggdrasil* - Star formation, $f_{\rm cov} = 1$ | 29.05 | 29.13 | 28.87 | 28.53 |

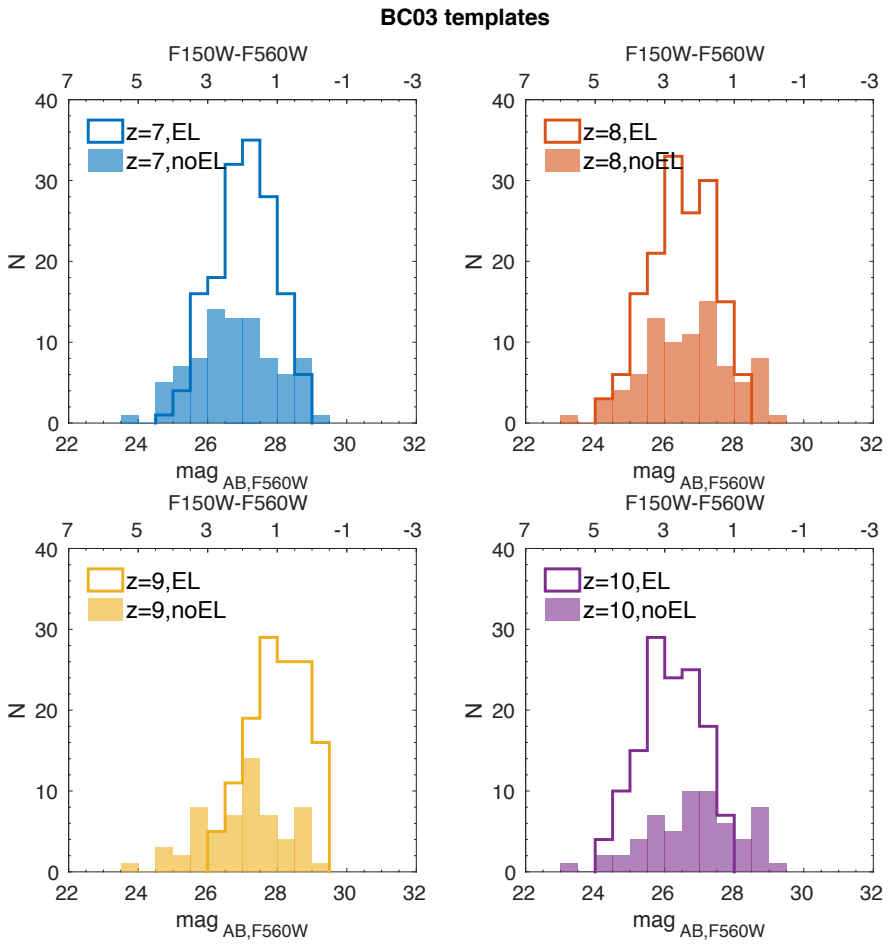


**Figure 4.21:** Expected MIRI F560W magnitude distribution for the Sample 3 galaxies simulated with the BC03 models at different redshifts. The cases of galaxies with emission lines (i.e., star-forming galaxies with ages lower than their characteristic SFH $\tau$) and without emission lines are shown in separate histograms. As the NIRCam F150W magnitude for all these galaxies has been fixed to [F150W]=29 mag, there is a direct correspondence between the MIRI F560W magnitudes and the F150W-F560W colours (top x axis).

effect of having (or not) ancillary photometry from *HST* and ground-based telescopes at wavelengths shorter than those to be observed with *JWST* (i.e., $\lambda < 0.6\,\mu$m).

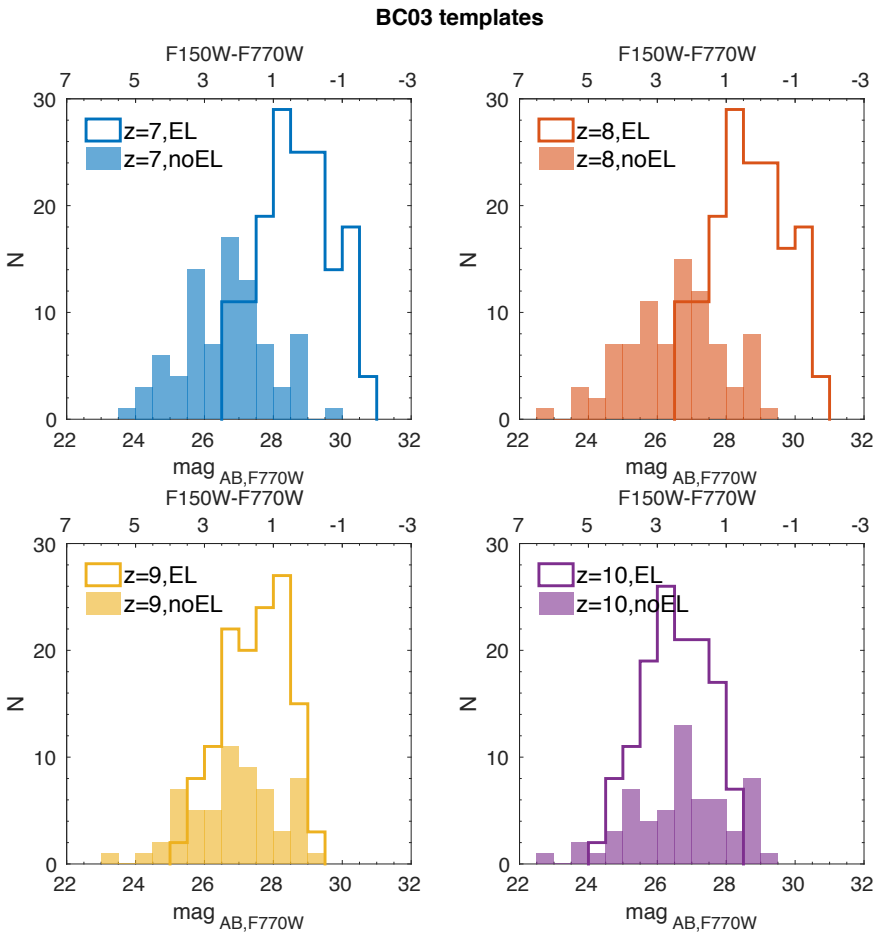


**Figure 4.22:** The same as Figure 4.21, but for the MIRI F770W magnitudes and F150W-F770W colours.

We performed our tests on three galaxy samples with known input redshifts: a sample of 2422 galaxies with spectroscopic redshifts $z = 0 - 6$ (Sample 1); a sample of 1375 galaxies with CANDELS consensus photometric redshifts at $z = 4 - 7$ (Sample 2); and a sample of 2124 mock galaxies at $z = 7 - 10$ (Sample 3), whose SEDs have been simulated with two template libraries, namely BC03 with manual addition of the main emission lines for star-forming galaxies (considered as those with age lower than the characteristic $\tau$ of the star formation history), and the *Yggdrasil* library. Besides, for Sample 3 we also explicitly investigated

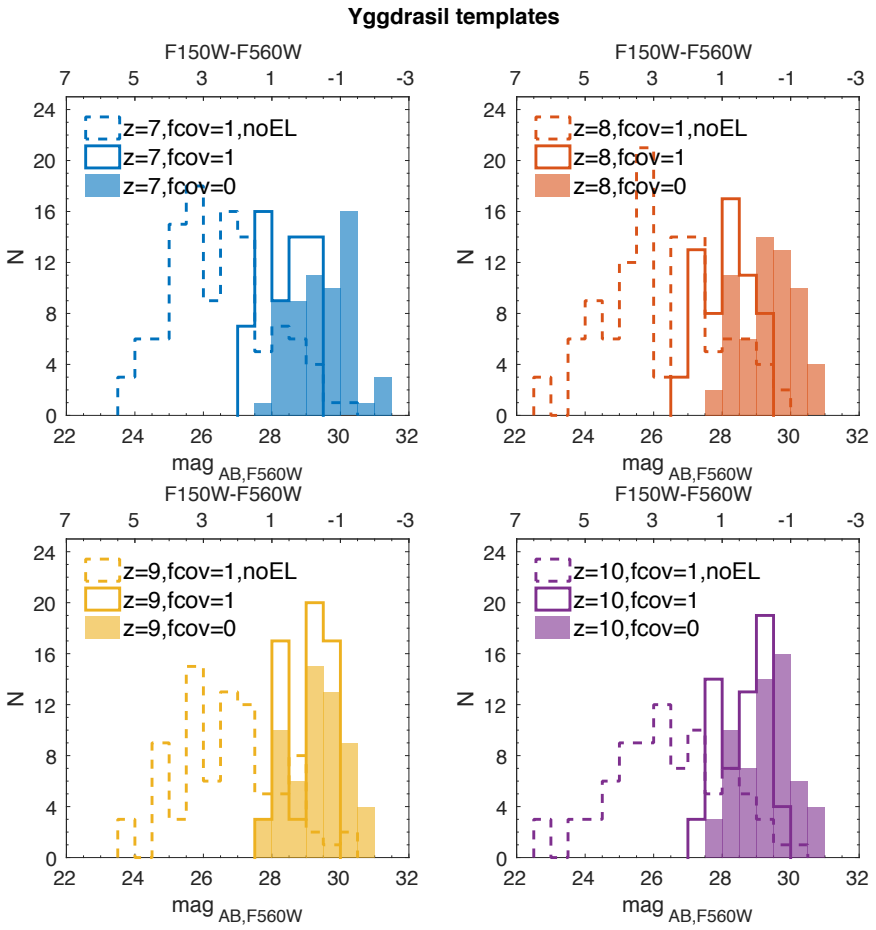


**Figure 4.23:** Expected MIRI F560W magnitude distribution for the Sample 3 galaxies simulated with the *Yggdrasil* models for galaxies in passive evolution (i.e. ages larger than their constant star formation period, *dashed line*) and galaxies that are still forming stars. The star forming galaxies are also divided in models with covering factors $f_{\rm cov} = 0$ (*filled area*) and 1 (*continued line*), as only the latter have emission lines and continuum nebular emission.. Note that the gas covering factor is irrelevant in the cases of galaxies in passive evolution, as no nebular emission is present any more in these galaxies. The top x axis shows the F150W-F560W colours.

the effect of having photometry with different $S/N$ values on the ability to recover the galaxy redshifts. In Samples 1 and 2, more than 90% of

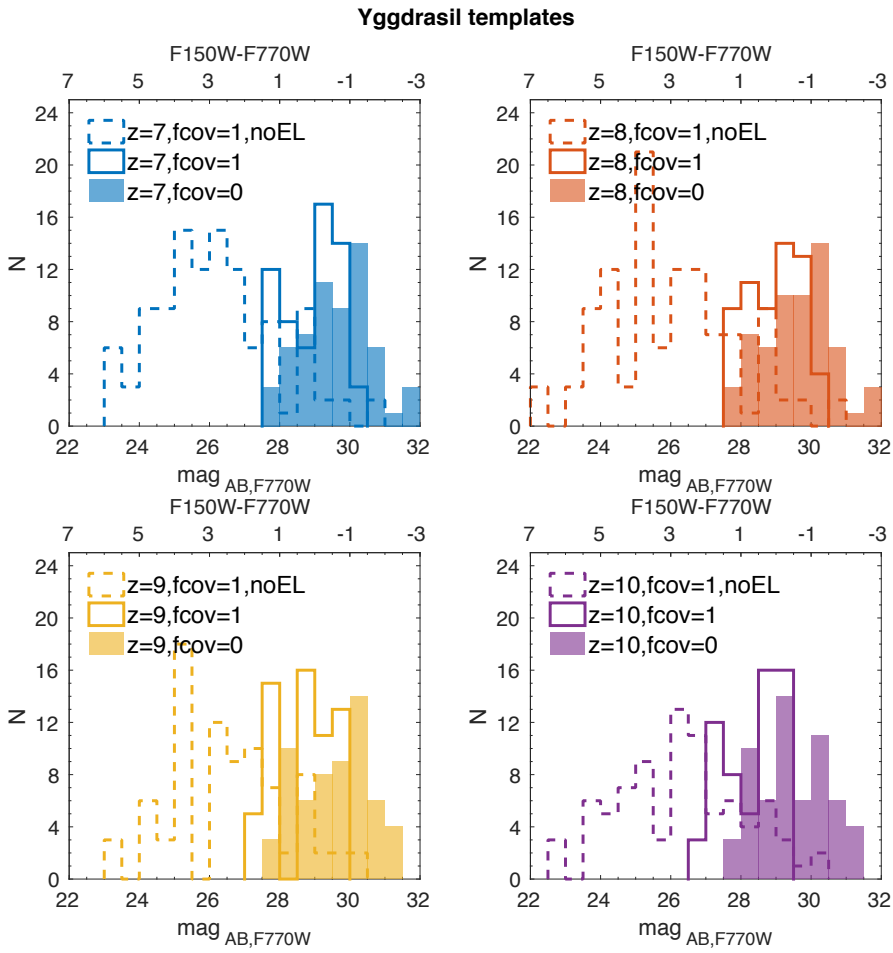


**Figure 4.24:** The same as Figure 4.23, but for the MIRI F770W magnitudes and F150W-F770W colours.

galaxies have F150W photometry with $S/N > 5$, so the test results based on these samples are not affected by the photometric quality.

These three samples altogether have allowed us to assess different effects in the photometric redshift estimation, such as the presence of high-$z$ contaminants and the leakage of high-$z$ sources towards low $z$. Note that our three samples are not meant to emulate a real galaxy population selected from a *JWST* NIRCam or MIRI blank field, but rather sample the typical redshifts and SED types of the galaxies that will be observed in these surveys, in order to test potential problems in the $z_{\rm phot}$ derivation.

Our main results are:

• *The NIRCam broad bands alone are not sufficient to obtain good-quality photometric redshift estimates at low and intermediate redshifts ($z < 7$).* For Sample 1, which is optimised to study the redshift range $z = 0 - 4$, the use of NIRCam data alone results in a high photometric redshift dispersion and outlier percentage ($> 10\%$). In Sample 2, which is particular suited to study the leakage of $z = 4 - 7$ sources to low $z$ due to redshift failure, $\sim 20\%$ ($\sim 9\%$) of the input sources with $z = 4 - 5$ ($z = 5 - 7$) are misidentified as lower $z$ galaxies. These effects are smaller at $z > 6$, as the Lyman break is shifted into the NIRCam bands.

• *Having photometry in the HST F435W and F606W bands, and if possible also in the ground-based $U$ band, is very important to have the fraction of low-$z$ contaminants under control.* This photometry is important to constrain the Lyman break shift and, thus, the redshifts of low-$z$ sources. Indeed, in Sample 1 the percentage of low-$z$ outliers changes from $> 10\%$ to $\sim 7\%$, and the normalised redshift difference distribution r.m.s. reduces in 40%. In Sample 2, the percentage of sources leaking from $z = 4 - 5$ ($z = 5 - 7$) to lower $z$ reduces from $\sim 20\%$ ($\sim 9\%$) to $\sim 2\%$ ($\sim 8\%$). At $z = 5 - 7$, the reduction in the percentage of leaking sources is exclusively due to the incorporation of the *HST* bands. The additional incorporation of $U$-band data has no effect because the Lyman break shifts inside the *HST* wavelength range at these redshifts.

• *MIRI F560W and F770W data can help mitigate the absence of photometry at $\lambda < 0.6\,\mu$m.* In Sample 1, the percentage of contaminants reduces from 41% (22%) to $\sim 11\%$ ($0\%$) at $z = 4 - 5$ ($z = 5 - 7$), by complementing the NIRCam data only with MIRI data in the photometric input catalogue. For the leaking sources in Sample 2, the addition of MIRI photometry to the NIRCam data reduces the percentage of outliers from $\sim 20\%$ ($\sim 9\%$) to $< 8\%$ ($< 4\%$) at the same redshifts. When both the *HST* and MIRI photometry are considered along with the NIRCam photometry, the percentage of leaking sources from $z = 4 - 5$ goes down to $\sim 1\%$.

• Among the different photometric configurations tested here, the MIRI F560W and F770W bands are the only ones that can meaningfully complement the NIRCam data in galaxy studies at $z \geq 7$. The importance of the *HST* data at $\lambda < 0.6\,\mu$m becomes negligible once the Lyman break shifts within the NIRCam bands, except to confirm the expected non-detections.

• For photometry with F150W $S/N = 10$, the NIRCam data alone allows for accurate redshift estimates for galaxies at $z \geq 7$ in most cases. The r.m.s. of the $|z_{\rm phot} - z_{\rm input}|/(1 + z_{\rm input})$ distributions for Sample 3 range between $\sigma < 0.01$ and 0.02 with NIRCam data alone. The addition of MIRI photometry has a mild effect, being useful to enhance the accuracy of the derived $z_{\rm phot}$.

• For sources with F150W $S/N = 5$, the benefit of incorporating MIRI photometry becomes more evident. In our reference case, in which the MIRI depth is one magnitude brighter than the NIRCam F150W depth, the incorporation of MIRI data significantly reduces the fraction of outliers with respect to the case with NIRCam data alone. This improvement is particularly noteworthy in the case of *Yggdrasil*-SED galaxies with emission lines, as the multiple nebular lines coupled with a moderate-quality $S/N$ make the SED fitting more challenging. The MIRI bands help extend the wavelength baseline for the SED fitting, and thus using NIRCam and MIRI data altogether results in a clear redshift recovery improvement.

• At F150W $S/N = 3$, the role of MIRI data in improving the redshift determination depends very much on the SED type. As 'old' galaxies are red, MIRI fluxes are brighter that NIRCam fluxes, so the incorporation of the MIRI data is of clear benefit for these sources. For star-forming galaxies, the presence of emission lines in the MIRI bands boosts the MIRI fluxes, but at the same time these galaxies have bluer continua, so the net effect is more variable in these cases.

• At fixed $S/N$, *the presence of multiple emission lines, like in the case of nebular emission, makes the correct redshift identification much more difficult.* Although the emission lines enhance the fluxes, the presence of emission lines in all passbands make the filter-convolved SEDs rather featureless and the SED fitting becomes more complicated.

In addition, we analysed the MIRI magnitudes of our Sample 3 simulated galaxies at $z \geq 7$. As we have normalised all the SEDs to [F150W]=29 mag, the F150W-MIRI colours directly correspond to MIRI magnitude values. Analysing this expected MIRI photometry has allowed us to assess what types of high-$z$ galaxies will likely be detected in MIRI deep surveys. For a different F150W normalisation, one simply has to scale these results, as the galaxy colours are fixed for each SED model.

A MIRI survey with a detection limit of [F560W]=28 mag should enable the detection of the vast majority of the NIRCam sources with

[F150W]=29 mag at $z = 7 - 10$, provided that these sources are at least mildly evolved. The youngest galaxies which are still forming stars (*Yggdrasil*-SED galaxies with ages $< 100\,\mathrm{Myr}$) will remain mostly undetected. Although in the case of gas covering factor $f_{\mathrm{cov}} = 1$ the nebular lines make the MIRI fluxes much brighter than in the case of $f_{\mathrm{cov}} = 0$, the continua of these young galaxies are very blue, so the resulting MIRI fluxes are not very high even in the case of nebular emission.

At the same MIRI reference depth, the F770W filter will provide fewer detections than the F560W filter at $z \geq 7$. Among the NIRCam sources with [F150W]=29 mag, evolved galaxies at $z \geq 7$ and some line emitters at $z = 9$ and 10 will be detected in F770W, but very few line emitters at $z = 7$ and 8.

Conversely, our colour analysis shows that detecting the majority of red MIRI galaxies at $z \geq 7$ will require NIRCam data at least three magnitudes deeper. This is the case both for 'passive galaxies' (galaxies which finished forming stars) and for galaxies which are red simply because of the presence of main emission lines.

As an overall summary, we argue that the results presented here constitute a useful reference for designing deep imaging surveys with *JWST*. We conclude that NIRCam and MIRI will have complementary roles and the optimal observing strategy and filter combination to be adopted will depend on each observing program's science goals. As adding MIRI imaging to the NIRCam observations would significantly enlarge the requested observing times, observers must clearly assess the need and importance of the former for their specific studies.

MIRI observations with both the F560W and F770W filters are necessary along with the NIRCam data if a correct identification of low and moderate redshift ($z < 7$) sources are desired in fields without $\lambda < 0.6\,\mu\mathrm{m}$ coverage. Alternatively, a less expensive strategy would be limiting galaxy surveys to fields with ancillary $\lambda < 0.6\,\mu\mathrm{m}$ data of matching depth and obtaining only NIRCam data, but the lack of any MIRI imaging would still result in a slightly higher percentage of redshift outliers and a lower overall recovered-redshift precision.

If the main science goal is simply identifying the bulk of the galaxy population at $z = 7 - 10$, proposing an observing program based on ultra-deep NIRCam data alone will be adequate. However, adding MIRI imaging will help improve the identification of red sources and is of utmost importance to recover stellar ages and stellar masses at $z > 7$ (Chapter 5). Therefore, observing with both cameras will be necessary for a comprehensive study of galaxy evolution since early cosmic times.

*Acknowledgements:* This work is partly based on observations taken with the NASA/ESA *Hubble Space Telescope*, which is operated by the Association of Universities for Research in Astronomy, Inc., under NASA contract NAS5-26555; with the *Spitzer Space Telescope*, which is operated by the Jet Propulsion Laboratory, California Institute of Technology under a contract with NASA; and the Very Large Telescope operated by the European Southern Observatory (ESO) at Cerro Paranal. LB and KIC acknowledge the support of the Nederlandse Onderzoekschool voor de Astronomie (NOVA). KIC also acknowledges funding from the European Research Council through the award of the Consolidator Grant ID 681627-BUILDUP. OLF acknowledges funding from the European Research Council Advanced Grant ID 268107-EARLY. PGP-G acknowledges support from the Spanish Government MINECO Grants AYA2012-31277 and AYA2015-70815-ERC. LG acknowledges support from the Spanish Government MINECO Grants AAYA2012-32295. JP acknowledges the UK Science and Technology Facilities Council and the UK Space Agency for their support of the UK's *JWST* MIRI development activities. We thank Macarena García-Marín, Alistair Glasse and Álvaro Labiano for providing us the most updated versions of the *JWST* MIRI filter transmission curves. We also thank an anonymous referee for a careful and constructive report.

## Appendix 4.A SAMPLE 3: ANALYSIS OF ADDITIONAL REDSHIFTS

In Section 4.2.1.3 we consider four redshifts for our Sample 3 analysis: $z = 7$, 8, 9 and 10. These four redshifts are representative of most of the entire redshift range $z = 7 - 10$, except for a few exception that we study here. For this analysis, we consider only BC03 templates to which we manually ad the main emission lines. We analyse how these emission lines move in and out NIRCam and MIRI filters to identify all possible configurations (Fig. 4.25). For each filter, we only take into account the wavelength range where its transmission is above 20%. To cover the redshift ranges that are unrepresented by our original analysis (corresponding to the shaded areas in Fig. 4.25), we re-test the Sample 3 redshift recovery at four additional redshifts, namely, $z = 7.1, 7.3, 8.7$, and $9.2$.

The results of our new tests are shown in Fig. 4.26 (for $S/N = 5$). At $z = 7.1$, the main difference respect to the $z = 7$ configuration is that the [O III] line moves out of the F356W NIRCam filter while H$\beta$ is still inside. The results when using NIRCam broad bands alone are very similar to the

$z = 7$ case, with similar r.m.s. values, 0.023 in this case (compared with 0.025 at $z = 7$) and similar distribution shape. The number of outliers decreases from $\sim 8\%$ to 0 when adding the F560W band, but it does not change when adding the F770W band. Also the r.m.s. improves more when adding the F560W filter rather than with the F770W one.

At $z = 7.3$ the main difference respect to the $z = 7$ configuration and the previous one is that there are no emission lines inside the F356W band. When using NIRCam bands alone, it is already possible to obtain a good redshift estimation with totally no outliers and a small r.m.s.. This is because the absence of emission line inside the F356W band creates a strong contrast with the closest bands, allowing the code to properly identify the main SED features. Moreover, this contrast happens in a narrow redshift range, confining the range of possible redshift solutions and producing a very small r.m.s. value. This is the most favourable configuration for the NIRCam bands among all considered redshifts. By adding the MIRI bands there is only a slight improvement to the already good redshift estimation.

The case of $z = 8.7$ is representative of the redshift range where no emission lines at all are present in the MIRI bands, while [O III], H$\beta$ and [O II] are inside the NIRCam wavelength range. The main difference between this case and the $z = 8$ one is that the flux observed in the F115W band, where the Lyman break falls, is fainter and more often is below the 2$\sigma$ detection limit. When using the NIRCam bands only the derived distribution is broad, but there are almost no outliers (0.5$\%$). When adding the MIRI bands, and in particular the F560W band, the r.m.s. drops by about a half.

Finally, the $z = 9.2$ case corresponds to a redshift in which [O III] is just outside the F444W band, but H$\beta$ is still inside, while the opposite situation happens in the F560W MIRI band. The redshift estimation with NIRCam bands alone is generally good, with an r.m.s. of 0.019 and only one outlier. When adding the MIRI bands, there is a slight improvement in the redshift estimation (r.m.s.$\sigma$=0.012) and no outliers.

The cases presented here are slightly different from the cases presented in the main body of the chapter, but do not lead to any significantly different conclusion. Considering all eight analysed redshifts and $S/N = 5$, the redshift estimation by using only NIRCam broad bands alone is particularly good at $z \sim 7.3$ and 8, but is the worst at $z = 8.7$ and 9. Adding MIRI bands, the redshift estimation improves at all considered redshifts, and, in the majority of cases, F560W decreases the r.m.s. a bit more than F770W.

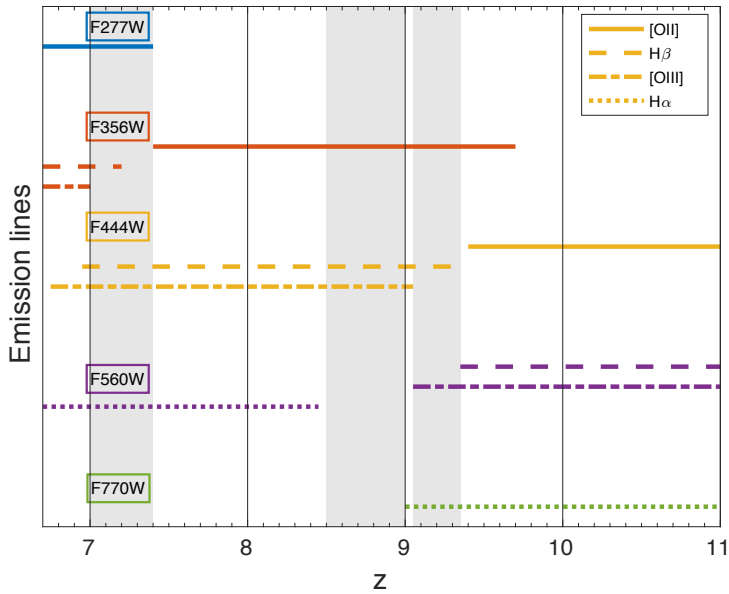


**Figure 4.25:** Emission lines present inside NIRCam and MIRI bands at high redshifts. Different colours indicate different bands. *Blue:* F277W; *red:* F356W; *yellow:* F444W; *purple:* F5602; and *green:* F770W. The shortest wavelength NIRCam bands are not shown because they do not contain emission lines in this redshift range. Different line styles represent different emission lines: [O II] (*continuous line*); H$\beta$ (*dashed line*); [O III] (*dot-dashed line*); and H$\alpha$ (*dotted line*). Vertical black lines indicate the redshifts considered in sample 3 ($z = 7, 8, 9$ and $10$). These specific redshifts are representative of all $z = 7 - 10$ redshifts, except those in the grey areas, which are instead analysed in this appendix.

## Appendix 4.B SAMPLE 3: AN ALTERNATIVE OBSERVATIONAL STRATEGY

In Sample 3 we derive fluxes for all NIRCam broad bands assuming the same integration time for all of them. However, the sensitivity of NIRCam peaks around 2 $\mu$m, so different integration times could be considered in order to compensate for different sensitivities. Therefore, we test this alternative scenario by considering observations of the same depth for all NIRCam bands, i.e., the F150W band depth, and we re-derive photometric redshifts for all galaxies in Sample 3. In particular, this method implies deeper observations for the less sensitive bands, i.e. F070W, F090W,

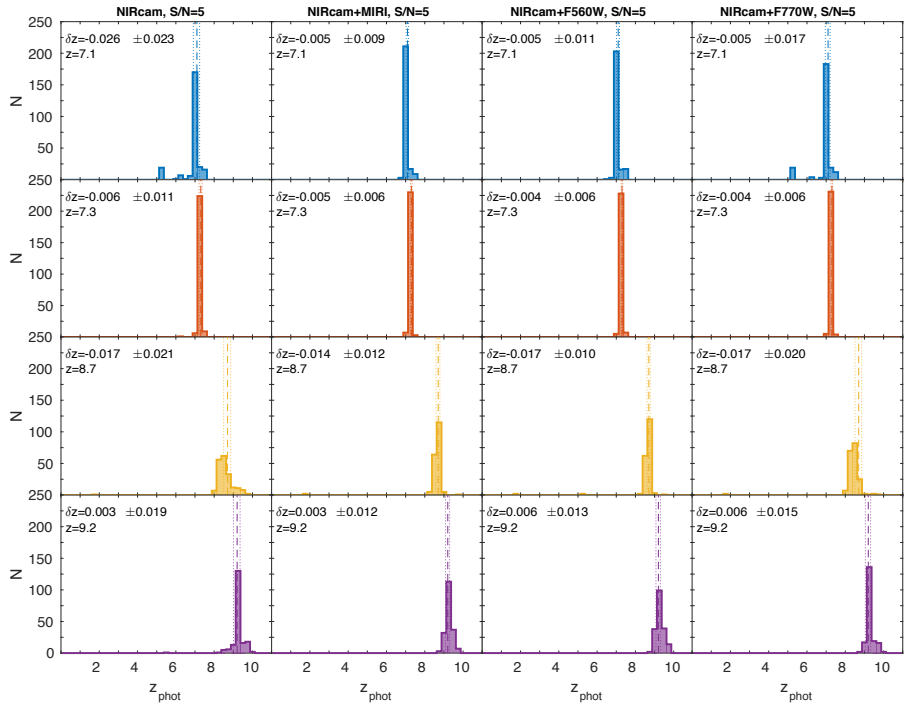


**Figure 4.26:** Photometric redshifts obtained for the BC03 simulated galaxies with (F150W) $S/N = 5$ at different fixed redshifts. *From top to bottom*: input redshifts $z$ =7.1, 7.3, 8.7 and 9.2. Photometric redshifts in each column are obtained with different combinations of bands. *From left to right:* 8 NIRCam broad bands; 8 NIRCam broad bands, MIRI F560W and MIRI F770W; 8 NIRCam broad bands and MIRI F560W only; 8 NIRCam broad bands and MIRI F770W only. The vertical lines indicate the $3\sigma$ interval around the mean normalised redshift difference. On the top left of each panel we quote the mean of $(z_{phot} - z_{input})/(1 + z_{input})$ and the r.m.s of $|z_{phot} - z_{input}|/(1 + z_{input})$.

F115W and F444W, respect to the method considered before, but shallower observations for the most sensitive bands, i.e. F200W and F277W. We do this test for both BC03 and Yggdrasil templates and for all three $S/N$ values considered before (3,5 and 10).

We compare the mean and r.m.s. of the normalised redshift difference $|z_{phot} - z_{fiduc.}|/(1 + z_{fiduc.})$ for the current case and that where we assume the same integration time in all NIRCam filters. Our results are shown in Table 4.11, while the r.m.s. values are also shown in Figure 4.27. At $S/N = 10$, the derived results considering the same depth are slightly

**Table 4.11:** Mean of $(z_{phot} - z_{input})/(1 + z_{input})$ and r.m.s of $|z_{phot} - z_{input}|/(1 + z_{input})$ for two different observational strategies: the same integration time and the same depth in all NIRCam filters. Photometric redshifts are derived considering only NIRCam bands for four redshifts ($z = 7, 8, 9$ and $10$) and both BC03 and *Yggdrasill* templates.

| | Same integration time | | | Same observational depth | | |
|---|---|---|---|---|---|---|
| | $S/N = 10$ | $S/N = 5$ | $S/N = 3$ | $S/N = 10$ | $S/N = 5$ | $S/N = 3$ |
| z=7 (BC03) | -0.009±0.011 | -0.030±0.025 | -0.057±0.030 | -0.007±0.005 | -0.030±0.022 | -0.070±0.036 |
| z=8 (BC03) | -0.021±0.009 | -0.031±0.013 | -0.018±0.031 | -0.017±0.009 | -0.023±0.014 | -0.025±0.031 |
| z=9 (BC03) | -0.003±0.008 | 0.001±0.028 | -0.018±0.032 | -0.003±0.007 | 0.003±0.023 | -0.011±0.032 |
| z=10 (BC03) | -0.002±0.010 | -0.006±0.014 | -0.083±0.029 | -0.002±0.009 | -0.080±0.011 | -0.042±0.031 |
| z=7 (Ygg) | 0.001±0.020 | -0.067±0.026 | -0.233±0.029 | -0.005±0.018 | -0.036±0.023 | -0.209±0.028 |
| z=8 (Ygg) | -0.022±0.012 | -0.209±0.018 | -0.237±0.024 | -0.018±0.011 | -0.164±0.019 | -0.246±0.025 |
| z=9 (Ygg) | 0.005±0.019 | -0.084±0.028 | -0.290±0.037 | -0.001±0.013 | -0.031±0.032 | -0.244±0.036 |
| z=10 (Ygg) | -0.013±0.011 | -0.122±0.028 | -0.338±0.030 | -0.015±0.011 | -0.070±0.024 | -0.307±0.035 |

better or similar than the one derived with the same integration times. On the other hand, at $S/N = 3$, results are similar or slightly worse. At $S/N = 5$ the results are mixed, depending on the type of template and redshift considered. These results reveal a different importance of deep observations with the most sensitive and less sensitive NIRCam bands. In particular, deep observations with the less sensitive bands seem to improve results generally when the $S/N$ is high, while deep observations with the most sensitive bands are more crucial at low $S/N$ values. It is worth noticing that, despite the fact that reaching the same depth in all NIRCam filters improves the results derived using NIRCam bands alone, these results are still worse that those derived using NIRCam and MIRI bands together.

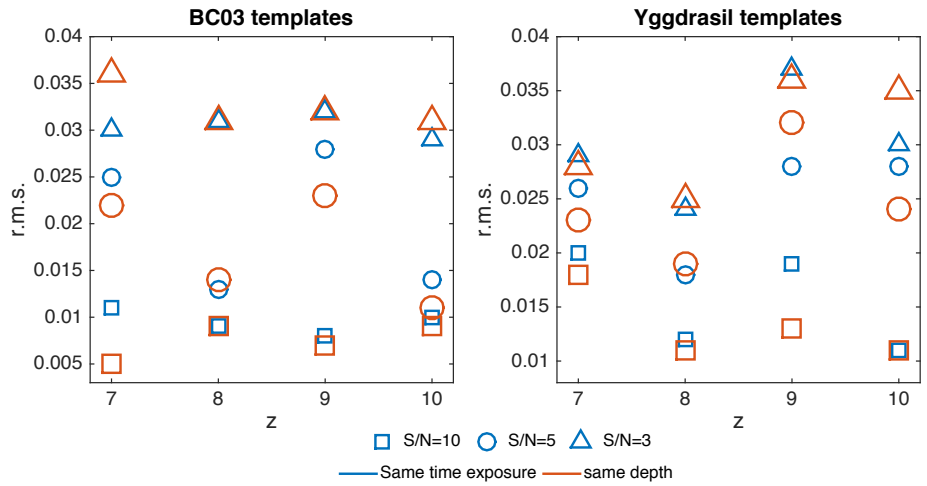


**Figure 4.27:** Redshifts vs. r.m.s values of $|z_{phot} - z_{input}|/(1+z_{input})$ derived with the NIRCam broad bands considering the same integration time (*blue symbols*) or the same observational depth (*red symbols*). Different symbols correspond to different $S/N$ values: $S/N = 10$ (squares), 5 (circles) and 3 (triangles). *Left*: BC03 templates; *right*: *Yggdrasil* templates.

# 5. Recovering the properties of high redshift galaxies with different *JWST* broad-band filters

*L. Bisigello, K. I. Caputi, L. Colina, O. Le Fèvre,*
*H. U. Nørgaard-Nielsen, P. G. Pérez-González,*
*P. van der Werf, O. Ilbert, N. Grogin, A. Koekemoer*
*2017,ApJS,231,3B*

*Imaging with the* James Webb Space Telescope (JWST) *will allow for observing the bulk of distant galaxies at the epoch of reionisation. The recovery of their properties, such as age, colour excess E(B-V), specific star formation rate (sSFR), and stellar mass, will mostly rely on spectral energy distribution fitting, based on the data provided by JWST's two imager cameras, namely the Near Infrared Camera (NIRCam) and the Mid Infrared Imager (MIRI). In this work we analyse the effect of choosing different combinations of NIRCam and MIRI broad-band filters, from 0.6 μm to 7.7 μm, on the recovery of these galaxy properties. We performed our tests on a sample of 1542 simulated galaxies, with known input properties, at $z = 7 - 10$. We found that, with only 8 NIRCam broad-bands, we can recover the galaxy age within 0.1 Gyr and the colour excess within 0.06 mag for 70% of the galaxies. Additionally, the stellar masses and sSFR are recovered within 0.2 and 0.3 dex, respectively, at z=7-9. Instead, at z=10, no NIRCam band traces purely the $\lambda > 4000$Å regime and the percentage of outliers in stellar mass (sSFR) increases by $> 20\%$ ($> 90\%$), in comparison to z=9. The MIRI F560W and F770W bands are crucial to improve the stellar mass and the sSFR estimation at z=10. When nebular emission lines are present, deriving correct galaxy properties is challenging at any redshift and with any band combination. In particular, the stellar mass is systematically overestimated in up to 0.3 dex on average with NIRCam data alone and including MIRI observations only marginally improves the estimation.*

## 5.1 INTRODUCTION

Fitting the spectral energy distribution (SED) of galaxies from broad band photometry allows for deriving a variety of galaxy properties, such as photometric redshifts, stellar masses, colour excess, ages, and metallicities, with different degrees of precision, depending on the available data and used models. SED fitting is a particularly powerful tool to study the properties of galaxies up to high redshifts, due to the fainter fluxes usually observable with photometry respect to spectroscopy.

The stellar mass is one of the most important quantities to derive for a galaxy, because it correlates with a large number of global properties, such as star formation rate (SFR; e.g. Brinchmann et al., 2004; Noeske et al., 2007; Rodighiero et al., 2011) and metallicity (e.g. Tremonti et al., 2004; Erb et al., 2006; Maiolino et al., 2008), and it is central in galaxy evolution. Fortunately, once the redshift is well determined, stellar masses are one of the most robust parameters estimated from the SED fitting (e.g. Caputi et al., 2015), while other parameters, such as age and colour excess, are generally more difficult to estimate, given the degeneracy between them. However, the inclusion of nebular emission can have a large effect on the stellar masses (e.g. Stark et al., 2013; Santini et al., 2015). At low and intermediate redshifts, the emission line equivalent widths are relatively low for most galaxies, therefore, nebular emission can be safely ignored in stellar mass calculations. However, at higher redshifts, young galaxies are more common, therefore, the effect of nebular emission is expected to be more important.

In addition, stellar masses are derived by multiplying the galaxy luminosity with a mass-to-light ratio, thus the mass estimation also depends on the wavelengths of the available observations. Observations at rest-frame $\lambda > 4000$ Å, and ideally at $\lambda > 1\,\mu m$, are necessary to derive stellar masses because the mass-to-light ratio at these wavelengths are relatively insensitive to age and colour excess. Therefore, to derive accurate stellar masses in a wide range of redshifts, it is necessary to observe in the near-IR at low and intermediate redshifts, and in the mid-IR at high redshifts.

The *James Webb Space Telescope* (*JWST*[1]; Gardner et al., 2009) is the premier infrared space observatory for the next decade with a 6.5-meter primary mirror. It has four scientific instruments on board with imaging, spectroscopic, and coronographic modes, covering a wide range of wavelengths from the visible to the mid-IR (0.6-28 $\mu$m) with superb sensitivity and resolution. In particular, the two imaging cameras, namely

[1] http://www.jwst.nasa.gov

the Near Infrared Camera (NIRCam; Rieke et al., 2005) and the Mid Infrared Instrument (MIRI; Rieke et al., 2015; Wright et al., 2015), will be used to carry out deep blank-field imaging surveys to study how galaxies have assembled and evolved since early cosmic times. For these surveys, SED-fitting analysis will be performed to derive galaxy properties, such as galaxy stellar mass, ages, and colour excess, and therefore it is important to understand the effect of different filter combination choices on the ability to estimate these quantities.

NIRCam[2] is equipped with eight broad-band filters (i.e. F070W, F090W, F115W, F150W, F200W, F277W, F356W, and F444W) together with a number of medium and narrow-band filters, covering the range from 0.6 to 5 $\mu$m. The MIRI imager[3] is complementary to NIRCam in wavelength, covering between 5 and 28 $\mu$m with nine broad-band filters, to observe both the redshifted stellar light at high-z and the hot dust radiation at low-z. Only the two shortest wavelengths MIRI filters are considered in this work (i.e. F560W and F770W), because they are the most sensitive and therefore those that will be mostly used for high-z galaxy studies.

Because of the complementary wavelength range covered by NIRCam and MIRI, they should ideally be both included in deep galaxy surveys, particularly for z $\geqslant$ 7 where NIRCam observes the rest-frame UV/optical of the SED while MIRI covers the rest-frame optical/near-IR. However, because of the different detector technology used at near- and mid-IR wavelengths, MIRI is less sensitive than NIRCam, making observations with this instrument more time-expensive. In this work, we address this issue, analysing the galaxy property estimation with different NIRCam and MIRI filter combinations and for different spectral templates. We treat all situations equally without judging how common different spectral types are expected to be, in order to leave the reader decide the optimal approach for each science case.

In this work we aim to evaluate the effect of different *JWST* broad-band filter combinations on deriving secure galaxy properties, i.e. stellar masses, colour excess, and age, for high-z galaxies. We apply our test to a sample of simulated galaxies at $z = 7, 8, 9,$ and 10 derived from Bisigello et al. (2016a, hereafter B16), where the photometric redshift recovery was analysed in detail for the same combinations of *JWST* broad-band filters.

The structure of the Chapter is as follows. In Section 6.2 we describe the analysed sample, the acquisition of the photometry in the pertinent NIRCam and MIRI bands, and the derivation of galaxy

[2]http://www.stsci.edu/jwst/instruments/nircam
[3]http://www.stsci.edu/jwst/instruments/miri

properties. We present our results at different redshifts in Section 5.3: in particular, we analyse stellar mass, age, colour excess, and specific star formation rate (sSFR). In Section 7.1 we summarise our main findings and conclusions. Throughout this chapter, we adopt a cosmology with $H_0$ =70 $\mathrm{km\,s^{-1}\,Mpc^{-1}}$, $\Omega_M = 0.27$, $\Omega_\Lambda = 0.73$. All magnitudes refer to the AB system (Oke & Gunn, 1983) and we consider a Chabrier (2003) initial mass function (IMF).

## 5.2 SAMPLE SELECTION AND TEST METHODOLOGY

### 5.2.1 Sample construction

Our analyses is based on a sample of 1542 simulated galaxies at $z = 7 - 10$ presented in B16. The sample is based on simulated galaxies derived using templates from Bruzual & Charlot (2003, BC03 hereafter); with the manual addition of the main emission lines and templates obtained with the population synthesis code *Yggdrasil* (Zackrisson et al., 2011). The main difference between the two types of templates is the incorporation of emission lines. The BC03 models do not include emission lines, so when galaxies are young and star-forming, we manually add the main emission lines (H$\alpha$, H$\beta$, [O III] at 5007Å and [O II] at 3727Å), whose rest-frame equivalent widths have been assumed to change with redshift and metallicity (see B16 for more details). In the *Yggdrasil* templates, nebular emission lines are automatically incorporated together with the nebular continuum emission when galaxies are young and the gas covering factor $f_{cov}$ >0. For this second family of templates, rest-frame equivalent widths change with metallicity rather than redshift. In Fig. 5.1, there is an example of an Yggdrasil SED template with $f_{cov} = 1$ at the four considered redshifts (7, 8, 9, and 10), to show the amount of emission lines that contaminate the *JWST* broad-band filters analysed on this work at each redshift.

A second difference between the two types of template is the star formation history. In particular, the BC03 models have declining star formation histories, while *Yggdrasil* templates have step function star formation histories. It is necessary to remember this difference when analysing the sSFR estimation for the two types of templates, as discussed in more detail in Section 5.3.3. An additional BC03 SED model with increasing star formation history is analysed in Appendix 5.A.

For both templates we consider a large range of parameters consistent with $z = 7 - 10$ (Table 5.1). We do not include galaxies with Population III stars among *Yggdrasil* templates, as in B16, because the stellar mass is not

defined for them. All templates are normalised at 29 AB mag at 1.5 $\mu$m, corresponding to the pivot wavelength of the NIRCam F150W broad-band filter.

The full sample consists of 1542 galaxies: there are 417 SED models at each redshift 7 and 8 (216 BC03 templates and 201 *Yggdrasil* templates) and 354 SED models at each redshift 9 and 10 (180 BC03 templates and 174 *Yggdrasil* templates). The distribution of the stellar mass for all templates in this sample (corresponding to the adopted normalisation) is shown in Fig. 5.2. Differences in the two mass distributions are due to the different star formation histories used for the two types of templates and the presence of young galaxies without emission lines ($f_{cov} = 0$) among the *Yggdrasil* templates that are not present in the BC03 templates. All results are valid also for lower masses, as long as the SED shapes and S/N values are the same. Note that our sample is not intended to emulate the distribution of galaxy SED in a real galaxy population, but rather span the different types of SED types of the galaxies that will be observed in the high-z *JWST* NIRCam and MIRI blank fields, on an equal basis.

**Table 5.1:** Parameter values used to create BC03 and *Yggdrasil* SED models of the simulated galaxies at z$= 7 - 10$ that are analysed in this work.

| Parameter | Values (BC03) | Values (Ygg) |
|---|---|---|
| metallicity | $Z_\odot$, $0.4Z_\odot$, $0.2Z_\odot$,$0.02Z_\odot$[a] | $Z_\odot$,$0.4Z_\odot$,$0.2Z_\odot$,$0.02Z_\odot$[a] |
| SFH type | declining | step function |
| SFH [Gyr] | 0.01,0.1,1,10 | 0.01,0.03,0.1 |
| $f_{\rm cov}$ | – | 0,[b]1 |
| E(B-V)[c] | 0,0.1,0.25 | 0,0.1,0.25 |
| age [Gyr] | 0.01,0.05,0.2,0.4,0.6[d] | 0.01,0.05,0.2,0.4,0.6[d] |
| $z$ | 7,8,9,10 | 7,8,9,10 |

[a] for this metallicity we considered only ages $t$ <0.2 Gyr.
[b] templates of old galaxies with no star formation ongoing do not change with the covering factor, so, for these galaxies, we considered only $f_{cov}$ =1.
[c] following Calzetti et al. reddening law (Calzetti et al., 2000)
[d] we considered this age only up to redshift $z = 8$.

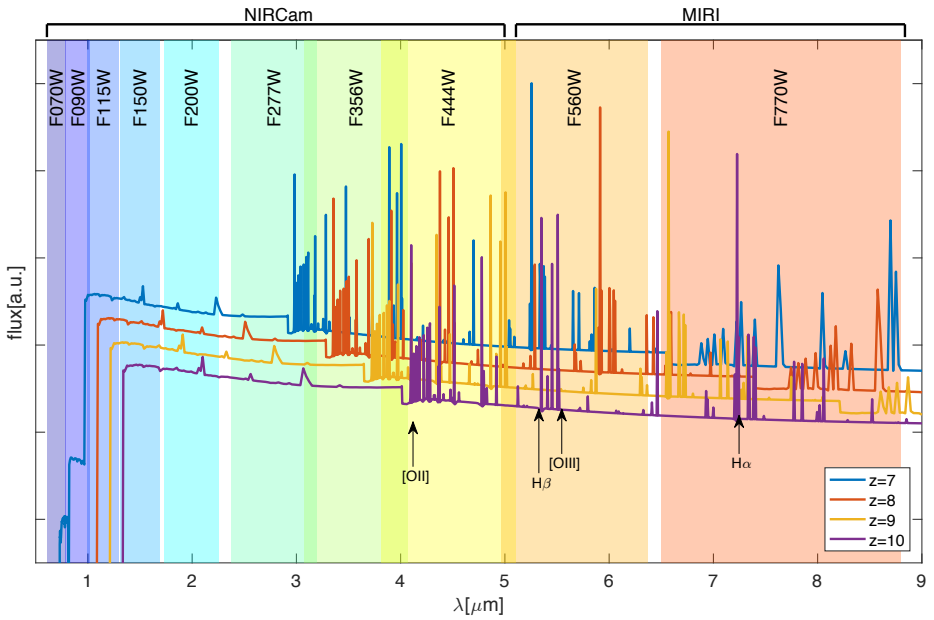


**Figure 5.1:** Four examples of SED templates from the population synthesis code *Yggdrasil* with $f_{cov}$ =1. The coloured areas specify the wavelength range of the 8 NIRCam broad-band filters and MIRI F560W and F770W. This figure illustrates the amount of emission lines incorporated in these SED templates and in which *JWST* broad-band filters they are observed at each analysed redshift.

### 5.2.2 Interpolation/Extrapolation of JWST photometry

All galaxies in the sample have mock observations for the 8 NIRCam broad bands, MIRI F560W and F770W broad bands from B16, derived by convolving each SED template with the NIRCam and MIRI filter transmission curves (Meyer et al., 2004; Bouchet et al., 2015; Glasse et al., 2015). We normalise each template at 29 AB mag at 1.5 $\mu$m, corresponding to the NIRCam F150W filter pivot wavelength, and we scale the fiducial stellar mass of each template accordingly to this normalisation. One of the major causes of errors in the stellar mass derivation is a wrong redshift estimation. In our analysis, we want to study each parameter independently and, therefore we associate a signal-to-noise value of 10 with the flux at the F150W band, which corresponds to ∼8-9 hours per pointing of exposure time with low background level[4]. Considering these

[4]derived using the JWST time exposure calculator https://jwst.etc.stsci.edu

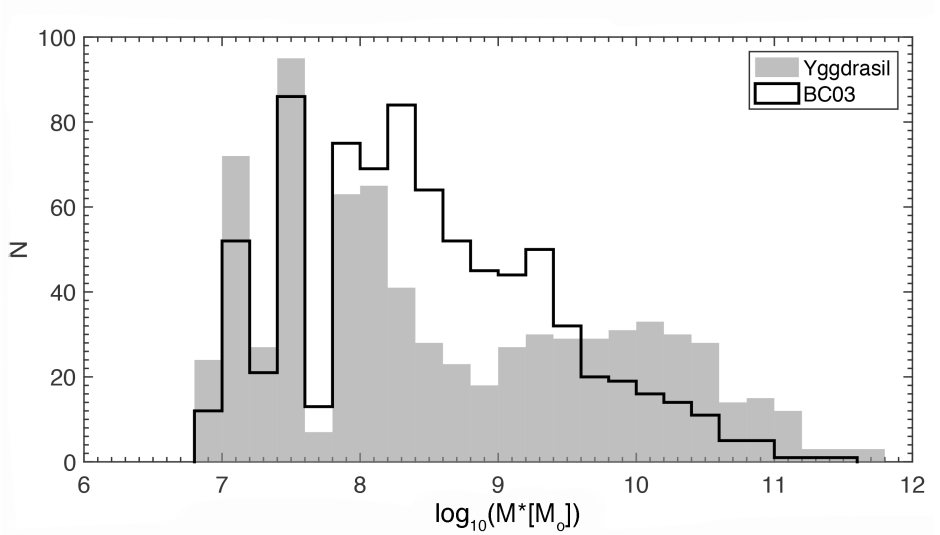


**Figure 5.2:** Input stellar masses of galaxies simulated with BC03 templates (*black line*) and *Yggdrasil* models (*grey area*). All these stellar masses correspond to SED models normalised at 29 AB magnitude at observed 1.5 $\mu$m. We considered a Chabrier (2003) IMF.

high signal-to-noise values, the photometric redshift is well determined for $> 99\%$ of the galaxies in our sample (see B16). We scale the photometry of the other NIRCam bands considering the same integration time, but different sensitivities, according to each band. For the MIRI bands, all fluxes correspond to the SED templates normalised to 29 mag at $1.5$ $\mu$m. The S/N values on the MIRI bands have been scaled assuming that a S/N=10 corresponds to 28 mag in these bands. We consider only a signal-to-noise of 10 to limit the effects of redshift uncertainties and bad photometry. Indeed, in B16 the number of outliers in redshift (galaxies with $|z_{phot} - z_{fiducial}|/(1+z_{fiducial})$ >0.15) for this S/N value was less than $1\%$ at all considered redshifts. Therefore, variations in galaxy property estimates obtained here are mainly due to degeneracies between galaxy templates and are not expected to be solved with just a higher integration time. Differences in the S/N value are expected not to change significantly the results of this work, as long as $S/N \gtrsim 10$.

A 28 AB mag with a S/$N$ =10 in MIRI corresponds to ∼196 hours per pointing of exposure time with F560W and a low-level backgrounds. However, as explained in more detail in section 5.3.1.3, considering a S/N=5 for a 28 AB magnitude on the MIRI bands will not create a major

difference for the stellar mass estimation and it will be possible with ∼47 hours per pointing of exposure time.

Each mock flux is randomised 100 times within the error bars and we considered as non-detection every flux below the $2\sigma$ level. As a conservative approach, when running the SED-fitting code, we adopt a $3\sigma$ upper limit, rather than $2\sigma$, in all cases of non-detections.

More details about the *JWST* photometry and redshift derivation are presented in B16.

### 5.2.3 Galaxy properties derivation

We use the expected *JWST* photometry for our simulated galaxy sample to test how accurately it is possible to derive different properties, i.e. stellar mass, age, colour excess, and sSFR. As in B16, we perform these tests with different combinations of *JWST* bands:

- 8 NIRCam broad bands
- 8 NIRCam broad bands and 2 MIRI bands (F560W and F770W)
- 8 NIRCam broad bands and MIRI F560W only
- 8 NIRCam broad bands and MIRI F770W only

We consider these band combinations to understand in which situations NIRCam broad-band filters are sufficient to properly recover galaxy properties, and in which cases adding the two shortest-wavelength MIRI filters can significantly improve the estimations. We consider only these two MIRI broad-band filters because they are the most sensitive ones, thus making them the filters most likely to be used in high-z galaxy surveys. As deep observations with MIRI are significantly more time consuming that those with NIRCam, because of different detector technology in the near and mid-IR, observation strategies may opt to use only one of the two bands. Therefore, we consider this situation by also analysing filter combinations with only one of the two MIRI filters.

For all filter combinations, we run the public code *LePhare* (Arnouts et al., 1999; Ilbert et al., 2006) to derive stellar mass, age, colour excess, and sSFR, allowing for a large variety of templates. A full list of the parameter values used for the SED fitting is presented in Table 5.2.

First, when running *LePhare*, we consider a library containing the same templates used to derive *JWST* photometry, i.e. BC03 templates with incorporated emission lines and *Yggdrasil* templates with a more refined grid of colour excess values and z=0-11. However, when using the BC03 templates, we limit the used templates to only those corresponding to the pre-determined photometric redshift. For these templates, we add manually the main emission lines, whose rest-frame equivalent widths

**Table 5.2:** Parameter values used for the SED fitting runs of the simulated galaxies at z$= 7 - 10$ that are analysed in this work. For both types of templates we used the original template, BC03 or *Yggdrasil*, with a denser grid of colour excess values and a wider redshift range than the original templates used to derived the mock photometry (see table 5.1). Moreover, in both cases, we considered also an additional BC03 templates with old ages.

| Parameter | Values (BC03) | Values (Ygg) | Values (Additional BC03) |
|---|---|---|---|
| metallicity | $Z_\odot$, $0.4Z_\odot$, $0.2Z_\odot$,$0.02Z_\odot$ | $Z_\odot$,$0.4Z_\odot$,$0.2Z_\odot$,$0.02Z_\odot$ | $Z_\odot$,$0.4Z_\odot$,$0.2Z_\odot$,$0.02Z_\odot$ |
| SFH type | declining | step function | declining |
| SFH [Gyr] | 0.01,0.1,1,10 | 0.01,0.03,0.1 | 0.01,0.1,1,10 |
| $f_{\rm cov}$ | – | 0,1 | – |
| E(B-V)[a] | 0, 0.05, 0.1,...,1 | 0, 0.05, 0.1,...,1 | 0, 0.05, 0.1,...,1 |
| age [Gyr] | 0.01,0.05,0.2,0.4,0.6 | 0.01,0.05,0.2,0.4,0.6 | 1,1.5,2.5,5 |
| $z$[b] | 0-11 | 0-11 | 0-11 |

[a] following the Calzetti et al. reddening law (Calzetti et al., 2000).
[b] this is the redshift range in the SED fitting run.

change with redshift and metallicity (see B16 for more details). However, we note that the use of templates that change with redshift introduces an unnecessary level of degeneracy in parameter space. Although the redshifts are correctly recovered in the vast majority of cases, assigning the "wrong" line equivalent widths could create more scatter in the derived stellar mass. In particular, this happens when it is not possible to determine the level of the continuum and therefore the equivalent width of the emission lines. This is the case when there is not a clean measurement of the near-IR continuum at $\lambda > 4000\,\text{Å}$, without contamination by emission lines, e.g. when using only 8 NIRCam broad bands at z=7. In this case, the level of the continuum can be determined by observing at rest-frame $\lambda > 4000\,\text{Å}$ (i.e. with the F770W band at z=7), but it is necessary to increase the number of used filters to cover all possibilities in a wide range of redshifts. However, since the redshift estimation is mostly not affected by this problem, and it is already possible to derive a good photometric redshift using 8 NIRCam bands if the S/N$\geqslant$10, we decide to first estimate the photometric redshift using all templates and then derive the stellar mass, together with age and colour excess, limiting the templates to those corresponding to the derived redshift.

In the SED fitting, we also include templates of older galaxies and higher extinction values than those expected at z$>$7, to allow for degeneracies between redshift, dust, and age. In particular, we include templates from

BC03 with solar metallicity, ages from 0.01 to 5 Gyr, exponentially declining star formation histories with different characteristic times $\tau$ from 0.01 to 10 Gyr, and apply colour excess following the Calzetti et al. reddening law (Calzetti et al., 2000) with extinction values E(B-V)$= 0 - 1$, with a step of 0.05 mag.

Each galaxy in the sample has 100 sets of photometry, obtained by randomising fluxes within each error bar using a normal distribution. We derive the median of the photometric redshifts of the 100 runs of each galaxy and recovered the parameter values of the median $z_{phot}$ solutions, despite its equivalence with the fiducial redshift, although the redshifts themselves are correctly recovered in most cases. So, we proceed in two steps: we derive the median stellar mass among the recovered solutions, and then we retrieve the parameters values of the median stellar mass solution. To summarise, we consider the parameter set of the template corresponding to the median photometric redshift and median stellar mass as the final output values of stellar mass, colour excess, age, and sSFR of each galaxy. We consider the input values of each used SED model as fiducial values.

## 5.3 RESULTS

### 5.3.1 Stellar masses

In this section we present our stellar mass results, derived using NIRCam broad bands alone and adding alternatively the F560W and F770W MIRI bands. All masses are derived from the normalisation of each SED template, using all available bands. It is important to remember that, at S/N=10, the number of outliers in redshift ($|z_{output} - z_{fiducial}|/(1 + z_{fiducial})$ >0.15) is less than $1\%$ for both BC03 and *Yggdrasil* templates with all band combinations (Bisigello et al., 2016a). Because the considered redshifts are four fixed values ($z = 7$, 8, 9, and 10), we show the output mass estimation for each case separately, and for each plot we quote the mean and the r.m.s values of the $\Delta log(M^*) = log(M^*_{output}) - log(M^*_{fiducial})$ distribution, where fiducial values for the stellar mass are the input values of each template. Our results are shown in Fig. 5.3-5.5 for BC03 and *Yggdrasil* templates separately.

#### 5.3.1.1 Galaxies simulated with BC03 templates

For the BC03 templates, the results for the stellar mass recovery are shown in Fig. 5.3. The outlier fractions for each *JWST* filter combination are

**Table 5.3:** Number (percentage) of outliers in stellar mass among the 792 (216 at each $z = 7$ and 8, and 180 at each $z = 9$ and 10) galaxies simulated with BC03 templates and manual addition of emission lines, for different combinations of *JWST* filter sets and different redshifts. Between square brackets there is the number of galaxies with emission lines among the outliers. Outliers are defined as those values beyond $3\sigma_{logM^*}$ of the distribution $\Delta log_{10}(M^*) = log_{10}(M^*_{output}) - log_{10}(M^*_{fiducial})$, with $\sigma_{logM^*}$ =0.04 dex.

| Bands | $N_{outlier,z=7}$ | $N_{outlier,z=8}$ | $N_{outlier,z=9}$ | $N_{outlier,z=10}$ |
|---|---|---|---|---|
| 8 NIRCam broad bands | 41 [41] (19.0%) | 12 [12] (5.6%) | 46 [46] (25.6%) | 56 [55] (31.1%) |
| 8 NIRCam bands+MIRI F560W, F770W | 50 [50] (23.1%) | 21 [21] (9.7%) | 28 [28] (15.6%) | 24 [24] (13.3%) |
| 8 NIRCam bands+MIRI F560W | 50 [50] (23.1%) | 24 [24] (11.1%) | 10 [10] (5.6%) | 34 [34] (18.9%) |
| 8 NIRCam bands+MIRI F770W | 39 [39] (18.1%) | 11 [11] (5.1%) | 14 [14] (7.8%) | 25 [25] (13.9%) |

listed in Table 5.3. Outliers are defined as galaxies with $\Delta log(M) = log_{10}(M^*_{output}) - log_{10}(M^*_{fiducial}) > 3\sigma_{logM^*}$, with $\sigma_{logM^*}$ =0.04 dex, which is the minimum $\sigma_{logM^*}$ obtained with all considered filter combinations.

First, we analyse the results considering only 8 NIRCam broad-band filters. The mass difference distribution is quite narrow up to $z = 9$, with $\sigma_{logM^*}$ =0.05-0.08 dex, but it becomes broad at the highest redshift, with $\sigma_{logM^*}$ =0.29 dex. The fraction of outliers is high at all redshifts: at $z = 7 - 9$ it is between 5.6% and 25.6% and it is even higher (31.1%) at $z = 10$. The wings of the distribution are almost totally composed of galaxies with emission lines, which also make up almost all the outliers. We analyse galaxies with emission lines further in Section 5.3.1.2.

Second, we analyse the results derived by using both MIRI bands together with the 8 NIRCam broad-band filters. At z= $7 - 8$, the incorporation of the MIRI bands does not improve the already small r.m.s. values obtained with NIRCam alone. The number of outliers when adding MIRI bands is slightly higher than when considering only NIRCam bands; however the stellar mass offset is less than 0.15 dex for the majority of cases, and never more than 0.3 dex. Moreover, while the stellar mass estimation worsens when adding the two MIRI bands, the estimation of other parameters, such as age or colour excess, generally improves (see Section 5.3.2.1). At $z = 9$, instead, the r.m.s. value does not significantly change, but the mean decreases as well as the number of outliers, which becomes $\sim$16%.

At $z = 10$, the importance of the MIRI bands becomes more evident. Indeed, the r.m.s. value becomes similar to other redshifts, decreasing from 0.29 dex with 8 NIRCam bands to 0.08 dex when adding the two MIRI

bands. Furthermore, the fraction of outliers decreases from 31.1% with 8 NIRCam bands to 13.3% with the two MIRI bands. This happens because few NIRCam bands cover a rest-frame wavelength redward of the 4000 Å break at increasing redshifts, i.e. at $z = 10$ no NIRCam broad-band filters purely cover $\lambda > 4000$ Å.

When the MIRI bands are considered one at a time, the r.m.s. values and outlier fractions are generally similar to the case with both MIRI bands at all redshifts, with small differences in one or the other band depending on the redshift.

Overall, when considering BC03 templates and NIRCam observations alone, the stellar mass estimation is generally good for galaxies without emission lines and for galaxies with emission lines at $z \leq 9$, while it becomes more difficult at $z = 10$. Indeed, at $z = 10$ no NIRCam band purely covers the rest-frame $\lambda > 4000$ Å and it is difficult to set the level of the continuum and therefore, derive the stellar mass. Adding the two MIRI bands does not significantly improve the already good mass estimation at the lowest redshifts, while it improves it substantially at $z = 10$ by adding more information at $\lambda > 4000$ Å.

#### 5.3.1.2 Galaxies simulated with Yggdrasil templates

Figure 5.4 shows the distribution of the difference between the recovered stellar masses and the fiducial ones for galaxies simulated with the *Yggdrasil* templates at each fixed redshift and for all *JWST* filter combinations. The fractions of outliers of the full sample of *Yggdrasil* simulated galaxies are listed in table 5.4. Outliers are defined as galaxies with $\Delta log(M) = log(M^*_{output}) - log(M^*_{fiducial}) > 3\sigma_{logM^*}$, with $\sigma_{logM^*}$ =0.15 dex, which is the minimum $\sigma_{logM^*}$ obtained with all considered filter combinations.

When considering only 8 NIRCam bands, the $\Delta log(M)$ distributions appear peaky with long tails, particularly towards positive values. The r.m.s. values are similar at $z = 7$ and 8, namely $\sigma_{logM^*}$ =0.19 and 0.17 dex respectively, and they increase at higher redshifts up to 0.25 dex at $z = 10$. The fraction of outliers ranges between 4.5% at $z = 8$ and 12.6% at $z = 10$.

When adding both MIRI bands, the mass estimation slightly improves at all redshifts, except at $z = 9$. In particular, the main improvement is in the number of outliers at z=10, which is reduced by more than half. Adding the two MIRI bands at z=9 does not significantly change the mass estimation, except for galaxies with emission lines for which the estimation became worse. However, the estimation of other parameters, such as age and colour excess, generally improves while the stellar mass does not (see

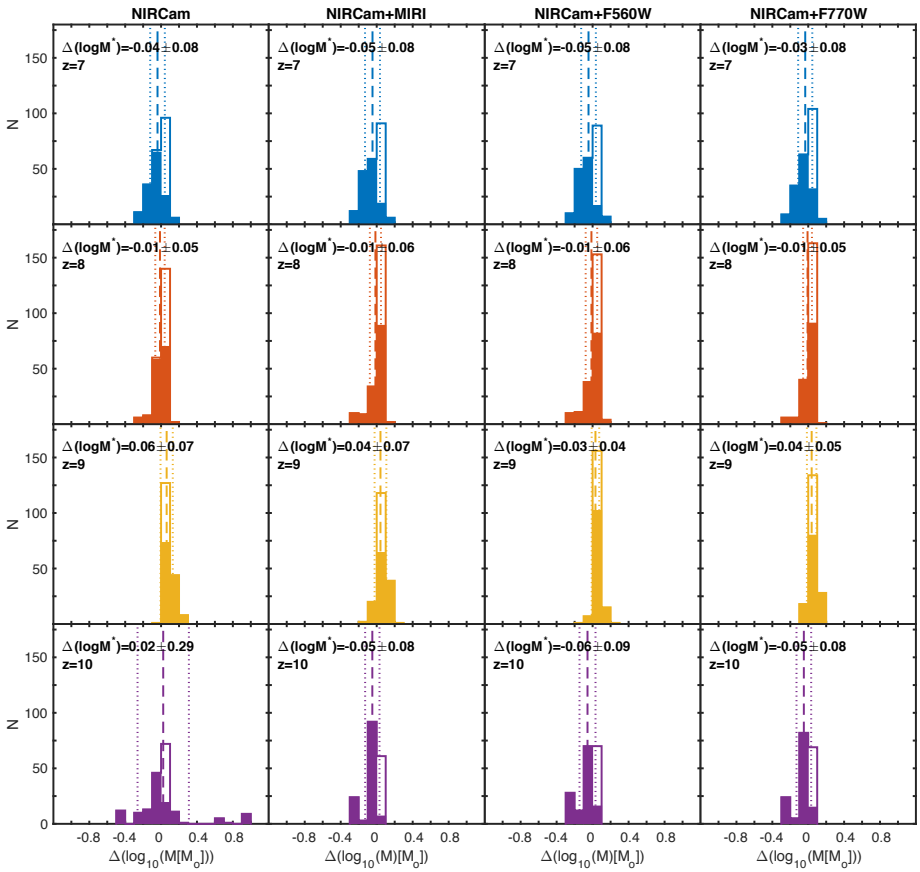


**Figure 5.3:** Differences between the derived and the fiducial stellar mass for the BC03 simulated galaxies at different fixed redshifts, i.e. $\Delta log_{10}(M^*) = log_{10}(M^*_{output}) - log_{10}(M^*_{fiducial})$. *From top to bottom*: redshifts $z = 7, 8, 9,$ and 10. Stellar masses in each column are obtained with different combinations of *JWST* bands. *From left to right:* 8 NIRCam broad bands; 8 NIRCam broad bands, MIRI F560W and MIRI F770W; 8 NIRCam broad bands and MIRI F560W only; 8 NIRCam broad bands and MIRI F770W only. The vertical lines indicate the mean and the 1 $\sigma_{logM^*}$ values, which are quoted at the top-left of each panel. The coloured histograms represent galaxies with emission lines, while the open ones represent galaxies without emission lines.

Section 5.3.2.2). Indeed, for this particular redshift and for galaxies with emission lines, the stellar mass estimation, as well as other parameters, is also particularly difficult when including the MIRI bands. This is because

emission lines are present in all bands at $\lambda > 4000\,\text{Å}$, therefore it is not possible to determine the level of the continuum.

When analysing the two MIRI bands separately, we see that they have similar roles, but F560W decreases the r.m.s. and the fraction of outliers slightly more than F770W at $z > 7$.

Figure 5.5 shows the distribution of the difference between the recovered and the fiducial stellar mass, but only for galaxies with emission lines, which are young galaxies with covering factor $f_{cov}$ >0. Outliers are defined as galaxies with $log(M^*_{output}) - log(M^*_{fiducial}) > 3\sigma_{logM^*}$, with $\sigma_{logM^*}$ =0.15 dex, similar to the full *Yggdrasil* sample, and they are reported in table 5.4 between square brackets.

When considering only 8 NIRCam bands, the stellar mass is generally overestimated, with mean values between 0.10 dex and 0.27 dex. The r.m.s. values are higher than the values of the general sample, ranging between 0.26 dex and 0.32 dex, with a minimum value at $z \leq 8$. Among all outliers, galaxies with emission lines are the majority, but also a small fraction of galaxies without emission lines are present, in contrast to BC03 templates. Among the outliers with no emission lines, the majority (22 out of 31) are red and quenched galaxies, and the remaining are blue star-forming galaxies with $f_{cov}$ =0 that are not present among BC03 templates.

Adding the MIRI bands produces small improvements on the stellar mass recovery at z=7-8, while, as seen for the general sample, the two MIRI bands have the largest impact at z=10, with the r.m.s. that decreases of 0.09 dex while the mean changes from 0.25 dex to 0.07 dex. Similarly, when looking at the number of outliers, at $z < 9$ adding the two MIRI bands creates small differences ($\sim 20\%$) while at $z = 10$ the number of outliers is reduced to almost a half. At $z = 9$ the number of outliers with emission lines increases.

When considering the two MIRI bands separately, F560W improves the mass estimation slightly more than F770W, with smaller r.m.s. values at all redshifts, except at z= 9, and a lower number of outliers at $z > 7$.

Overall, when considering *Yggdrasil* templates, the stellar mass estimation derived with 8 NIRCam bands is generally good at z= $7 - 9$ but worsens with increasing redshift. Moreover, it is particularly difficult when galaxies have nebular emission lines. MIRI bands slightly improve the mass estimation of the general sample and particularly improve it at $z = 10$, because MIRI bands cover the rest-frame $\lambda > 4000\,\text{Å}$ that otherwise is purely covered by no NIRCam bands at this redshift. Moreover, adding MIRI bands improves the stellar mass recovery of galaxies with emission lines at all redshifts, except at $z = 9$.

**Table 5.4:** Number (percentage) of outliers in stellar mass among the 750 (201 at each $z = 7$ and 8, and 174 at each $z = 9$ and 10) galaxies simulated with *Yggdrasil* templates, 192 of which are with emission lines, for different combinations of *JWST* filter sets and different redshifts. Between square brackets there is the number of galaxies with emission lines among the outliers. Outliers are defined as those values beyond $3\sigma_{logM^*}$ of the distribution $\Delta log_{10}(M^*) = log_{10}(M^*_{output}) - log_{10}(M^*_{fiducial})$, with $\sigma_{log_{10}M^*}$ =0.15 dex.

| Bands | $N_{outlier,z=7}$ | $N_{outlier,z=8}$ | $N_{outlier,z=9}$ | $N_{outlier,z=10}$ |
|---|---|---|---|---|
| 8 NIRCam broad bands | 16 [15] (8.0%) | 9 [7] (4.5%) | 16 [15] (9.2%) | 22 [16] (12.6%) |
| 8 NIRCam bands+MIRI F560W, F770W | 16 [14] (8.0%) | 6 [5] (3.0%) | 21 [20] (12.1%) | 9 [7] (5.2%) |
| 8 NIRCam bands+MIRI F560W | 22 [22] (10.9%) | 9 [6] (4.5%) | 13 [13] (7.5%) | 14 [10] (8.0%) |
| 8 NIRCam bands+MIRI F770W | 15 [14] (7.5%) | 15 [13] (7.5%) | 22 [22] (12.6%) | 20 [15] (11.5%) |

#### 5.3.1.3 Stellar mass recovery with S/N=5 with MIRI

As explained before, the integration time for reaching a S/N=10 at 28 AB mag with MIRI is significantly longer than for NIRCam. However, when considering S/$N$ =5, instead of S/$N$ =10, at 28 AB mag for the MIRI bands and leaving S/N=10 for all NIRCam bands, the differences in the derived stellar masses are $< 5\%$ for 94% of the sample of *Yggdrasil* templates. This percentage varies a little with redshift, from ∼96% at z=7 to ∼92% at z=10. For BC03 templates the differences in the derived stellar masses are $< 5\%$ for 79% of the sample at z=7, 87% at z=8, 56% at z=9 and 85% at z=10.

Reaching mag=28 with a S/N=5 with MIRI is indeed possible, i.e. ∼38 (∼63) hours of exposure time with F560W band and a low-level (medium-level) background, and the stellar mass derived is similar to that obtained considering a S/$N$ =10 with MIRI for the majority of cases.

### 5.3.2 Age and colour excess

In this Section we present our results of age and colour excess recovery for galaxies derived both with BC03 templates and with *Yggdrasil* models. Because of the age-dust degeneracy, we decide to analyse the two properties together. Figures 5.6 - 5.8 show the difference between the derived and fiducial ages compared to the difference between the derived and fiducial colour excess values at each fixed redshift, for BC03 and *Yggdrasil* templates. For each plot we quote the mean and r.m.s. values of both the age difference ($t_{output} - t_{fiducial}$) and the colour excess difference ($E(B-V)_{output} - E(B-V)_{fiducial}$) distributions. As for the stellar masses, we present our results

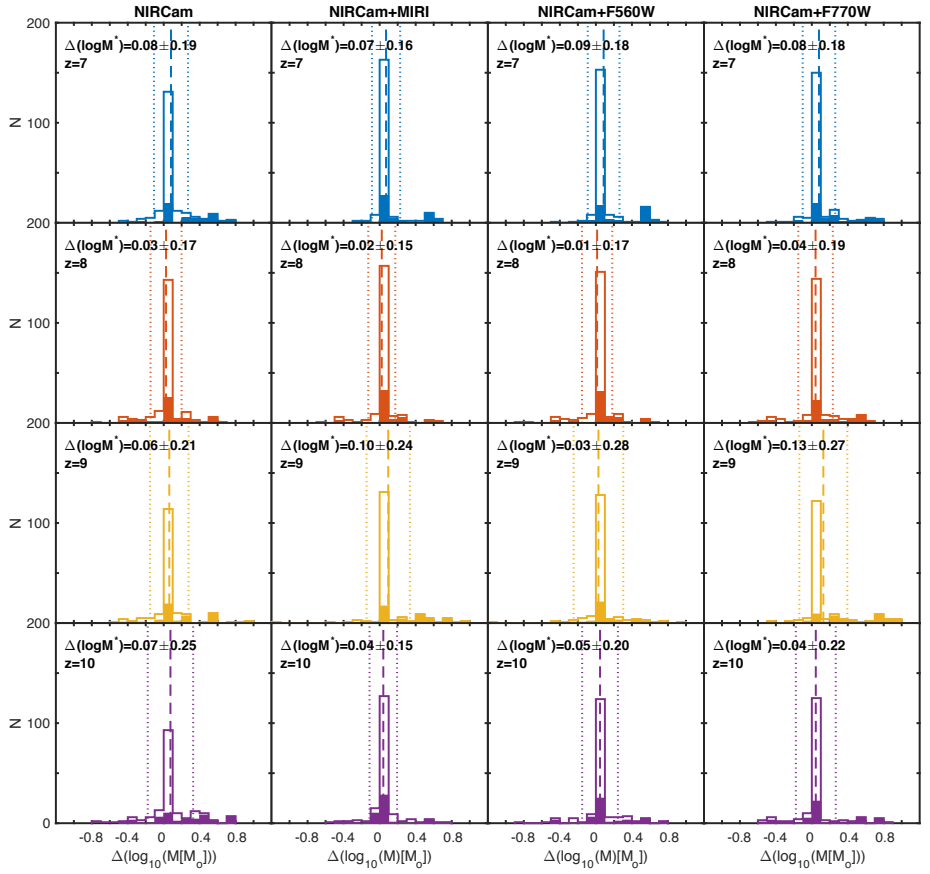


**Figure 5.4:** Differences between the derived and the fiducial stellar mass for the *Yggdrasil* simulated galaxies at different fixed redshifts, i.e. $\Delta log_{10}(M^*) = log_{10}(M^*_{output}) - log_{10}(M^*_{fiducial})$. *From top to bottom*: redshifts $z = 7, 8, 9,$ and 10. Stellar masses in each column are obtained with different combinations of *JWST* bands. *From left to right:* 8 NIRCam broad bands; 8 NIRCam broad bands, MIRI F560W and MIRI F770W; 8 NIRCam broad bands and MIRI F560W only; 8 NIRCam broad bands and MIRI F770W only. The vertical lines indicate the mean and the 1 $\sigma_{logM^*}$ values, which are quoted at the top-left of each panel. The coloured histograms represent galaxies with emission lines, while the open ones represent galaxies without emission lines.

derived using observations with only 8 NIRCam broad-band filters, adding both MIRI bands and only one of the two separately.

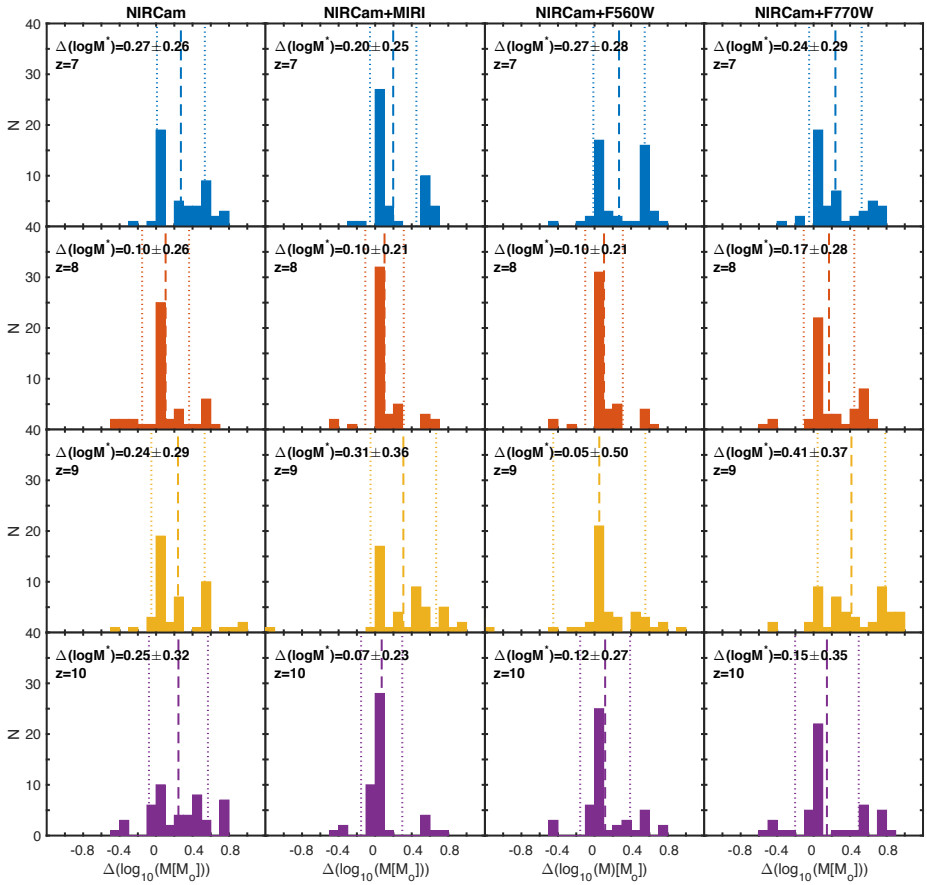


Figure 5.5: Zoom in of Fig. 5.4 showing only galaxies with emission lines.

#### 5.3.2.1 Galaxies simulated with BC03 templates

In Figure 5.6 we show the comparison between fiducial and output values, both for age and colour excess, for BC03 templates. Outliers are defined as galaxies with $|t_{output} - t_{fiducial}| > 3\sigma_t$ ($|E(B-V)_{output} - E(B-V)_{fiducial}| > 3\sigma_{E(B-V)}$), with $\sigma_t$ =0.01 Gyr ($\sigma_{E(B-V)}$ =0.02 mag), which is the minimum r.m.s. value for the age (colour excess) obtained with all considered filter combinations.

When considering only 8 NIRCam bands, the colour excess is estimated within $|\Delta E(B-V)|$ <0.2 mag for all objects at all redshifts, the mean of the distribution is <0.02 mag and the r.m.s. values are 0.02-0.06 mag, with the highest value at $z = 7$. The number of outliers is high at z=7

and decreases with redshifts, from $25.5\%$ to $0.0\%$. On the other hand, the age difference distribution has r.m.s. values between 0.05 (at z=9) and 0.10 (at z=7) and the mean values are between -0.03 Gyr and 0.02 Gyr. However, long tails are present up to $|\Delta t|$ =0.4 Gyr and the number of outliers ranges from a minimum of 15.0% at z=9 to a maximum of 36.1% at z=7. In general, the age and the colour excess r.m.s. values decrease with the redshift because the age-dust degeneracy is reduced due to the decreasing age of the Universe.

When adding both MIRI bands, the r.m.s. of the colour excess difference does not change significantly, but the number of outliers decreases at $z \leq 8$. On the other hand, the age r.m.s. slightly decreases at all redshifts, but the number of outliers decreases only at $z = 7$ and 10. Moreover, at $z > 7$ the age is never overestimated, while the colour excess is never underestimated.

The two MIRI bands play similar roles when considered separately, and neither of them improve the age or the colour excess estimation particularly more than the other one at all redshifts.

Similarly to the mass estimation, most of the outliers, both in age and colour excess, are galaxies with emission lines.

To conclude, with only NIRCam bands, both the colour excess and age estimation distribution present long tails and extreme outliers. The two MIRI bands improve the age estimations, mainly reducing the r.m.s., while they mainly reduce the number of outliers in the colour excess estimation.

#### 5.3.2.2 Galaxies simulated with *Yggdrasil* templates

In Figure 5.7 we show the comparison between fiducial and output values, both for age and colour excess, for *Yggdrasil* templates, for each redshift and different band combinations. Outliers are defined as galaxies with $|t_{output} - t_{fiducial}| < 3\sigma_t$ ($|E(B-V)_{output} - E(B-V)_{fiducial}| < 3\sigma_{E(B-V)}$), with $\sigma_t$ =0.01 Gyr ($\sigma_{E(B-V)}$ =0.01 mag) which is the minimum r.m.s. value obtained for the age (colour excess) with all considered filter combinations.

When considering only 8 NIRCam bands, the colour excess estimation is similar at all redshifts, with $\sigma_{E(B-V)}$ =0.04 mag. The number of outliers is also similar at all redshifts ($\sim 20-30\%$), with a minimum value at $z = 8$. The age difference distribution has $\sigma_t = 0.02 - 0.08$ Gyr, with a maximum value at z= 8, while the number of outliers is between 12.9% and 25.3%, increasing with redshift.

When including the two MIRI bands, both the age and the colour excess estimation are generally improved. In particular, for the colour excess, the r.m.s. value greatly decreases at $z = 7$ and does not change significantly at

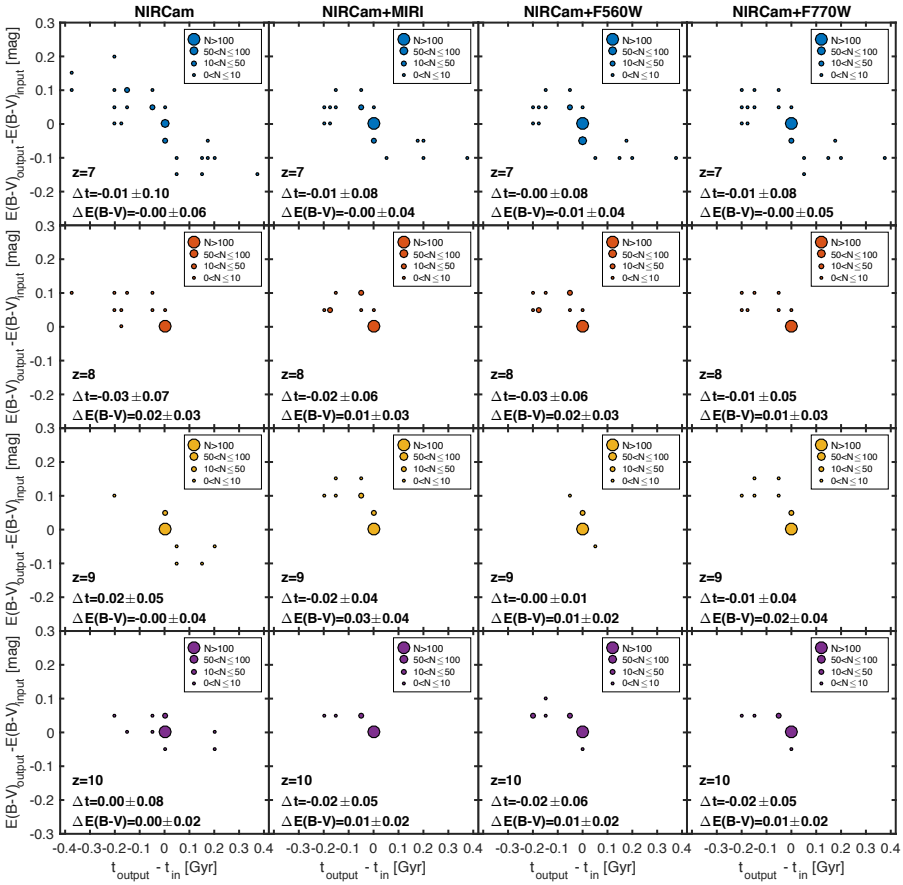


**Figure 5.6:** Difference between the derived age and the fiducial one, $t_{output} - t_{fiducial}$, against the difference between the derived colour excess and the fiducial one, E(B-V)$_{output}$-E(B-V)$_{fiducial}$, for galaxies simulated with BC03 templates at different fixed redshifts. *From top to bottom*: redshifts $z = 7, 8, 9,$ and 10. Ages in each column are obtained with different combinations of bands. *From left to right:* 8 NIRCam broad bands; 8 NIRCam broad bands, MIRI F560W and MIRI F770W; 8 NIRCam broad bands and MIRI F560W only; 8 NIRCam broad bands and MIRI F770W only. Galaxies are divided into bins of 25 Myr in age and 0.025 mag in colour excess and the size of each circle represents the number of galaxies inside each bin. The size of the dots increases with the number of galaxies inside the respective bin. Mean and r.m.s. values of the age and the colour excess estimation are shown at the bottom-left of each panel.

the other redshifts, while the number of outliers decreases at all redshifts and in particular at $z = 7$ and 10, where it is reduced to less than half. At $z = 9$, the r.m.s. slightly increases, because of a single galaxy for which the colour excess is highly overestimated (0.04 mag), otherwise, without this outlier, it would remain unchanged with respect to the value derived with only NIRCam broad-bands. When considering the age estimation, the r.m.s. values became 0.01 Gyr at all redshifts, decreasing the values derived with only 8 NIRCam bands, except at $z = 7$ where it remains 0.2 Gyr. The number of outliers decreases from 13-25$\%$, when considering only NIRCam bands, to $\sim 10\%$, with both MIRI bands. Moreover, there are no galaxies with $|\Delta t|$ >0.1 Gyr at z>8. The two MIRI bands improve age and colour excess estimations similarly, but the F560W decreases the r.m.s. of both the age difference and the colour excess difference a bit more than the other band.

In Figure 5.8, we show the comparison between fiducial and output values, both for age and colour excess, but only for galaxies with emission lines, which are young star-forming galaxies with covering factor $f_{cov} > 0$. The colour excess estimation for galaxies with emission lines does not present significant differences from the full *Yggdrasil* sample, both when considering only 8 NIRCam bands and when adding the two MIRI bands. The same thing happens generally to the age estimation. As for the stellar mass, not all outliers in age and colour excess are galaxies with emission lines.

To conclude, when considering only the 8 NIRCam bands, both the age and the colour excess difference distributions present long tails. Adding the two MIRI bands improves both the age and the colour excess estimation, slightly decreasing the r.m.s. values, but mainly reducing the number of outliers.

### 5.3.3 Specific star formation rates

In this Section we present our results for the sSFR of star-forming galaxies derived both with BC03 templates and with *Yggdrasil* models. As explained later in more detail, in BC03 and *Yggdrasil* SED templates SFR$\propto$M$^*$. So, to decouple stellar mass effects, we consider the sSFR instead of the SFR. Results are shown in figures 5.9-5.10 at four fixed redshift values and for different band combinations. In each case we quote the mean and the r.m.s. values of $\Delta log_{10}(sSFR) = log_{10}(sSFR_{output}) - log_{10}(sSFR_{input})$.

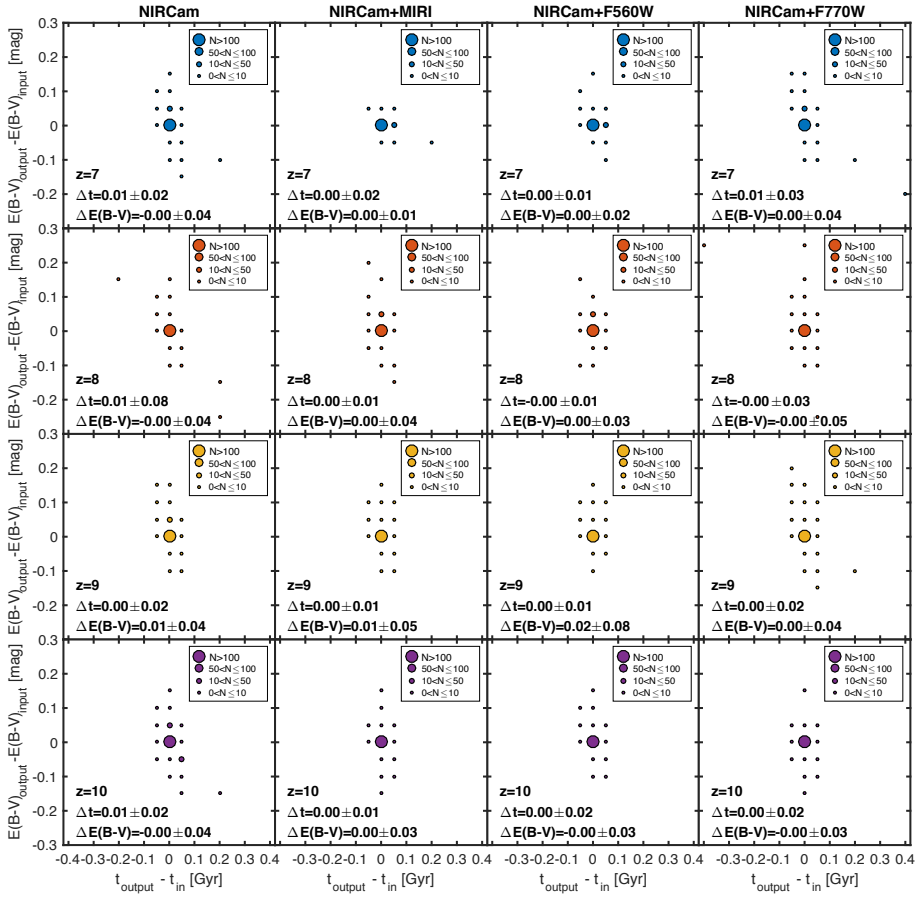


**Figure 5.7:** Difference between the derived age and the fiducial one, $t_{output} - t_{fiducial}$, against the difference between the derived colour excess and the fiducial one, E(B-V)$_{output}$-E(B-V)$_{fiducial}$, for galaxies simulated with *Yggdrasil* templates at different fixed redshifts. *From top to bottom*: redshifts $z = 7, 8, 9,$ and 10. Ages in each column are obtained with different combinations of bands. *From left to right:* 8 NIRCam broad bands; 8 NIRCam broad bands, MIRI F560W and MIRI F770W; 8 NIRCam broad bands and MIRI F560W only; 8 NIRCam broad bands and MIRI F770W only. Galaxies are divided into bins of 25 Myr in age and 0.025 mag in colour excess and the size of each circle represents the number of galaxies inside each bin. The size of the dots increases with the number of galaxies inside the respective bin. Mean and r.m.s. values of the age and the colour excess estimation are shown at the bottom-left of each panel.

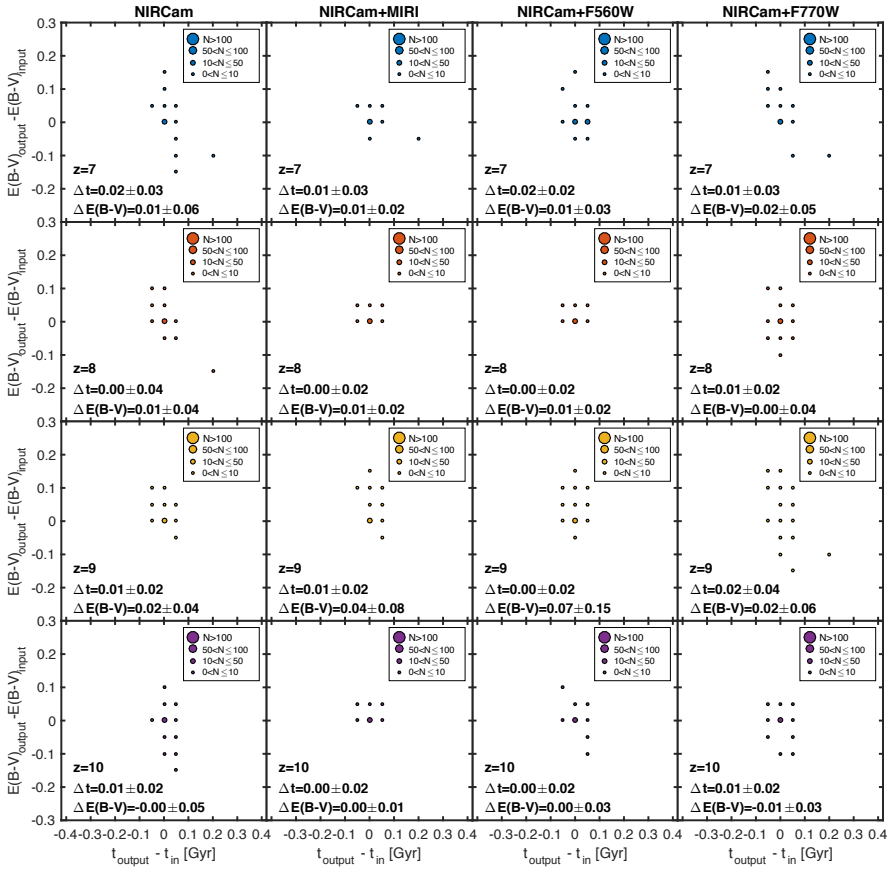


**Figure 5.8:** Difference between the derived age and the fiducial one, $t_{output} - t_{fiducial}$, against the difference between the derived colour excess and the fiducial one, E(B-V)$_{output}$-E(B-V)$_{fiducial}$, for galaxies simulated with *Yggdrasil* templates and emission lines at different fixed redshifts. *From top to bottom*: redshifts $z = 7, 8, 9,$ and 10. Ages in each column are obtained with different combinations of bands. *From left to right:* 8 NIRCam broad bands; 8 NIRCam broad bands, MIRI F560W and MIRI F770W; 8 NIRCam broad bands and MIRI F560W only; 8 NIRCam broad bands and MIRI F770W only. Galaxies are divided into bins of 25 Myr in age and 0.025 mag in colour excess and the size of each circle represents the number of galaxies inside each bin. The size of the dots increases with the number of galaxies inside the respective bin. Mean and r.m.s. values of the age and the colour excess estimation are shown at the bottom-left of each panel.

#### 5.3.3.1 Galaxies simulated with BC03 templates

For BC03 templates, which are characterised by exponentially declining star formation histories, the SFR is derived as:

$$SFR_{out} = \frac{e^{\frac{-t_{out}}{\tau_{out}}}}{\tau_{out}} \frac{M_{out}}{M_0(t_{out}, \tau_{out})} \tag{5.1}$$

where $t_{out}$, $\tau_{out}$, and $M_{out}$ are the derived values for the age, the characteristic time scale of the declining star formation history, and the stellar mass. $M_0$ is the mass of the original BC03 template that is used to normalised each template to one solar mass before the SED fitting and it depends on the age and $\tau$ value of each template. The sSFRs of BC03 templates depend both on the derived age and star formation history, and not on the derived stellar mass, because $sSFR_{out} = SFR_{out}/M_{out}$.

The comparison between the original and derived sSFRs are shown in figure 5.9 for all star-forming galaxies, which correspond to all galaxies with emission lines. Outliers are defined as galaxies with $log_{10}(sSFR_{output}) - log_{10}(sSFR_{fiducial}) > 3\sigma_{log(sSFR)}$, with $\sigma_{log(sSFR)}$ =0.14 dex, which is the minimum $\sigma_{log(sSFR)}$ obtained with all considered filter combinations. All galaxies simulated with BC03 templates are correctly identified as star-forming at each redshift and for all band combinations.

When considering only 8 NIRCam bands, the sSFR difference distribution is broad at z=7 and 10 with $\sigma_{log(sSFR)}$ =0.38 dex and 0.49 dex respectively, and it is narrower at the two intermediate redshifts with $\sigma_{log(sSFR)}$ ∼0.20 dex. Similarly, the number of outliers is high at z=7 and 10, $\sim 34\%$ and 29% respectively, and it decreases at intermediate redshifts to $\sim 15 - 16\%$. The mode is approximately null at z⩾8. On the other hand, the mean is around 0 at z=7 and 10, but the distribution is more asymmetric at the other two redshifts with $< log(sSFR) >$=0.12 dex at z=8 and -0.12 dex at z=9. The sSFR derivation depends on the age estimation, and this is particularly evident at z=7 to 9. In particular, at z=7 the age difference distribution is broad, therefore the sSFR difference distribution has a similar behaviour. At z=8, the age is always correct or underestimated, and so, following Equation 5.2, the sSFR difference is only positive or null, while the opposite happens at z=9. At z=10, the age estimation is better than at z=7, because the decreasing age of the Universe limits the age uncertainties; however, no NIRCam band purely covers rest-frame $\lambda > 4000\,\text{Å}$ at this redshift, and the estimation of the star formation history, therefore the characteristic time $\tau$, becomes challenging, as well as the sSFR estimation.

When adding the two MIRI bands, the sSFR estimation improves at z=7 and, particularly, at z=10, where $\sigma_{log(sSFR)}$ decreases by 0.08 and 0.27 dex, respectively. Similarly, the number of outliers decreases by $\sim 40\%$ at these two redshifts. At z=7, the MIRI bands improve the age estimation and therefore the sSFR difference distribution is narrower than what it seen with only the NIRCam bands. On the other hand, at z=10, the MIRI bands improve the $\tau$ estimation covering $\lambda > 4000\,\text{Å}$, which are otherwise purely observed in none of the NIRCam bands. At z=8, both the r.m.s and the number of outliers are similar to the values derived with only NIRCam bands, but the number of galaxies with $\Delta log_{10}(sSFR) \sim$0 slightly increases. At z=9, both the r.m.s and the number of outliers slightly increase. The age is generally properly estimated at this redshift, but the $\tau$ estimation is very difficult because emission lines are present in all bands at $\lambda > 4000\,\text{Å}$.

When considering the two MIRI bands separately, they have similar influence in the sSFR estimation. However, the F560W band reduces the outlier number slightly more at z=7 to 9 than the other MIRI band, but neither of them decreases the r.m.s. values at all redshifts more than the other.

Overall, with only the 8 NIRCam broad-band filters, the sSFR estimation is good at z=8 and 9. However, it becomes more difficult at z=7, because the age estimation is more uncertain, and at z=10, because no NIRCam band purely covers rest-frame $\lambda > 4000\,\text{Å}$, therefore the $\tau$ estimation is challenging. Adding the two MIRI bands improves the sSFR estimation at z=7 and 10, but not at intermediate redshifts where it is already good.

#### 5.3.3.2 Galaxies simulated with *Yggdrasil* templates

For *Yggdrasil* templates, which are characterised by a step function star formation history, the SFR is derived as:

$$SFR_{out} = \frac{SFR_{constant} M_{out}}{M_0(t_{out}, SFH)} \tag{5.2}$$

where SFR$_{constant}$ has different values depending on the duration of the star formation (0.01,0.03, or 0.1 Gyr), M$_{out}$ is the derived stellar mass, while $M_0$ is the original stellar mass of the template that it used to normalise each template to 1 $M_\odot$ before the SED fitting, which depends on the SFH and the age. Therefore, for *Yggdrasil* templates, the sSFR, defined as $sSFR_{out} = SFR_{out}/M_{out}$, depends mainly on the SFH and only marginally on the age.

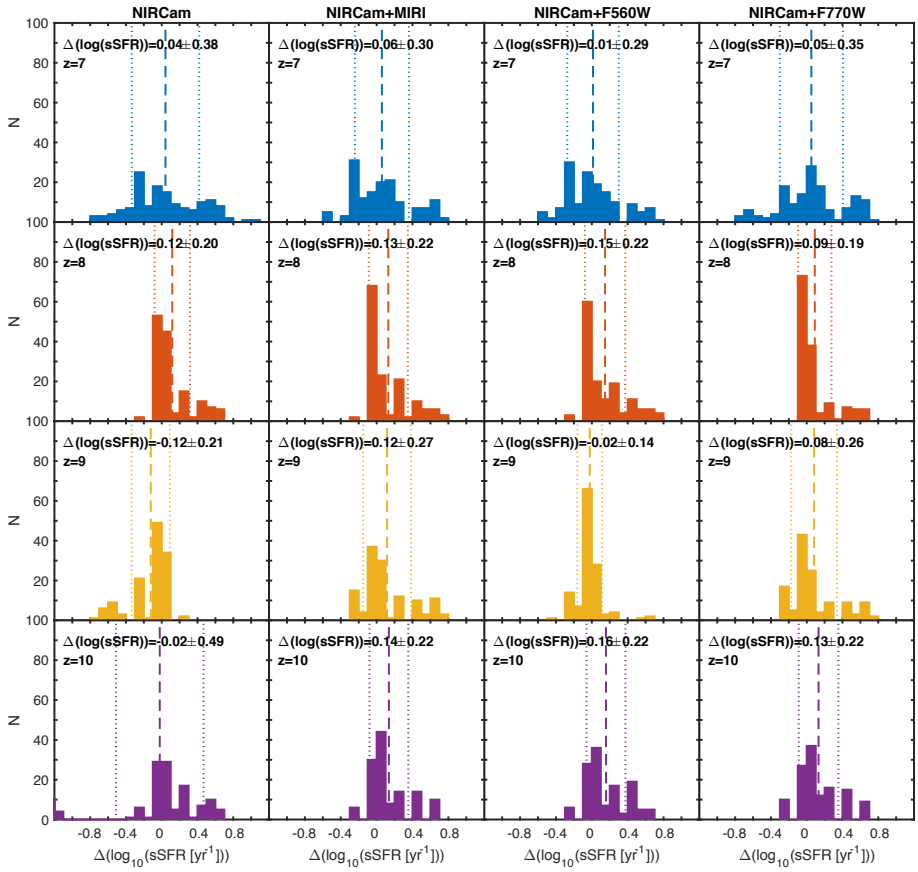


**Figure 5.9:** Differences between the derived and the fiducial sSFR for the BC03 simulated, star-forming galaxies at different fixed redshifts, i.e. $\Delta log_{10}(sSFR) = log_{10}(sSFR_{output}) - log_{10}(sSFR_{fiducial})$. *From top to bottom*: redshifts $z = 7, 8, 9,$ and 10. sSFRs in each column are obtained with different combinations of *JWST* bands. *From left to right:* 8 NIRCam broad bands; 8 NIRCam broad bands, MIRI F560W and MIRI F770W; 8 NIRCam broad bands and MIRI F560W only; 8 NIRCam broad bands and MIRI F770W only. The vertical lines indicate the mean and the 1 $\sigma_{log(sSFR)}$ values, which are quoted at the top-left of each panel.

The comparison between the original and the derived sSFR is shown in Figure 5.10 for all star-forming galaxies. Among *Yggdrasil* templates, there are two types of star-forming galaxies, with and without emission lines, depending on their covering factor. The sSFR depends mainly on the SFH, which has three discrete values, and as a consequence, the

sSFR difference does not show a smooth distribution, but three separated peaks, a central one and two secondary ones, at all redshifts and with all band combinations. Therefore, we defined outliers as galaxies in the two secondary peaks, i.e. $log_{10}(sSFR_{output}) - log_{10}(sSFR_{fiducial}) > 0.2$ dex. Some star-forming galaxies simulated with *Yggdrasil* templates are wrongly identified as quiescent, i.e. instantaneous SFR=0, and their fraction is listed in Table 5.5 for different redshifts and filter combinations.

First, we start our analysis considering only the 8 NIRCam bands. Between 3 and 6% of star-forming galaxies are wrongly identified as quiescent at all redshifts and they are mainly galaxies with $f_{cov}$ =1. This is because the presence of numerous emission lines inside all bands can be misidentified as a higher continuum with no emission lines, i.e. a red quiescent galaxy. The r.m.s value of the sSFR difference distribution is around 0.3 dex up to z=9 and then increases to 0.40 dex at z=10. Similarly, the number of outliers is between 20-25% at z=7 to 9 and increases to 40% at the highest redshift. Outliers are mainly galaxies with $f_{cov}$ =1. Indeed the presence of numerous emission lines inside all bands redward of the 4000 Å break complicates the identification of the continuum and therefore the estimation of the SFH. Similarly, at z=10 no NIRCam band purely covers rest-frame $\lambda > 4000$ Å, and therefore a proper estimation of the SFH history is difficult.

When adding the two MIRI bands, less than 4% of star-forming galaxies are wrongly identified as quiescent, improving the identification with only NIRCam bands at all redshifts, except at z=9. The r.m.s values are ∼0.26-28 at all redshifts, creating a small improvement up to z=9 and a more significant one at z=10. Similarly, the number of outliers is between 15 and 20%, slightly improving at all redshifts, especially at z=10. As noted earlier, the MIRI bands at z=10 can trace $\lambda > 4000$ Å, which improves the SFH estimation and consequently the sSFR derivation.

When considering each MIRI band separately, with F560W the fraction of star-forming galaxies wrongly identified as quiescent is smaller than with F770W. On the other hand, the two bands improve the r.m.s. values and the number of outliers similarly, with no clear preference.

Overall, with observations only with the NIRCam bands, it is possible to correctly estimate the SFH for $\sim 80\%$ of the galaxies up to z=9, but the estimation is more difficult at the highest redshift. Adding the two MIRI bands helps to improve the SFH estimation at all redshifts, especially at z=10.

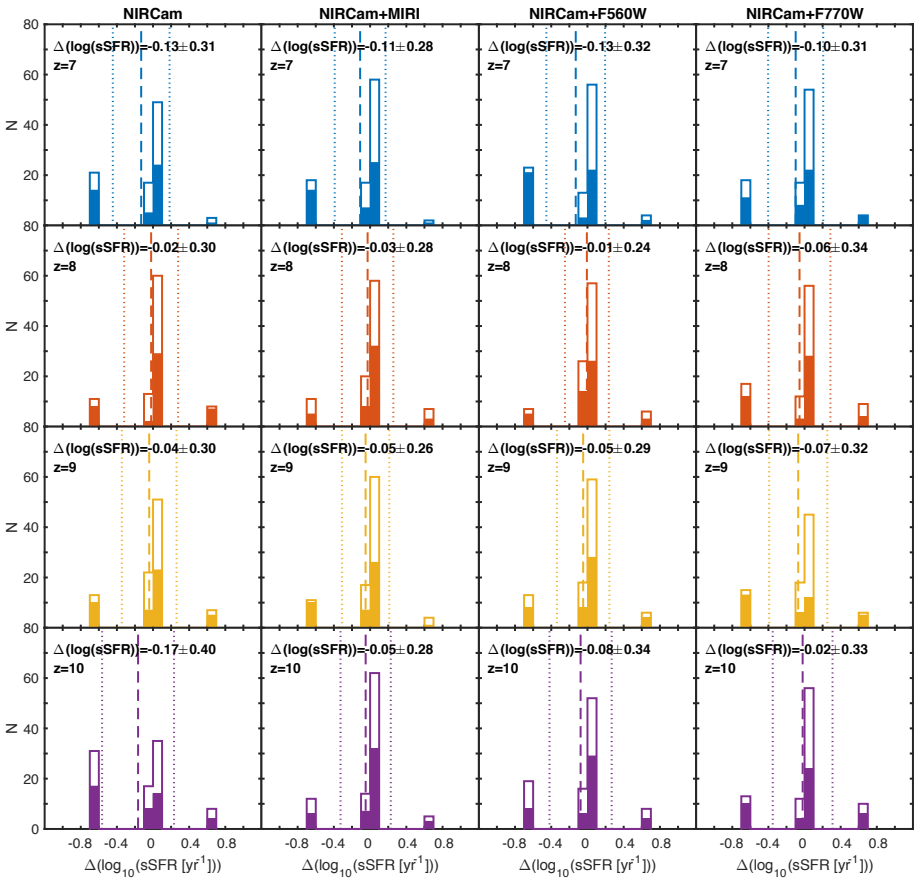


**Figure 5.10:** Differences between the derived and the fiducial sSFR for the *Yggdrasil* simulated, star-forming galaxies at different fixed redshifts, i.e. $\Delta log_{10}(sSFR) = log_{10}(sSFR_{output}) - log_{10}(sSFR_{fiducial})$. *From top to bottom*: redshifts $z = 7, 8, 9$, and 10. sSFRs in each column are obtained with different combinations of *JWST* bands. *From left to right:* 8 NIRCam broad bands; 8 NIRCam broad bands, MIRI F560W and MIRI F770W; 8 NIRCam broad bands and MIRI F560W only; 8 NIRCam broad bands and MIRI F770W only. The vertical lines indicate the mean and the 1 $\sigma_{log(sSFR)}$ values, which are quoted at the top-left of each panel. The coloured histograms represent galaxies with $f_{cov} = 1$, while the open ones represent galaxies with $f_{cov} = 0$.

## 5.4 SUMMARY AND CONCLUSIONS

**Table 5.5:** Number (percentage) of galaxies among the 384 star-forming galaxies, 96 at each redshift, simulated with *Yggdrasil* templates that are wrongly identified as quiescent, for different combinations of *JWST* filter sets and different redshifts. Templates are equally divided between $f_{cov}$ =0 and 1 and the number of misidentified galaxies with $f_{cov}$ =0 is showed in square brackets.

| Bands | $N_{outlier,z=7}$ | $N_{outlier,z=8}$ | $N_{outlier,z=9}$ | $N_{outlier,z=10}$ |
|---|---|---|---|---|
| 8 NIRCam broad bands | 6 [2] (6.5%) | 4 [2] (4.2%) | 3 [0] (3.1%) | 5 [0] (5.2%) |
| 8 NIRCam bands+MIRI F560W, F770W | 1 [0] (1.0%) | 0 [0] (0.0%) | 4 [0] (4.2%) | 3 [3] (3.1%) |
| 8 NIRCam bands+MIRI F560W | 0 [0] (0.0%) | 0 [0] (0.0%) | 4 [0] (4.2%) | 3 [0] (3.1%) |
| 8 NIRCam bands+MIRI F770W | 3 [0] (3.1%) | 2 [1] (2.1%) | 12 [0] (12.5%) | 5 [1] (5.2%) |

In this work we have tested the impact of having data in different *JWST* filter combinations on deriving stellar mass, age, colour excess, and sSFR for a sample of simulated galaxies at $z = 7-10$. In particular, we considered the 8 NIRCam broad-band filters and the two MIRI filters at the shortest wavelengths (F560W and F770W), which are the most sensitive among all MIRI filters and those which will be preferred for high-z galaxy surveys.

Our sample consists of 1542 simulated galaxies from B16, derived from BC03 templates with the manual addition of emission lines for star-forming galaxies (which are the ones with ages lower than the characteristic time $\tau$ of the star formation history) and *Yggdrasil* models. All galaxies in our sample have good photometric redshift estimations, as derived in B16, and therefore uncertainties on the photometric redshifts are not a significant source of error on the galaxy properties estimations performed here. The sample contains the typical SED types of the galaxies that will be observed in *JWST* NIRCam and MIRI high-z blank surveys, to test potential problems on deriving galaxy properties. Therefore, the used sample does not try to emulate the real distribution of galaxies at high redshift.

Our main results are:

- For galaxies with conventional SED types (i.e. BC03 templates), with the presence of at most some prominent emission lines, stellar masses can be well recovered with NIRCam broad-band data alone up to $z = 9$, provided that these data have sufficiently high S/N values ($> 10$). At $z = 10$, no NIRCam filter purely covers the rest-frame at $\lambda > 4000$ Å, and therefore the stellar mass estimation is more difficult, resulting in 31.1% of $3\sigma_{logM^*}$ outliers. For the same reason, the MIRI bands have an important role in improving the mass estimation at this redshift, reducing the number of outliers to $\sim 13\%$.

• When templates with rest-frame equivalent widths that evolve with redshift are considered, it is preferable to derive stellar masses in two steps, to avoid the code to use a template with rest-frame equivalent widths corresponding to a different redshifts. First, one should derive the photometric redshift, which is virtually unaffected by this problem, and after that, derive the stellar mass at the fixed obtained redshift.

• For galaxies with nebular continuum and emission, the stellar mass is generally overestimated when considering only NIRCam broad-band observations. The incorporation of MIRI bands is fundamental for proper stellar mass recovery, except at $z = 9$, where the stellar mass recovery remains challenging. The reasons are that, first, the number of NIRCam bands at $\lambda > 4000\,\text{Å}$ decreases with redshift, and second, emission lines contaminate these bands. In particular, at $z = 9$, emission lines are inside all NIRCam and MIRI bands at $\lambda > 4000\,\text{Å}$, and it is not possible to set the level of the continuum, making the mass estimation challenging.

• The NIRCam broad-band filters are sufficient to recover galaxy age for $> 64\%$ of the sample within 0.03 Gyr, and to recover the colour excess for $> 70\%$ of the sample within 0.06 mag. However, extreme outliers are present at all redshifts, particularly at $z < 9$. Indeed, at higher redshifts, thanks to the decreasing age of the Universe, the age-dust degeneracy is reduced.

• The two MIRI bands improve both the age estimation and the colour excess estimation, slightly decreasing the r.m.s. values, but mainly reducing the number of outliers.

• With observations in the 8 NIRCam broad-band filters, the sSFR estimation is challenging at z=10, where no NIRCam band purely covers the rest-frame at $\lambda > 4000\,\text{Å}$, so adding MIRI observations improves the sSFR derivation. At lower redshifts, NIRCam alone is generally sufficient to recover the sSFR for $\sim 70 - 80\%$ of star-forming galaxies within 0.4 dex.

The results presented in this chapter are a useful reference for the design of deep imaging surveys with *JWST* and to understand in which situations the time investment in MIRI observations is necessary to recover galaxy properties, i.e. stellar masses at the highest redshift. Indeed, for the majority of $7 \leqslant z \leqslant 9$ galaxies, it is possible to estimate the stellar mass, sSFR, age, and colour excess at all redshifts just using 8 NIRCam bands. However, adding the MIRI bands, both F560W and F770W, helps to improve the estimation of these quantities, and it is essential to recover the stellar mass and the sSFR of galaxies at z$= 10$. On the other hand, determining the stellar masses of young star-forming galaxies with emission lines ($f_{cov} > 0$) remains challenging at any redshift. Overall, it will be

necessary to observe with both cameras to perform an accurate study of galaxy evolution and mass assembly since early cosmic times.

*Acknowledgements:* LB and KIC acknowledge the support of the Nederlandse Onderzoekschool voor de Astronomie (NOVA). KIC also acknowledges funding from the European Research Council through the award of the Consolidator Grant ID 681627-BUILDUP. OLF acknowledges funding from the European Research Council Advanced Grant ID 268107-EARLY. PGP-G acknowledges support from the Spanish Government MINECO Grants AYA2012-31277 and AYA2015-70815-ERC. LC acknowledges support from the Spanish Government MINECO Grants AAYA2012-32295.

## Appendix 5.A INCREASING STAR FORMATION HISTORIES

Recent simulations of the high-redshift Universe predict that galaxies at z>6 have star formation rates that on average increase with time (Finlator et al., 2011; Jaacks et al., 2012; Zackrisson et al., 2017). Following these predictions, we test the stellar mass derivation for a set of templates with a single increasing SFH. In particular, we consider a BC03 template with a delayed star formation history with a $\tau$ value of 1 Gyr, for which the SFR increases up to 1 Gyr and then exponentially declines. We consider solar metallicity and the same extinction and age values used for the other BC03 templates. In particular, all ages used are below 1 Gyr so all templates analysed in this appendix have rising SFH. We manually add emission lines as done for the other BC03 templates. We derive mock photometry for the JWST bands and the output parameters, fixing the redshift, as described in this Chapter for the other BC03 SED templates.

The distribution of the difference between the derived stellar mass and the fiducial ones is shown in Figure 5.11. With only 8 NIRCam bands the stellar mass estimation is good at z=8-9, while the r.m.s. is 0.11 at the other redshifts. Adding the two MIRI bands mainly improves the stellar mass estimation at z=10, which is otherwise generally underestimated with only 8 NIRCam bands. The F560W generally improves more the stellar mass recovery respect to the F770W.

This simple test does not take into account possible degeneracies among delayed star formation histories with different $\tau$ values or different metallicities. However, as for the other BC03 templates with emission lines, the stellar masses are generally correctly derived with 8 NIRCam bands at

z=7-9 and the inclusion of MIRI bands is necessary to improve the recovery of the stellar mass at z=10.

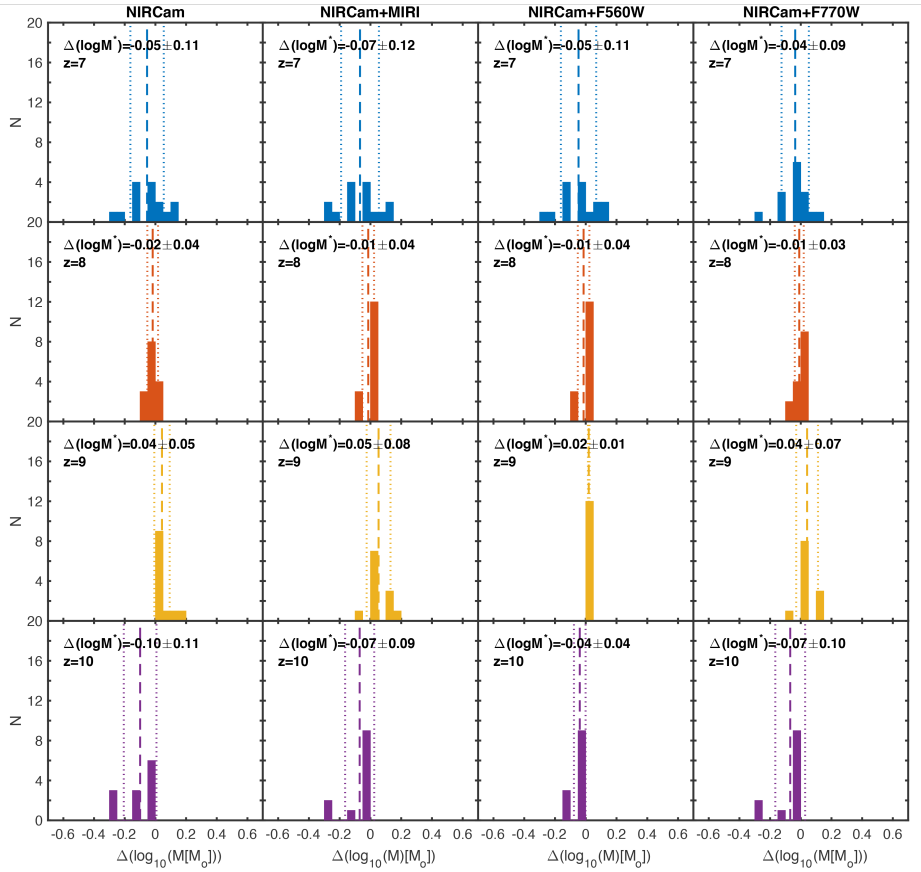


**Figure 5.11:** Differences between the derived and the fiducial stellar mass for the BC03 simulated galaxies with delayed SFH at different fixed redshifts, i.e. $\Delta log_{10}(M^*) = log_{10}(M^*_{output}) - log_{10}(M^*_{fiducial})$. *From top to bottom*: redshifts $z = 7, 8, 9,$ and 10. Stellar masses in each column are obtained with different combinations of *JWST* bands. *From left to right:* 8 NIRCam broad bands; 8 NIRCam broad bands, MIRI F560W and MIRI F770W; 8 NIRCam broad bands and MIRI F560W only; 8 NIRCam broad bands and MIRI F770W only. The vertical lines indicate the mean and the 1 $\sigma_{logM^*}$ values, which are quoted at the top-left of each panel.

# 6. Analysis of the SFR - $M^*$ plane at z<3: single fitting versus multi-Gaussian decomposition

*L. Bisigello, K. I. Caputi, N. Grogin, A. Koekemoer*
*submitted to A&A*

*The analysis of galaxies on the SFR-$M^*$ plane is a powerful diagnostic for galaxy evolution at different cosmic times. We consider a sample of 24463 galaxies from the CANDELS/GOODS-S survey to conduct a detailed analysis of the SFR-$M^*$ relation at redshifts 0.5$\leqslant z <$3 over more than three dex in stellar mass. To obtain SFR estimates, we utilise mid- and far-IR photometry when available, and rest-frame UV fluxes for all the other galaxies. We perform our analysis in different redshift bins, with two different methods: 1) a linear regression fitting of all star-forming galaxies, defined as those with specific star formation rates $\log_{10}(\mathrm{sSFR}/\mathrm{yr}^{-1}) > -9.8$, similarly to what is typically done in the literature; 2) a multi-Gaussian decomposition to identify the galaxy main sequence (MS), the starburst sequence and the quenched galaxy cloud. We find that the MS slope becomes flatter when higher stellar mass cuts are adopted, and that the apparent slope change observed at high masses depends on the SFR estimation method. In addition, the multi-Gaussian decomposition reveals the presence of a starburst population, which increases towards low stellar masses and high redshifts. We find that starbursts make $\sim 5\%$ of all galaxies at $z = 0.5 - 1.0$, while they account for $\sim 14\%$ of galaxies at $1 < z < 3$ with $\log_{10}(M^*)$ =8.25-11.25 $M_\odot$. In conclusion, the dissection of the SFR-$M^*$ in multiple components over a wide range of stellar masses is necessary to understand the importance of the different modes of star formation through cosmic time.*

## 6.1 INTRODUCTION

The majority of star-forming (SF) galaxies follow quite a tight relation between stellar mass (M*) and star formation rate (SFR) (Noeske et al., 2007; Brinchmann et al., 2004), the so-called main sequence (MS), up to high redshifts (Whitaker et al., 2012; Steinhardt et al., 2014; Tasca et al., 2015). This relation is a key point to understand the evolution of galaxies and the interplay between secular effects, like gas depletion and gas infall, and more stochastic effects, such as mergers (Peng et al., 2014; Tacchella et al., 2016). For this reason, in the last decade, several works have been devoted to study this relation and its evolution with redshift (Oliver et al., 2010; Karim et al., 2011; Rodighiero et al., 2011; Whitaker et al., 2014; Johnston et al., 2015; Shivaei et al., 2015; Kurczynski et al., 2016).

In spite of this wide range of studies, a general consensus on the MS slope and its evolution with redshift has not been reached. This is because different sample selections, SFR derivations and fitting techniques influence the derived MS making the comparison between different works difficult. For example, as explained by Speagle et al. (2014), the MS derived using criteria that select blue, highly star-forming and not-dusty galaxies will be steeper than the MS derived with other selection mechanisms. Ideally, having no pre-selection of the star-forming population, by using colours or a specific star formation rate (sSFR) cut, would seem the right approach to avoid influencing the derived MS slope. However, a sample with no pre-selection of SF galaxies could be contaminated by quenched galaxies, particularly at high stellar masses, producing a flatter MS than that derived from samples containing only SF galaxies.

To have a MS that does not require pre-selection and is not contaminated by quenched galaxies, Renzini & Peng (2015) defined the MS as the ridge line in the SFR-stellar mass-number density 3D distribution surface. With this definition they could clearly distinguish between SF galaxies in the MS and quenched galaxies below the MS at redshift $z\sim0.05$, without influencing the slope of the derived MS.

As discussed exhaustively by Calzetti (2013), different SFR indicators are used across the wavelength spectrum, including X-ray, ultra-violet (UV), optical, infrared (IR), radio, and emission lines, based on direct stellar light, dust-processed light or ionised gas emission. SFR derived from the UV light has been largely used because it is dominated by the light of very young stars, and therefore is optimal to trace recent SF. Moreover, it is possible to derive the SFR in a wide range of redshifts observing the rest-frame UV redshifted to optical wavelengths. However, the presence of dust obscuring the UV light makes the derived SFR uncertain.

After the launches of the *Spitzer Space Telescope* and *Herschel Space Telescope*, observations at IR wavelengths started to be used more commonly to derive SFR, particularly for dusty galaxies. However, it is not possible to obtain IR data for large galaxy samples, and IR observations are less sensitive and have a smaller angular resolution than UV-optical observations. Moreover, several observations in the IR are necessary to reconstruct the IR spectral energy distribution (SED) at 3-1000 $\mu$m and therefore $L_{IR}$, which is then linked to the SFR. A series of relation between monochromatic IR luminosities and total IR luminosities have been derived during the last years (e.g. Chary & Elbaz, 2001; Bavouzet et al., 2008; Rieke et al., 2009). However, these relations were obtained from different samples, at different redshift ranges and using different monochromatic IR luminosities, and therefore the derived MS could be influenced by the relation used to convert from monochromatic IR luminosities and $L_{IR}$.

The aim of this work is to analyse the $SFR - M^*$ plane from z=0.5 to z=3, by comparing the traditional MS derivation method, after pre-selecting the SF galaxies with sSFR cut, with the ridge line definition from Renzini & Peng 2015, obtained by fitting three Gaussian components to the sSFR distribution. In addition, we also analysed the effect of different $SFR_{IR}$ derivation methods on the bright-end of the MS.

The structure of the chapter is as follows. In Section 6.2 we present our sample selection, while in Section 6.3 we describe the derivation of photometric redshifts and stellar masses by SED fitting. In Section 6.4 we report the different used methods to derive SFR, from the UV and from the IR. In Section 6.5 we analyse the sources on the $SFR - M^*$ plane, while in Section 6.6 we summarise our main findings and conclusions. Throughout this chapter, we adopted an $H_0$ =70 kms$^{-1}$Mpc$^{-1}$, $\Omega_M$ =0.27, $\Omega_\Lambda$ =0.73 cosmology and a Salpeter (1955) initial mass function over (0.1-100) $M_\odot$.

## 6.2 SAMPLE SELECTION

### 6.2.1 Data

The GOODS-S field (Giavalisco et al. 2004) has been targeted with deep observations at different wavelengths over more than a decade. It is centred at $\alpha$(J2000)=$3^h32^m20^s$ and $\delta$(J2000)=$-27^\circ48''20^s$ and covers an area of approximately $10' \times 16'$. In this study, we collect datasets in this field from the UV to the mid-IR, from both ground-based and space telescopes.

In particular, in the optical and near-IR, the GOODS-S field has been observed with the *Hubble Space Telescope* (*HST*), the Very Large Telescope (VLT) and *Spitzer* as part of the CANDELS survey (Grogin et al., 2011;

Koekemoer et al., 2011). In this work, we use the CANDELS GOODS-S multi-wavelength photometric catalogue (Guo et al., 2013) that includes 17 bands: U Blanco/CTIO, U VLT/VIMOS, F435W, F606W, F775W, F814W and F850LP HST/ACS, F098M, F105W, F125W and F160W HST/WFC3, $K_s$ VLT/ISAAC, $K_s$ VLT/HAWK-I (Fontana et al., 2014) and 3.6, 4.5, 5.8 and 8.0 $\mu$m Spitzer/IRAC (Ashby et al., 2015). The sources of this catalogue are detected in the F160W band and we correct all fluxes for galactic extinction.

The HAWK-I K band data available in the Guo et al. (2013) catalogue do not cover the full GOODS-S field, therefore we complement these observations with other K VLT/HAWK-I observations (P.I. N.Padilla) that are shallower than the observations in the Guo et al. (2013) catalogue in the same band but cover the full field. To extract photometry in this band, we run SExtractor (Bertin & Arnouts, 1996) using a 1.5$\sigma$ threshold over 4 contiguous pixels and an aperture of 3″. A low detection threshold is used to find a counterpart for all secure detections at 1.6$\mu$m. We correct the 3″ fluxes to total fluxes and ensure no offset with respect to Guo et al. (2013).

The GOODS-S field has been observed also at mid- and far-IR wavelengths. In particular, we include in our data set observations taken with the Multiband Imaging Photometer (MIPS; Rieke et al., 2004) on *Spitzer* at $24\,\mu$m and observations done by the Photodetector Array Camera and Spectrometer (PACS; Poglitsch et al., 2010) on *Herschel* (Pilbratt et al., 2010) at 70$\mu$m, 100$\mu$m and 160$\mu$m as part of the PACS (Poglitsch et al., 2010) *Evolutionary Probe* (PEP, Lutz et al. 2011) and GOODS-*Herschel* (Elbaz et al., 2011) programs.

### 6.2.2 Sample selection and counterpart identifications

Our main catalogue consists of 34930 galaxies that are part of the CANDELS catalogue and are detected in the F160W band, with the addition of HAWK-I K band observations that cover the full GOODS-S sample and observations in the mid- and far-IR with *Spitzer* and *Herschel*.

First, we cross-match the CANDELS catalogue with the wide HAWK-I/K band observations with a 1″ search radius. When more than one counterpart is present in the K-band ($\sim 7\%$ of the catalogue), mainly because of the low threshold used for the source extraction in this band, we consider the brightest K band source as a counterpart, which is usually also the closest one.

For the *Spitzer*/MIPS $24\,\mu$m catalogue we consider only sources brighter than 80 $\mu$Jy, for which the catalogue completeness is $\sim 80\%$ and the spurious sources are less than $10\%$ (e.g. Papovich et al., 2004). To

identify the optical counterpart of each $24\,\mu$m-detected source, we match the MIPS catalogue and the CANDELS+HAWK-I/K catalogue using a $2''$ searching radius respect to the HAWK-I/K source positions. Among the initial $24\,\mu$m-detected galaxies, 733 ($98\%$) have an optical-IR counterpart. The remaining 8 objects, detected at $24\,\mu$m, do not have any CANDELS counterpart within $2''$. However, visual analysis of these sources shows that they could be associated with extended sources or multiple objects around the MIPS detection. We do not consider $24\,\mu$m fluxes when multiple optical counterparts are associated with the same $24\,\mu$m source. To conclude, 644 sources have photometry also at $24\,\mu$m, corresponding to the $88\%$ of the total MIPS catalogue and $\sim 2\%$ of the total CANDELS catalogue.

At far-IR wavelengths, Magnelli et al. 2013 derived two different catalogues from PEP observations: in one of them, sources are extracted blindly in the three bands and then they are matched with a $24\,\mu$m-detected source catalogue; in the other one, sources are extracted using the $24\,\mu$m source positions as prior. We match our catalogue with both PEP catalogues with a radius of $1''$ by comparing the $24\,\mu$m positions. Around $90\%$ (585) of objects detected at $24\,\mu$m are also detected at least in one of the 3 PEP bands, in particular $\sim 50\%$ of the $24\,\mu$m sources are detected at 70 $\mu$m, $86\%$ at 100 $\mu$m and $78\%$ at 160 $\mu$m.

## 6.3 PHOTOMETRIC REDSHIFTS AND STELLAR MASSES

Our catalogue is different, in the optical and near-IR, from the Guo et al. (2013) catalogue due to the presence of the HAWKI-K band observations which covers the full field. For this reason we derive both the photometric redshift and stellar mass using our own catalogue. In particular, to obtain these quantities, we run the code *LePhare* (Arnouts et al., 1999; Ilbert et al., 2006) to obtain the best SED templates based on a $\chi^2$ fitting procedure. We use Bruzual & Charlot (2003) templates with solar metallicity, a range of exponentially declining star formation histories with different characteristic time scales $\tau$ from 0.1 to 10 Gyr, and ages ranging from 0.05 to 13.5 Gyr. We allow for redshift between 0 and 6, we apply the Calzetti et al. reddening law (Calzetti et al., 2000) for the galactic extinction with $A_V$ values from 0 to 4 and we also allow *LePhare* to include nebular emission. We fit models by using all the optical bands and the two shortest-wavelength IRAC bands, because the two longest-wavelength bands have a lower S/N than the shortest-wavelength bands and they could be contaminated by polycyclic aromatic hydrocarbon (PAH) emissions at low redshift.

We compare our photometric redshifts with spectroscopic redshifts available in the literature in the GOODS-S field. We use secure spectroscopic redshifts ($z_{spec}$) present in the ESO public compilation in the Chandra Deep Field South (CDFS; Cristiani et al., 2000; Croom et al., 2001; Bunker et al., 2003; Dickinson et al., 2004; Stanway et al., 2004b,a; Strolger et al., 2004; Szokoly et al., 2004; van der Wel et al., 2004; Doherty et al., 2005; Le Fèvre et al., 2005; Mignoli et al., 2005; Ravikumar et al., 2007; Popesso et al., 2009; Balestra et al., 2010; Silverman et al., 2010; Kurk, J. et al., 2013; Vanzella et al., 2008) and spectroscopic redshifts from Morris et al. 2015, for a total of 2635 matches in the CANDELS catalogue. The deviation of our photometric redshifts from the spectroscopic ones is $\delta z = |z_{phot} - z_{spec}|/(1+z_{spec}) = 0.039 \pm 0.032$ for the full sample, excluding outliers with $\delta z > 0.15$ that correspond to $\sim 11\%$ of the sample (Fig. 6.1).

We divide our sample in three redshift bins, in order to study the position of galaxies on the SFR-M* plane: $0.5 \leqslant z < 1$, $1 \leqslant z < 2$, and $2 \leqslant z < 3$. In these three redshift bins there are 6881, 9578, and 8004, respectively, making a total of 24463 galaxies.

### 6.3.1 Stellar mass completeness

In order to calculate the stellar mass completeness of our sample, we follow the empirical approach presented in Schreiber et al. (2015). In particular, the CANDELS sample is selected at 1.6 $\mu$m, where the light-to-mass ratio is quite stable. Indeed, a tight relation is present between the stellar mass and the observed luminosity at 1.6 $\mu$m that can be described as a power-law plus a Gaussian scatter in the log space. We derive this relation and the related scatter directly from the data in different redshift bins. At each redshift bin, it is possible to derive the $3\sigma$ limit for the $L_{1.6\mu m/(1+z)}$ from the $3\sigma$ detection limit in the F160W band. Then, we randomly extract points inside the Gaussian scatter of this relation in a wide range of stellar masses and luminosities and we derive the percentages of galaxies above the $3\sigma$ detection limit in each 0.1 dex stellar mass bin. The 90% completeness limits are at $\log_{10}(M^*/M_\odot)$=7.35, 7.95, and 8.25 at $0.5 < z \leqslant 1$, $1 < z \leqslant 2$, and $2 < z \leqslant 3$, respectively.

## 6.4 STAR FORMATION RATES

For the full CANDELS sample, we derive the SFR from the rest-frame UV continuum flux corrected for dust extinction using the Calzetti et al. (2000) reddening law and the $A_v$ value derived from the SED fitting. Depending

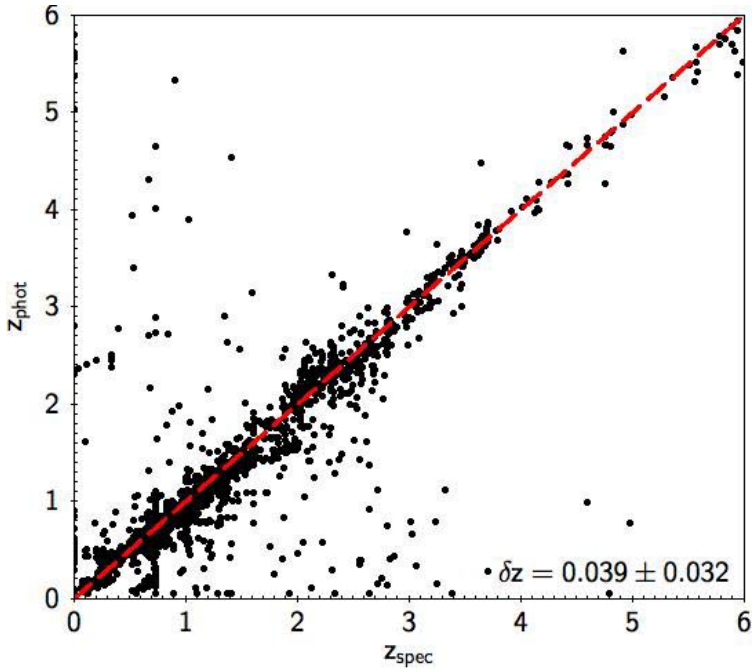


**Figure 6.1:** Comparison between photometric redshifts derived in this work and spectroscopic redshifts presented in the literature (Cristiani et al., 2000; Croom et al., 2001; Bunker et al., 2003; Dickinson et al., 2004; Stanway et al., 2004b,a; Strolger et al., 2004; Szokoly et al., 2004; van der Wel et al., 2004; Doherty et al., 2005; Le Fèvre et al., 2005; Mignoli et al., 2005; Ravikumar et al., 2007; Popesso et al., 2009; Balestra et al., 2010; Silverman et al., 2010; Kurk, J. et al., 2013; Vanzella et al., 2008; Morris et al., 2015). The deviation is $\delta z = |z_{phot} - z_{spec}|/(1+z_{spec}) = 0.039 \pm 0.032$, excluding the $11\%$ of outliers with $\delta z > 0.15$.

on the considered redshift, we use observed fluxes in the U-band, F435W, F606W or F775W band. These UV fluxes are converted then to SFR using the relation derived by Kennicutt (1998):

$$SFR[M_{\odot}yr^{-1}] = 1.4 \times 10^{-28} L_{\nu}[ergs\ s^{-1}Hz^{-1}] \quad (6.1)$$

For the subsample of galaxies detected at $24\,\mu$m, we also derive the SFR from the dust-processed stellar light in the IR. In particular, the total IR luminosity from 3 to 1000 $\mu$m is related to the SFR, as it was found by Kennicutt (1998):

$$SFR[M_{\odot}yr^{-1}] = \frac{L_{FIR}[L_{\odot}]}{5.8 \times 10^{9}} \quad (6.2)$$

However, in general, we do not observe directly the total IR luminosity and several methods are presented in the literature to estimate this total luminosity from a monochromatic luminosity. In this work, we consider 5 different methods to derive the total IR luminosity:

- the relation by Chary & Elbaz (2001) between IR and monochromatic luminosities, using the observed $24\,\mu$m flux;
- the relation by Bavouzet et al. (2008) between IR and monochromatic luminosities, using the observed flux at $24\,\mu$m;
- the relation by Bavouzet et al. (2008) between IR and monochromatic luminosities, using the observed flux at 70 $\mu$m;
- the relation by Rieke et al. (2009) between IR total luminosity and observed flux at $24\,\mu$m;
- a direct fit to the available IR observations, from $24\,\mu$m to 160 $\mu$m, by using IR templates presented in Rieke et al. (2009).

When analysing the impact of IR observations on the SFR-M* plane, we consider only SFR derived from the IR, as the UV SFR contribution to the total SFR is minor for the majority of $24\,\mu$m detected galaxies (Caputi et al., 2008). When IR observations are not available, we consider SFR derived from the UV corrected for dust-extinction.

### 6.4.1 K-corrections

Every method explained in the previous paragraph converts a monochromatic luminosity at a reference wavelength into total IR luminosity. Because the IR observations are available in specific bands, which do not always correspond to the one used in the previously mentioned relations, we need to apply a k-correction to obtain the luminosity at the reference wavelength used in each method. We start from models of pure starburst galaxies (Rieke et al., 2009) that have IR luminosities from $10^{9.75}$ to $10^{13}$

$L_\odot$. We convolve each model with the $24\,\mu$m, 70$\mu$m, 100$\mu$m and 170$\mu$m filters. Then we calculate the k-correction by dividing the observed flux by the flux at the reference wavelength. We use this ratio to calculate the total IR luminosity and we compare it with the one associated with the used template. We iterate the process until the output IR luminosity corresponds to the IR luminosity of the used model.

### 6.4.2 IR luminosity derivation

We derive the total IR luminosities by using four different relations between monochromatic and total IR luminosities and, independently, by fitting SED models to the observed fluxes at $24\,\mu$m, 70 $\mu$m, 100 $\mu$m and 160 $\mu$m.

1. Chary & Elbaz (2001, here after C&E) studied different samples of nearby galaxies and for galaxies with $L_{IR} > 10^{10}$ $L_\odot$ they derived three relations between total IR luminosity and monochromatic luminosity at 6.7 $\mu$m, 12 $\mu$m and 15$\mu$m:

$$L_{IR} = \begin{cases} 11.1^{+5.5}_{-3.7} \times L^{0.998}_{15\mu m} & : z \leqslant 0.8 \\ 0.89^{+0.38}_{-0.27} \times L^{1.094}_{12\mu m} & : 0.8 > z \leqslant 1.6 \\ 4.37^{+2.35}_{-2.13} 10^{-6} \times L^{1.62}_{6.7\mu m} & : z > 1.6 \end{cases} \tag{6.3}$$

   Close to each relation we show the redshift range in which we implement it, in order to apply the smallest k-correction to covert from the observed flux at $24\mu$m to the flux at the wavelength considered in each relation.

2. In Bavouzet et al. (2008), the total IR luminosity is related to the monochromatic luminosity at 8, 24 and 70 $\mu$m by:

$$L_{IR} = \begin{cases} 377.9 \times L^{0.83}_{8\mu m} \\ 6856 \times L^{0.71}_{24\mu m} \\ 7.90 \times L^{0.94}_{70\mu m} \end{cases} \tag{6.4}$$

   In this case we use observations at $24\,\mu$m (here after Ba24) and 70 $\mu$m (here after Ba70), when available. In order to apply the smallest k-correction possible, in Ba24, we use the first relation at z>0.5 and the second one for closer objects. Similarly, in Ba70, we use the third relation at z$\leqslant$0.5, the second one at 0.5<z$\leqslant$5 and the first one otherwise.

3. In Rieke et al. (2009) (here after Ri09), the SFR is related directly to the $24\,\mu$m observed flux by:

$$log(SFR) = A(z) + B(z)(log(4\pi D_L^2 f_{24,obs}) - 53) \tag{6.5}$$

where $D_L$ is the luminosity distance and values for A and B are listed in the same paper for different redshifts below 3. We do not apply this relation at z>3. We derive IR luminosity for Ri09 by reversing eq. 6.2.

Finally, when at least two observations are present in the IR, we again use the templates from Rieke et al. (2009) to directly fit observations at 24, 70, 100 and 160 $\mu$m using a $\chi^2$ fitting procedure to estimate the best solutions among all templates. However, there is a large scatter on the PAH features strength among different SED templates. In order for our results to not be too dependent by the used SED template, we multiply by two the error bars associated to $24\,\mu$m fluxes, which contained PAH features between z$\sim$0.8 to z$\sim$2.8. We also derive $L_{IR}$ by SED fitting without including observations at $24\,\mu$m, but the difference is less than 20% for the 99% of the sample with observations in at least two bands.

To estimate the errors associated with the IR luminosity for each monochromatic relation, we consider both the propagation of the flux and photometric redshift errors inside each relation and the intrinsic scatter of each relation. The mean errors are 0.28 dex for C&E, 0.26 dex for Ba24, 0.34 dex for Ba70, and 0.37 dex for Ri09. The mean error of Ba70 is higher than the mean error of Ba24, because S/N associated with the flux at 70$\mu$m are generally smaller than the ones at $24\,\mu$m. The Ri09 relation produces larger error bars than the other relations, because the scatter of their relation, as derived in their paper, is larger than the one in the other relations.

On the other hand, to estimate the IR luminosity errors for the SED fitting technique, we analyse the probability distribution, $P(L_{IR}) \propto e^{-\chi^2/2}$, and we derive the full width half maximum associate to this distribution for each galaxy. The mean IR luminosity error associated with the SED fitting method is 0.14 dex.

In Figure 6.2, we show the relation between IR luminosity and photometric redshift for each conversion formulae used to derive the bolometric infrared luminosity $L_{IR}$. The C&E method produces $L_{IR} > 10^{14} L_\odot$ at z>3, that are not present in other methods. The IR luminosities derived with Ba24 and Ba70 have the shallowest increment with redshift among the methods tested here and, in particular, IR luminosities remain below $10^{13} L_\odot$ for the majority of cases. IR luminosities derived fitting the IR photometry are always L< $10^{13} L_\odot$, because this is the maximum luminosity present in the used templates.

In Figure 6.3, we show the comparison between UV, dust-corrected SFR and IR SFR, derived by fitting the IR SED, for the galaxies which have both quantities. The two SFRs are overall consistent, in particular at $0.5 \leqslant z < 1$.

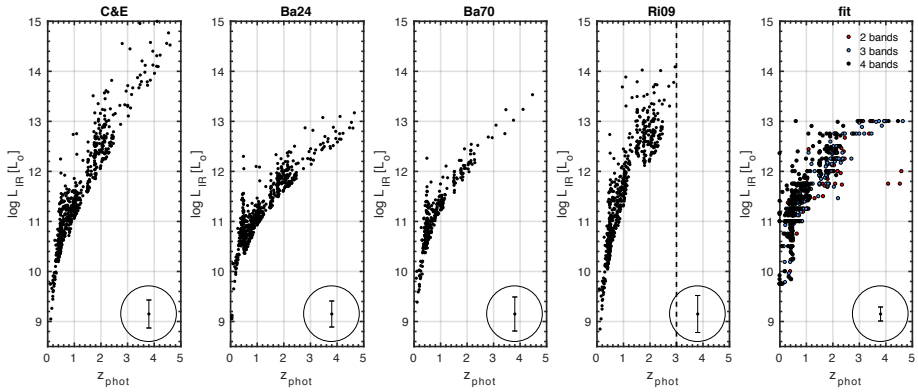


**Figure 6.2:** Photometric redshift compared to the IR luminosity derived using different methods: *From left to right:* C&E, Ba24, Ba70, Ri09 and IR SED fitting. In the fourth panel, the dashed vertical line corresponds to the redshift limit below which the relation to derive IR luminosity is calibrated. In the fifth panel, points are coloured coded depending on the number of bands with detection: (*black*) 4 bands, (*blue*) 3 bands and (*red*) 2 bands. On the bottom part of each plot, the mean error bar associate to each method is shown.

However, the $\text{SFR}_{UV}$ tends to be underestimated at high SFR and redshifts, particularly at $2 \leqslant z < 3$. This comparison is different when comparing the $\text{SFR}_{UV}$ with $\text{SFR}_{IR}$ derived with other methods, but these quantities remain in overall agreement.

## 6.5 ANALYSIS OF SOURCES ON THE $SFR - M^*$ PLANE

We divide our sample in three redshift bins, $0.5 \leqslant z < 1$, $1 \leqslant z < 2$, and $2 \leqslant z < 3$, in order to study the SFR-M* plane and the MS slope at different redshifts. Moreover, we consider two different fitting techniques to derive it.

Firstly, we remove quenched galaxies from our sample selecting only galaxies with $\log_{10}(sSFR) > -9.8$ and we derive the MS by fitting a linear regression using all non-quenched galaxies in each redshift bin. This method is similar to what is usually found in the literature and it allows us to make a direct comparison with previous works.

Secondly, we follow Renzini & Peng (2015) who analysed the three-dimensional SFR-M* relation (SFR vs. stellar mass vs. number of galaxies inside each SFR-M* bin). In this way, they identified two peaks, one for

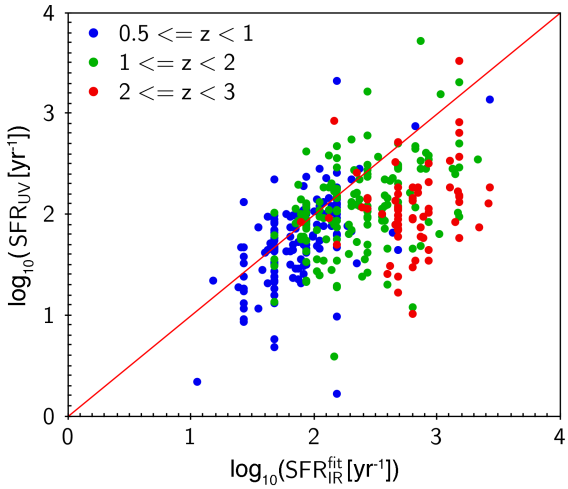


**Figure 6.3:** SFR derived from the fit of the IR SED ($SFR_{IR}^{fit}$) compared to dust-corrected UV SFR, for galaxies which have both quantities. Galaxies are divided in the three redshift bins analysed in this work: $0.5 \leqslant z < 1$ (*blue*), $1 \leqslant z < 2$ (*green*), and $2 \leqslant z < 3$ (*red*).

quenched galaxies and one for MS galaxies, and defined the MS as the ridge line of the MS distribution. This definition has the advantage of not requiring a pre-selection to derive the MS position and, at the same time, is not influenced by the presence of quenched galaxies when deriving the MS. Following their approach, we divide galaxies in stellar mass bins of 0.25 dex and we fit the sSFR distribution inside each stellar mass bin with three different Gaussian distributions, corresponding to the quenched galaxies (QG), the MS galaxies and the starburst galaxies (SB). In Renzini & Peng (2015) the third component (starburst galaxies) was not evident because this population is rare at the low redshifts that they considered ($0.02 < z < 0.085$). We use the sSFR instead of the SFR, because the three components are more clearly separated in the sSFR distribution than in the SFR one. Other studies have analysed the sSFR distribution at different stellar masses (e.g. Ilbert et al., 2015), but they did not model this distribution to separate among SF, quenched and starburst galaxies and derive the MS. Finally, we fit an orthogonal distance regression (ODR) to the derived peak positions of the three Gaussian components in each stellar mass bin, in order to take into account the stellar mass bin size as well as the errors associated with each Gaussian peak position. The sequences derived by using this method are sensitive to the adopted stellar mass bin, however, the results are all consistent.

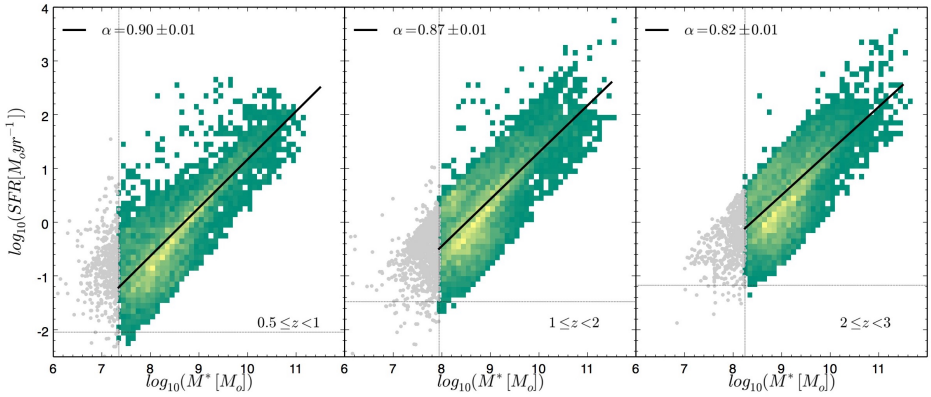


**Figure 6.4:** SFR-M* plane with the best linear fits to all SF galaxies at different redshifts: 0.5$\leqslant z <$1 (*left*), 1$\leqslant z <$2 (*center*) and 2$\leqslant z <$3 (*right*). The slope of each sequence is reported on the top-left of each panel. In the background there are all SF galaxies in our sample above the stellar mass completeness, divided in SFR-M* bins of 0.1×0.1 dex. Each bin is coloured coded depending on the number of galaxies inside each bin, from green to yellow in a linear scale. The vertical black dotted lines are the 90% completeness limit in stellar mass in each redshift bin, galaxies below this limit are plotted as grey points and are not included in the fit. The horizontal dotted black lines are the 3$\sigma$ detection limit in SFR in each redshift bin.

### 6.5.1 Single fitting to $SFR - M^*$ plane

Here we discuss the SFR-M* plane derived using a single linear regression fitting to all SF galaxies, as it commonly found in the literature. In Figure 6.4 we show the linear regression for all SF galaxies, which are selected to have $\log_{10}(sSFR) >$-9.8. The derived slopes are 0.90±0.01, 0.87±0.01, and 0.82±0.01, at 0.5$\leqslant z <$1, 1$\leqslant z <$2, and 2$\leqslant z <$3, respectively.

Figure 6.5 shows the comparison between our derived slopes and some values presented in the literature. The scatter among different methods is very large and our values are within this range. In particular, our values are above the values derived by Speagle et al. (2014), which combine results from numerous previous work, and are more similar to recent values derived by Kurczynski et al. (2016). However, in Speagle et al. (2014) the MS is derived for galaxies with $\log_{10}(M^*) >$9.5, therefore we re-derive the MS in a similar stellar mass range to compare the two works. The derived slopes are 0.74±0.01, 0.67±0.01, and 0.72±0.01 at 0.5$\leqslant z <$1, 1$\leqslant z <$2, and 2$\leqslant z <$3, respectively, which are consistent with the median inter-

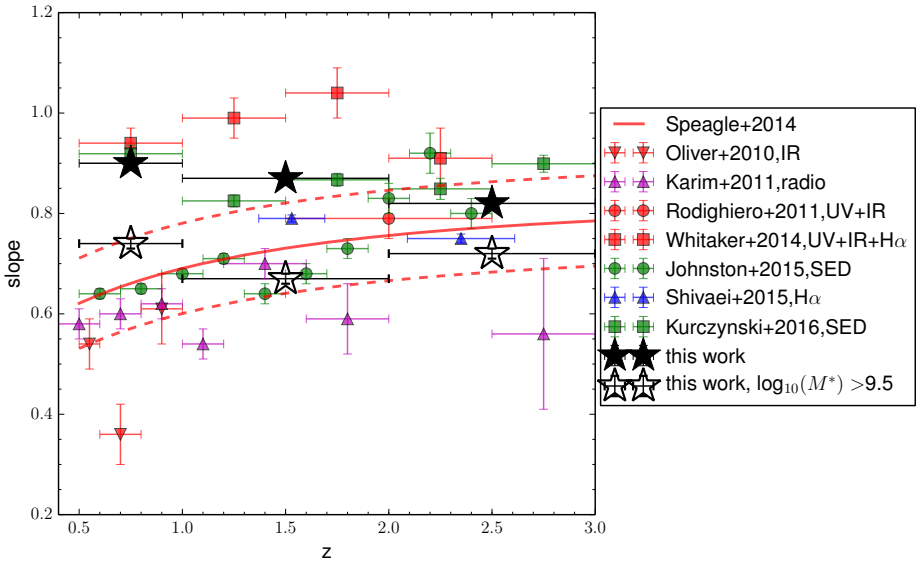


**Figure 6.5:** Comparison between some MS slopes presented in the literature and the slopes derived in this work using all SF galaxies (*black stars*) and only SF galaxies with $\log_{10}(M^*)$ >9.5 (*empty stars*). All other slopes are taken from: Oliver et al. (2010) (*red triangles*), Karim et al. (2011) (*magenta triangles*), Rodighiero et al. (2011) (*red circles*), (Whitaker et al., 2014) (*red squares*), Johnston et al. (2015) (*green circles*), Shivaei et al. (2015) (*blue triangles*) and Kurczynski et al. (2016) (*green squares*). The red continuous line shows the relation derived by Speagle et al. (2014) and the dotted red lines are the median inter-publication scatter around the fit.

publication scatter around the relation found by Speagle et al. (2014). This analysis makes evident to which extent the derived MS slope is influenced by the considered stellar mass range.

When using IR-based SFR for the MS, the MS slopes remain almost unchanged. This is because the fit is dominated by low-intermediate stellar mass galaxies that are the most numerous ones and whose SFR is based on observed UV fluxes.

### 6.5.2 Multi-Gaussian decomposition of the SFR-M* plane

Here we discuss the SFR-M* plane derived separating SB, SF and QG galaxies by fitting the sSFR distribution with three Gaussian components in different stellar mass and redshift bins.

In Figure 6.6 we show the best Gaussian fits of the sSFR distribution for our sample, in the three considered redshift bins and for stellar masses between $\log_{10}(M^*)$ =7.5 and 11.25. We analyse only stellar mass bins with more than 50 galaxies. The three Gaussian components used in the fit, one for each galaxy mode (QG, MS and SB), have different relative positions and relative heights, changing both with stellar masses and redshift. In particular, at high stellar masses the three components are more separated one from the other than at low stellar masses.

Figure 6.7 shows the best ODR fits of each sequence using the Gaussian peak positions, in the three redshift bins. The SB sequence has a slope close to unity up to $\log_{10}(M^*)$ =11. The MS has a slope between 0.93±0.03 and 0.84±0.06, decreasing with the redshift, but a flattening is present at high stellar masses, in particular at z<2. This flattening has been observed previously in other works with different methods (Whitaker et al., 2014; Tomczak et al., 2016) and, because this flattening is present in our data after selecting only SF galaxies, it is not due to contamination by quenched galaxies. However, the inclusion of IR observations influences this flattening, as it is explained in detail in section 6.5.2.2. When fitting only data points with $\log_{10}(M^*)$ <10.25, below the high mass bending, the slope is close to unity at all redshifts and with a mild evolution. In particular, the slopes are =1.02±0.01, 1.06±0.02, and 1.03±0.04, at $0.5 \leqslant z < 1$, $1 \leqslant z < 2$, and $2 \leqslant z < 3$, respectively. On the other hand, the QG sequence is less defined that the other two, with the high-mass part ($\log_{10}(M^*)$ >10) well separated from the MS and the low-mass part very close to the MS, resulting in a slope between 0.59 and 0.69. A similar behaviour has been observed also with low-z galaxies by Renzini & Peng (2015).

#### 6.5.2.1 The evolution of the starburst and quenched galaxy fractions

In Figure 6.8 we show the sSFR probability density distribution in the three analysed redshift bins, above each stellar mass completeness. In this plot it is already evident that the number of starburst and quenched galaxies varies with redshift. The evolution of the QG fraction at low stellar masses is caused by selection effects, because some of these galaxies could be below the detection limit. On the other hand, there is clear increment on the number of SB between z∼0.75 and z∼1.5.

To investigate more this evolution, we study the fraction of the three different galaxy modes at different stellar masses and redshifts. In particular, in Figure 6.9 we show the ratio between the number of starburst (quenched) galaxies respect to the total number galaxies for

different stellar mass and redshift bins. Galaxies in our sample are classified depending on the three Gaussian fits of the sSFR distribution in each stellar mass bin. The number of galaxies in each mode is derived by integrating the associated Gaussian component in each stellar mass and redshift bin. In general, MS galaxies are the dominant mode, however, at $\log_{10}(M^*)$ >10.5 and z<2, quenched galaxies are >25%. At $\log_{10}(M^*)$ >10, the number of QG decreases with increasing redshift, while it is almost constant at low-intermediate stellar masses ($\lesssim 20\%$). Above this stellar mass ($\log_{10}(M^*) \sim$10) QG are also more separated from the MS, while below they are very close to the MS. This could be a stellar mass of transition between two different dominant quenching mechanisms. At z>1, the fraction of QG decreases at $\log_{10}(M^*)$ <9, however, this fraction is underestimated in this redshifts and stellar mass range because QG are below the 90% stellar mass completeness. On the other hand, the fraction of SB galaxies increases with the redshift, particularly at $\log_{10}(M^*)$ <9. Moreover, this fraction increases by $\gtrsim$2 between redshift $\sim$0.75 and $\sim$1.5. Between z=2 and z=3, the fraction of SB is similar, at least down to $\log_{10}(M^*)$ =8.5. Below this stellar mass, the sample is below $90\%$ completeness limit in stellar mass. The fraction of SB galaxies also decreases with increasing stellar mass, except at $\log_{10}(M^*)$ >10.5 at z$= 2-3$. This stellar mass range at this redshift could be contaminated by active galactic nuclei (AGN). However, these SB galaxies, when detected at $24\,\mu$m, they do not show extreme IR fluxes and, moreover, only one galaxy in each stellar mass bin is classified as AGN at X-ray wavelengths (Luo et al., 2017). Overall, looking at the total mass range above the 90% completeness ($\log_{10}(M^*)$ =8.25-11.25), SB galaxies are $\sim 5\%$ of the total number of galaxies at 0.5$\leqslant z <$1 and $\sim 14\%$ at 1$\leqslant z <$2 and 2$\leqslant z <$3.

For comparison with other works, Rodighiero et al. (2011) defined starburst as galaxies with sSFR 2.5$\sigma$ above the MS and found that 2-3% of galaxies with $\log_{10}(M^*)$ =10-11.5 are SB at 1.5$\leqslant z <$2.5, while in our work the SB fraction is generally higher in the same stellar mass range. However, Sargent et al. (2012) found a higher fraction of SB galaxies, by using the same data of Rodighiero et al. (2011) but a technique similar to the one use in this work.

Caputi et al. (2017) found that $\sim 15\%$ of all galaxies with $\log_{10}(M^*)$ >9 at z$= 4-5$ are SB. Although at these higher redshifts, SB galaxies are characterised by a much higher sSFR. This fraction is slightly higher than the fraction of SB galaxies we found at z=2-3 ($\sim 10\%$) in the same stellar mass range, showing that the evolution of the fraction of SB in this stellar mass range seems to continue up to z=5.

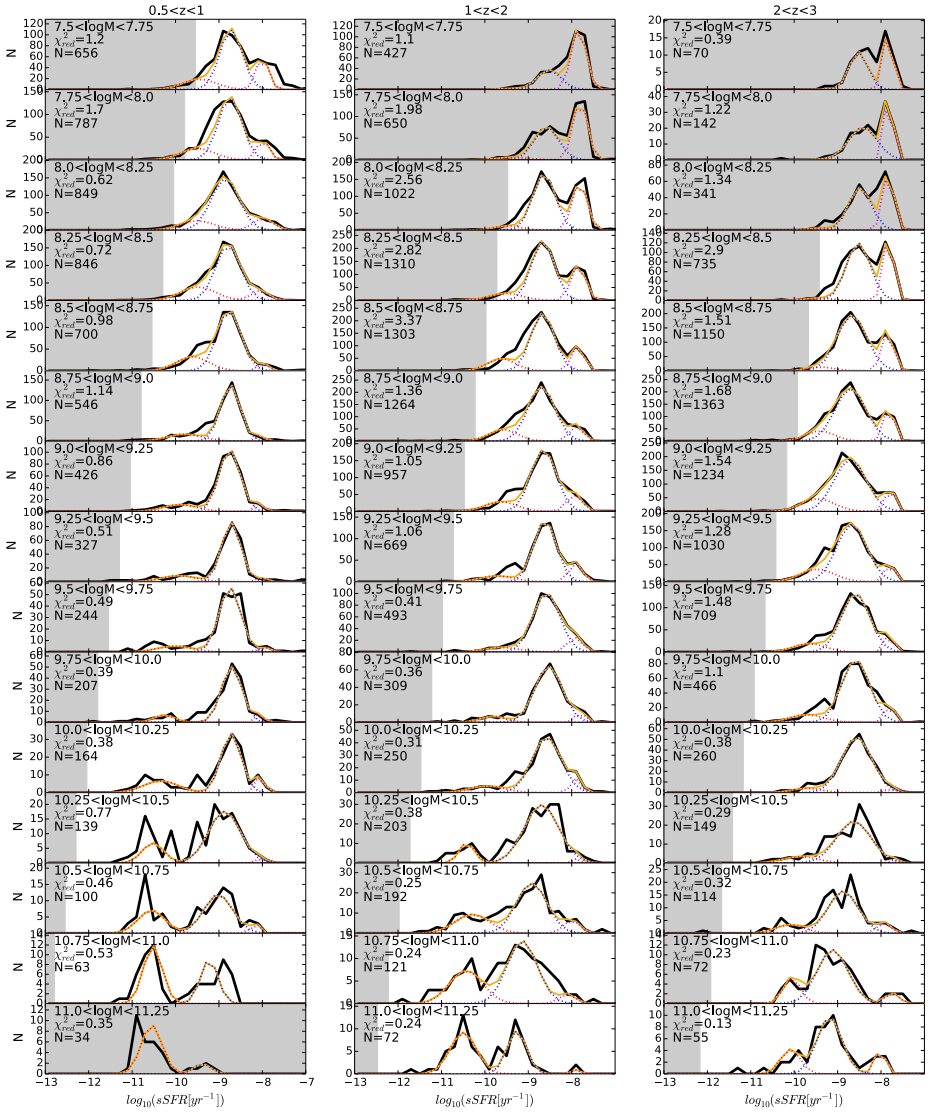


**Figure 6.6:** sSFR distribution of the CANDELS sample in different z and stellar mass bins. Each column shows a different redshift bin: $0.5 \leqslant z < 1$ (*left*), $1 \leqslant z < 2$ (*central*) and $2 \leqslant z < 3$ (*right*). Each row shows a different stellar mass bin, with a width of 0.25 dex, from $7.5 \leqslant log_{10}(M^*) < 7.75$ (*top*) to $11 \leqslant log_{10}(M^*) < 11.25$ (*bottom*). Black thick continuous lines show the sSFR distribution and the yellow thin continuous lines are the best fitted models. Dotted lines are the different Gaussian components: quenched galaxies (*red*), MS galaxies (*blue*) and starburst galaxies (*magenta*). The $\chi^2_{red}$ of each fit and the number of galaxies in each bin are shown in the top-left of each panel. Grey areas show the sSFRs and stellar masses for which this sample is not complete (below the $3\sigma$ limit in sSFR or below the 90% completeness in stellar mass), or panels that have too low statistic (N<50).

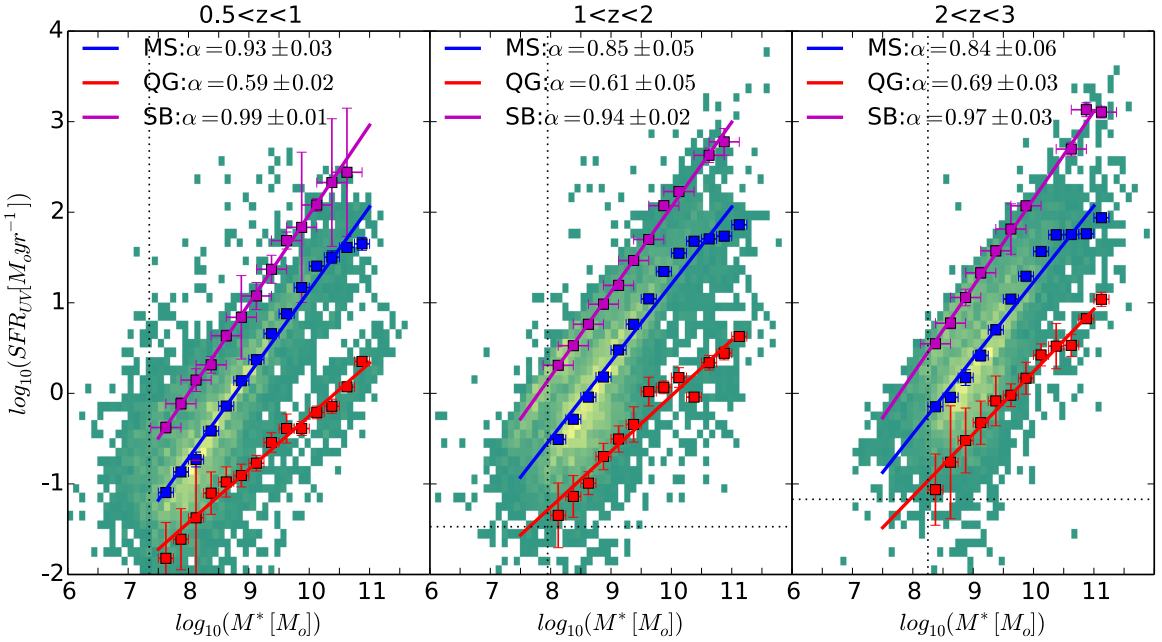


**Figure 6.7:** SFR-M* plane with the best ODR fits for the three galaxy modes: quenched galaxies (*red line*), MS galaxies (*blue line*) and SB galaxies (*magenta line*). The slope of each sequence is reported on the top-left of each panel. Squared symbols are the Gaussian peak positions of the three components in each stellar mass bins with the associated error in the position, as derived from the fit. In the background there are all galaxies in our sample divided in SFR-M* bins of 0.1×0.1 dex. Each bin is coloured coded depending on the number of galaxies inside each bin, from green to yellow in a linear scale. The vertical black dotted lines are the 90% completeness limit in stellar mass in each redshift bin. The horizontal dotted black lines are the 3$\sigma$ detection limit in SFR in each redshift bin.

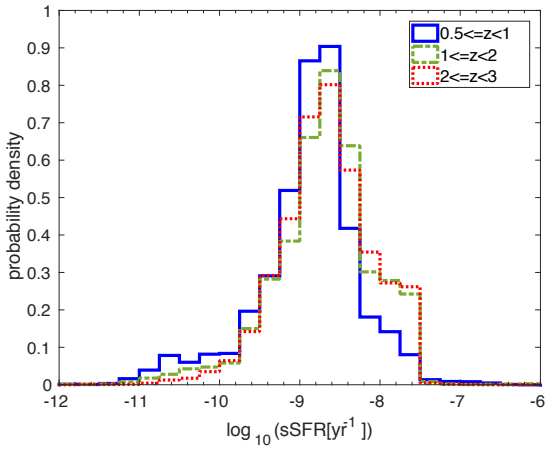


Figure 6.8: sSFR probability density distribution of all CANDELS galaxies in different z, only considering sources above stellar mass completeness.

#### 6.5.2.2 Impact of using different IR conversion formulae to derive the bolometric IR luminosity

In Figure 6.10, we show the SFR-M* plane, with $SFR_{IR}$ derived using the 5 different $L_{IR}$ conversion formulae analysed in this chapter. When IR observations are not available, we use the dust-corrected, UV-based SFR. The MS is derived in each case by fitting an ODR to the Gaussian mean in the sSFR distribution in each 0.25 dex stellar mass bin. The best fit values derived using this method are listed in Table 6.1.

Observations in the IR are available only for galaxies with $\log_{10}(M^*) \gtrsim 10$, therefore in this work we can mainly analyse the impact of different $L_{IR}$ conversion formulae on the high-mass end of the MS and, in particular, on its flattening. The MS slopes change of less than 0.1 with all methods and at all redshifts. In particular, at $0.5 \leqslant z < 1$, the Ba24 method shows the flattest slope, $0.86 \pm 0.05$, while the SED fit method has the steepest slope, $0.95 \pm 0.03$. At $1 \leqslant z < 2$, adding the IR observations decreases the slope of 0.02 dex for all methods, excluded the SED fit method for which the slope increases of 0.01. At $2 \leqslant z < 3$, the differences are slightly higher than in the lower redshift bin, between -0.02 and +0.05. However, taking into account the errors associated to each slope, all slopes derived by using only UV data or including IR observations are consistent with each other.

When including IR observations, the flattening of the MS change depending on the $L_{IR}$ conversion formulae used and, in some cases (e.g. Ba24 method at z=2-3) the MS is consistent with no flattening. Therefore,

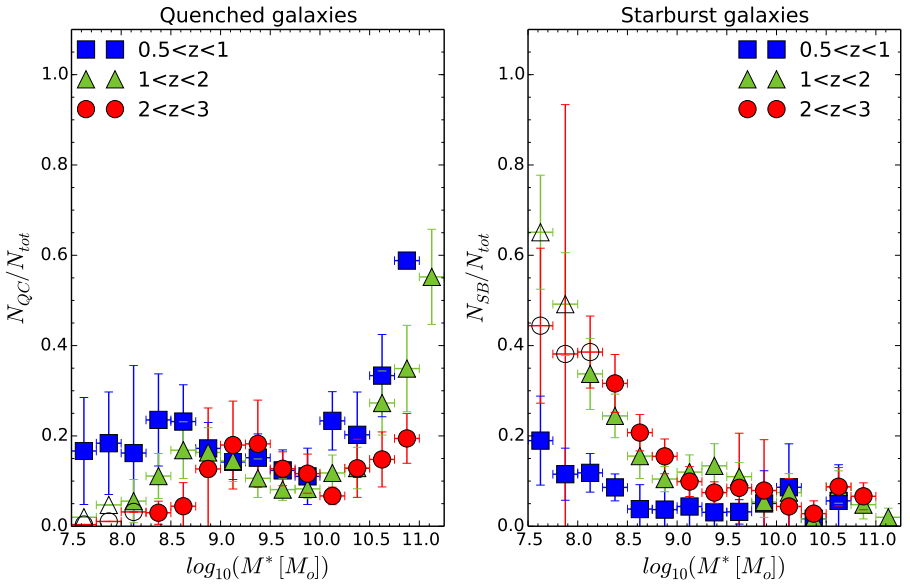


**Figure 6.9:** *Left:* ratio between QG and the total number of galaxies in our sample at different stellar masses. *Right:* ratio between SB and the total number of galaxies in our sample at different stellar masses. Points are divided into three different redshift bins: $0.5 \leqslant z < 1$ (*blue squares*), $1 \leqslant z < 2$ (*green triangles*) and $2 \leqslant z < 3$ (*red circles*). Empty symbols correspond to stellar mass bins where the sample is below the 90% mass completeness.

a careful inclusion of IR observations is necessary to properly quantify the flattening of the MS at high stellar masses.

**Table 6.1:** Slope and intercept ($log_{10}SFR = a + b \cdot log_{10}M^*$) of the MS in different redshift bins and for different $SFR_{IR}$ derivation methods. The MS is derived by using an ODR fitting to the mean position of the MS Gaussian component in the SFR distribution inside each 0.25 dex stellar mass bin.

| method | $0.5 \leq z < 1$ | | $1 \leq z < 2$ | | $2 \leq z < 3$ | |
|---|---|---|---|---|---|---|
| | a | b | a | b | a | b |
| $SFR_{UV}$ | -8.12±0.31 | 0.93±0.03 | -7.32±0.51 | 0.85±0.05 | -7.17±0.54 | 0.84±0.06 |
| $SFR_{UV}$ & $SFR_{IR}^{C\&E}$ | -7.83±0.33 | 0.89±0.04 | -7.13±0.55 | 0.83±0.06 | -7.09±0.62 | 0.83±0.06 |
| $SFR_{UV}$ & $SFR_{IR}^{B24}$ | -7.53±0.43 | 0.86±0.05 | -7.08±0.55 | 0.83±0.06 | -7.62±0.48 | 0.89±0.05 |
| $SFR_{UV}$ & $SFR_{IR}^{B70}$ | -8.25±0.31 | 0.94±0.03 | -7.16±0.50 | 0.83±0.05 | -7.39±0.67 | 0.86±0.07 |
| $SFR_{UV}$ & $SFR_{IR}^{Ri09}$ | -7.86±0.33 | 0.89±0.03 | -7.09±0.54 | 0.83±0.06 | -7.00±0.66 | 0.82±0.07 |
| $SFR_{UV}$ & $SFR_{IR}^{fit}$ | -8.33±0.32 | 0.95±0.03 | -7.40±0.49 | 0.86±0.05 | -7.41±0.71 | 0.87±0.07 |

## 6.6 SUMMARY AND CONCLUSIONS

In this work we have studied the SFR-M* plane for a sample of 24463 galaxies at $0.5 \leqslant z \leqslant 3$ with photometry from the UV through the near-IR. In particular, we firstly derived the MS with a linear fitting and, secondly, we studied quenched, star-forming and starburst galaxies, separating them by fitting their sSFR distribution with three Gaussian components. In addition, we analysed the impact of different bolometric IR luminosities conversion formulae on the MS of SF galaxies for a subsample with IR observations.

In our first method, we derived the MS of star-forming galaxies applying a method commonly used in the literature. Specifically, we fitted a linear regression for all SF galaxies, defined as all galaxies with $\log_{10}(sSFR) >$ -9.8. The derived MS slope depends on the stellar mass range considered and our results are consistent with the values found in the literature once we considered the same stellar mass range.

As a second step, we decomposed the sSFR distribution in different stellar mass and redshift bin. Three components are evident (quenched, SF and SB galaxies) with different importance depending on the stellar mass and the redshift considered. In particular, the SB population increases in

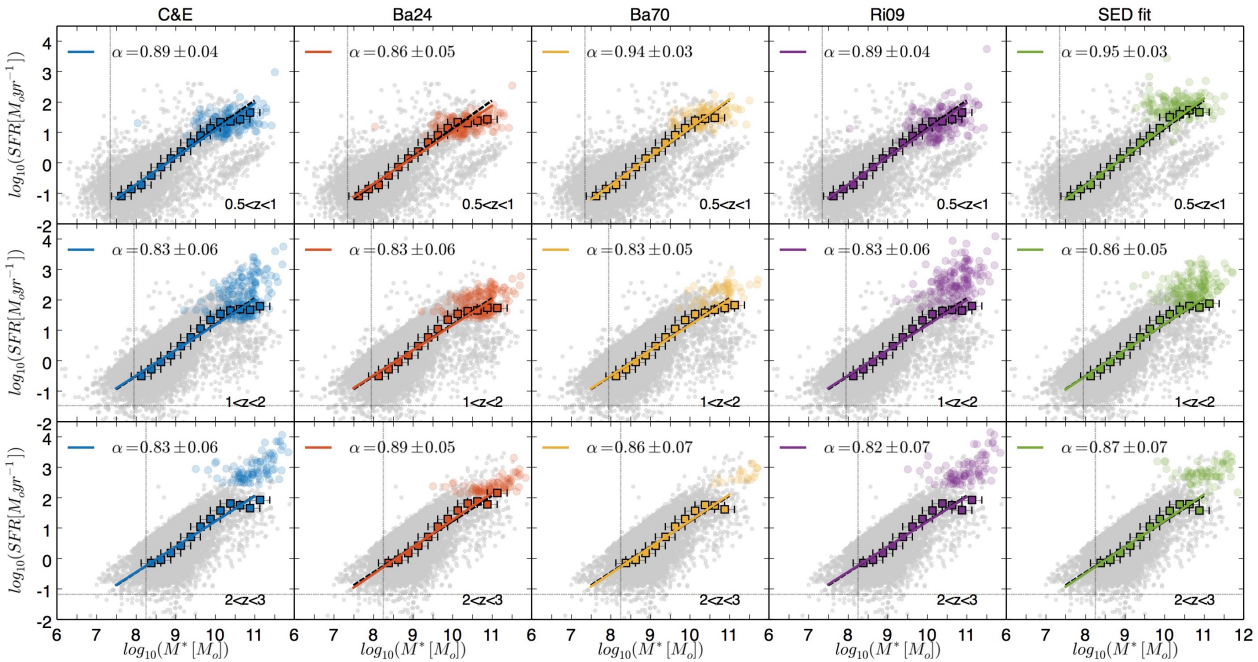


**Figure 6.10:** SFR versus stellar mass for different redshift bins. *From top to bottom:* redshifts $0.5 < z \leq 1$, $1 < z \leq 2$ and $2 < z <\leq 3$. Grey points are all CANDELS data in the GOODS-S without IR observations and their SFR is derived from the UV. Coloured points in each panel are the $24\,\mu$m detected galaxies and in each column their SFR are obtained with different methods. *From left to right:* C&E, Ba24, Ba70, Ri09 and IR SED fitting. In each panel, the black dashed line shows the best fit for the MS using the CANDELS data with SFR derived only from the UV, as shown in Fig 6.5. The coloured lines show the best fit adding the $24\,\mu$m detected galaxies and the slope values of each MS is reported at the top-left of each panel. Each MS is derived with an ODR fit using the Gaussian mean position derived fitting the sSFR distribution in each stellar mass bins. The mean positions of the MS Gaussian component in each stellar mass bin are shown in each panel with coloured squares. Error bars are the errors in the mean position of the MS Gaussian component derived from the fit.

number with increasing redshift, especially for galaxies with $\log_{10}(M^*)$ <9 between z$\sim$0.75 and z$\sim$1.5, where their fraction increases from less than 20$\%$ up to 40$\%$. The SB fraction increases also with decreasing stellar mass. Overall, SB galaxies are $\sim 5\%$ at z=0.5-1 and $\sim 14\%$ at z=1-3, respect to the total number of galaxies with $\log_{10}(M^*) = 8.25 - 11.25$ at the same redshifts. On the other hand, the quenched galaxies increase in number with stellar masses and they are a substantial fraction at $\log_{10}(M^*)$ >10.5 at z<2 (20-60$\%$). The fraction of quenched galaxies also decreases with redshift. The slope of the MS changes from 0.93$\pm$0.03 at $0.5 < z \leq 1$ to 0.84$\pm$0.06 at $2 < z <\leq 3$, decreasing with the redshift. However, a slight bending is present at high stellar masses ($\log_{10}(M^*)$ >10.25) and the MS at lower masses is consistent with a slope of $\sim 1$ and a mild evolution with redshift. A tight sequence of SB galaxies is also present, with a slope close to unity. On the other hand, quenched galaxies show a less clear sequence, they seem separated from the MS at $\log_{10}(M^*)$ >10 and closer to the MS at lower stellar masses.

In addition, we analysed the impact of using different IR luminosity derivation method on the high mass-end of the MS. In particular, we considered two methods to convert $24\,\mu$m luminosity to $L_{IR}$ (C&E and Ba24), one to convert 70$\mu$m luminosity to $L_{IR}$ (Ba70), one to convert flux at $24\,\mu$m to SFR (Ri09), and a fifth one that derives the $L_{IR}$ by fitting 24-160$\mu$m observations by using empirical IR SED templates.

In general, the slope of the MS changes by <0.1 when including the $SFR_{IR}$, with all different $L_{IR}$ derivation methods, both with a simple linear regression and decomposing the sSFR distribution with the Gaussian components. However, a proper analysis and inclusion of the $SFR_{IR}$ is essential when analysing the MS slope at high stellar mass and its possible flattening. Indeed, this flattening is visible when using only the UV-based SFR, while the MS is consistent with no flattening with some other IR-based SFR.

Overall, using different fitting techniques and different $L_{IR}$ derivation methods, we derived slopes between 0.86 and 0.95, at $0.5\leqslant z <1$, between 0.83 and 0.87, at $1\leqslant z <2$, and between 0.82 and 0.89 at $2\leqslant z <3$, with a scatter of $\sim$0.1. A dependence of the MS slope with the stellar mass is evident, therefore a flatterer (steeper) MS slope could be derived limiting the study to high (low) stellar masses. Depending on the analysed redshift and stellar mass range, it could be necessary to distinguish between quenched, SF and starburst galaxies in order to derive the MS without contaminants.

*Acknowledgements:* This work is based on observations taken by the CANDELS Multi-Cycle Treasury Program with NASA/ESA HST, which is operated by the Association of Universities for Research in Astronomy, Inc., under NASA contract NAS5-26555. *Herschel* is an ESA space observatory with science instruments provided by European-led Principal Investigator consortia and with important participation from NASA. LB and KIC acknowledge the support of the Nederlandse Onderzoekschool voor de Astronomie (NOVA). KIC also acknowledges funding from the European Research Council through the award of the Consolidator Grant ID 681627-BUILDUP. We thank N.D. Padilla for the useful discussions.

# 7. Conclusions and future prospects

## 7.1 Thesis highlights

Astronomy is a science largely based on the data analysis, and these data are the final product of continuous research and developments both in physics and engineering. This PhD thesis deals with different parts of this procedure, starting from the test of an instrument calibration method and the image correction for an instrumental effect, through the design of future observations and ending with an example of a scientific analysis of astronomical observations. The common aim of all these different steps and instruments analysed in this thesis is the expansion of our knowledge of galaxy formation and evolution at different cosmic epochs by observing in the infrared wavelength range. Below, I report the main highlights and conclusions of this PhD thesis.

### 7.1.1 MKID calibration method

In the traditional calibration method of MKID arrays, an astronomical point source is scanned with every pixel of the array. However, A-MKID will have 25000 pixels and this calibration method would be very time expensive. For this reason, in Chapter 2, I proposed and tested an alternative calibration method, based on MKID readout frequency response. I demonstrated the

validity of this calibration method by comparing the responsivity derived with a calibrated optical source in the lab with the responsivity predicted by the method based on the readout frequency response. The latter has the advantage of being fast enough to be used in large arrays, such as A-MKID, and of not requiring additional observations, because it is based on data that are already necessary to identify the spatial position of KIDs in the array. Moreover, the noise equivalent temperature derived with this calibration method, which is a measurement of the sensitivity of the instrument, is linear to $\pm 10\%$ over a wide range of readout frequency offset and power, respect to $> 50\%$ variation of the optical source calibration method at large readout frequency offset and powers.

Overall, I found that this method is ideal to calibrate large MKID arrays, such as A-MKID. In fact, this method is now standardly apply in the lab in Groningen.

### 7.1.2 Crosstalk in MKIDs

The crosstalk effect, which consists on the coupling between KIDs due to the proximity of their resonance frequencies, is not a negligible effect on large MKIDs. In Chapter 3, I analysed this effect on an array of 880 KIDs and found that $\sim 72\%$ of all KIDs of the array are coupled with at least another detector, above -30dB level. With a careful analysis of the point spread function, I identified the coupled detectors and subtracted their contribution from the original image. This is a valid method to correct astronomical images for the crosstalk effect a posteriori, storing the information about the crosstalk of the array. Moreover, by measuring the Quality-factor and the resonance frequency of each KID, I modelled the general level of crosstalk as a function of the frequency separation between KIDs, assuming the same dip depth for all detectors. In particular, I found that a crosstalk of $\sim$-25 dB corresponds to a separation in frequency of about 10 bandwidths between KIDs. This result can be used as a general description of the crosstalk when designing future MKID arrays.

In the future, a more complex model, which, for example, take into account asymmetries and deviations from the Lorenztian shape in the transmission, is necessary to predict with more precision the crosstalk of individual KIDs directly from the transmission.

### 7.1.3 Deriving galaxy properties with JWST

All astronomical observations are conducted on the basis of a careful balance between the quality of the results and the used exposure time, in

order to maximise the first and minimise the second. As it is the case for the most galaxy surveys conducted with current telescopes, SED fitting will be the main method used to derive galaxy properties in blank galaxy surveys with JWST, by using observations with the two imaging cameras on board. The quality of galaxy properties derivation with this method highly depends on the wavelength coverage. Following these ideas, in Chapter 4 and 5 I performed some tests in order to understand the necessary JWST band coverage to derive good quality galaxy properties, i.e. photometric redshift, stellar mass, age, colour excess and specific star formation rate, by using observed galaxies between z=0.5-6 and simulated galaxies at z=7-10. I considered 8 NIRCam broad-band filters, MIRI F560W and F770W broad-band filters and ancillary ground-based and HST (F435W and F606W) observations.

I found that the 8 NIRCam broad-bands alone are not sufficient to recover good photometric redshifts for galaxies at z<7. Indeed, in order to distinguish between 4000 Å and the Lyman break and improve the photometric redshift estimation, observations with HST F435W and F606W bands, and ground-based U band if possible, are indeed necessary. For galaxies at z=7-10, NIRCam data alone are sufficient to derive good photometric redshifts, if the signal-to-noise is high (S/N>10), and observations with the MIRI F560W and F770W bands improve the redshift recovery, particularly at lower S/N values.

If galaxies between z=7 and 9 have a conventional (BC03) SED shape, then observations with the 8 NIRCam broad-bands are also sufficient to properly recover their stellar masses. However, at z=10, MIRI observation are crucial to detect the continuum at $\lambda > 4000\,\text{Å}$ and have a good estimation of the stellar mass.

When considering other galaxy properties, the NIRCam broad-bands are also sufficient to estimate both the age and the colour excess for the majority of galaxies at all redshifts and to derive the specific star formation rate up to z=9. The MIRI bands are necessary to remove some extreme outliers on age and colour excess and to properly estimate the specific star formation rate at z=10.

Overall, these tests are a useful reference when planning JWST observations to understand the best band coverage depending on the redshift analysed and the scientific aim of the observations. In general, observations with both cameras are necessary in order to perform an accurate study of galaxy evolution and mass assembly up to early cosmic times.

#### 7.1.3.1 The role of emission lines on galaxy properties estimation

The impact of emission lines on the stellar mass estimation is already known at low-redshift (e.g. Stark et al., 2013; Santini et al., 2015) and their occurrence may be more frequent at high redshifts, when galaxies were in general very young. In the tests presented in this thesis I included a type of templates with a complex set of nebular emission lines, in order to analyse their effect on the galaxy properties derivation (*Yggdrasil* templates; see Chapters 4-5).

The main result is that multiple emission lines boost the fluxes making the galaxy brighter in some bands, but their presence in all broad-bands make the SED convolved with the filters featureless and the galaxy properties estimation challenging. Indeed, by using only NIRCam broad-band filters the photometric redshift is difficult and the stellar mass is generally overestimated. The addition of observations with the two most sensitive MIRI broad-band filters only mildly improves the estimation of both quantities.

The first spectroscopic observations of young, high-redshift galaxies with JWST will probably determine the frequency and the importance of nebular emission lines in high-z galaxies and allow us to understand how much we need to worry about the stellar mass estimation derived with broad-band photometry in these cases. The first spectroscopic samples will be useful to calibrate the stellar corrections that need to be applied on the stellar masses derived from the photometric analysis.

### 7.1.4 The SFR-M$^*$ plane

SFR and stellar mass are two fundamental quantities to study galaxy evolution and mass assembly at different cosmic times. It is important, for example, to understand how galaxies populate the main-sequence in the SFR-M$^*$ plane at different redshifts. In Chapter 6 I analysed the SFR-M$^*$ plane for a sample of galaxies at z=0.5-3, using publicly available photometry from the UV to the mid-IR. In particular, I applied a multi-Gaussian fitting to the sSFR distribution at different redshift ranges to separate quenched, star-forming and starburst galaxies. This method allowed me to derive the MS without contamination from quenched or starburst galaxies and without applying a colour cut selection, as it is usually done in the literature.

The derived main sequence slope shows a slope close to unity al low stellar mass and a flattening at high stellar mass, as it was also previously found in the literature. However, this observed slope change at high stellar

masses depends on the SFR estimation method and a careful analysis of the total IR luminosity is necessary to confirm this flattening.

Interesting, the fraction of starburst and quenched galaxies derived in this thesis varies both with redshift and stellar mass. In particular, starbursts make $\sim 5\%$ of all galaxies at z=0.5-1.0, while their fraction increases to $\sim 14\%$ of all galaxies at 1<z<3 with $\log_{10}(M^*)$ =8.25-11.25. An open question is indeed the reason for this change in the fraction of starburst galaxies with stellar mass, which could be due, for example, to a higher frequency of mergers among low stellar mass galaxies than among high stellar mass ones. Moreover, the fraction of starburst galaxies generally increases with decreasing stellar mass, particularly at $\log_{10}(M^*)$ <9. On the other hand, the fraction of quenched galaxies increases with increasing stellar mass and decreasing redshift.

Overall, the separation of these different components in the SFR-M* plane over a wide range of stellar masses is fundamental to understand the importance of the different modes of star formation at different cosmic times.

## 7.2 FUTURE PROSPECTS

The arrival of new telescopes has the main purpose of answering to some fundamental questions that guided their construction, but, even more interesting, it brings to other unexpected discoveries. Therefore, trying to list the future prospects of JWST or A-MKID is difficult and would probably be incomplete. Here, I concentrate to some questions and opportunities for the next future that arises from this thesis.

• The construction of A-MKID took more than expected, but have deepened our understanding of KID technology, which now seems more appealing and feasible for future ground and space missions than before. Large, deep surveys are fundamental to extend sub-mm galaxy samples both in number and luminosities. A-MKID will hopefully be only one among future sub-mm instruments which will help us to collect statistically significant information on sub-mm galaxies.

• As discussed in this thesis, the presence of nebular emission lines can extremely complicate the recovery of fundamental galaxy properties, such as redshift and stellar mass. With JWST spectral capabilities, it will be possible to observe a sample of high-z galaxies to analyse their SED and better understand how important it is, in reality, the contribution of these nebular emission lines. In case their contribution is not negligible as it is expected, it could be necessary to conduct complementary studies on

different observational strategies than the ones reported in this thesis, which could include, for example, some JWST medium-band filters. Moreover, future JWST spectra could be used as empirical templates to also understand if all of the currently used galaxy templates should be considered as equally likely at high redshifts.

• With a moderate integration time it may be possible to observe with NIRCam the UV light of galaxies in the core of the main-sequence up to high redshift, taking into account that a $\log_{10}(SFR) \sim 0$ corresponds to a $\mathrm{mag}_{UV} \sim 29$ at z$\sim$12. Therefore, it will be possible to analyse the SFR-M$^*$ relation up to very high redshift, passing the cosmic peak of star formation and reaching the early stage of the Universe's life. Moreover, the analyses of galaxies with low stellar mass, which is now possible only at low redshifts (z$<$2), will be also extended up to z$\sim$5, allowing us to understand if the starburst fraction continues to increase with redshift and what is their contribution to the cosmic star formation rate density.

# Bibliography


Anders, P. & Fritze-v. Alvensleben, U. 2003, A&A, 401, 1063

Arnouts, S., Cristiani, S., Moscardini, L., et al. 1999, MNRAS, 310, 540

Ashby, M. L. N., Willner, S. P., Fazio, G. G., et al. 2015, ApJS, 218, 33

Bagnasco, G., Kolm, M., Ferruit, P., et al. 2007, in Proc. SPIE, Vol. 6692, Cryogenic Optical Systems and Instruments XII, 66920M

Balestra, I., Mainieri, V., Popesso, P., et al. 2010, A&A, 512, A12

Bardeen, J., Cooper, L. N., & Schrieffer, J. R. 1957, Physical Review, 108, 1175

Baselmans, J. 2012, Journal of Low Temperature Physics, 167, 292

Baum, W. A. 1957, AJ, 62, 6

Bavouzet, N., Dole, H., Le Floc'h, E., et al. 2008, A&A, 479, 83

Behroozi, P. S., Wechsler, R. H., & Conroy, C. 2013, ApJ, 770, 57

Bender, A. N., Ade, P. A. R., Anderson, A. J., et al. 2016, in Proc. SPIE, Vol. 9914, Millimeter, Submillimeter, and Far-Infrared Detectors and Instrumentation for Astronomy VIII, 99141D

Bertin, E. & Arnouts, S. 1996, A&AS, 117, 393

Bisigello, L., Caputi, K. I., Colina, L., et al. 2016a, ApJS, 227, 19

Bisigello, L., Yates, S. J. C., Murugesan, V., et al. 2016b, Journal of Low Temperature Physics, 184, 161

Bouchet, P., García-Marín, M., Lagage, P.-O., et al. 2015, PASP, 127, 612

Bourne, N., Dunlop, J. S., Merlin, E., et al. 2017, MNRAS, 467, 1360

Bouwens, R. J., Bradley, L., Zitrin, A., et al. 2014, ApJ, 795, 126

Bouwens, R. J., Illingworth, G. D., Oesch, P. A., et al. 2012, ApJ, 754, 83

Brinchmann, J., Charlot, S., White, S. D. M., et al. 2004, MNRAS, 351, 1151

Bruzual, G. & Charlot, S. 2003, MNRAS, 344, 1000

Buat, V. & Xu, C. 1996, A&A, 306, 61

Bunker, A. J., Stanway, E. R., Ellis, R. S., et al. 2003, MNRAS, 342, L47

Calvo, M., Roesch, M., Désert, F.-X., et al. 2013, A&A, 551, L12

Calzetti, D. 2013, Star Formation Rate Indicators, ed. J. Falcón-Barroso & J. H. Knapen, 419

Calzetti, D., Armus, L., Bohlin, R. C., et al. 2000, ApJ, 533, 682

Caputi, K. I., Deshmukh, S., Ashby, M. L. N., et al. 2017, ArXiv e-prints

Caputi, K. I., Dunlop, J. S., McLure, R. J., et al. 2012, ApJLett, 750, L20

Caputi, K. I., Ilbert, O., Laigle, C., et al. 2015, ApJ, 810, 73

Caputi, K. I., Lilly, S. J., Aussel, H., et al. 2008, ApJ, 680, 939

Cardamone, C. N., van Dokkum, P. G., Urry, C. M., et al. 2010, ApJS, 189, 270

Chabrier, G. 2003, PASP, 115, 763

Chary, R. & Elbaz, D. 2001, ApJ, 556, 562

Chervenak, J. A., Irwin, K. D., Grossman, E. N., et al. 1999, Applied Physics Letters, 74, 4043

Cristiani, S., Appenzeller, I., Arnouts, S., et al. 2000, A&A, 359, 489

Croom, S. M., Warren, S. J., & Glazebrook, K. 2001, MNRAS, 328, 150

Dahlen, T., Mobasher, B., Faber, S. M., et al. 2013, ApJ, 775, 93

Dale, D. A. & Helou, G. 2002, ApJ, 576, 159

Day, P. K., LeDuc, H. G., Mazin, B. A., et al. 2003, Nature, 425, 817

de Visser, P. J., Goldie, D. J., Diener, P., et al. 2014, Physical Review Letters, 112, 047004

Desert, F. X., Boulanger, F., Leger, A., et al. 1986, A&A, 159, 328

Dickinson, M., Stern, D., Giavalisco, M., et al. 2004, ApJLett, 600, L99

Doherty, M., Bunker, A. J., Ellis, R. S., et al. 2005, MNRAS, 361, 525

Dole, H., Lagache, G., & Puget, J. 2006, in Astronomical Society of the Pacific Conference Series, Vol. 357, Astronomical Society of the Pacific Conference Series, ed. L. Armus & W. T. Reach, 290

Doyon, R., Hutchings, J. B., Beaulieu, M., et al. 2012, in Proc. SPIE, Vol. 8442, Space Telescopes and Instrumentation 2012: Optical, Infrared, and Millimeter Wave, 84422R

Dunlop, J. S., McLure, R. J., Biggs, A. D., et al. 2017, MNRAS, 466, 861

Elbaz, D., Dickinson, M., Hwang, H. S., et al. 2011, A&A, 533, A119

Erb, D. K., Shapley, A. E., Pettini, M., et al. 2006, ApJ, 644, 813

Finlator, K., Oppenheimer, B. D., & Davé, R. 2011, MNRAS, 410, 1703

Fontana, A., Dunlop, J. S., Paris, D., et al. 2014, A&A, 570, A11

Fumagalli, M., Patel, S. G., Franx, M., et al. 2012, ApJLett, 757, L22

Galliano, F. 2004, PhD thesis, Service d'Astrophysique, CEA/Saclay, L'Orme des Merisiers, 91191 Gif sur Yvette, France

Gardner, J. P., Mather, J. C., Clampin, M., et al. 2009, Astrophysics and Space Science Proceedings, 10, 1

Geach, J. E., Chapin, E. L., Coppin, K. E. K., et al. 2013, MNRAS, 432, 53

Giavalisco, M., Ferguson, H. C., Koekemoer, A. M., et al. 2004, ApJLett, 600, L93

Glasse, A., Rieke, G. H., Bauwens, E., et al. 2015, PASP, 127, 686

Grogin, N. A., Kocevski, D. D., Faber, S. M., et al. 2011, ApJS, 197, 35

Guo, Y., Ferguson, H. C., Giavalisco, M., et al. 2013, ApJS, 207, 24

Güsten, R., Nyman, L. Å., Schilke, P., et al. 2006, A&A, 454, L13

Holland, W. S., Bintley, D., Chapin, E. L., et al. 2013, MNRAS, 430, 2513

Holland, W. S., Robson, E. I., Gear, W. K., et al. 1999, MNRAS, 303, 659

Hubble, E. P. 1925, ApJ, 62

Hubble, E. P. 1936, Realm of the Nebulae

Hughes, D. H., Dunlop, J. S., & Rawlings, S. 1997, MNRAS, 289, 766

Ikarashi, S., Ivison, R. J., Caputi, K. I., et al. 2017, ApJ, 835, 286

Ilbert, O., Arnouts, S., Le Floc'h, E., et al. 2015, A&A, 579, A2

Ilbert, O., Arnouts, S., McCracken, H. J., et al. 2006, A&A, 457, 841

Ilbert, O., Capak, P., Salvato, M., et al. 2009, ApJ, 690, 1236

Irwin, K. D. 2002, Physica C Superconductivity, 368, 203

Irwin, K. D., Audley, M. D., Beall, J. A., et al. 2004, Nuclear Instruments and Methods in Physics Research A, 520, 544

Jaacks, J., Nagamine, K., & Choi, J. H. 2012, MNRAS, 427, 403

Janssen, R. M. J., Baselmans, J. J. A., Endo, A., et al. 2013, Applied Physics Letters, 103, 203503

Johnston, R., Vaccari, M., Jarvis, M., et al. 2015, MNRAS, 453, 2540

Karim, A., Schinnerer, E., Martínez-Sansigre, A., et al. 2011, ApJ, 730, 61

Kennicutt, Jr., R. C. 1998, ApJ, 498, 541

Koekemoer, A. M., Faber, S. M., Ferguson, H. C., et al. 2011, ApJS, 197, 36

Konno, A., Ouchi, M., Ono, Y., et al. 2014, ApJ, 797, 16

Kuiper, G. P., Wilson, W., & Cashman, R. J. 1947, ApJ, 106, 243

Kurczynski, P., Gawiser, E., Acquaviva, V., et al. 2016, ApJLett, 820, L1

Kurk, J., Cimatti, A., Daddi, E., et al. 2013, A&A, 549, A63

Lagache, G., Puget, J.-L., & Dole, H. 2005, ARA&A, 43, 727

Le Fèvre, O., Tasca, L. A. M., Cassata, P., et al. 2015, A&A, 576, A79

Le Fèvre, O., Vettolani, G., Garilli, B., et al. 2005, A&A, 439, 845

Low, F. J. 1969, Science, 164, 501

Low, F. J. & Tucker, W. H. 1968, Physical Review Letters, 21, 1538

Luo, B., Brandt, W. N., Xue, Y. Q., et al. 2017, ApJS, 228, 2

Lutz, D. 2014, ARA&A, 52, 373

Lutz, D., Poglitsch, A., Altieri, B., et al. 2011, A&A, 532, A90

Madau, P. 1995, ApJ, 441, 18

Madau, P. & Dickinson, M. 2014, ARA&A, 52, 415

Magnelli, B., Popesso, P., Berta, S., et al. 2013, A&A, 553, A132

Maiolino, R., Nagao, T., Grazian, A., et al. 2008, A&A, 488, 463

Mazin, B. A. 2005, PhD thesis, California Institute of Technology, California, USA

Mazin, B. A. 2009, in American Institute of Physics Conference Series, Vol. 1185, American Institute of Physics Conference Series, ed. B. Young, B. Cabrera, & A. Miller, 135–142

Meyer, M. R., Rieke, M., Eisenstein, D., et al. 2004, in Bulletin of the American Astronomical Society, Vol. 37, American Astronomical Society Meeting Abstracts, 385

Mignoli, M., Cimatti, A., Zamorani, G., et al. 2005, A&A, 437, 883

Monfardini, A., Benoit, A., Bideaud, A., et al. 2011, ApJS, 194, 24

Monfardini, A., Swenson, L. J., Bideaud, A., et al. 2010, A&A, 521, A29

Morris, A. M., Kocevski, D. D., Trump, J. R., et al. 2015, AJ, 149, 178

Noeske, K. G., Weiner, B. J., Faber, S. M., et al. 2007, ApJLett, 660, L43

Oke, J. B. & Gunn, J. E. 1983, ApJ, 266, 713

Oliver, S., Frost, M., Farrah, D., et al. 2010, MNRAS, 405, 2279

Papovich, C., Dole, H., Egami, E., et al. 2004, ApJS, 154, 70

Pardo, J. R., Cernicharo, J., & Serabyn, E. 2001, IEEE Transactions on Antennas and Propagation, 49, 1683

Peng, Y.-j., Lilly, S. J., Renzini, A., et al. 2014, ApJ, 790, 95

Pentericci, L., Vanzella, E., Fontana, A., et al. 2014, ApJ, 793, 113

Pilbratt, G. L., Riedinger, J. R., Passvogel, T., et al. 2010, A&A, 518, L1

Poglitsch, A., Waelkens, C., Geis, N., et al. 2010, A&A, 518, L2

Popesso, P., Dickinson, M., Nonino, M., et al. 2009, A&A, 494, 443

Puget, J.-L., Abergel, A., Bernard, J.-P., et al. 1996, A&A, 308, L5

Rafelski, M., Teplitz, H. I., Gardner, J. P., et al. 2015, AJ, 150, 31

Ravikumar, C. D., Puech, M., Flores, H., et al. 2007, A&A, 465, 1099

Renzini, A. & Peng, Y.-j. 2015, ApJLett, 801, L29

Rieke, G. H., Alonso-Herrero, A., Weiner, B. J., et al. 2009, ApJ, 692, 556

Rieke, G. H., Su, K. Y. L., Stansberry, J. A., et al. 2005, ApJ, 620, 1010

Rieke, G. H., Wright, G. S., Böker, T., et al. 2015, PASP, 127, 584

Rieke, G. H., Young, E. T., Engelbracht, C. W., et al. 2004, ApJS, 154, 25

Rodighiero, G., Daddi, E., Baronchelli, I., et al. 2011, ApJLett, 739, L40

Rodighiero, G., Renzini, A., Daddi, E., et al. 2014, MNRAS, 443, 19

Salpeter, E. E. 1955, ApJ, 121, 161

Santini, P., Ferguson, H. C., Fontana, A., et al. 2015, ApJ, 801, 97

Sargent, M. T., Béthermin, M., Daddi, E., et al. 2012, ApJLett, 747, L31

Schaerer, D. 2002, A&A, 382, 28

Schreiber, C., Pannella, M., Elbaz, D., et al. 2015, A&A, 575, A74

Shivaei, I., Reddy, N. A., Shapley, A. E., et al. 2015, ApJ, 815, 98

Silverman, J. D., Mainieri, V., Salvato, M., et al. 2010, ApJS, 191, 124

Smail, I., Ivison, R. J., & Blain, A. W. 1997, ApJLett, 490, L5

Smail, I., Ivison, R. J., Owen, F. N., et al. 2000, ApJ, 528, 612

Smit, R., Bouwens, R. J., Labbé, I., et al. 2016, ApJ, 833, 254

Soifer, B. T., Helou, G., & Werner, M. 2008, ARA&A, 46, 201

Speagle, J. S., Steinhardt, C. L., Capak, P. L., et al. 2014, ApJS, 214, 15

Stanway, E. R., Bunker, A. J., McMahon, R. G., et al. 2004a, ApJ, 607, 704

Stanway, E. R., Glazebrook, K., Bunker, A. J., et al. 2004b, ApJLett, 604, L13

Stark, D. P., Schenker, M. A., Ellis, R., et al. 2013, ApJ, 763, 129

Steinhardt, C. L., Speagle, J. S., Capak, P., et al. 2014, ApJLett, 791, L25

Strolger, L.-G., Riess, A. G., Dahlen, T., et al. 2004, ApJ, 613, 200

Sturm, E., Lutz, D., Genzel, R., et al. 1999, Ap&SS, 266, 169

Swenson, L. J., Cruciani, A., Benoit, A., et al. 2010, Applied Physics Letters, 96, 263511

Szokoly, G. P., Bergeron, J., Hasinger, G., et al. 2004, ApJS, 155, 271

Tacchella, S., Dekel, A., Carollo, C. M., et al. 2016, MNRAS, 457, 2790

Tasca, L. A. M., Le Fèvre, O., Hathi, N. P., et al. 2015, A&A, 581, A54

Tielens, A. G. G. M. 2008, ARA&A, 46, 289

Tomczak, A. R., Quadri, R. F., Tran, K.-V. H., et al. 2016, ApJ, 817, 118

Tremonti, C. A., Heckman, T. M., Kauffmann, G., et al. 2004, ApJ, 613, 898

van der Wel, A., Franx, M., van Dokkum, P. G., et al. 2004, ApJLett, 601, L5

van Rantwijk, J., Grim, M., van Loon, D., et al. 2016, IEEE Transactions on Microwave Theory and Techniques, 64, 1876

Vanzella, E., Cristiani, S., Dickinson, M., et al. 2008, A&A, 478, 83

Vanzella, E., Fontana, A., Pentericci, L., et al. 2014, A&A, 569, A78

Weiß, A., Kovács, A., Coppin, K., et al. 2009, ApJ, 707, 1201

Whitaker, K. E., Franx, M., Leja, J., et al. 2014, ApJ, 795, 104

Whitaker, K. E., van Dokkum, P. G., Brammer, G., et al. 2012, ApJLett, 754, L29

Wright, G. S., Wright, D., Goodson, G. B., et al. 2015, PASP, 127, 595

Yates, S. J. C., Baselmans, J. J. A., Baryshev, A. M., et al. 2014, Journal of Low Temperature Physics, 176, 761

Zackrisson, E., Binggeli, C., Finlator, K., et al. 2017, ApJ, 836, 78

Zackrisson, E., Rydberg, C.-E., Schaerer, D., et al. 2011, ApJ, 740, 13

Zmuidzinas, J. 2012, Annual Review of Condensed Matter Physics, 3, 169

# Riassunto
## *Sunto*


Meno di un secolo fa la nostra concezione dell'Universo era limitata alla nostra Galassia, la Via Lattea, in quanto gli astronomi erano convinti che essa costituisse l'intero Universo. Nel 1925, Edwin Hubble misurò la distanza del primo oggetto chiaramente al di fuori della Via Lattea e l'Universo iniziò a popolarsi di numerose galassie che, da allora, vengono studiate come pilastri portanti dell'Universo.

Uno degli aspetti più affascinanti dell'Universo è il fatto che, guardando galassie sempre più lontane da noi, stiamo allo stesso tempo guardando nel passato e, così, ci è possibile studiare come le galassie,

*Manco de un secoło fa a nostra inpressión deł'Universo xèra limità ała nostra stesa Gałasia, la Via Làtea, e i astronomi i xèra convinti che la costituise tutto l'Universo. Intel 1925, Edwin Hubble xè stá il primo che el ga misurá ła distansa de un mistiero pałesemente fòra dała Via Làtea, e l'Universo, da chel momento, ga tacá riempirse de tantisime gałasie, che i no xè altro che i piłastri portanti deł'Universo.*

*Una dełe robe pi bełe deł'Universo xè il fato che, vardando łe gałasie pi foravìa te ste vardando, in contemporanea, in drio in tel tempo e, così, xè posibiłe studiar come łe gałasie, e in generałe l'Universo, se sia formà*

e in generale l'Universo, si siano formati ed evoluti. Fino ad oggi, sono state osservate galassie fino a circa 12.7 miliardi di anni fa, che corrisponde a $\sim$750 milioni di anni dopo il Big Bang, e i telescopi di prossima generazione spingeranno ulteriormente questo limite, permettendoci di osservare le prime galassie formate nell'Universo.

Le lunghezze d'onda infrarosse costituiscono la parte dello spettro elettromagnetico tra la luce visibile ($<0.7\,\mu$m) e le microonde ($>1$ mm). Queste lunghezze d'onda sono importanti per osservare sia la luce emessa dalle stelle di galassie lontane, la quale è spostata a lunghezze d'onda più lunghe a causa dell'espansione dell'Universo, sia la luce occultata di stelle che viene assorbita e riemessa dalla polvere che le circonda.

Questa tesi di dottorato analizza le prestazioni di futuri strumenti infrarossi, i quali sono centrali nello studio della formazione ed evoluzione delle galassie. Questi strumenti sono il rivelatore ad induttanza cinetica nel microonde (A-MKID, dall'inglese Apex Microwave kinetic Inductance Detector), il quale sarà operativo nel telescopio APEX, e le due fotocamere NIRCam e MIRI, le quali faranno parte del telescopio spaziale *James Webb* (JWST). Inoltre, come parte di questa tesi, ho condotto uno studio che illustra l'importanza scientifica di ottenere tassi di formazione stellare e masse stellari affidabili, le quali, appunto, sono

*e sia cambiá. Fin uncò, xè sta viste gałasie lontàn fin 12.7 miłiardi de ani fa, che xè come dire $\sim$750 miłioni de ani dopo il Big Bang, e i tełescopi che vegnarà i paràrà vànti sto limite par vardare anca łe prime gałasie che se ga formà intel'Universo.*

*Łe lunghese d'onda infrarose le xè che ła parte deło spetro ełetromagnètego che sta tra la luxè vixibiłe ($<0.7\,\mu$m) e łe microonde ($>1$mm). Ste lunghese d'onda łe xè importanti par vardare la luxè che la vien da łe stełe dełe gałasie foravìa, che la xè sponstà a lunghese d'onda pi longhe par via de l'espanxion del'Universo, ma anca par vardare la luxè dełe stełe che la vien asorbia e riemesa dała polvare che la sta torno.*

*Sta tesi de dotorato la varda łe prestasiòn dei stumenti infrarosi che vegnarà, i quałi i xè xentrałi intelo studio dea formaxiòn e evoluxiòn dełe gałasie. Sti strumenti i xè il revełatore a indutanxa cinetica intel microonde (A-MKID, dał'inglexe Apex Microwave kinetic Inductance Detector), che el funxionará intel tełescopio APEX, e łe dò fotocamare NIRCam e MIRI, che le farà parte deło tełescopio spaxiałe James Webb (JWST). In pi, come parte de sta tesi, go anca fato uno studio par vardar l'importanza sìentifica de 'vére ła quantità de formaxiòn stełare e le mase stełari jùste, łe quałi łe vien, appunto, da oservaxioni intel vixibiłe e intel infraroso.*

ottenute a partire da osservazioni nell'ottico e nell'infrarosso.

## APEX e A-MKID

A-MKID è uno strumento per il telescopio APEX (Fig. 7.3) il quale è un antenna radio di 12 metri posizionato ad un'altezza di 5105 metri sul livello del mare, nell'Osservatorio Llano de Chajnantor nelle Ande cilene, ed è operativo sin dal 2005. Chajnantor fu scelto come luogo per il telescopio APEX perché si tratta di uno dei luoghi più secchi del pianeta e le osservazioni a lunghezze d'onda sub-millimetriche (0.3-1.0 mm) sono altamente sensibili alla presenza di vapore acqueo. APEX è una collaborazione tra l'Istituto di radioastronomia Max Planck (MPIfR), l'osservatorio spaziale di Onsala (OSO) e l'organizzazione europea per la ricerca astronomica nell'emisfero australe (ESO) ed è la più grande antenna nell'emisfero australe ad osservare a lunghezze d'onda sub-millimetriche.

A-MKID è uno strumento in parte olandese and in parte tedesco ed è costituito da rilevatori ad induttanza cinetica (kinetic inductance detectors in inglese) ed osserverà attraverso le finestre di trasmissione atmosferica a 350 $\mu$m e 850 $\mu$m con una risoluzione di 7 secondi d'arco a 350 $\mu$m e 17 secondi d'arco a 850 $\mu$m. Il punto di forza di A-MKID è il suo ampio campo visivo, i.e. $>15\times15$ arcmin$^2$ che corrisponde

*A-MKID xè no strumento pal tełescopio APEX (Fig. 7.3) che el xè na antenna radio de 12 metri che la xè cata a 5105 metri sora el liveło del mare, intel Oservatorio Llano de Chajnantor intele Ande cilene, e el funxiona dal 2005. Chajnantor xè sta scelto come posto pal tełescopio APEX perché xè trata de uno dei posti pi suti del mondo e le lunghese d'onda submiłimetriche (0.3-1 mm) łe xè sensibiłi ała presenxa de vapore acqueo, cioè ała nibia. APEX xè na colaboraxion tra l'Istituto de radioatronomia Max Planck (MPIfR), l'oservatorio spaxiale de Onsala (OSO) e l'organizaxion europea par la ricerca astronomica intel emisfero austrałe (ESO) e xè la pi granda antena intel emisfero austrałe che el poe vardare a lunghese d'onda sub-miłimetriche.*

*A-MKID xè no strumento en parte ołandese e in parte tedesco e el xè fato de revełatori a indutanxa cinetica (kinetic inductance detectors in inglexe) e el vardarà intele finestre de trasmixion atmosferica a 350 $\mu$m e 850 $\mu$m con na risoluxion de 7 secondi d'arco a 350 $\mu$m e 17 secondi d'arco a 850 $\mu$m. El punto de forxa de A-MKID xè el so campo de vista, $>15\times15$ arcmin$^2$ che xè circa un terxo deł'area dea Luna intel ziel. Sto grando campo de vista xè dovuo al grando numero de pixel che ghe xè intelo strumento*

all'incirca a un terzo dell'area occupata dalla Luna nel cielo. Questo ampio campo visivo è dovuto al grande numero di pixel presenti all'interno dello strumento (>3000) edè fondamentale per osservare ampie zone di cielo e rilevare oggetti che sono luminosi ma rari, come, per esempio, le galassie sub-millimetriche.

Le galassie sub-millimetriche sono galassie molto luminose e con molta polvere a z$\sim$ 3. In particolare, queste galassie sono molto luminose a lunghezze d'onda sub-millimetriche ma sono molto tenui nell'ottico, a causa dell'assorbimento della luce stellare da parte della polvere. Queste galassie sono interessanti in quanto sono considerate una fase evolutiva cruciale della formazione delle galassie più massive, compatte e passive (cioè che non formano nuove stelle) osservate a basso redshift, cioè relativamente vicino alla Via Lattea.

*(>3000) xè importante par vardare grandi zone del ziel e catare gałasie che le xè ciare ma rare, come, par esempio, łe gałasie sub-miłimetriche.*

*Łe gałasie sub-miłimetriche le xè gałasie tanto ciàre a lunghese d'onda sub-miłimetriche ma fiache intel vixibiłe, parché la luxè stełare la vien asorbia dala polvare. Ste gałasie le xè interesanti in quanto le xè considerà na parte evolutiva importante intela formaxion de le gałasie pi massive, fisse e pasive (cioè che non łe forma nove stełe) viste a basso redshift, cioè chi tacà.*

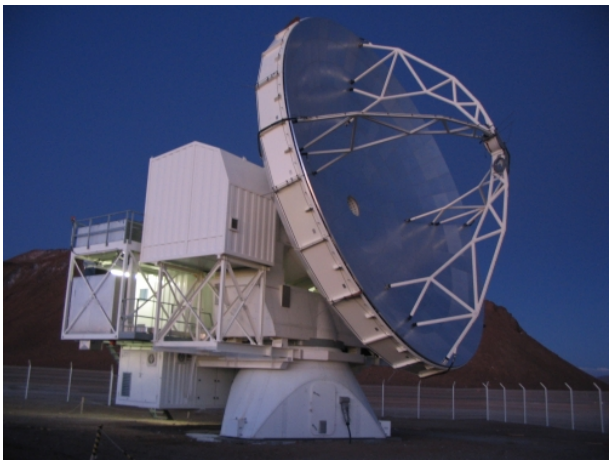

**Figura 7.1:** Telescopio APEX. Crediti: pagina internet di APEX

## JWST

JWST (Fig. 7.4) è un telescopio spaziale infrarosso che sarà lanciato nel 2018 e sarà operativo per 5-10 anni ed è una collaborazione tra l'agenzia spaziale americana (NASA), quella europea (ESA) e quella canadese (CSA). Ha uno specchio primario di 6.5 metri suddiviso in 18 segmenti esagonali che permettono allo specchio di piegarsi per essere contenuto all'interno del razzo e saranno poi mossi nella giusta posizione dopo il lancio. Quando verrà lanciato, JWST sarà il più grande telescopio mai inviato nello spazio.

JWST osserverà a lunghezze d'onda infrarosse, tra 0.6 $\mu$m e 28.5 $\mu$m, con squisita risoluzione angolare usando i 4 strumenti disponibili a bordo, cioè NIRCam, MIRI, NIRSpec e NIRISS. In dettaglio, NIRCam ha 29 filtri, con ampiezza extra-larga, larga, media e stretta, che possono osservare tra 0.6 e 5 $\mu$m, mentre MIRI osserverà con 9 filtri larghi tra 5 e 28 $\mu$m.

La combinazione di questi due strumenti è indispensabile per osservare la luce ottica emessa dalla stelle, la quale è spostata a lunghezze d'onda infrarosse a causa dell'espansione dell'Universo. In questo modo sarà possibile osservare galassie fino a redshift z$\sim$10, cioè solo $\sim$500 milioni di anni dopo il Big Bang, per poter studiare la formazione ed evoluzione delle galassie per 13 miliardi di anni.

*JWST (fig. 7.4) xè un tełescopio spaxiałe infraroso che el vegnarà lancià intel 2018 e el sarà funxionante par 5-10 ani e el xè na colaboraxion tra l'agenzia spaxiale americana (NASA), queła europea (ESA) e queła canadese (CSA). El ga no specio primario de 6.5 metri diviso in 18 tocheti esagonałi che ghe permete de starghe dentro al razo e , poi, sti tocheti i se sistemerà dopo el lancio. Quando el vegnarà lancià, JWST el sarà el tełecopio pi grando mai invià intelo spaxio.*

*JWST vardarà a lunghese d'onda infrarose, tra 0.6 $\mu$m e 28.5 $\mu$m, con squisita risoluxion angołare usando i 4 strumenti che el ga, che i xè NIRCam, MIRI, NIRSpec e NIRISS. In detajo, NIRCam el ga 29 filtri, con ampieza extra-larga, larga, media e streta, che i poe vardare tra 0.6 e 5 $\mu$m, mentre MIRI vardarà con 9 filtri larghi tra 5 e 28 $\mu$m.*

*La cobinaxion de sti do strumenti la xè indispensabiłe par vardare la luxè vixibiłe emesa dałe stełe che la vien spostà a lunghese d'onda infrarose par l'espanxion del'Universo. In sto modo sarà posibiłe vardare łe gałasie fin a redshift z$\sim$10, cioè sołamente $\sim$500 miłioni de ani dopo el Big Bang, par poter studiar ła formaxion ed evoluxion dełe gałasie par 13 miłiardi de ani.*

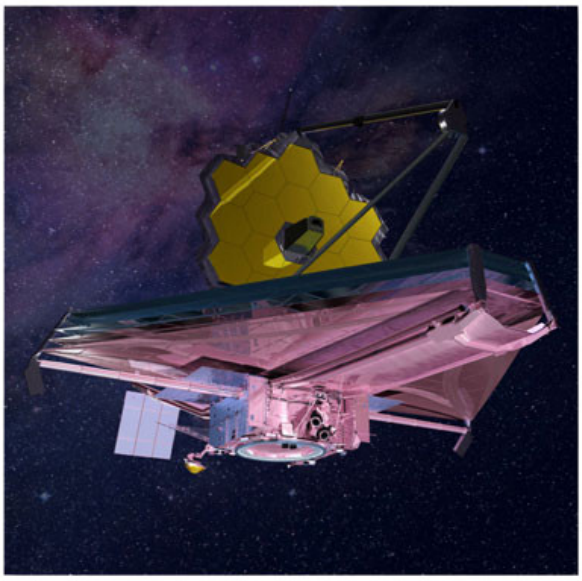

**Figura 7.2:** Riproduzione artistica di JWST. Crediti: NASA

## QUESTA TESI

In questa tesi di dottorato, ho analizzato differenti aspetti delle prestazioni di A-MKID e JWST e, inoltre, ho condotto uno studio sul tasso di formazione stellare e la massa in stelle per un gruppo di galassie a z<3 (cioè fino a 11.3 miliardi di anni fa). Questo studio potrà essere esteso in futuro a distanze maggiori utilizzando JWST. Di seguito sono riportati le conclusioni e i punti principali di questa tesi di dottorato.

- Il punto di forza di A-MKID è il suo ampio campo visivo, dovuto al grande numero di pixel. Però, questo pregio rappresenta anche una sfida, in quanto i metodi di calibrazione usati tradizionalmente richiedono un tempo troppo lungo

*In sta tesi de dotorato, go analizà difarenti aspeti dełe prestaxion de A-MKID e JWST e, in pi, go fato no studio sułа quantitá de formaxion stełare e dea masa stełare de un mucio de gałasie a z<3 (fin a 11.3 miłiardi de ani fa). Sto studio el podarà esare slargà a distanse pi grandi con JWST intei ani che varà. Intela prosima parte ghe xè scrite łe conclusioni e i punti pi importanti de sta tesi de dottorato.*

- *El punto de forxa de A-MKID xè el so campo de vista largo, che el xè dovù al grando numero de pixel. Però, sto pregio xè pure na sfida, in quanto par usar i metodi de calibraxion sołiti serve un tempo masa lungo par calibrare la matrice*

per calibrare l'intera matrice. Per questa ragione, nel Capitolo 2, ho proposto e collaudato un metodo di calibrazione alternativo e ho dimostrato la sua validità, confrontandolo con un metodo tradizionale di calibrazione usato in laboratorio. Il nuovo metodo da me testato è sufficientemente veloce da poter essere usato su rivelatori MKID con numerosi pixel e, inoltre, richiede dati che sono già disponibili. Di conseguenza, questo metodo di calibrazione é ideale per A-MKID.

- In uno rivelatore MKID, alcuni pixel sono accoppiati uno all'altro, perché sono troppo vicini in frequenza. Come risultato, quando un fotone è assorbito da un rivelatore, tutti i pixel ad esso associato risponderanno al medesimo segnale. Questo effetto è chiamato crosstalk e può essere solo minimizzato con una progettazione accurata dello strumento. Nel Capitolo 3, ho analizzato l'effetto crosstalk per una matrice di 880 pixel e ho trovato che la maggior parte dei pixel è accoppiata con almeno un altro pixel, mostrando un segnale spurio sopra 0.1% rispetto al segnale massimo. Di conseguenza, ho identificato i rivelatori accoppiati e ho sottratto il loro segnale dall'immagine di partenza, dimostrando che è possibile correggere a posteriori un'immagine astronomica per l'effetto crosstalk.

- Nei Capitoli 4 e 5, ho simulato osservazioni con i filtri larghi di JWST/NIRCam e MIRI di galassie fino a z=10 (che corrisponde a $\sim$ 13

*intiera. Par sta rajone, intel Capitolo 2, go proposto e provà un difarente metodo de calibraxion e go dimostrà che el xè vałido, paragonandolo a un metodo de calibraxion usà de sołito intel laboratorio. El novo metodo che go testà xè sufijentemente veloce da poder esare usà intei rivełatori MKID con un saco de pixel e, in pi, pa farlo serve dati che i xè sa usà par altri motivi. Perciò, sto novo metodo de calibraxione xè parfeto par A-MKID*

- *Intel revełatore MKID, calche pixel po essere ligà uno a chealtro, parchè i xè masa tacà in frequenxa. El risultato xè che, quando un fotone el vien asorbio da un revełatore, tutti i pixel che xè ligà a queo e risponde ało steso segnałe. Sto efeto vien ciamà crosstalk (chel vol dir ciacołe incroxa) e el pò esare soltanto minimizà pianificando ben ło strumento. Intel Capitolo 3, go analizà na matrice de 880 pixel e go catà che la major parte dei pixel i xè ligà almanco a 'naltro, mostrando un segnałe in pi sora 0.1% paragonà al segnałe masimo. De conseguenza, go identificà i rivełatori ligà e go cavà el loro segnał dala imagine iniziałe, demostrando che xè posibiłe coregere a posteriori na imagine astronomica par sto efeto crosstalk.*

- *Intei Capitoi 4 e 5, go simułà oservaxioni con i filtri larghi de JWST/NIRCam e MIRI de gałasie fino a z=10 (che vol dire $\sim$13 miłiardi de ani fa) par capire quałe xè la mijor combinaxion de filtri de JWST par 'vère le proprietà dełe gałasie, come ła loro distansa e ła loro masa*

miliardi di anni fa) per comprendere quale sia la miglior combinazione dei filtri di JWST per ottenere le proprietà delle galassie, come la loro distanza e la loro massa in stelle. Ho trovato che osservazioni ausiliarie a lunghezze d'onda minori di quelle osservabili con JWST (per esempio con alcuni filtri del telescopio spaziale Hubble) saranno necessarie per ottenere distanze sufficientemente corrette per galassie a z<7 (cioè fino a 12.7 miliardi di anni fa). A z=7-9 (tra 12.7 e 12.9 miliardi di anni fa), i filtri larghi di NIRCam saranno sufficienti per ottenere le proprietà di queste galassie, a patto che il segnale sia almeno dieci volte più elevato del rumore (S/N>10). A z=10 (corrispondente a 13 miliardi di anni fa), invece, sia i filtri di NIRCam che quelli di MIRI saranno necessari per ottenere la distanza e la massa in stelle delle galassie. Tuttavia, per alcuni tipi particolari di galassie (cioè galassie con righe d'emissione nebulari) a z=7-10, sarà complicato ottenere le loro proprietà usando una qualsiasi combinazione di filtri larghi di JWST e dovremo aspettare le prime osservazioni di JWST per capire la frequenza e l'importanza di questa tipologia di galassie. In generale, tutte le analisi condotte in questi due capitoli saranno una referenza utile quando si pianificheranno future osservazioni con JWST.

- Il tasso di formazione stellare e la massa in stelle sono due quantità fondamentali nello studio

*in stełe. Go catà che oservaxioni a lunghese d'onda pi curte de quełe che poe vardare JWST (par esempio con alcuni filtri del tełescopio spaxiale Hubble) le xè necesarie par 'vère redshift justi par le gałasie a z<7 (cioè fin 12.7 miłiardi de ani fa). A z=7-9 (tra 12.7 e 12.9 miłiardi de ani fa), i filtri larghi de NIRCAm i xè sufijenti par 'vère e proprietà dełe gałasie, basta che el segnałe sia almanco diexe volte pi forte del rumore (S/N>10). A z=10 (che vol dir 13 miłiardi de ani fa), invese, sia i filtri de NIRCam che quei de MIRI i xè necesari par 'vère ła distansa e la masa in stełe dełe gałasie. Tutavia, par alcuni tipi particołari de gałasie (cioè gałasie con righe d'emissione nebulari) a z=7-10, xè dificiłe 'vère e loro proprietà con qualsiasi tipo de combinaxion de filtri larghi de JWST e dovaremo spetare e prime oservaxioni de JWST par capire a frequensa e importansa de sto tipo de gałasie. In generałe, tutte e anałisi fate in sti do capitoi le xè utiłi quando se decidendarà łe oservasioni che vegnarà con JWST.*

- *La quantità de formaxion de stełe e la masa in stełe le xè do quantità fondamentali intelo studio del'evoluxion dele gałasie e dela loro cresita in masa in difarenti periodi cosmici. La major parte dele gałasie łe mostra na streta relaxion tra ste do quantità, ciamà sequienza principałe (main sequence en inglexe), che la xè pò spiegar con na formaxion de stełe longa e stabiłe. D'altro canto, calche gałasia, ciamà starburst, le forma un saco de stełe par la masa*

dell'evoluzione delle galassie e della loro crescita in massa in diversi tempi cosmici. La maggior parte della galassie mostra una stretta correlazione tra queste due quantità, chiamata sequenza principale (main sequence in inglese), spiegabile con una formazione stellare lunga e stabile. D'altro canto, alcune galassie, chiamate starburst, detengono tassi di formazione stellare molto più elevata di quanto ci si aspetterebbe data la loro massa in stelle, mentre altre, chiamate passive, mostrano nessuna o poca formazione stellare rispetto alla loro massa in stelle. Nel Capitolo 6, ho analizzato il tasso di formazione stellare e la massa in stelle di un gruppo di galassie a redshift z=0.5-3 (tra 5 e 11.3 miliardi di anni fa), con lo scopo di analizzare la frazione delle differenti modalità di formazione stellare a diverse masse stellari e distanze. Ho trovato che la frazione di galassie starburst aumenta col aumentare della loro distanza da noi e col diminuire della massa in stelle, questo potrebbe essere spiegato con una simile variazione nel tasso di incontri e fusioni tra galassie. La frazione di galassie passive invece aumenta coll'aumentare della massa in stelle e diminuisce all'aumentare della loro distanza da noi. Questo tipo di analisi potrà essere esteso a distanze maggiori con JWST, al fine di comprendere se la frazione di galassie starburst ha continuato ad aumentare in passato e quale sia il loro contributo alla formazione

*che le gà, mentre altre, ciamà passive, le mostra poco o niente de formaxion de stełe. Intel Capitolo 6, go analizà la quatità de formaxion de stełe e la masa in stełe de un mucio de gałasie a redshift z=0.5-3 (tra 5 e 11.3 miłiardi de ani fa), con l'obietivo de studiar la fraxion dei diversi modi de formare stełe a difarenti mase stełari e distanse. Go catà che la fraxion de gałasie starburst crese col cresere deła distansa da nojaltri e col calare dela massa in stełe, questo podaria esare dovù a un simiłe cambiamento intel numero de incontri e fuxion tra gałasie. La fraxion de gałasie pasive invese crese col cresere dela masa e cala col cresere deła distansa da nojaltri. Sto tipo de analisi el sarà posibiłe a distanse majori con JWST, così podaremo capire se la fraxion de gałasie starburst el ga continuà a cresare intel passà e quałe xè el loro contributo intela formaxione stełare globałe deł'Univeso.*

stellare globale dell'Universo.

# SAMENVATTING

Minder dan een eeuw geleden was ons begrip van het universum beperkt tot ons eigen sterrenstelsel, de Melkweg, en astronomen dachten dat dit ons hele universum omvatte. In 1925 mat Edwin Hubble de afstand tot het eerste object dat zich duidelijk buiten de Melkweg bevond en vanaf dat moment werd duidelijk dat het universum uit talrijke sterrenstelsels bestaat, die sindsdien bestudeerd zijn als de bouwstenen van het universum.

Één van de meeste fascinerende aspecten van de astronomie is dat sterrenstelsels die verder weg staan zich verder in het verleden bevinden en dat we dus terug kijken in de tijd. Op deze manier kunnen we bestuderen hoe het universum en de sterrenstelsels zijn gevormd en geëvolueerd. Tot nu toe zijn er waarnemingen van sterrenstelsels tot aan 12.7 miljard jaar geleden, slechts $\sim$750 miljoen jaar na de oerknal. De volgende generatie telescopen zal deze grens verder verschuiven en ons in staat stellen om de eerste sterrenstelsels die vormden in het universum te observeren.

Infrarode golflengtes bevatten het deel van het elektromagnetische spectrum tussen het zichtbare licht ($<0.7\,\mu$m) en microgolven ($>1$ mm). Deze golflengtes zijn belangrijk om het door het uitdijen van het heelal roodverschoven stellaire licht van erg verafgelegen sterrenstelsels waar te nemen. Daarnaast kunnen we op deze golflengtes het door omringend

stof geabsorbeerde en opnieuw uitgezonden vertroebelde licht van sterren zien.

Dit proefschrift richt zich op de analyse van de kwaliteit van uitvoering van toekomstige infrarood instrumenten met sleutelposities voor studies naar sterrenstelselevolutie en -vorming. In het bijzonder zal het gaan over de APEX Microwave Kinetic Inductance Detector (A-MKID) voor de APEX-telescoop en de twee beeldcameraś (NIRCam en MIRI) aan boord van de *James Webb Space Telescope* (JWST). Daarnaast heb ik met een studie het wetenschappelijke belang van betrouwbare stervormingssnelheden en stellaire massaś aan de hand van optische en nabij-infrarode waarnemingen aangetoond.

## APEX en A-MKID

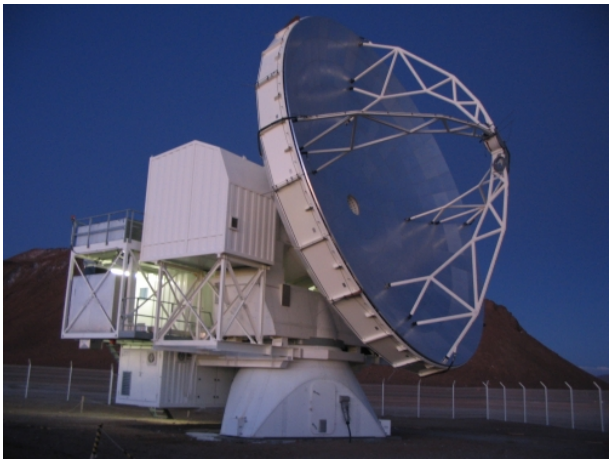

**Figuur 7.3:** APEX telescoop. Credits: APEX's webpagina

A-MKID is een instrument voor de APEX telescoop (Fig. 7.3), een 12 meter grote radioantenne die zich op een hoogte van 5105 meter bevindt als onderdeel van de Llano de Chajnantor Observatorium in de Chileense Hoge Andes die sinds 2005 operationeel is. Chajnantor werd gekozen als locatie voor de APEX omdat het één van de droogste plekken op deze planeet is en submillimeter waarnemingen (0.3-1.0 mm) zeer gevoelig zijn voor waterdampen.

A-MKID is een Duits Nederlands PI instrument voor APEX gemaakt met kinetische-inductiedetectoren. Het zal waarnemen met een resolutie van 7 boogseconde op 350 $\mu$m en 17 boogseconde op 850 $\mu$m waar de atmosfeer

transparant is. De grootste kracht van A-MKID is zijn grote blikveld van $>$ $\mathrm{boogseconde}^2$, wat grofweg overeenkomt met een derde van het oppervlak van de maan aan de hemel door het hoge aantal pixels van de camera ($>$3000). Dit is ideaal om waarnemingen te doen van grote gebieden van de hemel met als doel om heldere maar zeldzamen objecten, oftewel sub-mm sterrenstelsels, waar te nemen.

Sub-mm sterrenstelsels zijn zeer heldere en stoffige sterrenstelsels op z$\sim$3 die erg helder zijn op sub-mm golflengtes, maar erg zwak op rustsysteem optische golflengtes doordat het licht is verzwakt door stof. Ze zijn erg interessant omdat ze een cruciale evolutionaire fase vertegenwoordigen in de vorming van de meest massieve, compacte en kalme sterrenstelsels die waargenomen zijn op lage roodverschuivingen.

## JWST

JWST (Fig. 7.4) is een infrarood ruimtetelescoop die in 2018 gelanceerd zal worden en die 5-10 jaar operationeel zal zijn. Het is een samenwerking van de National Aeronautics and Space Administration (NASA), European Space Agency (ESA) en de Canadian Space Agency (CSA). Om de spiegel op te vouwen in de raket heeft de telescoop een 6,5 meter primaire spiegel gemaakt van 18 hexagonale segmenten die zich vervormen tot de juist vorm na de lancering. Ten tijde van de lancering zal het de grootste telescoop zijn die ooit de ruimte ingestuurd is.

JWST zal op infrarode golflengtes tussen 0.6 $\mu$m en 28.5 $\mu$m met buitengewone hoekresolutie waarnemen, door gebruik te maken van de vier instrumenten aan boord, te weten NIRCam, MIRI, NIRSpec en NIRISS. NIRCam heeft bovendien 29 filters met extra brede, brede, middelgrote en smalle doorlaatbanden die een bereik van 0.6-5 $\mu$m beslaan. Aanvullend zal MIRI beelden in negen breedband filters van 5 tot 28 $\mu$m maken.

De combinatie van deze twee instrumenten is essentieel om het rustsysteem optische licht te volgen dat is roodverschoven naar het infrarood door de uitdijing van het universum. Op deze manier wordt het mogelijk om sterrenstelsels tot aan z$\sim$10, oftewel de eerste 500 miljoen jaar na de oerknal, te observeren, zodat het mogelijk is om de evolutie en vorming van sterrenstelsels gedurende 13 miljard jaar te bestuderen.

## Dit proefschrift

In dit proefschrift heb ik de verschillende aspecten van het functioneren van A-MKID en JWST geëvalueerd en heb ik de stervormingssnelheid

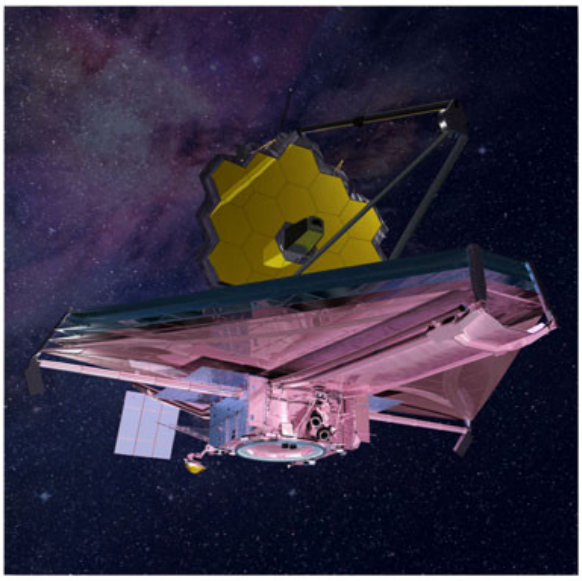

Figuur 7.4: Artist impression van JWST. Credits: NASA

en stellaire massa van een verzameling van sterrenstelsels op z$<$ 33 bestudeerd. Deze verzameling kan worden uitgebreid naar hogere roodverschuiving met JWST. Dit zijn de voornaamste hoogtepunten en conclusies van dit proefschrift.

• De voornaamste kracht van A-MKID is zijn grote blikveld als gevolg van het grote aantal pixels. Dit grote aantal pixels is echter ook een uitdaging omdat het gebruik van traditionele kalibratiemethodes een erg lange tijd vereist om de gehele collectie te kalibreren. Om deze reden heb ik in hoofdstuk 2 een alternatieve kalibratiemethode voorgesteld en getest, om vervolgens de geschiktheid te demonstreren aan de hand van een vergelijking met een traditionele kalibratiemethode in het lab. De nieuwe methode is snel genoeg om gebruikt te worden voor de kalibratie van de grote MKID arrays en is gebaseerd op al beschikbare data, waardoor de methode ideaal is voor A-MKID.

In een MKID array kunnen sommige pixels, doordat ze te dicht bij elkaar liggen met hun frequentie, gekoppeld zijn aan elkaar, zodat wanneer een foton door een detector wordt geabsorbeerd alle pixels die aan deze detector gekoppeld zijn op ditzelfde signaalreageren. Dit effect heet ”crosstalkën het kan alleen geminimaliseerd worden met een zorgvuldig ontwerp van de array. In hoofdstuk 3 heb ik de crosstalkeffecten geanalyseerd bij een array van 880 pixels en gevonden dat de meerderheid

van pixels gekoppeld zijn aan tenminste één andere pixel, door een onecht signaal van meer dan 0.1% boven de maximale respons aan te tonen. Daarom heb ik de gekoppelde detectoren geïdentificeerd en hun bijdrage van het originele beeld afgetrokken, daarmee aantonend dat het mogelijk is om sterrenkundige beelden na afloop te corrigeren voor het effect van crosstalk.

• In hoofdstukken 3 en 4 heb ik de waarnemingen van sterrenstelsels tot aan z=10 (∼13 miljard jaar geleden) met JWST/NIRCam en MIRI filters gesimuleerd met als doel om de beste combinatie van JWST breedbandfilters om de eigenschappen van sterrenstelsels, bijvoorbeeld roodverschuiiving en stellaire massa, te begrijpen. Ik heb gevonden dat de hulpwaarnemingen op kortere golflengtes dan die gebruikt zullen worden door JWST (bijvoorbeeld Hubble Space Telescope banden) noodzakelijk zijn om de roodverschuiving van sterrenstelsels op z<7 te reconstrueren. Op z=7-9 zullen de NIRCam breedbandfilters voldoende zijn om de sterrenstelseleigenschappen te achterhalen voor de meerderheid van sterrenstelsels, zo lang het signaal tenminste 10 keer sterker is dan het ruisniveau (S/N>10). Op z=10 zijn echter zowel de NIRCam als MIRI breedbanden nodig om zowel de roodverschuiving als de stellaire massa te achterhalen. Voor sommige specifieke type sterrenstelsels (oftewel sterrenstelsels met emissielijnen geproduceerd in nevels) op z=7-10 zal het echter lastig zijn om sterrenstelseleigenschappen te bepalen met elke combinatie van JWST breedband filters. De frequentie en het belang van dit type sterrenstelsels zal duidelijk worden met de eerste JWST observaties. Al deze testen zijn nuttige referenties om toekomstige JWST observaties te plannen.

• Stervormingssnelheden (Star formation rates in het Engels, hierna SFR) en stellaire massa's zijn twee fundamentele grootheden om sterrenstelselevolutie en de samenkomst van massa op verschillende kosmische tijden te bestuderen. De meerderheid van sterrenstelsels laat een nauwe relatie zien tussen deze twee grootheden, de zogenaamde hoofdreeks, die wordt verklaard met een langdurende, stabiele manier van stervorming. Hier tegenover staat dat sommige sterrenstelsels, ook wel zogenaamde "starbursts"genoemd, hogere stervormingsnelheden laten zien dan verwacht aan de hand van hun stellaire massa, terwijl andere sterrenstelsels, kalme stelsels genoemd, erg lage stervormingsnelheden laten zien voor hun stellaire massa. In hoofdstuk 6 heb ik de SFR en stellaire massa van een verzameling sterrenstelsels op z=0.5-4 geanalyseerd om de fractie te bepalen van elke modus van stervorming voor verschillende stellaire massa's en roodverschuivingen. Ik heb gevonden dat de fractie van starburststelsels toeneemt met toenemende roodverschuiving

en afnemende stellaire massa, wat verklaard kan worden door een toenemende frequentie van samensmeltende sterrenstelsels bij lagere massa sterrenstelsels en hogere roodverschuiving. De fractie van kalme sterrenstelsels neemt daarentegen toe met toenemende stellaire massa en afnemende roodverschuiving. Dit type analyse kan in de toekomst met JWST worden uitgebreid naar hogere roodverschuiving om te begrijpen of de fractie van starburststelsels blijft toenemen met roodverschuiving en wat the bijdrage van starbursts is aan de kosmische stervorminggeschiedenis.

%colorcol8

# Acknowledgements

A bit more than four years ago I applied for a PhD position just after searching on Google Maps the location of the city, unknown at that time to me, of Groningen. I did not know anything about the Netherlands, Groningen or the Kapteyn Institute and, now that I am finished, I can say that I have been extremely lucky. I am happy of these years spent at the Kapteyn, of my PhD project, of the work that I did and, in general, of all the experiences I had here. Therefore, I will briefly thank all those people that helped me to finish this PhD thesis or shared some of their time with me. My memory is known for being quite full of holes, so I ask in advance for forgiveness to everyone who should be in these acknowledgements but I forgot to include.

First of all, I would like to thank Karina for supporting and guiding me during these four years. Working with you has been extremely smooth and stimulating, and I am grateful you had a nice plan B when it was sure that A-MKID would not start to operate before the end of my PhD thesis. Moreover, thanks for always giving me nice advices both at work and outside the working environment.

The part of this PhD thesis related to engineering was particularly difficult for me, so I thank Andrey for assisting me in the first steps of my project. Moreover, I would like to thank Stephen for his patience

in explaining to me the “black magic” behind KID technology all those (numerous) times when Andrey was not available, and for showing me all the work done in the lab.

Paul, we did not interact too much during my PhD, but I would like to thank you for always being available when I needed you.

I am also very grateful to the reading committee of this thesis, Paolo, Hervè, and even more to Scott for his patience in correcting my English.

I would like to thank all secretaries of both Kapteyn and SRON, as well as both computer groups, who helped me several times during these four years.

During these years working both at Kapteyn and at SRON I met numerous friendly people, who made me feel comfortable, built a nice work environment and shared with me their free time.

I would like to thank my officemates, Cristiana, Olmo, Niels and Johan, for all the funny moments and numerous chats about tv series, Dutch and Italian traditions, pictures of cute little girls or crochet and, even more, for supporting and cheering up each other during these years. I would also like to thank our moka for making a good (Italian) coffee.

Wouter, Soh, Will and Smaran, thanks for all the useful discussion during our group meetings and for the gossips/chats outside. Wouter, thank you also a lot for translating my Summary in Dutch.

Thanks to all my football teammates, too many to be listed here individually, who allow me to play one more time my favourite sport and did not comment on my scarce skills.

One of my favourite hobby is role play gaming, therefore I would like to thank all the players that in these years shared with me fantastic adventures with dragons, orcs and wizards: Wouter (again), Mustafa, Nadine, Davide (Poppo), Enrico, Cristiana, Lorenzo, Crescenzo, Alessandro e Olmo. Moreover, thanks to everyone who was so brave to try the live role play games organised by Antonino and me, becoming first politicians in the ‘30 and then cowboys. So thanks (again, for some) to Mustafa, Tugba, Wouter, Anastasia, Cristiana, Davide M., Mery, Manolis, Davide P., Lorenzo, Enrico, Katia, Hanna. I hope I am not forgetting anyone and that we will play together again.

Grazie anche a tutti gli italiani, Davide M. e P., Crescenzo, Lorenzo, Olmo, Enrico, Cristiana, Alessandro, Marisa, Francesco e Filippo, per aver in generale sopportato la mia acidità verso l’Olanda (alla fine non è proprio così male) e per aver condiviso con me serate o pause caffè in compagnia, piene di cibo, chiacchiere e allegria.

Anastasia, thanks for convincing Antonino to be stubborn and for all the chats and the wine/tequila evenings.

And thanks, in general, to all persons who shared funny evenings and nice moments with me at work or in their free time.

Grazie alla mia amata Compagnia del dente d'avorio e affiliati, Peo, Seba, Igor, Erica, Mirko, Emmanuele e Elena, per continuare a litigare con skype e la connessione internet pur di sentirmi e giocare assieme.

Infine grazie Antonino "semplicemente" per essere al mio fianco, perchè mi supporti e sopporti in tutto quello che faccio, perchè mi calmi e rallegri nei momenti più tesi e in generale perchè stai divedendo con me il tuo tempo.

Grazie a tutta la mia famiglia, mamma, papà, Ele, Polipa e Tommaso il mio biondo preferito, per avermi incoraggiato e accompagnato in tutti questi anni. Ve vojo ben e speteme che prima o poi torno casa da voialtri!